The primary cilium is a unique lipid microdomain engineered to transduce extracellular cues

Dissertation zur
Erlangung des Doktorgrades (Dr. rer. nat.)
der Mathematisch-Naturwissenschaftlichen Fakultät
der Rheinischen Friedrich-Wilhelms-Universität Bonn

vorgelegt von

Fabian Kaiser

aus Troisdorf

Bonn, 2022

Angefertigt mit Genehmigung der Mathematisch-Naturwissenschaftlichen Fakultät
der Rheinischen Friedrich-Wilhelms-Universität Bonn

Erstgutachterin (Betreuerin):	Prof. Dr. Dagmar Wachten
Zweitgutachter:	Prof. Dr. Christoph Thiele
Fachnahes Mitglied:	Prof. Dr. Michael J. Pankratz, PhD
Fachfremdes Mitglied:	Prof. Dr. Ute Vothknecht

Tag der Promotion: 03.03.2022
Erscheinungsjahr: 2022

Declaration

Parts of this thesis have already been published or submitted for publication:

Paper:

Klausen, C., **F. Kaiser**, B. Stüven, J.N. Hansen, and D. Wachten. 2019. Elucidating cyclic AMP signaling in subcellular domains with optogenetic tools and fluorescent biosensors. *Biochem. Soc. Trans*. 47:1733-1747. DOI: 10.1042/BST20190246

Hansen, J.N., **F. Kaiser,** C. Klausen, B. Stuven, R. Chong, W. Bonigk, D.U. Mick, A. Moglich, N. Jurisch-Yaksi, F.I. Schmidt, and D. Wachten. 2020. Nanobody-directed targeting of optogenetic tools to study signaling in the primary cilium. *eLife*. 9. DOI: 10.7554/eLife.57907

Kaiser F., M. Huebecker, and D. Wachten. 2020. Sphingolipids controlling ciliary and microvillar function. *FEBS Lett*. 594:3652-3667. DOI: 10.1002/1873-3468.13816

Hansen J. N., **F. Kaiser,** P. Leyendecker, B. Stüven, J.-H. Krause, S. F. Derakhshandeh G., J. Irfan, M. Kraut, H. Theis, A. D. Drews, E. De-Domenico, K. Händler, D. J. P. Henderson, D. U. Mick, and D. Wachten. 2022. A novel cAMP signalosome in primary cilia – a nexus driving gene expression and kidney cyst formation. In revision for publication in EMBO Rep.

Poster:

Kaiser F. and Wachten D.
How phosphoinositides control protein function in primary cilia. “Immunoscience Days 2017” of the Immunosensation excellence cluster, 13.-14.11.2017, Biomedizinisches Zentrum (BMZ), University Hospital, Bonn, Germany

Kaiser F. and Wachten D.
How phosphoinositides control protein function in primary cilia. “Annual meeting 2018” of the Bonner Forum Biomedizin (BFB), 22.-23.02.2018, Sportschule Hennef, Hennef, Germany

Kaiser F. and Wachten D.
Lipid-protein interactions in the primary cilium. “Annual meeting 2018” Transregio (Collaborative Research Centre) 83, 29.-30.10.2018, Life and Medical Sciences (LIMES) Institute, University of Bonn, Bonn

Kaiser F. and Wachten D.
Lipid-protein interactions in the primary cilium. “Cluster Science Days 2018” of the Immunosensation excellence cluster, 05.-06.11.2018, Biomedizinisches Zentrum (BMZ), University Hospital, Bonn, Germany

Kaiser F., Beckert V., Jikeli J.F., Vianden C., Hansen, J.N., and Wachten D.
How lipid-protein interactions control protein function in primary cilia. Annual meeting 2019” of the Bonner Forum Biomedizin (BFB), 14.-15.02.2019, Sportschule Hennef, Hennef, Germany

Kaiser F., Beckert V., Jikeli J.F., Vianden C., Hansen, J.N., and Wachten D.
How lipid-protein interactions control protein function in primary cilia. “Annual meeting 2018” Transregio (Collaborative Research Centre) 83, 27.-30.10.2019, Marsilius-Kolleg, University of Heidelberg, Heidelberg

Kaiser F., Klausen C., Hansen, J.N., Leyendecker P., Thiele, C., and Wachten D.
How lipid-protein interactions control protein function in primary cilia. Annual meeting 2019” of the Bonner Forum Biomedizin (BFB), 27.-28.02.2020, Sportschule Hennef, Hennef, Germany

Kaiser F., Klausen C., Hansen, J.N., Leyendecker P., Thiele, C., and Wachten D.
How lipid-protein interactions control signaling in primary cilia. “Cluster Science Days 2020” of the Immunosensation excellence cluster, 09.-10.11.2020, Biomedizinisches Zentrum (BMZ), University Hospital, Bonn, Germany

Kaiser F., Klausen C., Hansen, J.N., Leyendecker P., Thiele, C., and Wachten D. The primary cilium is a unique lipid microdomain engineered to transduce extracellular cues. “Cluster Science Days 2021” of the Immunosensation excellence cluster, 09.-10.11.2021, Biomedizinisches Zentrum (BMZ), University Hospital, Bonn, Germany

Abstract

Cilia are membrane protrusions located at the surface of almost every vertebrate cell. Cilia come in two different flavors: motile cilia, which generate a fluid flow or propel cells for active movement, and immotile, also called primary cilia. Primary cilia are considered as cellular antennae that receive extracellular signals and transduce them into a cellular response. Primary cilia dysfunction has been linked to severe human diseases, collectively termed ciliopathies. However, the underlying molecular mechanisms are not well understood. The Hedgehog (Hh) pathway is the predominantly studied pathway in primary cilia. It signals via G protein-coupled receptors (GPCRs) to control ciliary cyclic adenosine monophosphate (cAMP) levels and, thereby, the transcription of Hh target genes. Dysregulation of the Hh signaling has been proposed to underlie the development of ciliopathies and human cancer. Subcellular signaling is crucially determined by the local lipid environment. The lipid identity of the primary cilium determines ciliary signaling and seems to be disturbed under pathophysiological conditions. However, the ciliary lipid domain architecture, its regulation, and how it controls ciliary signaling remains elusive. To delineate the lipid composition, I established a method to isolate and enrich the primary cilia membrane (CM) followed by mass spectrometric analysis. My results demonstrate that the CM is enriched in glycosphingolipids (GSLs), which determine the biophysical properties of the membrane. In turn, the ciliary localization of Hh signaling components is altered, i.e., the localization of ciliary GPCRs. To analyze downstream signaling, I established fluorescent cAMP biosensors to measure cAMP dynamics in the primary cilium and, thereby, unravel the molecular mechanisms underlying ciliary cAMP signaling under physiological and pathological conditions.

Zusammenfassung

Zilien sind Membranausstülpungen, die sich an der Oberfläche fast aller Wirbeltierzellen befinden. Es gibt zwei Arten von Zilien: bewegliche Zilien, die einen Flüssigkeitsstrom erzeugen oder Zellen zur aktiven Bewegung antreiben, und unbewegliche Zilien, auch Primärzilien genannt. Primäre Zilien werden als zelluläre Antennen betrachtet, die extrazelluläre Signale empfangen und sie in eine zelluläre Reaktion umwandeln. Eine Funktionsstörung der primären Zilien wird mit schweren menschlichen Krankheiten in Verbindung gebracht, die unter dem Begriff Ziliopathien zusammengefasst werden. Die zugrundeliegenden molekularen Mechanismen sind jedoch nicht gut verstanden. Der Hedgehog (Hh)-Signalweg ist der am meisten untersuchte Signalweg in primären Zilien. Er sendet Signale über G-Protein-gekoppelte Rezeptoren (GPCRs), um den ziliären Gehalt an zyklischem Adenosinmonophosphat (cAMP) und damit die Transkription von Hh-Zielgenen zu steuern. Es wird angenommen, dass eine Dysregulation der Hh-Signalübertragung der Entwicklung von Ziliopathien und Krebs beim Menschen zugrunde liegt. Die subzelluläre Signalübertragung wird entscheidend durch die lokale Lipidumgebung bestimmt. Die Lipididentität des primären Ziliums bestimmt die ziliäre Signalübertragung und scheint unter pathophysiologischen Bedingungen gestört zu sein. Die Architektur der ziliaren Lipiddomäne, ihre Regulierung und die Art und Weise, wie sie die ziliare Signalübertragung steuert, sind jedoch noch nicht bekannt. Um die Lipidzusammensetzung zu beschreiben, habe ich eine Methode zur Isolierung und Anreicherung der primären Zilienmembran (ZM) mit anschließender massenspektrometrischer Analyse entwickelt. Meine Ergebnisse zeigen, dass die ZM reich an Glycosphingolipiden (GSL) ist, die die biophysikalischen Eigenschaften der Membran bestimmen. Im Gegenzug ist die ziliäre Lokalisierung von Hh-Signalkomponenten verändert, d.h. die Lokalisierung von ziliären GPCRs. Um die nachgeschaltete Signalübertragung zu analysieren, habe ich fluoreszierende cAMP-Biosensoren entwickelt, um die cAMP-Dynamik im primären Zilium zu messen und dadurch die molekularen Mechanismen zu entschlüsseln, die der ziliären cAMP-Signalübertragung unter physiologischen und pathologischen Bedingungen zugrunde liegen.

Table of Contents

1 INTRODUCTION 1

1.1 Cilia and their function in mammalian cells 1

1.2 Ciliopathies 1

1.3 Structure and maintenance of primary cilia 2

1.4 The ciliary Hedgehog signaling pathway 4

1.5 Membrane lipids in ciliary signaling 7

1.5.1 Phosphatidylinositol phosphates in ciliary signaling 8

1.5.2 Sphingolipids in ciliary signaling 11

1.6 Hypothesis and thesis aim 13

2 MATERIALS AND METHODS 15

2.1 Reagents and Materials 15

2.2 Solutions and buffers 19

2.3 Antibodies 21

2.3.1 Primary antibodies 21

2.3.2 Secondary antibodies 22

2.4 Mice 23

2.5 Molecular Biology 23

2.5.1 Plasmids and primers 23

2.5.2 Escherichia coli culture 26

2.5.3 Genotyping cells and mice using PCR 28

2.5.4 RNA isolation for RT-qPCR 29

2.5.5 Generation of cDNA using RT 29

2.5.6 Reverse-transcription quantitative PCR (RT-qPCR) 29

2.6 Mammalian tissue culture 30

2.6.1 Poly-L-lysine coating of glass coverslips 30

2.6.2 Isolation of mouse embryonic fibroblasts 30

2.6.3 Isolation of mouse adult fibroblasts 31

2.6.4 Immortalization of mouse embryonic and adult fibroblasts 31

2.6.5 Isolation and DNA from cell lines 32

2.6.6 Maintenance of cell lines 32

2.6.7 Preparing back-ups and re-culturing of cultured cells 33

2.6.8 Transient gene expression using PEI transfection 34

2.6.9 Transient gene expression using Lipofectamine2000 transfection 35

2.6.10 Transient gene expression using BacMAM transduction 36

2.6.11 Production of ShhN *36*
2.6.12 Hh activity assay *37*
2.6.13 Cytodex3 microcarrier cell culture and cilia isolation *37*
2.6.14 Generation of cell lines with stable gene expression using Lentiviral transduction *38*
2.7 PROTEIN BIOCHEMISTRY 38
2.7.1 Protein preparation using whole cell lysates *38*
2.7.2 The bicinchoninic acid (BCA) assay for quantification of protein concentrations *39*
2.7.3 Sodium dodecyl sulphate-polyacrylamide gel electrophoresis (SDS-PAGE) *39*
2.7.4 Western Blot analysis *39*
2.7.5 Dot Blot analysis *40*
2.7.6 Immunocytochemistry (ICC) *40*
2.7.7 Magnetic-bead coupling to VHH anti-ALFA *41*
2.7.8 ALFA-tag specific pull-down using VHH anti-ALFA coupled magnetic beads *42*
2.8 CONFOCAL MICROSCOPY 42
2.9 LIVE CELL IMAGING 42
2.9.1 FRET imaging at the CellR System *42*
2.9.2 R-FlincA imaging at the CellR System *43*
2.9.3 FRET imaging at the Andor Spinning Disk microscope *44*
2.9.4 cADDis imaging at the Andor Spinning Disk microscope *45*
2.9.5 Di-4-ANEPPDHQ and Pro12A live cell imaging and analysis *45*
2.10 CILIA ISOLATION 46
2.11 LIPIDOMIC ANALYSIS USING MASS SPECTROMETRY 47
2.11.1 Lipid extraction from mIMCD-3 cells and isolated primary cilia *47*
2.11.2 Mass spectrometry *47*
2.12 SOFTWARE APPLICATIONS 48
2.13 STATISTICS 48
3 RESULTS 49
3.1 CILIOGENESIS IN MAMMALIAN TISSUE CULTURE 49
3.2 ANALYSIS OF THE CILIARY MEMBRANE LIPID-ENVIRONMENT USING THE ENVIRONMENT-SENSITIVE, SOLVATOCHROMIC DYES DI-4-ANEPPDHQ AND PRO12A 50
3.2.1 GP imaging and analysis *53*
3.3 ANALYZING GSL FUNCTION IN PRIMARY CILIA SIGNALING USING GBA2 64
3.3.1 Adapting CiliaQ analysis for unbiased quantification of ciliary immunofluorescence *64*
3.3.2 Analyzing GBA2-dependent ciliary Hh signaling using SMO labeling *67*
3.3.3 Analyzing Hedgehog downstream signaling using Ptch1 and Gli1 expression *75*
3.4 ANALYZING GSL FUNCTION IN PRIMARY CILIA SIGNALING USING GBA1 78

3.4.1 Analyzing GBA1-dependent ciliary Hh signaling using SMO labeling and Hh-dependent gene expression ... 78

3.5 ANALYZING CILIARY CAMP SIGNALING ... 81

3.5.1 Characteristics of the mlCNBD-FRET and AKAR4 FRET-based cAMP biosensors ... 82

3.5.2 Setting up FRET imaging for mlCNBD-FRET and AKAR4 using three-cube imaging ... 84

3.5.3 Functional characterization of mlCNBD-FRET and AKAR4 targeting strategy using HEK293 cells 87

3.5.4 Functional characterization of R-FlincA targeting strategy using HEK293 cells and optogenetics 90

3.5.5 Nanobody-directed ciliary targeting to preserve sensor function ... 93

3.5.6 Establishing FRET imaging for ciliary imaging ... 95

3.5.7 Functional characterization of ciliary-targeted cAMP biosensors ... 96

3.5.8 Analyzing ciliary Hh-dependent cAMP signaling using ciliary-targeted cADDis-mCherry ... 101

3.6 ESTABLISHING KNOCKOUT CELLS OF THE 5´INOSITOL PHOSPHATASE INPP5E TO STUDY ITS ROLE IN CILIARY CAMP SIGNALING ... 105

3.7 GENERATION OF *INPP5E* KNOCKOUT CELLS USING CRISPR-CAS9 ... 105

3.7.1 CRISPR-Cas9 targeting design ... 106

3.7.2 Inpp5e-directed CRISPR-Cas9 targeting and identification of Inpp5e-KO candidate cell lines ... 107

3.7.3 Verification of Inpp5e-KO candidate cell lines using Western Blot analysis and immunocytochemistry ... 109

3.8 ISOLATION AND PURIFICATION OF PRIMARY CILIA FOR LIPID EXTRACTION AND MASS-SPECTROMETRIC ANALYSIS OF THE CILIARY MEMBRANE LIPID COMPOSITION ... 112

3.8.1 Establishing specific isolation of primary cilia using shearing-forces and Ca^{2+} shock ... 112

3.8.2 Preliminary lipidomic analysis of isolated mIMCD-3 primary cilia ... 115

3.8.3 Establishing the ALFA-tag for cilia-specific pull-down ... 116

4 DISCUSSION ... 124

4.1 ANALYZING CILIARY CAMP DYNAMICS USING CAMP BIOSENSORS TO DELINEATE CILIARY SIGNALING AND FUNCTION ... 124

4.2 THE ROLE OF GSLS IN CILIARY CAMP SIGNALING ... 131

4.3 HOW ARE CILIARY GSLS REGULATED? ... 133

5 REFERENCES ... 137

6 APPENDIX ... 152

DANKSAGUNG ... 177

List of figures

Figure 1: Ciliopathies in the human body. 2
Figure 2: Primary cilia structure, maintenance, and function. 4
Figure 3: Model of ciliary Hedgehog signaling. 5
Figure 4: Model of putative lipid distribution in the apical and periciliary plasma membrane as well as in the ciliary membrane. 8
Figure 5: General structure of phosphatidylinositol phosphates (PIPs) and the putative roles of phosphatidylinositol 4-phosphate (PI(4)P) and phosphatidylinositol 4,5-biphosphate ($PI(4,5)P_2$ in ciliary Hedgehog signaling.. 10
Figure 6: Overview of sphingolipids (SPLs) and the action of the non-lysosomal ß-glucosidase, GBA2. 11
Figure 7: Hypothesis. 14
Figure 8: Ciliogenesis in vitro. 50
Figure 9: The environment-sensitive membrane dyes Di-4-ANEPPDHQ and Pro12A. 52
Figure 10: Schematic overview of environment-sensitive dye measurements and analysis. 54
Figure 11: Analysis pipeline to determine the membrane order. 56
Figure 12: Analysis of PM with Di-4-ANEPPDHQ and Pro12A. 57
Figure 13: Photoselection with polarized light. 59
Figure 14: Set-up to compensate for photoselection in the LEICA SP8 confocal laser scanning microscope. 61
Figure 15: Analysis of the lipid order in the plasma membrane (PM) and ciliary membrane (CM) by Di-4-ANEPPDHQ and Pro12A imaging using circularly polarized light.. 63
Figure 16: Analyzing ciliary Hedgehog signaling using the subcellular localization of Smoothened (SMO) as a read-out. 65
Figure 17: CiliaQ simplified workflow. 66
Figure 18: Time course for the treatment of fibroblasts to analyze Hh signaling.. 67
Figure 19: Analysis of ciliary Hh signaling using Smo labeling in mAFB. 68
Figure 20: Establishing the generation of soluble Sonic Hedgehog (SHH) ligand. 69
Figure 21: Analysis of ciliary Hh signaling using Smo labeling in ciliated mAFB and SHH stimulation 71
Figure 22: Hh activity assay to determine a non-saturating concentration of hSHH. 72
Figure 23: Analysis of ciliary Hh signaling using Smo labeling in ciliated GBA2 mEFB and hSHH stimulation.. 74
Figure 24: Analyzing ciliary Hedgehog signaling using Ptch1 and Gli1 gene expression.. 75
Figure 25: Analyzing ciliary Hedgehog signaling using Hh target gene expression in Gba2 mAFB and mEFB. 77
Figure 26: Analysis of ciliary Hh signaling using Smo labeling in ciliated Gba1 mEFB and hSHH stimulation. 79
Figure 27: Analyzing ciliary Hedgehog signaling using Hh target gene expression in Gba1 mEFB 80
Figure 28: Working principle of the direct cAMP biosensor mlCNBD-FRET and the indirect cAMP biosensor AKAR4. 83
Figure 29: Measuring FRET using three-cube imaging. 84
Figure 30: FRET correction at the CellR imaging system. 86

Figure 31: FRET correction values at the Andor Spinning Disk imaging system.. 87
Figure 32: Set-up to characterize mlCNBD-FRET and AKAR4 in non-ciliated HEK293 cells. 88
Figure 33: Functional characterization of the mNPHP3(201) ciliary-targeting strategy for FRET-based cAMP biosensors. 89
Figure 34: Functional characterization of the single fluorescent protein (FP) cAMP biosensor R-FlincA in non-ciliated HEK293 cells. 92
Figure 35: Targeting mlCNBD-FRET to the primary cilium using nanobodies. 93
Figure 36: Functional characterization of the cilia-targeted mlCNBD-FRET biosensor in non-ciliated cells.. 94
Figure 37: Establishing live cell imaging of the cilary-targeted mlCNBD-FRET sensor in ciliated mIMCD-3 cells. . 96
Figure 38: Functional characterization of the nanobody-targeted mlCNBD-FRET biosensor in ciliated cells. 97
Figure 39: Functional characterization of the cilia-targeted mNPHP3(201)-AKAR4-NES biosensor in ciliated mIMCD-3 cells. 98
Figure 40: Functional characterization of the cilia-targeted, ratiometric 5-HT_6-cADDis-mCherry cAMP biosensor in ciliated cells.. 100
Figure 41: Functional characterization of the cilia-targeted, ratiometric 5-HT_6-cADDis-mCherry biosensor in ciliated mIMCD-3 cells.. 101
Figure 42: Analyzing ciliary Hh-dependent cAMP dynamics using 5-HT_6-cADDis-mCherry. 102
Figure 43: Functional characterization of the cilia-targeted, ratiometric mNphp3(201)-cADDis-mCherry biosensor in ciliated mIMCD-3 cells.. 104
Figure 44: CRISR-Cas9 target design and characteristics of Inpp5e.. 106
Figure 45: Sanger sequencing chromatograms.. 108
Figure 46: Interpretation of the Sanger sequencing data.. 109
Figure 47: Immunodetection of INPP5E. 110
Figure 48: Characterization of mIMCD-3 wild-type and mIMCD-3 Inpp5e-KO candidate cell lines using immunofluorescent labeling. 111
Figure 49: Establishing adherent cell growth on microcarrier for primary cilia isolation. 114
Figure 50: Mass spectrometric analysis of isolated cilia and whole-cell samples from mIMCD-3 cells. 116
Figure 51: Generating extracellular ALFA tagged SMO to improve accuracy and reproducibility of primary cilia isolation. 118
Figure 52: Generating extracellular ALFA tagged PTCH1 to improve accuracy and reproducibility of primary cilia isolation. 119
Figure 53: Characterization of mIMCD-3 cells with stable ALFA-tagged protein expression using ICC and confocal microscopy. 121
Figure 54: Generation and characterization of stable ALFA-SMO or ALFA-PTCH1 expressing monoclonal cell lines using fluorescent-activated cell sorting (FACS) and immunolabeling with confocal microscopy.. 123
Figure 55: Spatial manipulation of ciliary cAMP using optogenetics. 128

List of figures

Figure 56: Ciliary cAMP signaling evokes a specific gene expression signature compared to somatic cAMP signaling. *128*
Figure 57: Putative model of further ciliary cAMP compartmentalization into nanodomains. *129*
Figure 58: Plasmid map of CAG-Enhancer-Gag-Pol-RRE-rb globulin. *152*
Figure 59: Plasmid map of CAG-Enhancer-VSVG-G-human beta globulin. *153*
Figure 60: Plasmid map of pc3-mNPHP3-AKAR4HANES. *154*
Figure 61: Plasmid map of pc3-mNPHP3-Cerulean-4. ..... *155*
Figure 62: Plasmid map of pc3-mNPHP3-Citrin-3. ..... *156*
Figure 63: Plasmid map of pc3-mNPHP3-R-FlincA-12.. ..... *157*
Figure 64: Plasmid map of pc3-mNPHP3(201)-mlCNBD-FRET-1. ..... *158*
Figure 65: Plasmid map of pc3.1-mNPHP3(201)-VHH-enhancer-mCherry-7. ..... *159*
Figure 66: Plasmid map of pc3.1-VHH-enhancer-mCherry #4. ..... *160*
Figure 67: Plasmid map of pc3.1mlCNBD-FRET#9. ..... *161*
Figure 68: Plasmid map of pcA-Cerulean. *162*
Figure 69: Plasmid map of pcA-Citrine. *163*
Figure 70: Plasmid map of pcDNA3-AKAR4. ..... *164*
Figure 71: Plasmid map of pcDNA3-AKAR4-NES. *165*
Figure 72: Plasmid map of pcDNA3.1-Shh-N.. ..... *166*
Figure 73: Plasmid map of pcDNA3.1zeo_mCherry.. ..... *167*
Figure 74: Plasmid map of pcDNA4-HisMaxB_R-FlincA. *168*
Figure 75: Plasmid map of pcDNA4-HisMaxB_R-FlincA-mut.. ..... *169*
Figure 76: Plasmid map of pEGFP-N1-bPAC #1 ..... *170*
Figure 77: Plasmid map of pInducer20_minus_CMV_ALFAtag-(235-236)-mPtch1. ..... *171*
Figure 78: Plasmid map of pInducer20_minus_CMV_ALFAtag-(51-52)-mSmo. *172*
Figure 79: Plasmid map of pX459-sgRNA#1-INPP5E.. ..... *173*
Figure 80: Plasmid map of pX459-sgRNA#2-INPP5E.. ..... *174*
Figure 81: Plasmid map of pX459-sgRNA#3-INPP5E.. ..... *175*
Figure 82: Plasmid map of SV-40 large T Antigen. *176*

List of tables

Table 1: Reagents 15
Table 2: Materials 17
Table 3: Fluorescent dyes 19
Table 4: Primary antibodies. 21
Table 5: Secondary antibodies. 22
Table 6: Plasmid Information 24
Table 7: Genotyping PCR primer-specific information 26
Table 8: RT-qPCR primer-specific information 26
Table 9: DreamTaq™ master mix and PCR mix 28
Table 10: Genotyping PCR 29
Table 11: RT-qPCR instrument settings 30
Table 12: Mammalian cell-line specific information 32
Table 13: PEI transfection 35
Table 14: Lipofectamine2000 transfection 36
Table 15: BacMAM transduction 36

Abbreviations

2M5HT	2-methyl-5-hydroxytryptamine
5-HT_{1A}	Serotonin receptor 1A
5-HT_6	5-hydroxytryptamine receptor subtype 6
Å	Ångström
a.u.	Arbitrary units
A488	Alexa Fluor 488
A647	Alexa Fluor 647
AA	Amino acid
AC	Adenylyl cyclase
AC-α-TUB	Acetylated-α-tubulin
AKAP	A-kinase anchoring protein
AKAR	A-kinase activity reporter
AOBS	Acousto-Optical Beam Splitter
aPKC	Atypical protein kinase C
APS	Ammoniumpersulfat
ARL13B	ADP-ribosylation factor-like protein 13B
aSMase	Acid sphingomyelinase
ATP	Adenosine triphosphate
BacMam	Baculovirus gene transfer into Mammalian cells
BB	Blocking buffer
BBC	Basal cell carcinoma
BCA	Bicinchonic acid
BMP	Bone morphogenic proteins
bp	Base pair
bPAC	Bacterial photoactivated adenylyl cyclase
$CaCl_2$	Calcium chloride
cAMP	Cylic adenosine monophosphate
CAV-1	Caveolin-1
CD62L	L-selectin
cDNA	Complementary DNA
Cer	Ceramide
CER	Cerulean
CFP	Cyan fluorescent protein
CIT	Citrine
CM	Ciliary membrane
CNBD	Cyclic nucleotide-binding domain
CNX	Calnexin
cp	Circularly permuted
cpmNG	CpmNeonGreen
CRISPR	Clustered regularly interspaced short palindromic repeats
CT	ChemiBLOCKER + TritonX-100

cT	Cycle threshold
Cy3	Cyanine Dye 3
D1R	Dopamine D1 receptor
Da	Dalton
DAPI	Phenyl-indole, Dihydrochloride
DMSO	Dimethylsulfoxide
DSB	Double-strand break
EC_{50}	The half maximal effective concentration
EDTA	2,2′,2″,2‴-(Ethane-1,2-diyldinitrilo)tetraacetic acid
EGFR	Epidermal growth factor receptor
EP4	Prostaglandin E_2 receptor 4
ER	Endoplasmic reticulum
ES	Extracellular solution
et al.	Et alii
FACS	Fluorescent-activated cell sorting
FAPP2	PI(4)P adaptor protein-2
Fiji	Fiji is just ImageJ
FLOT2	Flotillin-2
FP	Fluorescent protein
FRET	Förster Resonance Energy Transfer
GBA1	The acid β-glucosidase
GBA2	The non-lysosomal β-glucosidase
GBA3	The cytosolic β-glucosidase
GCGR	Glucagon receptor
GCS	Glucosylceramide synthase
GFP	Green fluorescent protein
GlcCer	Glucosylceramide
GLI-A	Activator form of glioma-associated transcription factors
GLI-FL	Full-length glioma-associated transcription factors
GLI-R	Repressor form of glioma-associated transcription factors
GLI1, 2, 3	Glioma-associated transcription factors 1, 2, and 3
GLTP	Glycolipid transfer protein
GM1	Ganglioside GM1
GM3	Ganglioside GM3
GP	Generalized polarization
GPCR	G protein-coupled receptor
GPR161	G protein-coupled receptor 161
GPRK2	G protein-coupled receptor kinase 2
GRE	Gli-responsive element
GSL	Glycosphingolipid
$G\alpha_i$	Inhibitory G protein alpha subunit
$G\alpha_s$	Stimulatory G protein alpha subunit

h	Hour(s)
HCl	Hydrogen chloride
HEK293	Human embryonic kidney cells
HeLa	Human cervical cancer cells derived from Henrietta Lacks
HEPES	4-(2-hydroxyethyl)-1-piperazineethanesulfonic acid
Hh	Hedgehog
HSB	Hue-saturation-brightness
hSHH	Human SHH
IBMX	3-Isobutyl-1-methylxanthine
IC_{50}	The half maximal inhibitory concentration
ICC	Immunocytochemistry
IFT	Intraflagellar transport
INPP5B	Inositol polyphosphate-5-phosphatase B
INPP5E	Inositol polyphosphate-5-phosphatase E
Isoproterenol	Isoproterenol Hydrochloride
KCl	Potassium chloride
K_D	Dissociation constant
KO	Knockout
Laurdan	6-Dodecanoyl-2-Dimethylaminonaphthalene
L_d	Liquid-disordered
L_o	Liquid-ordered
LUT	Lookup table
M-β-CD	Methyl-β-cyclodextrin
mAFB	Mouse adult fibroblasts
MDCK	Mardin-Darby Canine Kidney
mEFB	Mouse embryonic fibroblasts
$MgCl_2$	Magnesium chloride
mIMCD-3	Mouse cells derived from the terminal part of the inner medullary collection duct
mPIC	Mammalian proteinase-inhibitor cocktail
MZ-21 (alias AMP-DNM)	N-(5′-adamantane-1′-yl-methoxy)-pentyl-1-deoxynojirimycin
Na_2HPO_4	Disodium hydrogen phosphate
NaCl	Sodium chloride
NaH_2PO_4	Sodium dihydrogen phosphate
NaOH	Sodium hydroxyde
NaP	Sodium phosphate
NB-DNJ	N-butyldeoxynojirimycin
NES	Nuclear export signal
NHEJ	Non-homologous end joining
OCRL	Lowe oculocereborenal syndrome protein
PAGE	Polyacrylamide gel electrophoresis

PBS	Phosphate buffered saline
PBS-T	PBS-Tween
PC	Phosphatidylcholine
PC-O	Ether-linked phosphatidylcholine
PCR	Polyermase chain reaction
PDE	Phosphodiesterase
PDGFRα	Platelet-derived growth factor α
PEI	Polyethylenimine
PFA	Paraformaldehyde
PI	Phosphatidylinositol
$PI(4,5)P_2$	Phosphatidylinositol 4,5-biphosphate
PI(4)P	Phosphatidylinositol 4-phosphate
PIP	Phosphatidylinositol phosphate
PKA	Protein kinase A
PKA-C	PKA catalytic subunit
PKA-Riα	PKA regulatory subunit type I α
PLL	Poly-L-lysine
PM	Plasma membrane
PTCH1	12-transmembrane receptor Patched1
RGB	Red-green-blue
RT	Room temperature
RT-qPCR	Reverse-transcription quantitative PCR
RTK	Receptor tyrosine kinase
SAG	Smoothened agonist
SDS	Sodium dodecyl sulfate
SHH	Sonic Hedgehog
ShhN	Sonic Hedgehog without cholesterol modification produced from *ShhN* cDNA
SM	Sphingomyelin
SMO	G protein-coupled receptor Smoothened
SPL	Sphingolipid
SSTR3	Somatostatin receptor 3
SV40	Simian-Virus 40
TAG	Triacylglyceride
TEMED	Tetramethylethylendiamin
TGN	*Trans*-Golgi network
TGR5	Takeda G protein-coupled receptor 5
AC	Transmembrane adenylyl cyclase
Transforming growth factor β	Transforming growth factor β
Tris	2-Amino-2-(hydroxymethyl)propane-1,3-diol
TULP3	Tubby-like protein 3
TZ	Transition Zone

V2R	Vasopressin receptor 2
WB	Western Blot
Wnt	Wingless Int-1
WT	Wild type
x g	x times gravitational force (9.81 m/sec2)
YFP	Yellow fluorescent protein
α	Donor bleed-through value
β	Acceptor cross-excitation

Base units and decimal (sub-)multiples of the base units are designated according to the international unit system “Système International d’Unités”.

Nucleotides are abbreviated by the initial letter of their bases (A: adenine, C: cyanine, G: guanine and T: thymine).

Amino acids (AA) are referred to using the one letter code:

Alanine	A	Leucine	L
Arginine	R	Lysine	K
Asparagine	N	Methionine	M
Aspartate	D	Phenylalanine	F
Cysteine	C	Proline	P
Glutamate	E	Serine	S
Glutamine	Q	Threonine	T
Glycine	G	Tryptophan	W
Histidine	H	Tyrosine	Y
Isoleucine	I	Valine	V

1 Introduction

1.1 Cilia and their function in mammalian cells

Cilia are membrane protrusions emanating from the surface of a variety of different cell types. There are two types of cilia: motile and immotile cilia. Motile cilia propel cells for active movement or generate a fluid flow (Gilpin et al., 2020; Mitchison and Valente, 2017), whereas immotile, also called primary cilia, have long been ignored as a vestigial organelle, whose function remained enigmatic. Primary cilia were already discovered at the end of the 19th century (termed at this time "Zentralgeissel") (Bloodgood, 2009; Zimmermann, 1898). However, at first, only specialized primary cilia, like the connecting cilium together with the outer segment of rod and cones from photoreceptor cells, and cilia from olfactory neurons were appreciated for their function to transduce light and olfactory stimuli, respectively (Bloom, 1954; De Robertis, 1956). We now know that almost every vertebrate cell contains a primary cilium, which functions as a signaling hub to sense extracellular stimuli and locally transduce these signals to orchestrate sensory, developmental, and homeostatic pathways (Garcia et al., 2018; Huangfu et al., 2003; Nachury and Mick, 2019; Nauli et al., 2003; Wachten and Mick, 2021). A detailed understanding of the molecular mechanisms underlying the sensory function of primary cilia is, however, missing.

1.2 Ciliopathies

Dysfunction or absence of cilia leads to severe human diseases, collectively termed ciliopathies (**Figure 1**). Of note, dysfunction of ciliary proteins, but also of non-ciliary proteins that are required for ciliary function can cause ciliopathies. Ciliopathies are genetic disorders: So far, over 180 ciliopathy genes have been identified and over 240 more genes are under investigation (Reiter and Leroux, 2017). Ciliopathies often display pleiotropic phenotypes, as cilia are present on almost every cell in our body, where they exert cell-type specific functions. In primary cilia, ciliopathies are due to defects in ciliogenesis, cilia maintenance, or ciliary protein trafficking. Despite

tremendous efforts, the molecular mechanisms underlying ciliary signaling processes are by large ill-defined and the causes of ciliopathies are, thus, poorly understood.

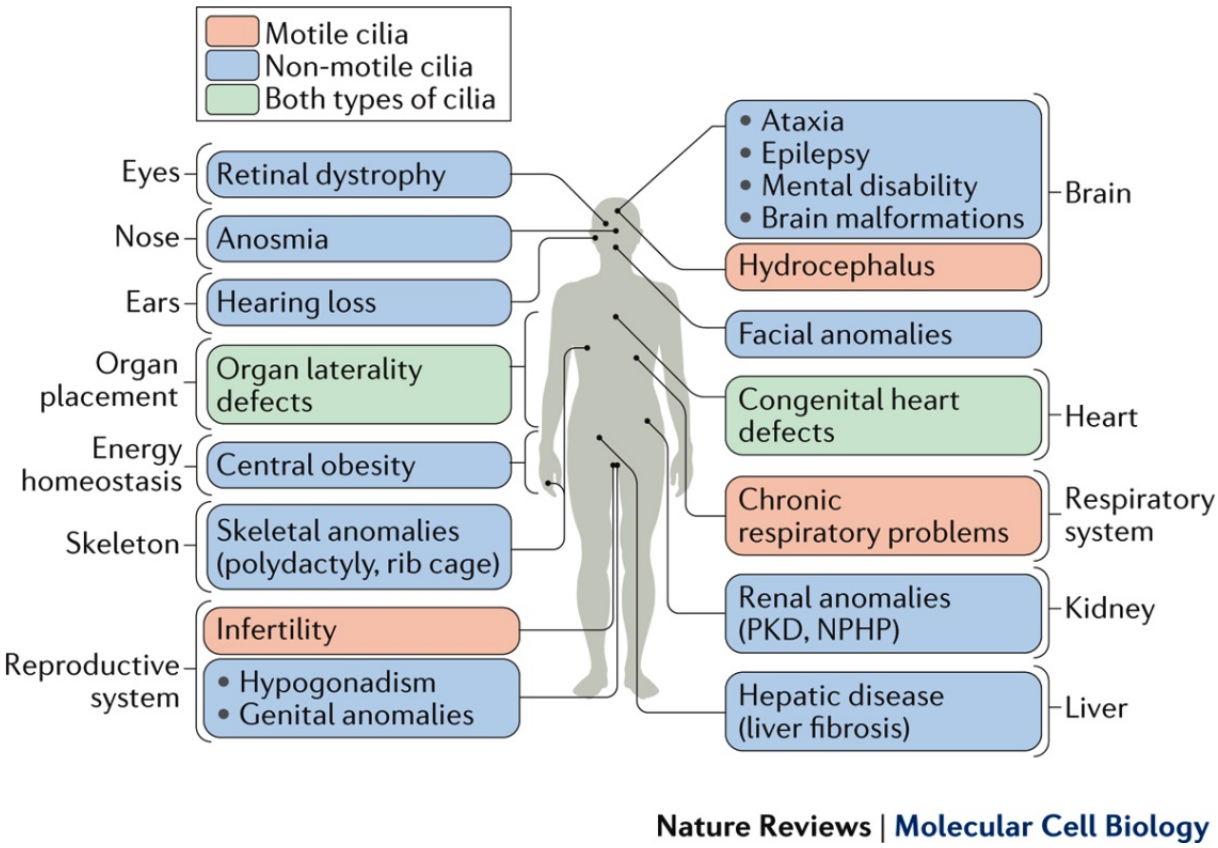

Figure 1: Ciliopathies in the human body. The figure shows the different organs or tissues that are affected in the different ciliopathies, and the principle phenotypic manifestations of the disease in each organ. Ciliopathies that are caused primarily by defects in motile cilia are shown in orange, those that result from defects in non-motile (primary) cilia are shown in blue, and those associated with defects in both types of cilia are shown in green. NPHP, nephronophthisis; PKD, polycystic kidney disease. Figure and legend taken from (Reiter and Leroux, 2017).

Although ciliopathies are rare, the number of diseases identified as ciliopathies is constantly increasing. Currently, treatment options are limited to symptomatic therapies (Gerhardt, 2019). Thus, there is an urgent need to shed light on the molecular mechanisms underlying ciliary signaling that might pave the way to develop curative therapies for ciliopathies.

1.3 Structure and maintenance of primary cilia

The ciliary membrane (CM) is continuous with the plasma membrane (PM) and the ciliary lumen is also connected to the cytosol. Nevertheless, the cilium has a distinct membrane and protein composition, which is required for its function (Rohatgi and Snell, 2010). Specific structures and mechanisms maintain this unique identity (**Figure 2A**): Originating from the mother centriole, the basal body is anchored to the

PM via transition fibers at the transition zone (TZ), where Y-links connect the axoneme with the CM (Gilula and Satir, 1972; Reiter et al., 2012; Ye et al., 2018). The basal body forms the base of the axoneme, the ciliary core structure consisting of 9 microtubule doublets, which protrude from the PM and are covered by the CM (Anderson, 1972; Satir and Christensen, 2007). Primary cilia are assembled and maintained by the intraflagellar transport (IFT) machinery (Rosenbaum and Witman, 2002). IFT-A and IFT-B, in combination with the BBSome and the TZ, maintain the unique ciliary identity and function (Rosenbaum and Witman, 2002; Wingfield et al., 2018): The TZ restricts free diffusion from the cytosol and lateral diffusion from the adjacent PM into the cilium (Garcia et al., 2018). IFT-B is a 16-subunit complex that assembles in IFT-trains for bidirectional movement of cargo inside the cilium. In association with the microtubule motor protein kinesin-2, IFT-trains move cargo to the ciliary tip (anterograde transport), where the IFT-trains undergo remodeling to associate with the microtubule motor protein dynein-2 for retrieving cargo (retrograde transport) (Wingfield et al., 2018). The 6-subunit complex IFT-A and the 8-subunit complex BBSome function as adaptors for ciliary transportation of membranous cargo, i.e., IFT-A mediates ciliary cargo entry and the BBSome retrieval and ciliary exit (Nachury, 2018). The hetero-oligomeric BBS-chaperonin complex mediates BBSome assembly at the basal body (Seo et al., 2010). Thus, the coordinated interplay between the IFT machinery, BBSome, and TZ, which is yet not fully understood, dynamically regulates the ciliary protein identity.

Precise regulation of the ciliary protein identity is crucial for the primary cilium to adequately respond to extracellular cues and, in turn, change cellular function by, e.g., changing gene expression or other unknown mechanisms (Anvarian et al., 2019; Garcia et al., 2018; Nachury and Mick, 2019) (**Figure 2B**).

In specialized sensory primary cilia of olfactory neurons, odorant-binding to G protein-coupled receptors (GPCRs) evokes an intracellular response, which is conveyed via the second messenger cyclic adenosine monophosphate (cAMP). Here, the underlying mechanisms have already been well described (Kaupp, 2010). In recent years, a picture emerged that the signal transduction in the prototypic primary cilium uses similar signaling strategies (**Figure 2B**) (Wachten and Mick, 2021). However, a

detailed understanding, as it has been established in the cilia of olfactory neurons, is lacking.

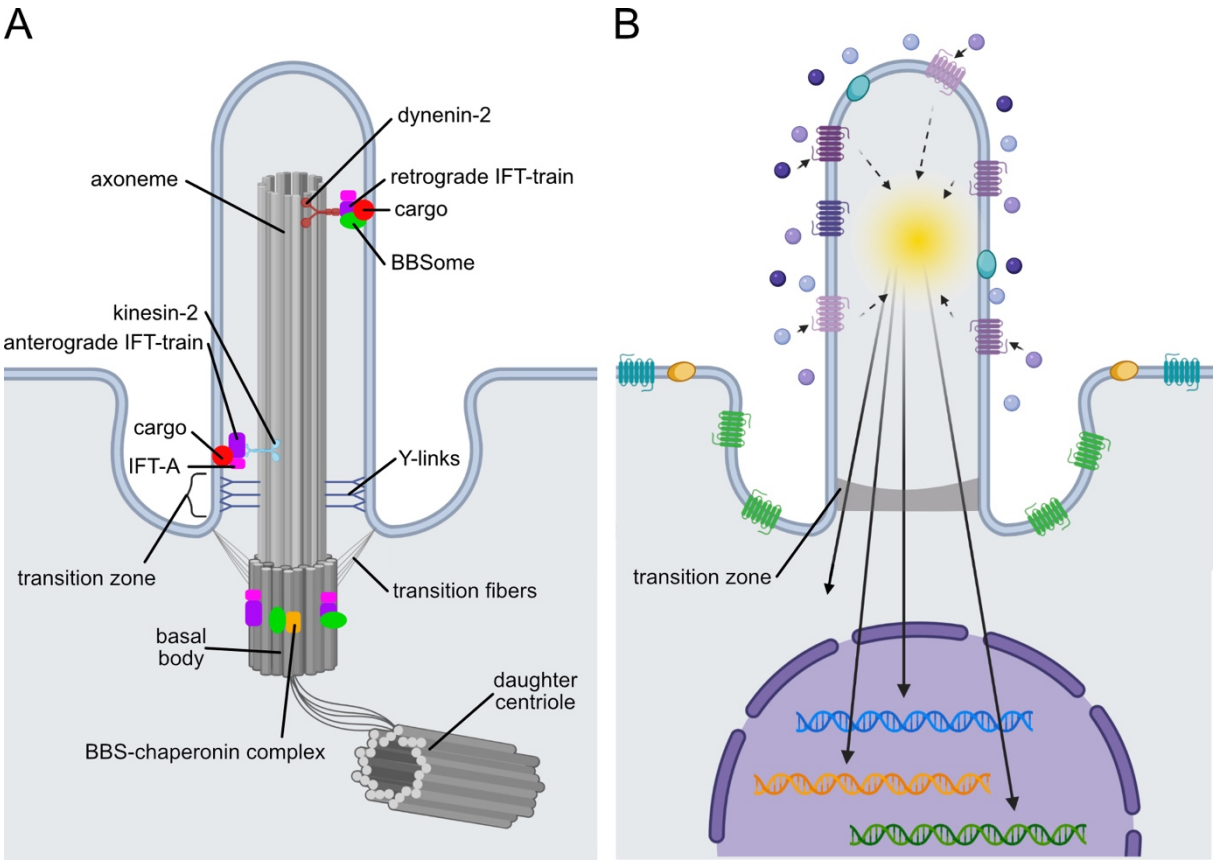

Figure 2: Primary cilia structure, maintenance, and function. A: The axoneme originates from the mother centriole-derived basal body and forms the core of the primary cilium. Transition fibers anchor the basal body to the plasma membrane, which is continuous with the ciliary membrane. The transition zone (TZ) serves as a sieve-like gate to the cytosol. The intraflagellar transport (IFT) machinery in combination with the BBSome maintains the cilium by facilitating kinesin-2 dependent anterograde transport using IFT -B build IFT-trains for movement and IFT-A as an adaptor for membranous cargo, whereas retrograde transport relies on IFT-train remodeling and the BBSome as an adaptor. The BBS-chaperonin complex mediates BBSome assembly at the ciliary base. **B:** Dynamic remodeling and precise control of the ciliary protein identity by the IFT machinery, BBSome, and TZ allows the cell to properly receive external signals and transduce them into an intracellular response. Figures partly generated using *biorender*.

One exemption is the ciliary Hedgehog (Hh) signaling pathway. This is the best-studied ciliary signaling pathway, employing GPCR signaling, putatively via cAMP.

1.4 The ciliary Hedgehog signaling pathway

Hh signaling pathway is conserved amongst vertebrates and was first discovered in flies (Goodrich et al., 1996; Hahn et al., 1996; Nusslein-Volhard and Wieschaus, 1980). Despite many similarities, Hh signaling in vertebrates differs significantly from flies, and in the following, I will focus solely on vertebrate Hh signaling. Hh signaling plays a crucial role in embryonal development, adult stem cell homeostasis, and cancer (Ingham and McMahon, 2001; Marini et al., 2011; Petrova and Joyner, 2014; Rohatgi

and Scott, 2007). Canonical Hh signaling in vertebrates relies on primary cilia (Huangfu and Anderson, 2005; Huangfu et al., 2003), and numerous studies established a well-accepted model of ciliary Hh signaling (**Figure 3**):

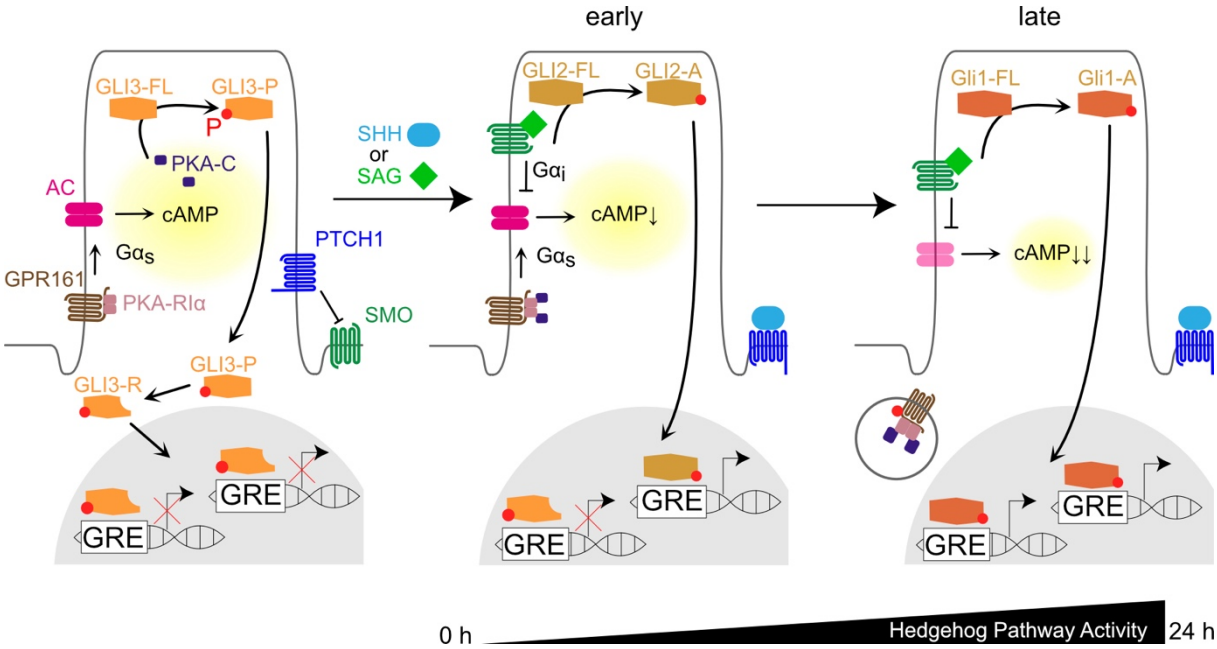

Figure 3: Model of ciliary Hedgehog signaling. The following proteins are part of the Hedgehog signaling cascade: Constitutive active orphan G-protein coupled receptor 161 (GPR161), Protein Kinase A (PKA) with regulatory (RIα) and catalytic (PKA-C) subunits, stimulatory G protein alpha subunit ($G\alpha_s$), transmembrane adenylyl cyclase (AC), cyclic adenosine monophosphate (cAMP), glioma-associated oncogene protein 1-3 (GLI1-3) full length (FL), PKA-phosphorylated (P), repressor (R) and active (A) forms, Patched 1 receptor (Ptch1), Smoothened receptor (SMO), Sonic Hedgehog ligand (Shh), Smoothened agonist (SAG), GLI responding element (GRE). For a detailed explanation, see the text.

In the ligand-free state, the constitutively active, orphan GPR161 localizes to the primary cilium, where it suppresses Hh signaling (Mukhopadhyay et al., 2013) by stimulating ciliary transmembrane adenylyl cyclases (ACs) and, in turn, increasing cAMP levels (Bishop et al., 2007; Moore et al., 2016; Vuolo et al., 2015). In addition, GPR161 functions as an A-kinase anchoring protein (AKAP) for the Protein kinase A (PKA) regulatory subunit type I α (PKA-RIα), localizing PKA to the cilium (Bachmann et al., 2016; Mick et al., 2015). In turn, the PKA catalytic subunit (PKA-C) phosphorylates full-length glioma-associated transcription factors (GLI-FL) 2 and 3 in the cilium to trigger their proteolytic cleavage into a repressor form (GLI-R, mainly GLI3-R). GLI-R re-locates to the nucleus to repress Hh-dependent gene expression on GLI responding elements (GRE) (Niewiadomski et al., 2014). The regulatory switches that activate Hh signaling are the 12-transmembrane receptor Patched1 (PTCH1), which resides in the CM under basal conditions, and the $G\alpha_i$ protein-coupled receptor Smoothened (SMO), which is excluded from the ciliary membrane and

inhibited from activation by PTCH1 (Kinnebrew et al., 2019; Kinnebrew et al., 2021; Taipale et al., 2002). Hh signaling is activated by binding of Sonic Hedgehog (SHH) to its receptor PTCH1. Synthetic compounds that bind to SMO, like the SMO agonist (SAG), can also induce Hh signaling (Chen et al., 2002; May et al., 2021; Rohatgi et al., 2007). Upon ligand binding, PTCH1 leaves the cilium and, in turn, SMO gets activated, enters the cilium and facilitates Hh activation by several mechanisms (Corbit et al., 2005; Rohatgi et al., 2009). First, SMO directly inhibits PKA activity and additionally reduces cAMP levels by inhibiting AC activity through its coupled $G\alpha_i$ (Arveseth et al., 2021; May et al., 2021; Riobo, 2014). Second, SMO mediates non-PKA phosphorylation of GLI-FL at the tip of the primary cilium by unknown mechanisms (Han et al., 2019; Kong et al., 2019). Thereby, GLI proteins reside in their activator form GLI-A (mainly GLI2-A, later GLI1-A and GLI2-A). GLI-A proteins shuttle into the nucleus and induce Hh-dependent gene expression (Gigante and Caspary, 2020; Humke et al., 2010; Kim et al., 2009; Wen et al., 2010). Although being counterintuitive, the reduced cAMP levels have been suggested to mediate PKA-dependent phosphorylation of GPR161 by the following mechanism (May et al., 2021; Smith et al., 2017): the relative amount of free and, thereby, active PKA-C depends on the cAMP concentration, i.e., the higher the cAMP concentration, the more PKA-C dissociates from the PKA regulatory subunit (PKA-R) and the more PKA is active. In turn, the local concentration of PKA-C that phosphorylates GPR161 is reduced as GPR161 anchors the PKA-R and not PKA-C. When cAMP levels are reduced upon Hh activation, PKA-C associates again with PKA-R. Strikingly, PKA has been shown to be able to proceed with phosphorylation even as an intact holoenzyme under certain conditions (Smith et al., 2017). Thus, even though the overall PKA activity might be reduced by the lowered cAMP concentration, the local PKA-C concentration at GPR161 and, therefore, GPR161 phosphorylation might be increased. In turn, PKA-dependent GPR161 phosphorylation triggers β-arrestin-mediated removal of GPR161 via endocytosis (Bachmann et al., 2016; May et al., 2021; Mukhopadhyay et al., 2013; Pal et al., 2016; Riobo, 2015).

Many ciliopathies feature polydactyly as well as midline and neural tube defects (Waters and Beales, 2011), which are due to defects in ciliary Hh signaling (Wheway et al., 2018). However, the molecular mechanisms underlying these defects are poorly understood.

1.5 Membrane lipids in ciliary signaling

Not only the protein, but also the lipid composition is dynamically regulated to conduct ciliary signaling. Generally, the lipid membrane bilayer in eucaryotic cells is asymmetric: Active processes enrich sphingolipids (SPLs) in the outer leaflet, whereas phosphatidylinositol phosphates (PIPs), phosphorylated derivates of the membrane lipid phosphatidylinositol (PI), are located in the inner leaflet of eukaryotic membranes (Dickson and Hille, 2019; Ikeda et al., 2006). Not surprisingly, SPLs and PIPs play essential roles in cellular signaling (Balla, 2013; D'Angelo et al., 2013). Besides Hh signaling, Wingless Int-1 (Wnt) and receptor tyrosine kinase (RTK) signaling, which includes signaling dependent on the platelet-derived growth factor α (PDGFRα), insulin, the epidermal growth factor receptor (EGFR), the transforming growth factor β (TGF-β), or bone morphogenic proteins (BMP) also rely at least to some extent on the primary cilium, too (Anvarian et al., 2019). Moreover, several GPCRs also localize to primary cilia (Wachten and Mick, 2021). PIPs and SPLs play essential roles in these pathways, which have not been analyzed in detail in a ciliary context. For example, the membrane composition of the inner and outer leaflet and the biophysical properties of the membrane play a key role in regulating Wnt signaling (Azbazdar et al., 2021). Furthermore, glycosphingolipids (GSLs) are known mediators of RTK signaling (Julien et al., 2013), and PI 4,5-biphosphate ($PI(4,5)P_2$) regulates RTK activity from the inner leaflet of the PM (Hedger et al., 2015). Moreover, both SPLs and PIPs can interact and regulate GPCR function (Jafurulla and Chattopadhyay, 2015) and, vice versa, GPCRs also control PIP metabolism (Oude Weernink et al., 2007). In the following subchapters, I will summarize the recent findings about the role of SPLs and PIPs in cilia, which lead to a model depicting the predominant lipid species in the apical and periciliary PM as well as in the CM (**Figure 4**).

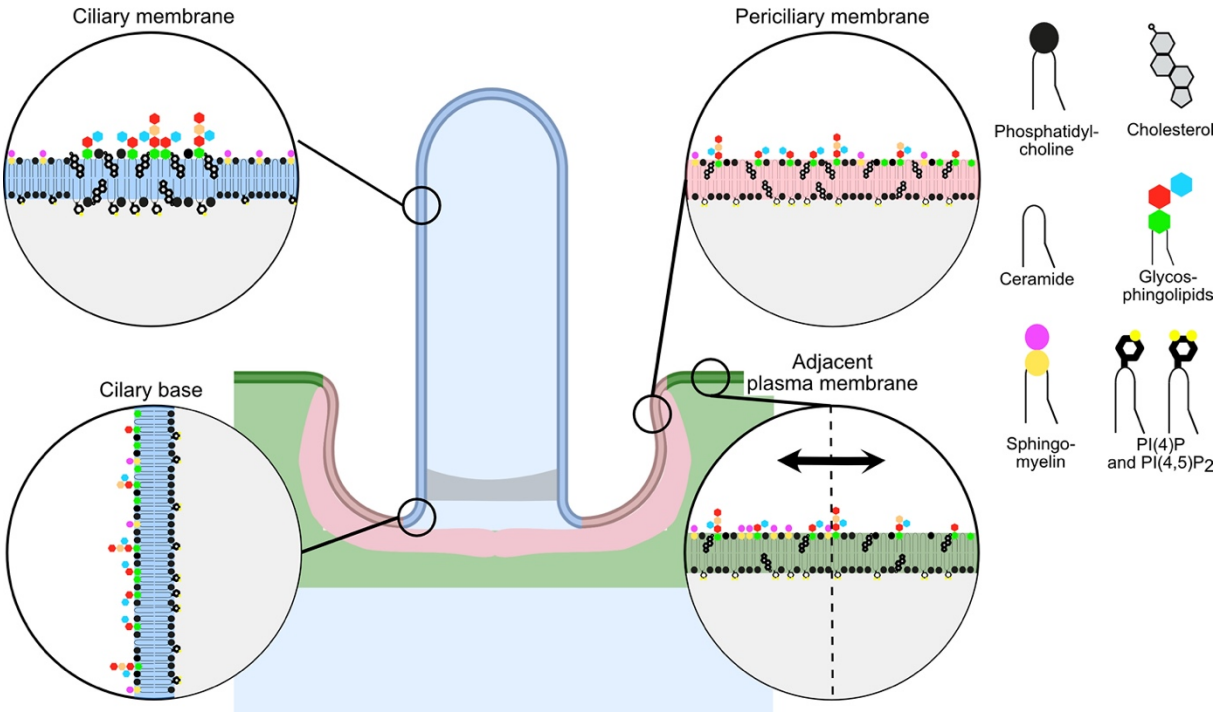

Figure 4: Model of putative lipid distribution in the apical and periciliary plasma membrane as well as in the ciliary membrane. The ciliary membrane is postulated to be rich in SPLs, especially sphingomyelin (SM), GM3, and GM1, and putatively forms cholesterol-based lipid rafts. It also displays PI 4-phosphate PI(4)P as the predominant PIP species. At the most distal part of the ciliary membrane, there is an indication of the region being cholesterol-poor. The periciliary and adjacent plasma membrane are postulated to also be enriched in PI 4,5-biphosphate ($PI(4,5)P_2$), and SPLs, while the conversion of SM to ceramide at the apical membrane at the position of the emanating cilium is crucial for ciliogenesis.

1.5.1 Phosphatidylinositol phosphates in ciliary signaling

Diacylglycerol forms the backbone of PI and is connected to the inositol headgroup via a phosphodiester linkage (**Figure 5A**). To current knowledge, only three of the five free -OH groups can naturally be phosphorylated, resulting in seven different PIP species (**Figure 5A**) that differentially control cellular signaling. They either interact with membrane proteins to activate them or bind to soluble proteins to anchor them at a specific place in the membrane. Furthermore, the different PIP species show an organelle-specific enrichment (Cockcroft and Raghu, 2018): Active transport and local remodeling using PIP-headgroup specific kinases and phosphatases allows the cell to define the subcellular enrichment and, thereby, determine organelle specificity. (Dickson and Hille, 2019).

The ciliary compartment is enriched in PI 4-phosphate (PI(4)P), which is maintained by the action of the Lowe oculocerebrorenal syndrome protein (OCRL), Inositol polyphosphate-5-phosphatase B (INPP5B), and E (INPP5E), whereas the adjacent PM predominantly contains $PI(4,5)P_2$ (Chavez et al., 2015; Garcia-Gonzalo et al., 2015;

Luo et al., 2013; Luo et al., 2012; Prosseda et al., 2017). Under physiological conditions, when re-entering the cell cycle through growth-factor stimulation, ciliary PI(4)P is converted into $PI(4,5)P_2$, to facilitate ciliary disassembly through F-actin polymerization (Phua et al., 2017). INPP5E appears to be the major contributor to maintain ciliary PI(4)P levels and INPP5E dysfunction leads to ciliary $PI(4,5)P_2$ enrichment that is associated with the ciliopathies Joubert and MORM syndrome (Bielas et al., 2009; Chavez et al., 2015; Garcia-Gonzalo et al., 2015; Jacoby et al., 2009).

Ciliary signaling crucially relies on the PIP homeostasis: $PI(4,5)P_2$ facilitates binding of GPR161 and other GPCRs to IFT-A via the Tubby-like protein 3 (TULP3), thereby leading to the ciliary entry of these receptors (Mukhopadhyay et al., 2010). Once inside the cilium, GPR161 has to be released to regulate ciliary GPR161 levels, which is achieved by conversion of $PI(4,5)P_2$ to PI(4P) in the ciliary membrane via INPP5E (**Figure 5B**) (Chavez et al., 2015; Garcia-Gonzalo et al., 2015). Interestingly, a study in the fruit fly *Drosophila melanogaster* and mouse fibroblasts showed that SHH regulates PI(4)P, which directly binds SMO and PTCH1, and triggers SMO phosphorylation and activation through the G protein-coupled receptor kinase 2 (GPRK2) (Jiang et al., 2016). This study also proposed a model contrasting the other studies, in which the CM and the adjacent PM are enriched in $PI(4,5)P_2$, which is converted into PI(4)P upon Hh stimulation. However, experimental evidence is only based on ELISA measurements of whole-cell PIP levels without local resolution of the primary cilium.

Loss of INPP5E results in ciliary GPR161 enrichment and inhibition of ciliary GPR161 exit after Hh pathway stimulation as PI(4,5)P is not converted to PI(4)P, which inhibits the release of GPR161 from the IFT-A-TULP3-$PI(4,5)P_2$ complex once inside the cilium (**Figure 5B**) (Chavez et al., 2015; Garcia-Gonzalo et al., 2015). Downstream, on the transcriptional level, the expression of Hh target genes under basal conditions is not changed in *Inpp5e*-KO cells upon ciliary GPR161 enrichment, but the induction of *Ptch1* and *Gli1* is diminished after Hh pathway stimulation (**Figure 5B**) (Chavez et al., 2015; Garcia-Gonzalo et al., 2015).

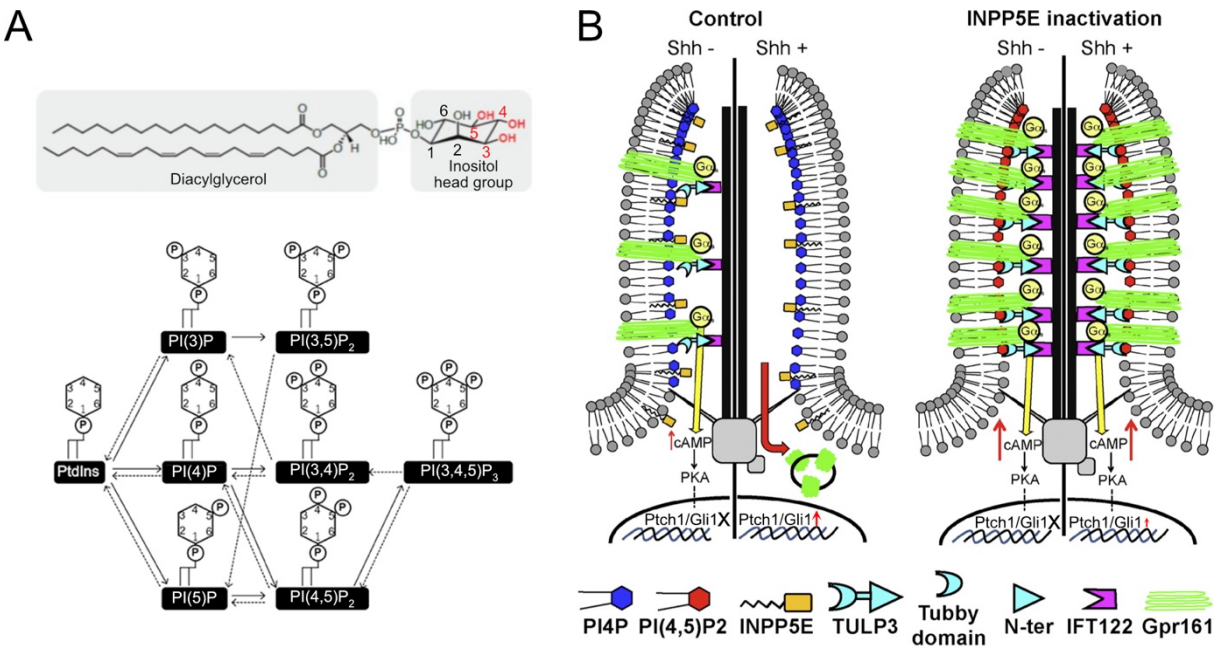

Figure 5: General structure of phosphatidylinositol phosphates (PIPs) and the putative roles of phosphatidylinositol 4-phosphate (PI(4)P) and phosphatidylinositol 4,5-biphosphate ($PI(4,5)P_2$ in ciliary Hedgehog signaling. A: PIP structure and numbering. PIP conversion is carried out by headgroup-specific kinases and phosphatases. A detailed overview can be found here (Balla, 2013). **B:** Model of how loss of INPP5B affects ciliary signaling. For further details, see text. Figures modified from (Nakada-Tsukui et al., 2019) (A), (Mazloumi Gavgani et al., 2018) (A), and (Chavez et al., 2015) (B).

However, whether indeed the altered GPR161 levels after INPP5E loss change ciliary cAMP levels has not been studied yet. Thus, delineating downstream signaling after INPP5E loss, especially in terms of cAMP dynamics, could set the base for treating ciliopathies using activity-modulating drugs for cilia-specific GPCRs.

1.5.2 Sphingolipids in ciliary signaling

SPLs are composed of a sphingoid long-chain base in amide linkage to a fatty acid with variable length, resulting in ceramide (Cer). Cer is either used to produce Sphingomyelin (SM) or, via the addition of a diverse family of glycans, converted into GSLs, which represent the largest group of SPLs (**Figure 6A**) (Sandhoff and Kolter, 2003).

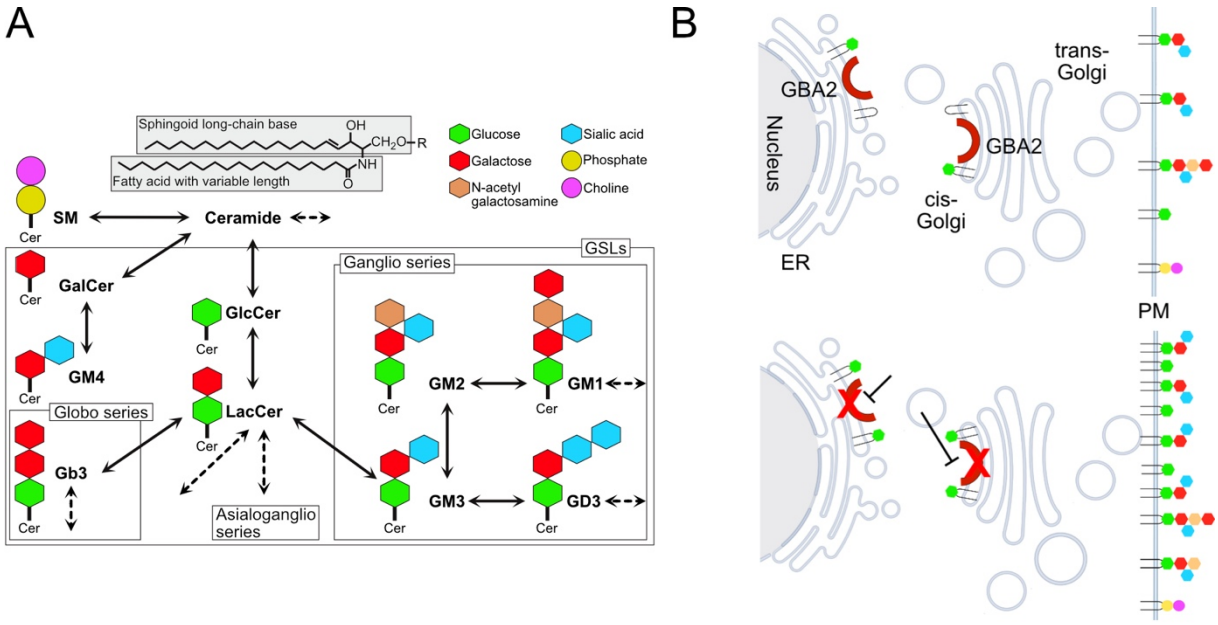

Figure 6: Overview of sphingolipids (SPLs) and the action of the non-lysosomal β-glucosidase, GBA2. A: SPLs consist of a sphingoid long-chain base, in amide linkage to a fatty of acid chain, which form Ceramide (Cer). SPLs are metabolized in a stepwise fashion by the addition or cleavage of different headgroup moieties, as depicted by the major SPL species. Figure modified from (Kaiser et al., 2020). **B:** GBA2 is located at the endoplasmic reticulum (ER) and the cis-Golgi, where it cleaves glucosylceramide (GlcCer) into glucose (Glc) and ceramide (Cer), thereby regulating glycosphingolipid (GSL) levels in the plasma membrane (PM). GBA2 loss or dysfunction results in GSL accumulation on the PM. Figure generated using biorender.

Directed transport mechanisms and specific localization of remodeling enzymes determine the subcellular SPL distribution (Yamaji and Hanada, 2015). However, the mechanisms regulating the SPL homeostasis in the primary cilium are unknown.

SPLs, especially GSL, are known mediators of cell-cell interactions via complementary binding to opposing PM molecules as well as modulators of transmembrane proteins (D'Angelo et al., 2013; Schnaar and Kinoshita, 2015). Because of their biophysical properties, SPLs together with cholesterol and selected proteins enrich and cluster in "lipid rafts", which are small microdomains in the membrane that display different biophysical properties compared to the adjacent membrane and (Schnaar and Kinoshita, 2015). One property is the "membrane order" describing the density of lipid packaging in the PM, which is increased by lipid rafts. Recent models suggest that lipid

rafts act as signaling platforms, bringing signaling scaffolds together and directly modulating the function of proteins (Sezgin et al., 2017).

Primary cilia have been proposed to contain high concentrations of sterols and SPLs (Chailley and Boisvieux-Ulrich, 1985; Kaneshiro et al., 1984; Montesano, 1979), indicating that lipid rafts might also form in the ciliary membrane. This has been underlined by the specific detection of lipid raft-associated gangliosides GM3 and GM1 in the ciliary membrane of Mardin-Darby Canine Kidney (MDCK) cells (Janich and Corbeil, 2007), and of the lipid raft marker Prominin-1 in primary cilia of neuroepithelial cells (Dubreuil et al., 2007). In addition, the lipid raft scaffold Flotillin-2 (FLOT2) and a structural component of cholesterol-rich raft domains, Caveolin-1 (CAV1), both localize to the TZ of mammalian cilia (Schou et al., 2017). Labeling with 6-Dodecanoyl-2-Dimethylaminonaphthalene (Laurdan) to determine the membrane order revealed a zone around the ciliary base that displayed an increased membrane order, compared to the adjacent PM, in MDCK cells (Vieira et al., 2006). In contrast, freeze-fracture electron microscopy of motile ependymal cilia showed a cholesterol-poor region at the most distal part of the ciliary membrane (Montesano, 1979).

SPLs were also shown to play pivotal roles during ciliogenesis. Deficiency of the PI(4)P adaptor protein-2 (FAPP2), which mediates glucosylceramide (GlcCer) transport to the *trans*-Golgi network (TGN) and facilitates the synthesis of complex GSLs, impairs the formation of condensed apical membrane domains and ciliogenesis in MDCK cells (Vieira et al., 2006). Furthermore, conversion of SM to Cer at the apical PM drives ciliogenesis in various mammalian cell lines: in MDCK cells, acid sphingomyelinase (aSMase) mediates the conversion (He et al., 2012), whereas in human embryonic stem cells and pluripotent stem-cell-derived neuroprogenitors, the neutral sphingomyelinase (nSMase) converts SM to Cer (He et al., 2014). Lastly, membrane sterols have been shown to drive Hh pathway activation (Deshpande et al., 2019), i.e., the sterol transporter PTCH1 regulates SMO by controlling SM-sequestered cholesterol levels in the ciliary membrane (Kinnebrew et al., 2019; Kinnebrew et al., 2021).

The levels of GlcCer, the precursor for complex GSLs, have to be tightly regulated to maintain GSL homeostasis and cellular signaling (Stirnemann et al., 2017; Woeste, 2018). Three hydrolases, the acid β-glucosidase GBA1 (Brady et al., 1965), the non-lysosomal β-glucosidase GBA2 (van Weely et al., 1993), and the cytosolic β-

glucosidase GBA3 (de Graaf et al., 2001) degrade GlcCer into glucose and Cer. So far, only for the specialized motile cilium, the sperm flagellum, a role for GSLs has been described as GlcCer is crucial for sperm development: Loss or inhibition of GBA2 function results in GlcCer accumulation and, in turn, causes severe morphological defects of the sperm head and male subfertility (Raju et al., 2015; Walden et al., 2007; Yildiz et al., 2006). In other cells, i.e., fibroblasts, accumulation of GlcCer in the absence of GBA2 increases the GSL content of the PM and, thereby, the membrane order (Raju et al., 2015) (**Figure 6B**). Whether loss of GBA2 not only affects the function of sperm flagella, but also of primary cilia, is not known yet.

In summary, the primary cilium contains a unique protein and lipid identity that the cell has to tightly regulate to ensure primary cilium function. SPL and PIP microdomains have been postulated to be localized in the CM, and SPLs play a pivotal role during ciliogenesis. However, how these lipids change the biophysical properties of the CM and, in turn, ciliary signaling, has not been studied yet. As GBA2 has been shown to play a crucial role in sperm flagella and in maintaining the PM GSL homeostasis, the regulation of the GSL homeostasis by GBA2 might also control primary cilia signaling and function. Moreover, the action of the INPP5E phosphatase in maintaining the ciliary PI(4)P homeostasis and the pathological consequences for ciliary Hh signaling has been shown, but the pivotal role of ciliary cAMP in this context is still undefined. Lastly, an unbiased approach to determine the dynamic lipidome of primary cilia, i.e., mass spectrometry, has yet not been applied to primary cilia as techniques that allow adapting mass spectrometry for the local resolution of subcellular organelles are missing.

1.6 Hypothesis and thesis aim

In my Ph.D., my major goal was to analyze the ciliary SPL- and PIP-dependent lipid identity and its role in ciliary signaling. Using immortalized cell lines, I aimed to 1.) analyze SPL-dependent biophysical properties of the ciliary membrane compared to the plasma membrane, 2.) analyze the role of GSLs in controlling ciliary protein homeostasis, signal transduction, and gene expression in the context of Hh signaling, 3.) analyze putative changes in ciliary cAMP signal transduction in ciliopathy models,

and 4.) establish a technique to isolate and purify primary cilia for an unbiased lipidome analysis.

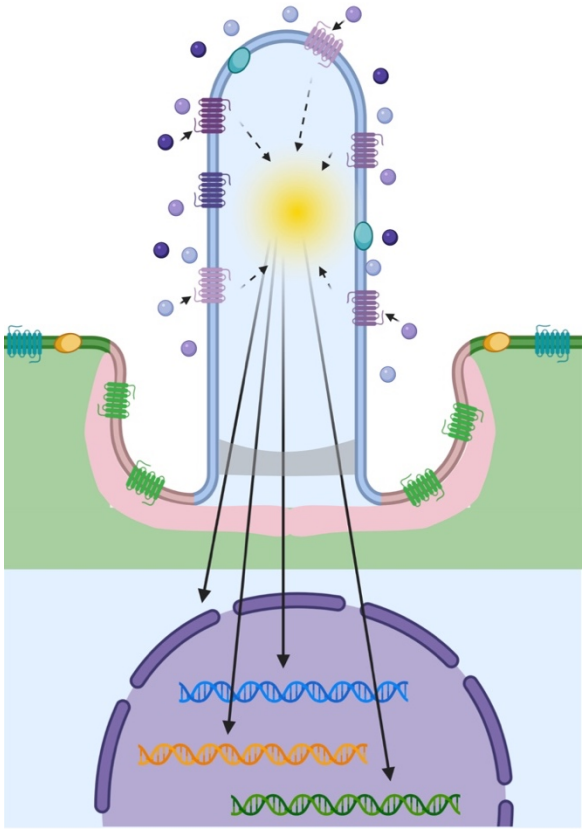

Figure 7: Hypothesis. The cell maintains a unique ciliary lipid- and protein-composition that is intertwined to dynamically regulate ciliary homeostasis and signal transduction. Thereby, the cell can control cilia-specific functions in a tissue-dependent manner.

We hypothesize that the cell maintains a unique ciliary lipid- and protein-composition that is intertwined to dynamically regulate ciliary homeostasis and signal transduction in a tissue-specific manner (**Figure 7**). Specifically, I used the current model of ciliary Hh signaling to study this hypothesis.

2 Materials and Methods

All solutions were prepared using grade 1 water (H_2O, ultrapure water defined by ISO 3696:1987 specifications) and sterilized by autoclavation for 20 min at 121°C or by sterile-filtration using 0.22 µm filter membranes, if not stated otherwise.

2.1 Reagents and Materials

Table 1: Reagents

Reagent	Supplier	Reference
2-Mercaptoethanol (β-ME)	Sigma Aldrich, St. Louis, USA	M3148-100ML
2-Methyl-5-hydroxytryptamine hydrochloride (2M5HT)	Tocris Bioscience, Bristol, UK	558
2-Propanol, LiChrosolv® (Isopropanol)	Supelco, Bellefonte, USA,	1.02781.1000
3-isobutyl-1-methylxanthine (IBMX)	applied biosystems, Waltham, USA	A0695
Acetic acid (for HPLC LiChropur™)	Supelco, Bellefonte, USA	5438080250
Acrylamide 4K solution	applied biosystems, Waltham, USA	A1672,0500
Agarose LE	GENAXXON bioscience, Ulm, Germany	M3044.0500
Ammonium acetate	Carl Roth, Karlsruhe, Germany	7869.2
Aqua-Poly/Mount	Tebi-Bio, Le Perray-en-Yvelines, France	#07918606-20
Bromphenolblue	Sigma Aldrich, St. Louis, USA	B0126
Calcium chloride ($CaCl_2$)	Carl Roth, Karlsruhe, Germany	CN93.1
ChemiBLOCKER	Merck Millipore, Billerica, USA	2170
Chloroform, LiChrosolv®	Supelco, Bellefonte, USA,	1.02444.1000
Collagenase from Clostridium histolyticum, Type II 125U/mg (Collagenase)	Sigma Aldrich, St. Louis, USA	C6885-100MG
Cytochalasin-D	Gibco, Amarillo, USA	PHZ1063
Di-4-ANEPPDHQ	Invitrogen, Waltham, USA	D36802
Di-sodium hydrogen phosphate Dihydrate (Na_2HPO_4 * $2H_2O$)	Merck Millipore, Billerica, USA	119753
Dimethyl Sulfoxide (DMSO)	Sigma Aldrich, St. Louis, USA	D45450
Dulbecco's phosphate-buffered saline (DPBS)	Gibco, Amarillo, USA	14190-094
Ethanol, LiChrosolv®	Supelco, Bellefonte, USA,	1.11727.1000

Ethylendiamintetraessigsäure Dinatriumsalz Dihydrat (EDTA * $2H_2O$)	Sigma Aldrich, St. Louis, USA	E5134
Forskolin	Sigma Aldrich, St. Louis, USA	# SLBP3308V
G418 (Geneticin)	Thermo Fisher Scientific, Waltham, USA	11811
Glucose	Carl Roth, Karlsruhe, Germany	X997.2
Glycerin	Sigma Aldrich, St. Louis, USA	G2289
Glycine for molecular biology	applied biosystems, Waltham, USA	A1067,5000
HEPES	Carl Roth, Karlsruhe, Germany	6763.2
Human Sonic Hedgehog (hSHH)	StemRD, Burlingham, USA	SHH-025
Internal Standard (IS)	Kindly provide by Prof. Dr. C. Thiele	For composition, see text
Isoprenaline hydrochloride (Isoproterenol)	Sigma Aldrich, St. Louis, USA	I5627
Magnesium chloride ($MgCl_2$)	Carl Roth, Karlsruhe, Germany	KK36.2
Methanol, LiChrosolv®	Supelco, Bellefonte, USA,	1.06035.1000
Methyl-β-Cyclodextrin (M-β-CD)	Sigma Aldrich, St. Louis, USA	C4767
MZ-21 (alias AMP-DNM)	Kindly provided by Prof. Dr. Johannes Aerts, Leiden University	Overkleeft et al., 1998
N-butyldeoxynojirimycin (NB-DNJ)	Sigma Aldrich, St. Louis, USA	no longer available
Natriumbicarbonat ($NaHCO_3$)	Sigma Aldrich, St. Louis, USA	S5761-500G
Natriumdihydrogenphosphat-Dihydrat (NaH_2PO_4 * $2H_2O$)	Merck Millipore, Billerica, USA	106342
NKH477	Sigma Aldrich, St. Louis, USA	N3290-5MG
Paraformaldehyde, 16% w/v aq. Solvent, methanol free (PFA)	Alfa Aesar, Landau, Germany	43368
Penicillin-Streptomycin (P-S)	Gibco, Amarillo, USA	15140-122
Poly-L-Lysine Hydrochloride (PLL)	Sigma Aldrich, St. Louis, USA	P1399
Potassium chloride (KCl)	Carl Roth, Karlsruhe, Germany	P017.2
Proteinase K	blirt, Gdańsk, Poland	RP102B
Smoothened agonist (SAG)	Sigma Aldrich, St. Louis, USA	SML1314
Sodium chloride (NaCl)	Carl Roth, Karlsruhe, Germany	HN00.2
Sodium dodecylsuflate (SDS), pellets	Carl Roth, Karlsruhe, Germany	8029.4
TEMED	applied biosystems, Waltham, USA	A1148
Tris-base	Merck Millipore, Billerica, USA	648310-M
Tris-HCL	Carl Roth, Karlsruhe, Germany	9090.3
Triton-X100	applied biosystems, Waltham, USA	3051.3

Trypsin-EDTA (0.05%)	Gibco, Amarillo, USA	25300062
TWEEN® 20	Sigma Aldrich, St. Louis, USA	P9416
Zeocin (100 mg/mL)	Thermo Fisher Scientific, Waltham, USA	J67140.8

Table 2: Materials

Material	**Supplier**	**Reference**
1 mL CryoTube™ vials	Thermo Fisher Scientific, Waltham, USA	377224
13 mm glass coverslips	Paul Marienfeld, Lauda-Königsfel, Germany	117530
96-well, 24-well, 6-well, and 10 cm CELLSTAR® plasticware	greiner bio-one, Kremsmünster, Austria	655 180, 662 160, 657 160, and 664 160
96-well half area white microplate	greiner bio-one, Kremsmünster, Austria	675075
CellCarrier™-96 ultra (96-blackwell)	PerkinElmer, Waltham, USA	6055302
Corning® 500 mL Erlenmeyer Flask w/ Ventilated Cap, polycarbonate, sterile	Merck Millipore, Billerica, USA	CLS431145
Cytodex® 3 microcarrier beads	Sigma Aldrich, St. Louis, USA	C3275-10G
dNTPs	Thermo Fisher Scientific, Waltham, USA	R0192
DMEM/F12 (1:1) (1x) + GlutaMAX	Gibco, Amarillo, USA	31331-028
DMEM (1x) + GlutaMAX	Gibco, Amarillo, USA	61965-026
DreamTaq™ Buffer (10X)	Thermo Fisher Scientific, Waltham, USA	B65
DreamTaq™ DNA Polymerase	Thermo Fisher Scientific, Waltham, USA	EP0705
Dual-Glo® 3 Luciferase Assay kit	Promega, Madison, USA	E2920
Fetal Bovine Serum (FCS)	BIOCHROM, Berlin, Germany	S 0115
GeneJuice	Sigma Aldrich, St. Louis, USA	70967
GeneRuler™ 1 kb Plus DNA Ladder	Thermo Fisher Scientific, Waltham, USA	SM1331
iScript cDNA Synthesis Kit	BIO-RAD, Hercules, USA	#1708891
iQ™ 96-Well PCR Plates, high profile, semi-skirted (96-well RT-qPCR plates)	BIO-RAD, Hercules, USA	#2239441
iQ SYBR® Green Supermix	BIO-RAD, Hercules, USA	#1708880
Lenti-X Concentrator	TaKaRa BIO, Kusatsu, Japan	631232
LB-Agar (Lennox)	Carl Roth, Karlsruhe, Germany	X965.1

L-Glutamine (200 mM, 100x)	Gibco, Amarillo, USA	25030-081
Lipofectamine 2000 Reagent	Invitrogen, Waltham, USA	11668-027
Lysogeny broth (LB)-medium	Carl Roth, Karlsruhe, Germany	X968.1
Mammalian protease inhibitor cocktail (mPic)	Sigma Aldrich, St. Louis, USA	P8340-1ML
MEM (1x) + GlutaMAX	Gibco, Amarillo, USA	41090-028
MEM NEAA (100x)	Gibco, Amarillo, USA	11140-035
MicroAMP™ Optical 384-Well Reaction Plate with Barcode (384-well RT-qPCR plate)	applied biosystems, Waltham, USA	4309849
MicroAMP™ Optical Adhesive Film	applied biosystems, Waltham, USA	4311971
Mini-PROTEAN Tetra Cell system	BIO-RAD, Hercules, USA	#1658001EDU
NucleoBond® Xtra Maxi EF	MACHEREY-NAGEL, Düren, Germany, Düren, Germany	740424.10
NucleoBond® Xtra Midi	MACHEREY-NAGEL, Düren, Germany, Düren, Germany	740410.100
NucleoSpin® Gel and PCR Clean-up	MACHEREY-NAGEL, Düren, Germany, Düren, Germany	740609.25
NucleoSpin® Plasmid	MACHEREY-NAGEL, Düren, Germany, Düren, Germany	740588.25
Nunc™ multiplate (4-well plate)	Thermo Fisher Scientific, Waltham, USA	176740
Odyssee® Blocking Buffer	LI-COR Biosciences, Lincoln, USA	927-40000
Opti-MEM™	Gibco, Amarillo, USA	11058-021
Pierce™ BCA Protein Assay Kit (BCA Assay Kit)	Thermo Fisher Scientific, Waltham, USA	23227
Pierce™ NHS-Activated Magnetic Beads	Thermo Fisher Scientific, Waltham, USA	88826
Polyethylenimine (PEI), branched	Sigma Aldrich, St. Louis, USA	408727
PowerTrack™ SYBR™ Green Master Mix	applied biosystems, Waltham, USA	A46109
Protein Marker VI (10-245 kDa) prestained	AppliChem, Darmstadt, Germany	A8889
PureLink™ RNA Mini Kit	Invitrogen, Waltham, USA	12183025
PVDF-membrane Immobilon-P	Merck Millipore, Billerica, USA	IPFL00010
Ratiometric Cilia-Targeted cADDis cAMP Assay Kit (5-HT_6-cADDis-mCherry)	Montana Molecular, Bozeman, USA	#D0211G
RNA loading dye	New England BioLabs (NEB), Ipswich, USA	B0363S

Semi-dry-blotter	Carl Roth, Karlsruhe, Germany	T788.1
Incu-Shaker CO2 Mini (Shaking incubator)	Benchmark Scientific, Sayreville, USA	H3501-E
Sodium Pyruvate 100 mM (100x)	Gibco, Amarillo, USA	11360-039
SuperSignal® West Pico Chemiluminescent Substrate	Thermo Fisher Scientific, Waltham, USA	34087
SureClean	Bioline USA, Taunton, USA	BIO-37046
Ultra-Clear™ Centrifuge Tubes 14x89 mm	BECKMAN COULTER, Brea, USA	344059
0.22 µm filter membranes	Merck Millipore, Billerica, USA	GSWP02500
µ-Slide 8 Well Glass Bottom (8-well IBIDI)	IBIDI, Gräfelfing, Germany	80806

Table 3: Fluorescent dyes

Dye	**Supplier**	**Reference**
4´,6-Diamidino-2-Phenylindole, Dihydrochloride (DAPI)	Invitrogen	D1306
Di-4-ANEPPDHQ	Invitrogen, Waltham, USA	D36802
Pro12A	Kindly provided by A.S. Klimchenko	(Danylchuk et al., 2020)

2.2 Solutions and buffers

Phosphate buffered saline (PBS) was prepared in a 10-fold stock with 1.3 M NaCl, 70 mM Na_2HPO_4, 30 mM NaH_2PO_4, and adjusted to pH 7.4 at RT using 1 M NaOH. Sterile PBS that was used for cell culture was purchased from Gibco (DPBS). For usage, the 10-fold PBS stock was diluted to a 1-fold concentration in H_2O.

PBS-Tween (PBS-T) was prepared by adding 0.05% (v/v) Tween-20 to PBS.

PBS-EDTA was prepared by adding 0.05% (w/v) EDTA to PBS.

Tris-EDTA (TE) buffer was prepared with 1 mM EDTA, and 10 mM Tris-HCl in H_2O adjusted to pH 8 at RT.

Tail lysis buffer was prepared with 100 mM EDTA in H_2O adjusted to pH ,8 at RT, 10 mM Tris-HCl, and 0.5% (w/v) SDS in H_2O. Before usage, 10% Proteinase K (dissolved in H_2O at 10 mg/mL) was added. Tail lysis buffer was not sterilized.

Extracellular solution (ES) was prepared with 120 mM NaCl, 5 mM KCl, 2 mM $MgCl_2$, 10 mM HEPES, 10 mM glucose in H_2O, and adjusted to pH 7.4 at RT using 1 M NaOH. The ES has a calculated osmolarity around 290 mOsmol, which slightly varies depending on the added NaOH for adjusting the pH. Osmolarity after adjusting the pH was controlled using an Osmolaritymeter. Solutions were discarded when depicting an osmolarity below 280 mOsmol or higher than 300 mOsmol. ES was not sterilized, but distributed in 15 mL Falcons and stored at -20°C until use. After usage, remaining ES was not re-frozen.

Total lysis buffer for whole cell lysates was prepared in H_2O with 10 mM Tris-HCl adjusted to pH 7.5 at RT, 150 mM NaCl, 0.5 mM EDTA, 1% (v/v) TritonX-100, and 1:500 mPIC. Total lysis buffer was not sterilized after preparation and mPIC was added right before usage. Total lysis buffer was not sterilized.

Deciliation buffer with high Ca^{2+} concentration was prepared with 112 mM NaCl, 3.4 mM KCl, 10 mM $CaCl_2$, 2 mM HEPES. Right before use, I added 2.4 mM $NaHCO_3$ and adjusted the pH to 7.0 at RT, followed by addition of 10 µg/mL Cytochalasin D and 0.5% mPIC. The deciliation buffer was not sterilized.

For Sodium dodecyl sulfate (SDS) polyacrylamide gel electrophoresis (PAGE), buffers were prepared according to the following procedures:
SDS running buffer was prepared as a 10-fold stock solution in H_2O with 250 mM Tris, 1.92 M glycine, and 1% (w/v) SDS that was diluted to a 1-fold stock with H_2O before usage. SDS running buffer was not sterilized.
SDS sample buffer was prepared as a 4-fold stock in H_2O with 200 mM Tris-HCl adjusted to pH 6.8 at RT, 8% (w/v) SDS, 4% (v/v) β-Mercaptoethanol, 50% (v/v) glycerin, and 0.04% (w/v) Bromphenolblue. SDS sample buffer was not sterilized.

For Western blotting, buffers were prepared according the following procedures:
The Western Blot Anodebuffer1 was prepared in H_2O with 300 mM Tris-HCl, 20% (v/v) Methanol, and adjusted to pH 10.4 at RT before the addition of Methanol.
The Western Blot Anodebuffer2 was prepared in H_2O with 25 mM Tris-HCl, 20% (v/v) Methanol, and adjusted to pH 10.4 at RT before the addition of Methanol.
The Western Blot Cathodebuffer was prepared in H_2O with 25 mM Tris-HCl, 40 mM Glycine, 20% (v/v) Methanol, and adjusted to pH 9.4 at RT before the addition of Methanol. Western Blot buffers were not sterilized.
Western Blot Blocking buffer (BB) was prepared by mixing one part PBS-T with one part of Odyssey Blocking Buffer.

2.3 Antibodies

2.3.1 Primary antibodies

All primary antibodies were diluted and incubated in CT solution consisting of one-part ChemiBLOCKER in nineteen-parts of PBS + 0.5% Triton-X100.

Table 4: Primary antibodies.

Antibody	Antigen	Species	Dilution ICC	Dilution WB	Supplier	Reference
Anti Ac-α-TUB	Ac-α-TUB	mouse IgG	1:500	1:2,000	Sigma-Aldrich	T6793
Anti ARL13B	ARL13B	mouse IgG	1:500	-	Abcam	ab136648
Anti ARL13B	ARL13B	rabbit IgG	1:500	-	Proteintech	17711-1-AP
Anti CNX	CNX	rabbit IgG	-	1:2,000	Sigma-Aldrich	C4731
Anti INPP5E	INPP5E	rabbit IgG	1:20 - 1:200	1:500 - 1:2,000	Proteintech	17797-1-AP
Anti $PI(4,5)P_2$	$PI(4,5)P_2$	mouse IgM	1:50 - 200	-	Santa Cruz	sc-53412
Anti PI(4)P	PI(4)P	mouse IgM	1:50 - 200		Echelon Biosciences	Z-P004
Anti Shh (H160)	SHH	rabbit IgG	-	1:2,000	Santa Cruz	SC-9024
Anti SMO	SMO	rabbit IgG	1:500	-	Kindly provided from	(Ocbina et al., 2011)

					the Anderson Lab	
Anti β-tubulin 2.1	β-tubulin	mouse IgG	-	1:2,000	Sigma-Aldrich	T4026
VHH Anti ALFA	ALFA-tag	alpaca VHH	1:1,000	1:10,000	Kindly provided by F. I. Schmidt	(Gotzke et al., 2019)

ICC: Immunocytochemistry, WB: Western Blot, IgG: Immunoglobolin G, IgM: Immunoglobolin M

2.3.2 Secondary antibodies

All secondary antibodies were diluted and incubated in CT solution consisting of one-part ChemiBLOCKER in nineteen-parts of PBS + 0.5% Triton-X100 + 1:10,000 DAPI if not stated otherwise.

Table 5: Secondary antibodies.

Antibody	**Antigen**	**Species**	**Dilution ICC**	**Dilution WB**	**Supplier**	**Reference**
dk anti ms Cy3	mouse IgG	donkey	1:500	-	Dianova	715-165-151
gt anti ms A488	mouse IgG	goat	1:400	-	Life Technologies	A11029
dk anti ms A647	mouse IgG	donkey	1:500	-	Invitrogen	A31571
dk anti ms IRDye680RD	mouse IgG	donkey	-	1:20,000	LI-COR Biosc.	926-68072
dk anti ms IRDye800CW	mouse IgG	donkey	-	1:20,000	LI-COR Biosc.	926-68072
dk anti rb A647	rabbit IgG	donkey	1:500	-	Dianova	711-605-152
dk anti rb Cy3	rabbit IgG	donkey	1:250	-	Dianova	711-165-152
gt anti rb A488	rabbit IgG	goat	1:500	-	Life Technologies	A11034
dk anti rb IRDye680RD	rabbit IgG	donkey	-	1:20,000	LI-COR Biosc.	926-32223
dk anti rb IRDye800CW	rabbit IgG	donkey	-	1:20,000	LI-COR Biosc.	926-32213

gt anti ms IgM Biotin	mouse IgM	goat	1:200-1:1,000	-	Jackson Immuno-Research Laboraties INC.	115-067-020
Streptavidin-Cy3	Biotin	-	1:1,000	-	Jackson Immuno-Research Laboraties INC.	016-160-084
rb anti camelid VHH HRP	Camelid VHH (Llama, Alpaca and Camel)	rabbit	-	1:5,000	GenScript	A01861

ICC: Immunocytochemistry, WB: Western Blot, IgG: Immunoglobolin G, IgM: Immunoglobolin M, ms: mouse, rb: rabbit, dk: donkey, gt: goat.

2.4 Mice

Mice deficient for GBA1 were generated as described in (Enquist et al., 2006).

Mice deficient for GBA2 were generated as described in (Yildiz et al., 2006).

All experiments were performed in agreement with the German law of animal protection and local institutional animal care committees (Landesamt für Natur, Umwelt und Verbraucherschutz, LANUV; Az 84-02.04.2014.A194). Mice were maintained in individually ventilated cages in the mouse facility of the University Hospital Bonn (Haus für Experimentelle Therapie, HET).

2.5 Molecular Biology

2.5.1 Plasmids and primers

Primers were synthesized by Eurofins MWG Operon (Ebersberg, Germany) and delivered as lyophilizate samples. Using TE buffer, the primers were dissolved to a concentration of 100 µM and stored at -20°C.

Plasmid information are shown in Table 6. Plasmid maps can be found in the appendix.

Table 6: Plasmid Information

Name	Internal identifier	Vector backbone	Expresses	Produced by / Reference
CAG-Enhancer-Gag-Pol-RRE-rb globulin	DW-0962	unknown	Gag-pol	Lab of Prof. Dagmar Wachten, JHK
CAG-Enhancer-VSVG-G-human beta globulin	DW-0963	unknown	VSV-G	Lab of Prof. Dagmar Wachten, JHK
pc3-mNPHP3-AKAR4HA-NES-1	DW-0518	pcDNA3.1 (+)	mNPHP3(201)-AKAR4-NES	Dr. Wolfgang Bönigk
pc3-mNPHP3-Cerulean-4	DW-0690	pcDNA3.1 (+)	mNPHP3(201)-Cerulean	Dr. Wolfgang Bönigk
pc3-mNPHP3-Citrin-3	DW-0691	pcDNA3.1 (+)	mNPHP3(201)-Citrine	Dr. Wolfgang Bönigk
pc3-mNPHP3-R-FlincA-12	DW-0840	pcDNA3.1 (+)	mNPHP3(201)-R-FlincA	Dr. Wolfgang Bönigk
pc3-mNPHP3(201)-mICNBD-FRET-1	DW-0431	pcDNA3.1 (+)	mICNBD-FRET	Lab of Prof. Dagmar Wachten
pc3.1-mNPHP3(201)-VHH-enhancer-mCherry-7	DW-0786	pcDNA3.1 (+)	mNphp3(201)-VHH_{enh}-mCherry	Lab of Prof. Dagmar Wachten, JHK / JNH
pc3.1-VHH-enhancer-mCherry #4	DW-0788	pcDNA3.1 (+)	VHH_{enh}-mCherry	Lab of Prof. Dagmar Wachten, JHK / JNH
pc3.1mICNBD-FRET#9	B0196b	pcDNA3.1 (+)	mICNBD_FRET	Lab of Prof. Dagmar Wachten, DW
pcA-Cerulean	DW-0807	pCA	Cerulean	Dr. Wolfgang Bönigk
pcA-Citrine	DW-0806	pCA	Citrine	Dr. Wolfgang Bönigk
pcDNA3-AKAR4	DW-0418	pcDNA3.1 (+)	AKAR4	Addgene #61619
pcDNA3-AKAR4-NES	DW-0420	pcDNA3.1 (+)	AKAR4-NES	Addgene #64727
pcDNA3.1-Shh-N	DW-0497	pcDNA3.1 (+)	ShhN	Addgene #37680

pcDNA3.1zeo_mCherry	DW-0471	pcDNA3.1 (+)	mCherry	Dr. Wolfgang Bönigk
pcDNA4-HisMaxB_R-FlincA	DW-0829	pcDNA4HMB	R-FlincA	Gift by Kozuki Horikaro, (Ohta et al., 2018)
pcDNA4-HisMaxB_R-FlincA-mut	DW-0830	pcDNA4HMB	R-FlincA_mut	Gift by Kozuki Horikaro, (Ohta et al., 2018)
pEGFP-N1-bPAC #1	DW-0839	pEGFP-N1	bPAC-GFP	Lab of Prof. Dagmar Wachten, JHK/FK
pInducer20_minus_CMV_ALFAtag-(235-236)-mPtch1	DW-0926	pInducer20_minus_CMV	ALFA-tagged-PTCH1	Lab of Prof. Dagmar Wachten and Prof Eicke Latz, FK / Fraser Duthie
pInducer20_minus_CMV_ALFAtag-(51-52)-mSmo	DW-0925	pInducer20_minus_CMV	ALFA-tagged SMO	Lab of Prof. Dagmar Wachten and Prof Eicke Latz, FK / Fraser Duthie
pX459-sgRNA#1-INPP5E	DW-0689	px459 V2.0	Cas9 and INPP5E guide RNA #1	Lab of Prof. Dagmar Wachten, FK
pX459-sgRNA#2-INPP5E	DW-0719	px459 V2.0	Cas9 and INPP5E guide RNA #2	Lab of Prof. Dagmar Wachten, FK
pX459-sgRNA#3-INPP5E	DW-0720	px459 V2.0	Cas9 and INPP5E guide RNA #3	Lab of Prof. Dagmar Wachten, FK
SV-40 large T Antigen	DW-0997	unknown	SV-40 large T Antigen	Kindly provided by Prof. Florian I. Schmidt

Table 7: Genotyping PCR primer-specific information

PCR	Primer sequence (5´to 3´direction)		Annealing temperature [°C]	Elongation time [s]
	Forward	Reverse		
GBA1 rec.	GTACGTTCATG-GCATTGCTGTTCACT	ATTCCAGCTGTC-CCTCGTCTCC	56	80
GBA1 WT flox	GTACGTTCATG-GCATTGCTGTTCACT	GGGCTGTTTGTA-AAATGCGTCTTTGG	56	80
GBA2-rec.	GCATGTACAAC-ACATACGATGTCCA	CCAGTCAGCAGT-ATCATGAATCAA	60	60
GBA2 WT	GTGCTGGCTCA-CTGAGCTGGA	CCAGTCAGCAGTA-TCATGAATCAA	60	60
INPP5E	AAACCCCATGC-CTCCTTTCA	CTGCAGGGACTG-GCCCCAT	62	40

WT: wild type, rec: recombinant

Table 8: RT-qPCR primer-specific information

PCR	Primer sequence (5´to 3´direction)		PrimerBank ID (if applicable)
	Forward	Reverse	
GAPDH	AGGTCGGTGT-GAACGGATTTG	TGTAGACCATG-TAGTTGAGGTCA	6679937a1
GLI1	TACCATGAGCC-CTTCTTTAGGA	GCATCATTGAA-CCCCGAGTAG	-
HPRT	TCAGTCAACGG-GGGACATAAA	GGGGCTGTACT-GCTTAACCAG	7305155a1
PTCH1	GCCTTGGCTGT-GGGATTAAAG	CTTCTCCTATCT-TCTGACGGGT	-

2.5.2 *Escherichia coli* culture

2.5.2.1 *Escherichia coli* strains

For cloning, the *Escherichia coli* (*E. coli)* strains XL1-Blue (#200249, Stratagene, California, USA) and DH5α (Thermo Fisher Scientific, Waltham, USA) were used.

2.5.2.2 Generation of competent cells

Competent *E. coli* cells were generated using the $CaCl_2$ method according to (Mandel and Higa, 1970). The cells were grown in 50 mL LB-medium in a shaker at 37°C until

they reached an optical density of 0.4 measured at 600 nm. At this point, the cells were cooled down on ice for 30 min and pelleted using a centrifuge with 5,000 x g for 10 min at 4°C. Subsequently, the pellet was resuspended in 5 mL ice-cold 0.1 M $CaCl_2$ solution containing 25% (v/v) glycerin and incubated for 2 h on ice. After incubation, the cells were distributed in 100-200 µL aliquots and snap-frozen with liquid nitrogen for long-term storage at -80°C until usage for transformation and retransformation.

2.5.2.3 Transformation and retransformation of competent cells

For one retransformation, 100 µL competent *E. coli* cells were thawed on ice and mixed with 50 ng DNA. Subsequently, cells were incubated for 20 min on ice. Following the incubation, cells were exposed to a heat shock for 1 min at 42°C in a water bath, followed by an incubation for 10 min on ice. Afterwards, 200 µL LB-medium was added and the cells were incubated for 30 min at 37°C on a shaking incubator. For transformation, the cells were streaked on a LB-Agar plate and incubated overnight at 37°C to generate single colonies of transformed cells. The next day, single colonies were picked and incubated at 37°C in a shaking incubator with 5 mL LB-medium for small-scale plasmid preparation. For Retransformation, the cells were added to 5 mL (small-), 250 mL (medium-) or 500 mL (large-scale plasmid preparation) and incubated overnight at 37°C.

2.5.2.4 Small-, medium-, and large-scale plasmid preparation

Small-, medium-, and large-scale plasmid preparations from *E. coli* cultures were performed with NucleoSpin® Plasmid, NucleoBond® Xtra Midi, and NucleoBond® Xtra Maxi EF kits, respectively, according to the manufacturer's instructions.

2.5.2.5 Cloning

Plasmids were cloned by template amplification and introduction of restriction sites using PCR and restriction digest with restriction enzymes from New England Biolabs (Ipswich, USA) and Roche Applied Science (Basel, Switzerland).

2.5.2.6 Sequencing of DNA

Sequencing of DNA was performed by Eurofins MWG Operon (Ebersberg, Germany). Plasmid DNA was sent with 50-100 ng/µL concentration in 15 µL reaction volume, whereas purified PCR products were sent with 1 ng/µL concentration in 15 µL reaction

volume. PCR products were either purified using the SureClean solution or the NucleoSpin® Gel and PCR Clean-up kit, according to the manufacturer's instructions.

2.5.3 Genotyping cells and mice using PCR

For genotyping, genomic DNA was isolated from tail tips of adult mice, from a limb of embryonic mice, or from approximately 5 x 10^5 cells according to the following protocol: The tissue was incubated in 500 µL tail lysis buffer and incubated overnight (tissue from adult mice) or for 4 h (tissue of embryonic mice or cells) at 56°C. Following, the dissociated tissue was pelleted for 5 min with 20,000 x g at RT. The DNA-containing supernatant was transferred into a new 1.5 mL reaction tube and mixed with 500 µL Isopropanol by gentle inversion. Subsequently, the DNA was pelleted for 30 min with 20,000 x g at 4°C. Afterwards, the supernatant was aspirated and the DNA pellet washed with 70% (v/v) Ethanol and centrifugation for 10 min with 20,000 x g at 4°C. Following aspiration of the supernatant, the pellet was dried at 37°C and resuspended in 50-100 µL TE buffer.

For genotyping polymerase chain reaction (PCR) was performed according Table 10. The annealing temperature and elongation time was set according to the used primer pairs Table 7.

Table 9: DreamTaq™ master mix and PCR mix

DreamTaq™ master mix (Thermo Scientific)	**PCR mix**
300 µL DreamTaq™ 10x buffer	1 µL DNA
32 µL DreamTaq™ Polymerase (5 U/µL)	1 µL of each primer (10 mM)
50 µL 100 µM dNTPs	8.3 µL DreamTaq™ master mix
868 µL H2O	add to 20 µL H_2O

Table 10: Genotyping PCR

Steps	Temperature [°C]	Duration [s]	Cycles
Initial denaturation	95	180	1
Denaturation	95	10	
Annealing	x	30	45
Elongation	72	x	
Final elongation	72	600	1
Cool down	8	∞	-

2.5.4 RNA isolation for RT-qPCR

Lysis and RNA preparation of frozen samples was performed according to the manufacturer's instructions using the PureLink™ RNA Mini Kit with the following details: For one well of a 4-well plate, 300 µL lysis buffer were used and the purified total RNA was eluted in 50 µL RNAse-free water. Following the isolation, the RNA concentration was determined using the FluoSTAR and 250 ng total RNA was run on an 2% agarose gel as an additional quality control. RNA was stored at -80°C for long-term storage.

2.5.5 Generation of cDNA using RT

Complementary DNA (cDNA) was generated from total RNA according to the manufacturer's instructions using the iScript ™ cDNA synthesis Kit. For one cDNA synthesis reaction, 250 ng RNA was used. cDNA was stored at -20°C for long-term storage.

2.5.6 Reverse-transcription quantitative PCR (RT-qPCR)

I analyzed expression of genes using gene-specific primer pairs Table 8 and RT-qPCR. The RT-qPCR was either performed in a 96-well RT-qPCR plate using the iQ5 instrument (BIO-RAD) or in a 384-well RT-qPCR plate using the Quant Studio 6 Pro instrument (ThermoFisher Scyentific) according to the manufacturer's instructions and the settings depicted in Table 11. For the 96-well reactions, I used the iQ SYBR® Green Supermix and for the 384-well reactions, I used the PowerTrack™ SYBR Green Master Mix. For the determination of primer efficiencies, I performed the RT-qPCR in triplicates, whereas for the analysis of gene expression, I performed the RT-qPCR in duplicates.

Gene expression analysis was performed according to Pfaffl using two reference genes (VanGuilder et al., 2008).

Table 11: RT-qPCR instrument settings

Step	**iQ5**			**Quant Studio 6 Pro**		
	Temperature (°C)	Duration (s)	Cycles	Temperature (°C)	Duration (s)	Cycles
Enzyme activation	95	180	1	95	120	1
Denature	95	10		95	5	
Annealing	60	30	45	60	30	40
Extension	72	30				

2.6 Mammalian tissue culture

2.6.1 Poly-L-lysine coating of glass coverslips

For Immunocytochemistry, cells were seeded on poly-L-lysine (PLL) coated glass coverslips. 10 mm glass coverslips were placed in 4-well dishes and coated with 500 µL 0.1 mg/mL PLL in PBS for 30 min at RT. Subsequently after coating, glass coverslips were washed once with 500 µL PBS. After PBS aspiration, coated glass coverslips were either used or stored at 4°C in the dark until usage.

2.6.2 Isolation of mouse embryonic fibroblasts

Mouse embryonic fibroblasts (mEFBs) were isolated at day 13.5 of pregnancy after a timed-mating. The pregnant mouse was anesthetized using isoflurane and killed using a cervical dislocation. The uterus was removed and placed into a 10 cm plastic dish on ice filled with PBS. Embryos were removed from the uterus in their intact yolk sac and each embryo placed into a new well of a 6-well dish on ice filled with PBS. Following, the embryos were removed from their yolk sac and part of the tail or limb placed into a 1.5 mL reaction tube for later DNA isolation and genotyping. After removing the head, liver, and heart, the remaining parts of the embryo were placed in 2 mL ice-cold 0.25% Trypsin in PBS. The following steps were performed under a safety work bench. The embryo parts were further cut into small pieces and transferred in the Trypsin solution into a 15 mL Falcon tube for overnight incubation at 4°C. After incubation, the embryonic tissue formed a pellet at the bottom of the Falcon tube and

around 1 mL of the Trypsin solution was aspirated before incubating the embryonic tissue in the remaining Trypsin for 30 min at 37°C in a water bath. After incubation, 8 mL of growth medium was added. The embryonic tissue-Trypsin-growth medium solution was mixed and transferred into a 50 mL Falcon after filtration through a 100 µm cell strainer. Another 8 mL of growth medium was added to the 15 mL Falcon and transferred to the 50 mL Falcon after filtration through the previously used cell strainer to increase the number of isolated cells. The content of the 50 mL Falcon was transferred on one to two 10 cm dish(es), depending on the isolated cell number, and incubated for 24 h at 37°C and 5% CO_2. After 24 h, cells were washed with 5˘mL PBS per dish and 10 mL growth medium was added for further incubation at 37°C and 5% CO_2.

2.6.3 Isolation of mouse adult fibroblasts

Mouse adult fibroblasts (mAFBs) were isolated from the tail of adult mice. The mouse was anesthetized using isoflurane and killed using a cervical dislocation. Subsequently, the tail was sterilized by cleaning with 70% (v/v) ethanol and cut into 3 pieces of equal size. From now on, the isolation was carried out under sterile conditions working under a safety work bench. Each piece was placed into one well of a 6-well plate with 3 mL growth medium to which 20 µL of a freshly prepared 5% (w/v) collagenase dissolved in growth medium was added. Subsequently, each tail piece was cut into smaller pieces and allowed to incubate for 3 h at 37°C and 5% CO_2. After the incubation, the tissue was mixed and the supernatant of all three pieces was pooled into a 15 mL Falcon tube. Isolated cells in the supernatant were pelleted using centrifugation at 600 x g for 5 min at RT. The supernatant was then aspirated and the pellet washed in 3 mL DPBS and pelleted again using centrifugation at 600 x g for 5 min at RT. The washed pellet was resuspended in 6 mL growth medium and distributed to 3-wells of a new 6-well plate. Cells were then incubated for 24 h at 37°C and 5% CO_2. Following, cells were washed thrice with DPBS followed by addition of 4 mL fresh growth medium to each well and subjected to maintenance.

2.6.4 Immortalization of mouse embryonic and adult fibroblasts

Primary mEFB and mAFB were immortalized using transfection with the SV-40 large T Antigen. In detail, 2 x 10^5 primary cells at passages 2-3 were seeded in a well of a

6-well dish and 24 h after seeding using Lipofectamine2000 as described in “Transient gene expression using Lipofectamine2000 transfection”. After transfection, cells were passaged every 3 days or when they reached confluency by splitting them in a 1:10 ratio. Cells were considered as immortalized at 10 passages after transfection and discarded when they would not reach confluency after 14 days after passaging.

2.6.5 Isolation and DNA from cell lines

Isolation of DNA from cell lines was performed as described above in “Genotyping cells and mice using PCR”.

2.6.6 Maintenance of cell lines

Cells were grown in their respective growth medium (Table 12) in 10 cm plastic dishes at 37°C with 5% CO_2 in the dark and passaged every 3-4 days at around 70% confluency using the following protocol: Cells were washed once with 5 mL PBS and incubated with 1 mL Trypsin-EDTA for 5-10 minutes on a hot plate at 37°C until their detachment. The reaction was stopped by the addition of 9 mL growth medium and resuspension of the cells. Cells were counted using a Neubauer counting chamber and seeded with the according numbers for maintenance or the desired experiment. Cells older than passage 15 were discarded. The passage count was set to 1 either at the time point of transfection when generating a stable cell line, or after thawing a back-up for re-culturing.

Table 12: Mammalian cell-line specific information

Cell line	Producer	Reference	Growth medium
HEK293	ATCC	CRL-1573	MEM + GlutaMAX (1x) + 10% FCS + 1% NEAA
HEK293-mlCNBD-FRET	Lab of Prof. Dagmar Wachten, D. Wachten / M. Klahre	-	MEM + GlutaMAX (1x) + 10% FCS + 1% NEAA + 0.8 µg/mL G418
HEK293T	ATCC	CRL-3216	GlutaMAX (1x) + 10% FCS
HeLa	CLS	300194	MEM + GlutaMAX (1x) +10% FCS +1% NEAA
mAFB	Generated during this study	-	DMEM + GlutaMAX (1x) + 10% FCS + 1% P-S

			+ 1% L-Glutamine + 1% Sodium pyruvate
mEFB	Generated during this study	-	MEM (1x) + 10% FCS + 1% Sodium pyruvate +1% P-S
mIMCD-3	ATCC	CRL-2123	DMEM/F12 (1:1) (1x) + GlutaMAX + 10% FCS
mIMCD-3 *ALFA-Smo* D2	Generated during this study	-	DMEM/F12 (1:1) (1x) + GlutaMAX + 10% FCS
mIMCD-3 *ALFA-Ptch1* B2	Generated during this study	-	DMEM/F12 (1:1) (1x) + GlutaMAX + 10% FCS
mIMCD-3 MCA3	Generated during this study	-	DMEM/F12 (1:1) (1x) + GlutaMAX + 10% FCS
mIMCD-3 *Inpp5e*-KO #A11	Generated during this study	-	DMEM/F12 (1:1) (1x) + GlutaMAX + 10% FCS
mIMCD-3 *Inpp5e*-KO #C6	Generated during this study	-	DMEM/F12 (1:1) (1x) + GlutaMAX + 10% FCS
mIMCD-3 *Inpp5e*-KO #E10	Generated during this study	-	DMEM/F12 (1:1) (1x) + GlutaMAX + 10% FCS
SHH-Light2	P.A. Beachy	(Taipale et al., 2000)	DMEM (1x) + GlutaMAX +10% FCS 1% L-Glutamine + 0.4 mg/mL G418 + 0.15 mg/mL Zeocin

2.6.7 Preparing back-ups and re-culturing of cultured cells

For long-term storage and resetting of the passage number, cells were crypreserved using the following protocol:

Cells were treated as described for maintenance, but instead of seeding, $5*10^5$ to $1*10^6$ cells were pelleted by centrifugation at 250 x g for 5 minutes at RT. The supernatant was aspirated and the cell pellet was resuspended in 1 mL growth medium containing 10% DMSO and transferred into a cryotube. The cryotube was placed at -80°C inside a freezing container, thereby ensuring a constant temperature decrease of 1°C per minute. After reaching -80°C, cells were transferred into a -150°C freezer.

For re-culturing cryopreserved cells, the following protocol was used:

Cryopreserved cells were thawed at 37°C in a water bath. As soon as the melting point was reached, cells were mixed with 20 mL of growth medium, which was pre-warmed to 37°C. Following, the cells were pelleted using a centrifuge at 250 x g for 5 min at

RT. Subsequently, the supernatant was aspirated and the cell pellet was resuspended in 20 mL growth medium and distributed equally on two 10 cm plastic dishes. Finally, cells were placed at 37°C with 5% CO_2. If the cell line was grown using selection with antibiotics, the respective antibiotics were applied after 2 h. After overnight growing, cells were washed once using 5 mL PBS and 10 mL growth medium was added to extract cells that died in the process of cryopreservation and re-culturing.

2.6.8 Transient gene expression using PEI transfection

For transient gene expression using PEI transfection, cells were seeded one day prior transfection to reach a confluency of 80% on the day of transfection. HEK293 and HEK293T cells were transfected using PEI. For transfection of different scales, DNA, PEI, Opti-MEM, and growth medium containing only 2% instead of 10% FCS, were mixed according to information in Table 13. In detail, DNA, Opti-MEM, and PEI were mixed accordingly and incubated for 10 min at RT. In the meantime, the growth medium was replaced with the respective amount of growth medium containing 2% FCS. After incubation, the PEI transfection mix was added dropwise to the well. The amount of DNA is related to the total amount of transfected DNA, i.e., if more than once plasmid was used for a single transfection, the amount of each DNA was distributed. Cells were incubated at 37°C with 5% CO_2 for 24-48 h before analysis.

Table 13: PEI transfection

Scale	DNA [µg]	Opti-MEM [µL]	PEI stock (1 µg/µL) [µL]	Medium with 2% FCS [mL]
10 cm dish	9.5	950	19	3.8
6-well plate	2.35	235	5	0.94
12-well plate	1.1	110	2	0.44
4-well plate	0.5	50	1	0.20
96-well plate	0.1	10	0.2	0.04
8-well IBIDI	0.25	25	0.5	0.10

2.6.9 Transient gene expression using Lipofectamine2000 transfection

For the transient gene expression using Lipofectaime2000 transfection, cells were seeded one day prior to transfection to reach a confluency of 90-95% on the day of transfection. mIMCD-3, mEFB, and mAFB cells were transfected using Lipofectamine2000. For transfection of different scales, DNA, Lipofectaime2000, and Opti-MEM were mixed according to information in Table 14. In detail, DNA, Opti-MEM for transfection mixtures were mixed in one reaction tube, while Lipofectamine2000 and Opti-MEM for transfection mixtures were mixed in another reaction tube. Both mixtures were incubated for 5 min at RT and subsequently mixed in into one reaction tube, followed by incubation for 20 min at RT. In the meantime, the cells were washed once with DPBS and the respective amount of Opti-MEM was added to each well. After incubation, the Lipofectamine2000 transfection mix was added dropwise to the well. The amount of DNA is related to the total amount of transfected DNA, i.e., if more than once plasmid was used for a single transfection, the amount of each DNA was distributed. Cells were placed into an incubator at 37°C with 5% CO_2. 4 - 6 h after transfection, cells were washed twice with DPBS, fresh growth medium was added and cells were incubated at 37°C with 5% CO_2 overnight. The next day, cells were either analyzed or the growth medium was replaced with growth medium containing only 0.5% FCS instead of 10% FCS (starvation medium) to induce cilia formation. Cilia formation was induced for 24-48 h before analysis.

Table 14: Lipofectamine2000 transfection

Scale	DNA [µg]	Opti-MEM for transfection mixtures [µL]	Lipofectamine2000 [µL]	Opti-MEM for well [mL]
10 cm dish	9	600	24	4.8
6-well plate	4	250	10	1.5
12-well plate	1.5	100	4	0.8
4-well plate	0.8	50	2	0.4
96-well plate	0.2	25	0.5	0.1
8-well IBIDI	0.4	50	1	0.2

2.6.10 Transient gene expression using BacMAM transduction

For the transient expression of 5-HT_6-cADDis-mCherry and mNphp3(201)-cADDis-mCherry (provided by Montana Molecular) using BacMAM transduction, cells were seeded one day prior to transfection to reach a confluency of 90-95% on the day of transduction. mIMCD-3 cells were transduced using BacMAM for expressing the cADDis sensor and its variants. For transduction of different scales, DNA, Baculovirus, and Opti-MEM were mixed according to Table 15. In detail, cells were washed once with DPBS and the transfection mixture was added dropwise into each well. Subsequently, cells were incubated for 30 min at RT, followed by incubation for 6 - 8 h at 37°C with 5% CO_2. After this incubation, the transfection medium was replaced with starvation medium containing 0.4 µL sodium butyrate per 100 µL medium and cells were incubated overnight at 37°C with 5% CO_2, before analysis.

Table 15: BacMAM transduction

Scale	Baculovirus (normal stock / concentrated stock) [µL]	Opti-MEM (for normal stock / for concentrated stock) [µL]	Sodium Butyrate [µL]
96-well plate	12.5 / 2.5	87.1 / 97.1	0.4
8-well IBIDI	25 / 5	174.2 / 194.2	0.8

2.6.11 Production of ShhN

To produce ShhN, I transfected HEK293 cells with pcDNA3.1-Shh-N, which encodes for *ShhN,* using PEI transfection as described above with the following difference:

instead of replacing the cells medium with medium containing only 2% FCS, I replaced the cells medium with 4 mL Opti-MEM and allowed the cells to express *ShhN* for 24 h. *ShhN* encodes for biological active SHH, but without being posttranslational modiefied with cholesterol, hereafter termed ShhN. ShhN is secreted into the supernatant as a result of lacking the cholesterol moiety. To harvest ShhN, the supernatant of transfected cells was transferred into 1.5 mL reaction tubes and cleared of cell debris by centrifugation with 20,000 x g for 10 min at 4°C. The ShhN supernatant was used for stimulation within 24 to 48 h post harvesting.

2.6.12 Hh activity assay

To determine Hh activity of different compounds in different concentrations, I performed a Hh activity assay using Shh-Light2 cells, which express a GLI-dependent *Firefly* luciferase and a constitutive-active *Renilla* luciferase (Taipale et al., 2000) according to the following procedure:

For every assay, a fresh back-up of Shh-Light2 cells were thawed and passaged once before the assay. Passaging was performed the day after thawing. For the assay, 7 x 10^4 cells per well were seeded on a 96-well plate in growth medium. The next day, the growth medium was replaced with starvation medium containing only 0.5% instead of 10% FCS and the respective stimulus. 24 h after stimulus addition, I performed a luciferase assay using the Dual-Glo® 3 Luciferase Assay kit. In detail, I washed each well using 90 µL DPBS and lysed the cells with 90 µL DPBS + 90 µL Dual-Glo reagent by gentle up- and down-pipetting. After lysis for 10 min at RT, I transferred 75 µL per well in duplicates in a 96-well half area white microplate and subsequently measured *Firefly* luminescence (FL) at the FluoStar (Omega, BMG LABTECH GmbH, Germany). After measuring, I added 37.5 µL Stop&Glo solution into each well and let the lysate incubate for another 10 min at RT. Subsequently, I measured *Renilla* luminescence (RL) at the FluoStar. For analysis, the data is normalized by calculating FL/RL. To determine the Hh activity of compounds, the data was expressed as relative fold changes compared to the respective control condition (ΔΔ Fold change).

2.6.13 Cytodex3 microcarrier cell culture and cilia isolation

For isolation of primary cilia, 1 x 10^7 mIMCD-3 cells were seeded in 100 mg Cytodex3 microcarrier in a Corning 500 mL Erlenmeyer flask with ventilated cap in 50 mL growth

medium. Cells were allowed to grow to confluency in the Incu-Shaker CO2 Mini shaking incubator at 37°C, 5% CO_2, and 60 RPM. After 2-3 days, most microcarrier were confluently grown with cells and the medium was replaced with starvation medium containing 0.5% FCS to induce ciliogenesis. 48 h after inducing ciliogenesis, the ciliated cells on the microcarrier were subjected to cilia isolation.

2.6.14 Generation of cell lines with stable gene expression using Lentiviral transduction

For the generation of the mIMCD-3 *ALFA-Smo* D2 and mIMCD-3 *ALFA-Ptch1* B2 cell lines, I generated Lentivirus using HEK293T cells and transduced mIMCD-3 MCA3 cells according to the following procedure:

I transfected HEK293T cells in a 6-well plate using GeneJuice transfection by mixing 5.5 µL GeneJuice with 1.5 µg pInducer20_minus_CMV_ALFAtag-(51-52)-mSmo, 0.65 µg CAG-Enhancer-Gag-Pol-RRE-rb globulin, and 0.35 µg CAG-Enhancer-VSVG-G-human beta globulin or 1.5 µg pInducer20_minus_CMV_ALFAtag-(235-236)-mPtch1, 0.65 µg CAG-Enhancer-Gag-Pol-RRE-rb globulin, and 0.35 µg CAG-Enhancer-VSVG-G-human beta globulin and filled up the transfection mix to 300 µL with serum-free medium. The transfection mix was allowed to incubate for 20 min at RT. In the meantime, the growth medium on the cells was replaced with 1 mL growth medium containing only 2% instead of 10% FCS. After the incubation, the transfection mix was added dropwise in the cells. The next day, the transfection medium was replaced with growth medium containing 30% instead of 10% FCS. Approximately 30 h after transfection, the supernatant containing Lentivirus was harvested and concentrated using the Lenti-X Concentrator according to the manufacturer's instructions. Concentrated Lentivirus from one 6-well plate well was added dropwise to the target cells being around 80% confluency in one 6-well plate well. Target cells were passaged three times and selected as described below in "Establishing the ALFA-tag for cilia-specific pull-down".

2.7 Protein Biochemistry

2.7.1 Protein preparation using whole cell lysates

Protein preparation was performed at 4°C or on ice. The cells were washed once with PBS and transferred into an 1.5 mL reaction tube in PBS-EDTA. Cells were pelleted

by centrifugation at 500 x g for 5 minutes at 4°C. Depending on the pellet size, cells were resuspended in 100 to 200 µL total lysis buffer and incubated for 30 min on ice. After incubation, cell debris was pelleted by centrifugation at 10,000 x g for 10 minutes at 4°C and the supernatant was used as whole cell lysate for subsequent steps. For long term storage, whole cell lysates were frozen using liquid nitrogen and stored at -80°C.

2.7.2 The bicinchoninic acid (BCA) assay for quantification of protein concentrations

To quantify protein concentrations, the Pierce™ NHS-Activated BCA Assay kit was used according to the manufacturer's instructions. For every experiment, the assay was calibrated using the protein standard, which was part of the kit. Absorption was measured in a plate reader (FluoStar)

2.7.3 Sodium dodecyl sulphate-polyacrylamide gel electrophoresis (SDS-PAGE)

Discontinuous gels were casted with a separation gel containing 10% acrylamide by mixing 1.5 mL Tris-HCl adjusted to pH 8.8, 60 µL 10% (w/v) SDS, 40 µL (w/v) APS, 6 µL TEMED, 2 mL 30% (v/v) acrylamide/bis-acrylamide (37.5:1) solution, and 2.42 mL H_2O, and a stacking gel containing 5% acrylamide by mixing 0.5 mL Tris-HCl adjusted to pH 6.8, 20 µL 10% (w/v) SDS, 40 µL (w/v) APS, 6 µL TEMED, 340 µL 30% (v/v) acrylamide/bis-acrylamide (37.5:1) solution, and 1.12 mL H_2O per gel.
Protein samples were adjusted to 45 µL using total lysis buffer and mixed with 15 µL 4-fold SDS sample buffer. Following, protein samples were boiled for 5 min at 95°C or incubated for 1 h at RT if the protein of interest was SMO. Gels were run in SDS running buffer using the Mini-PROTEAN Tetra Cell system at 15-25 mA until the 11 kDa band of the Protein Marker VI reached the bottom of the gel. Proteins that were separated using SDS-PAGE were subjected to Western Blot analysis.

2.7.4 Western Blot analysis

Proteins were blotted from the SDS-PAGE gel onto the PVDF membrane using discontinuous semi-dry Western blotting in the Semi-dry-blotter as follows: two filter papers were soaked in Western Blot Anodebuffer1 and placed on the anode, followed

by placing one filter paper soaked in Anodebuffer2 above, followed by placing the methanol-actiaved PVDF membrane above, followed by placing the H_2O-rinsed SDS-PAGE gel above, followed by placing three filter papers soaked in Cathodebuffer above, followed by placing the cathode above. The PVDF membrane and filter papers were cut into 8 x 9 cm larger pieces to fit on the SDS-PAGE gels. Proteins were blotted for 50 min at 2.4 mA per cm^2. After blotting, the PVDF membrane was briefly placed in methanol and washed with PBS.

Western blot analysis was performed using immunostaining with the antibodies depicted in Table 4 and Table 5. For immunostaining, the PVDF membrane was incubated for 30 min at RT in BB, followed by incubation with the primary antibody for 1 h at RT or overnight at 4°C. Following the incubation, the membrane was washed three times for 20 min in PBS-T at RT. Subsequently, the membrane was incubated with the secondary antibody for 1 h at RT or overnight at 4°C. Following the incubation, the membrane was washed three times for 20 min in PBS-T at RT and stored until imaging in PBS. After the final washing step, the membrane was imaged at the Odyssey Imaging System (LI-COR Biosciences) for the fluorescently-labelled secondary antibodies. For HRP-conjugated secondary antibodies, the membrane was incubated with the SuperSignal® West Pico Chemiluminescent Substrate according to the manufacturer's instructions and imaged at the SAPPHIRE Biomolecular Imager (azure biosystems, Dublin, USA).

2.7.5 Dot Blot analysis

To verify presence of SHH in the supernatant of *pcDNA3.1-Shh-N* transfected cells, I performed Dot Blot analysis. In detail, I placed 10 µL of the supernatant on a methanol-activated PVDF membrane and let the membrane incubate for 10 min at RT. After the incubation, I re-activated the membrane in methanol and proceeded with immunostaining as described above in "Western Blot analysis" using the anti SHH antibody and a fluorescently labelled secondary antibody.

2.7.6 Immunocytochemistry (ICC)

For ICC, cells were washed once with PBS and fixed for 10 min at RT using 4% PFA in PBS. Subsequently, cells were washed thrice with PBS and incubated for 30 min at RT with CT. Following, the cells were labeled for 1 h at RT or overnight at 4°C using

primary antibodies that were diluted accordingly (Table 4) in CT. After labeling, cells were washed thrice with PBS and labeled for 1 h at RT or overnight at 4°C in the dark using secondary antibodies that were diluted accordingly (Table 5) in CT with 1:10,000 DAPI. After labeling with the secondary antibodies, cells were washed once and mounted on an objective slide using one drop of Aqua-Poly/Mount and stored at 4°C in the dark.

2.7.7 Magnetic-bead coupling to VHH anti-ALFA

Buffers for coupling Pierce™ NHS-Activated Magnetic Beads to the VHH anti-ALFA nanobody and materials were kindly provided by Prof. Dr. Florian I. Schmidt. The following buffers and materials were used:
1 mM HCl (ice-cold), Coupling buffer: 50 mM borate pH 8.5, Wash Buffer: 0.1 M glycine, pH 2.0, Quenching buffer: 3 M ethanolamine, pH 9.0, Storage buffer: 50 mM borate pH 8.5 with 0.05% NaN_3, and GE Healthcare PD MiniTrap G-25 (with spinning adaptor).

The storage solution of 0.5 mg VHH anti-ALFA was replaced with 500 µL coupling buffer using the GE Healthcare PD MiniTrap G-25 columns according to the manufacturer's instructions. Following, 300 µL beads were placed in a 1.5 mL reaction tube on a magnet and the supernatant was replaced with 1 mL ice-cold 1 mM HCl and vortexed for 15 min (All vortexing steps at half maximum speed). Subsequently, the reaction tube was placed on the magnet and the HCl was replaced with 300 µL VHH anti-ALFA in coupling buffer. Then, the solution was vortexed for 30 s and incubated on a rotator for 2 h at RT. Every 5 min, the solution was vortexed for 15 s for the first 30 min of incubation and vortexed for 15 s every 15 min for the subsequent incubation time. After the incubation at RT, the solution was incubated overnight on rotator at 4°C. Following the overnight incubation, the reaction tube was placed on a magnet and the supernatant was aspirated. Following, VHH anti-ALFA coupled magnetic beads were washed thrice with 1 mL wash buffer and short vortexing in between each washing step. After the last washing step, the coupled-beads were incubated for 2 h at RT with quenching solution. After quenching, coupled-beads were washed once with 1 mL H_2O and resuspended in 100 µL storage buffer. Coupled-magnetic beads were stored at 4°C.

2.7.8 ALFA-tag specific pull-down using VHH anti-ALFA coupled magnetic beads

The following buffers were used for the ALFA-tag specific pull-down:
SDS Elution buffer: 50 mM Tris-HCl pH 8.0, 1 mM EDTA pH 8.0, 1% SDS
4x SDS-sample buffer, and Binding buffer: 20 mM NaP buffer (produced by mixing 15.1 mM Na_2HPO_4 with 4.9 mM NaH_2PO_4), 500 mM NaCl pH 7.4 + 2% (v/v) FCS.

For, cells were lysed using whole cell lysates as described in “Protein preparation using whole cell lysates“. For 1 x 10^7 cells, 20 µL VHH anti-ALFA coupled magnetic beads were used. The beads were once washed in binding buffer and incubated for 10 min at RT on a rotator with 1 mL binding buffer to allow equilibration. To bind protein to the beads, the equilibrated beads were put on a magnet and the binding buffer was aspirated. Following, the beads were resuspendend in binding buffer and incubated for 1 h at 4°C on a rotator. Five times, the beads were washed with binding buffer. After the last washing step, the beads were incubated with 200 µL SDS elution buffer for 1 h at RT and subjected to Western Blot analysis.

2.8 Confocal microscopy

At least 12 after mounting, fluorescence images were acquired using confocal z-stacks (step size 0.4-0.5 µm, 60x objective) on one of the following confocal laser scanning microscopes: Olympus FV1000, Nikon eclipse Ti, Leica SP5, or Leica SP8 with Lightning. All ICC images that are shown in this thesis are depicted as maximum projections of the acquired z-stacks.

2.9 Live cell imaging

2.9.1 FRET imaging at the CellR System

FRET imaging at the CellR System (Olympus), was performed in 96-well plates. HEK293 or HEK-mICNBD-FRET cells were seeded and transfected with pcA-Cerulean, pcA-Citrine, pcDNA3-AKAR4-NES, or pc3-mNPHP3-AKAR4HA-NES-1 (HEK293), pc3.1-VHHenhancer-mCherry, mNPHP3(201)-VHH-enhancer-mCherry-7, pcDNA3.1zeo_mCherry (HEK-mICNBD-FRET) using PEI. Fluorescence imaging of

live cells was performed using the CellR Imaging System consisting of an inverse, fully motorized wide-field microscope (IX81) with a monochromatic CCD camera (XM10), a reflector turret, and an illumination system with an excitation-filter wheel (MT20, 150 W Xenon arc burner). Measurements were performed with a 20x/0.75 objective (UPlanSApo, Olympus) at room temperature under atmospheric conditions. Before the measurement, cells were washed once with ES and measurements were performed in ES. The experimental recordings were as follows: Before and after each time-resolved measurements, the mCherry fluorescence (12% light intensity, 200 ms exposure time, 575/25 excitation filter, mCherry-B-0MF Semrock dichroic mirror, 630/20 emission filter) was measured. Time-resolved measurements captured the cerulean (12% light intensity, 100 ms exposure time, 430/25 excitation filter, M2CFPYFP Olympus dichroic mirror, 480/40 emission filter), the citrine fluorescence (12% light intensity, 100 ms exposure time, 500/20 excitation filter, M2CFPYFP dichroic mirror, 535–30 emission filter), and the FRET signal (12% light intensity, 100 ms exposure time, 430/25 excitation filter, M2CFPYFP dichroic mirror, 535–30 emission filter) every 5 s. After 120 s, cells were stimulated with 20 mM isoprenaline hydrochloride (isoproterenol, Sigma Aldrich) or ES as a control. Data was analyzed using Fiji/ImageJ by selecting mCherry positive cells with freehand ROIs and determining the mean fluorescence intensity for each ROI in each channel. Values were background subtracted and the FRET signal was corrected for bleed-through and cross-excitation with the following formula: corrected FRET = FRET – α * Cerulean – β * Citrine (with α being the determined bleed-through constant and β being the determined cross-excitation constant for the chosen experimental set-up; α and β values were calculated from single Cerulean or Citrine transfected cells of three independent experiments using the innate ImageJ tool ‘Coloc 2’, and are 0.75 and 0.02, respectively). Data were plotted as a change of cerulean/FRET corrected over time.

2.9.2 R-FlincA imaging at the CellR System

HEK293 cells were seeded and transfected with pcDNA4HMB_R-FlincA, pcDNA4HMB_R-FlincA_mut (Ohta et al., 2018) (generously provided by Kazuki Horikawa, Tokushima University, Japan), or pc3-mNPHP3-R-FlincA-12 and pEGFP-N1-bPAC using PEI. Imaging was performed using the CellR Imaging System. The experimental recordings were as follows: R-FlincA signal (57% light intensity, 200 ms

exposure time, 572/25 excitation filter, mCherry-B-0MF Semrock dichroic mirror, 630/20 emission filter) was measured every 5 s. At 120 s, cells were illuminated for 5 s with 2.1 mW/cm^2 white light, followed by further recording of R-FlincA signal every 5 s for 480 s. Subsequently, bPAC-GFP fluorescence (12% light intensity, 100 ms exposure time, 500/20 excitation filter, M2CFPYFP dichroic mirror, 535–30 emission filter) was measured. Data were analyzed using Fiji/ImageJ by selecting low-expressing bPAC-GFP cells with freehand ROIs and determining the mean fluorescence intensity for each ROI in the average signal recorded during the 120 s before white light exposure. Data were plotted as a change of fluorescence over time.

2.9.3 FRET imaging at the Andor Spinning Disk microscope

mIMCD-3 cells were seeded on PLL coated 8-well IBIDI plates or 96-blackwell plates and transfected after 24 h with pc3-mNPHP3-AKAR4HA-NES-1, pc3-mNPHP3-Cerulean-4, pc3-mNPHP3-Citrin-3, pc3-mNPHP3(201)-mICNBD-FRET-1, or mNPHP3(201)-VHH-enhancer-mCherry-7 + pc3.1mICNBD-FRET#9. The medium was replaced with starvation medium (0.5% FCS) on the following day to induce ciliogenesis. Confocal FRET imaging was performed at the DZNE Light Microscopy Facility using the Andor Spinning Disk Setup (built on an inverted Eclipse Ti Microscope, Nikon) at 37˚ C. For FRET imaging, the 445 nm laser (18% intensity, 445-, 514-, 640-triple dichroic mirror in the Yokogawa CSU-X1 unit and 5000 rpm disk speed) was used as excitation source, combined with a dual-cam CFP/YFP filter cube (509 nm dichroic mirror with 475/25 nm and 550/49 nm emission filters) to simultaneously measure Cerulean and Citrine (Venus) emission with the two EM-CCD cameras (100 ms exposure time, 300 EM gain, 5.36 frames per second frame rate, 10.0 MHz horizontal readout, 1.7 ms vertical readout time, 5x pre Amp gain, -70˚C camera temperature). The imaging procedure was as follows: Cells were washed once with ES buffer and measurements were performed in ES buffer. Cilia were imaged with a 100x/1.45 oil objective with 500 nm step size in 10 s intervals. After a stable baseline was obtained, cells were stimulated by drug addition. Cilia-specific fluorescence values were obtained by analyzing the recordings using CiliaQ as described earlier in “establishing FRET imaging for ciliary imaging”. The corrected FRET ratio normalized to the mean baseline value before stimulus addition, and plotted as a change over time.

2.9.4 cADDis imaging at the Andor Spinning Disk microscope

mIMCD-3 cells were seeded as described above. After 24 hr, cells were transduced with the 5-HT6-cADDis-mCherry or mNphp3(201)-cADDis-mCherry using BacMAM transduction as described above. 24 h after inducing ciliogenesis, cells measured at the DZNE Light Microscopy Facility using the Andor Spinning Disk Setup. For ratiometric cADDis imaging, cpGFP and mCherry were excited with the 448 nm (10%) and 561 nm (10%) lasers, respectively, in combination with a 405, 448-, 561-, 640-quad dichroic mirror in the Yokogawa CSU-X1 unit and 5000 rpm disk speed. Images were acquired on the two EM-CCD cameras simultaneously (100 ms exposure time, 300 EM gain, 5.36 frames per second frame rate, 10.0 MHz horizontal readout, 1.7 ms vertical readout time, 5x pre Amp gain, -70˚ C camera temperature) with a GFP/RFP emission filter cube (580 nm LP dichroic and 617/73 nm and 525/50 nm emission filters). The experimental procedure during imaging and data analysis was performed as described in the Materials and methods section “FRET imaging at the Andor Spinning Disk microscope”. Cilia-specific fluorescence values were obtained by analyzing the recordings using CiliaQ as described earlier in “establishing FRET imaging for ciliary imaging”. The ratio of mCherry/cpGFP was normalized to the mean baseline value before stimulus addition, and plotted as a change over time and plotted as a change over time.

2.9.5 Di-4-ANEPPDHQ and Pro12A live cell imaging and analysis

mIMCD-3 cells were seeded cilia formation was induced 24 h after seeding for 48 h by exchanging the growth medium with starvation medium containing only 0.5% FCS, instead of 10%. Respective wells were treated with 2 µM NB-DNJ for 48 h during starvation. At the day of imaging, respective wells were treated with 10 µM M-β-CD for 30 min at 37°C and 5% CO_2 in serum-free medium. For imaging, cells were washed once with ES and incubated with 5 µM di-4-ANEPPDHQ or 800 nM Pro12 in ES for 10 min at 37°C and 5% CO_2 in the dark. After incubation, cells were washed once with ES and imaged the following settings: Imaging was performed at the microscopy core facility of the University Hospital Bonn at the Leica SP8 with Lightning at 37°C. Before imaging, a quarter-wave plate was inserted into the manual internal fluorescence axis of the microscope and adjusted to 35° field rotation using the Abbe-Koenig field rotator

to achieve a 45° angle of incoming linearly-polarized light to hit the quarter-wave plate for the generation of circularly-polarized light. The probes were excited with 488 nm (di-4-ANEPPDHQ) or 405 nm (Pro12A) and emission was recorded with the HyD detectors in two channels setting the emission windows to 500-580 nm and 620-750 nm (di-4-ANEPPDHQ) or 410-455 nm and 470-535 nm (Pro12A). Cells were imaged using confocal microscopy with a 60x/1.40 NA oil objective with 0.5 µm step size. For analysis, cilia were selected manually using region of interests (ROIs) and images were analyzed using the GPcalc-master plugin for Fiji/ImageJ provided with the publication (Owen et al., 2011). From the generated generalize polarization (GP) histograms, the peak GP values were plotted and compared for the different conditions.

2.10 Cilia isolation

For cilia isolation, the culture was transferred into a 50 mL Falcon. Waiting for a few minutes between each step except centrifugation allowed the microcarrier gently to settle down. The microcarrier were washed twice with PBS and 90 µL microcarrier solution was mixed with 16% PFA and subjected to ICC as a control for the deciliation process. All following steps were performed on ice or at 4°C. After the final washing step, the PBS was replaced with 10 mL deciliation buffer and cells incubated for 15 min at 4°C on an orbital shaker at 240 RPM. Following, cells and microcarrier were pelleted in a centrifuge with 2,000 x g for 5 min at 4°C and 90 µL microcarrier solution was mixed with 16% PFA and subjected to ICC as a control for the deciliation process. The supernatant containing primary cilia was transferred into 12 mL ultracentrifuge tube and cilia were pelleted in an ultracentrifuge with 100,000 x g for 1 h at 4°C. Afterwards, cilia were resuspendend in100 µL ammonium acetate. The ammonium acetate-cilia solution was distributed equally in two 1.5 mL reaction tubes, which were rinsed with a 2:1 methanol-chloroform mixture and dried afterwards, and pelleted using a centrifuge with 20,000 x g for 120 min at 4°C. Following, the pellet from one tube was resuspendend in 45 µL whole cell lysis buffer and 15 µL 4x SDS sample buffer and subjected to Western Blot analysis. The pellet from the other tube was subjected to lipid extraction for mass spectrometry.

2.11 Lipidomic analysis using mass spectrometry

Lipidomic analysis using mass spectrometry was performed in cooperation with Prof. C. Thiele, Life & Medical Sciences Institute (LIMES), Biochemistry and Cell Biology of Lipids, University of Bonn, Germany

2.11.1 Lipid extraction from mIMCD-3 cells and isolated primary cilia

For lipid extraction, 1 x 10^6 cells or the isolated primary cilia from a 1 x 10^7 microcarrier cell culture were used. All 1.5 mL reaction tubes that were used during this procedure were washed with a 2:1 methanol-chloroform mixture and dried before usage.

Cells for lipid extraction were pelleted in a centrifuge at 300 x g for 5 min at 4°C, washed once with PBS and once with ammonium acetate. To each sample (cells and isolated cilia), 800 µL extraction mix (a 2:1 methanol-chloroform mixture) was added, which contained 10 µL (cells) or 5 µL (isolated cilia) IS (210 pmol PE(31:1), 396 pmol PC(31:1), 98 pmol PS(31:1), 84 pmol PI(34:0), 56 pmol PA(31:1), 51 pmol PG (28:0), 28 pmol CL(56:0), 39 pmol LPA (17:0), 35 pmol LPC(17:1), 38 pmol LPE (17:0), 32 pmol Cer(17:0), 99 pmol SM(17:0), 55 pmol GlcCer(12:0), 14 pmol GM3 (18:0-D3), 359 pmol TG(47:1), 111 pmol CE(17:1), 64 pmol DG(31:1), 103 pmol MG(17:1), 724 pmol Chol(d6), 45 pmol Car(15:0)). The sample was mixed by gently inverting the reaction tube, followed by pelleting the proteins using a centrifuge with 20,000 x g for 3 min at RT. The supernatant was transferred into a new 1.5 mL reaction tube and 300 µL acetic acid was added, followed by thorough shaking for 30 s. Subsequently, the tube was placed in a centrifuge at 20,000 x g for 5 min at RT for phase separation. After centrifugation, the upper aqueous phase was gently aspirated and the lower phase transferred into a new 1.5 mL reaction tube to be subsequently evaporated in a speed vac at 45°C for 10 min. The lipid pellet was resuspendend in 500 µL spray buffer (containing 8 parts isopropanol, 5 parts methanol, 1 part H_2O, and 10 mM ammomium acetate) and sonicated for 5 min. For long term storage, samples were stored at -80°C.

2.11.2 Mass spectrometry

For mass spectrometry, samples in spray buffer were infused at 10 µL/min into a Thermo Q Exactive Plus spectrometer equipped with the HESI II ion source for shotgun lipidomics. MS1 spectra (resolution 280 000) were recorded in 100 m/z windows from 290 to 400 m/z and 400 to 1,100 (pos.) and 700 - 1,500 m/z (neg.) followed by

recording MS/MS spectra (res. 70 000) by data independent acquisition in 1 m/z windows from 290 to 400 m/z and 400 to 1,100 (pos.) and 700 to 1,500 (neg.) m/z. Raw files were converted to .mzml files and imported into and analyzed by LipidXplorer software using custom mfql files to identify sample lipids and internal standards. For further data processing, absolute amounts were calculated using the internal standard intensities followed normalization of both samples to the respective level of phosphatidylcholine (PC), assuming that the relative PC levels in the whole cell ("Whole-Cell") and ciliary ("Cilia") lipid extractions are equal.

2.12 Software applications

Data and statistical analysis was performed using Microsoft® Excel for Mac (Version 16.56), GraphPad Prism 9 for MacOS (Version 9.3.0, GraphPad Software, LLC), MSConvert (Version 3.0.20310-42ec66a95), LipidXplorer (Version 1.2.8.1) (Herzog et al., 2011), SnapGene Viewer (Version 6.0, SnapGene® Viewer), and Design & Analysis Software (Version 2.4.3).

Image analysis was performed using Fiji/ImageJ (version v2.3.051; Java 1.8.0_202, U.S. National Institutes of Health, Bethesda, Maryland, USA), and CiliaQ (v0.1.5, Jan N. Hansen) (Hansen et al., 2021).

Data visualization and thesis compilation was performed using Microsoft® Word for Mac (Version 16.55), GraphPad Prism 9, EndNote X9 (Version X9.3.3), and Affinity Designer (Version 1.10.4)

2.13 Statistics

Statistics were performed using GraphPad Prism 9. Statistical significances and performed tests are depicted in the respective figures and legends.

3 Results

3.1 Ciliogenesis in mammalian tissue culture

The primary cilium is a transient organelle that is dynamically regulated during the cell cycle. In general, a solitary primary cilium emanates perpendicular from the apical cell surface in the G_0 phase, and is re-absorbed when entering the cell cycle (**Figure 8A**). Thus, primary cilia are only present on non-proliferating cells (Rieder et al., 1979; Tucker et al., 1979). However, the ciliation rate of non-proliferating cells *in vivo* and *in vitro* varies (Wheatley, 2018). To synchronize and maximize ciliation *in vitro*, cells in tissue culture are usually grown to confluency to induce contact inhibition and deprived of serum to further stop cells from proliferating (Eagle and Levine, 1967; Tucker et al., 1979). Although I grew cells *in vitro* as monocultures and optimized for ciliogenesis, cells do show heterogeneity in cilia length and ciliation rate (**Figure 8B**). I analyzed primary cilia characteristics *in vitro* using immunocytochemistry (ICC) and confocal microscopy in several epithelial cell lines commonly used to study primary cilia function *in vitro:* mouse cells derived from the terminal part of the inner medullary collection duct (mIMCD-3), human cervical cancer cells derived from Henrietta Lacks (HeLa), and mouse embryonic and adult fibroblasts (mEFB and mAFB, respectively). I labeled cells with DAPI to stain DNA (blue) and either an antibody against acetylated α-tubulin (AC-α-TUB) or the ADP-ribosylation factor-like protein 13 B (ARL13B), which both label primary cilia (Caspary et al., 2007; LeDizet and Piperno, 1991) (**Figure 8C**). mIMCD-3 cells were highly heterogeneous and many cells did not show primary cilia. Moreover, cells without cilia appeared to overlap, indicating a loss of contact inhibition and further proliferation. Consequently, I generated mIMCD-3 monoclonal cell lines that I selected for the highest ciliation rate and contact inhibition. The clone mIMCD-3 MCA3 showed the best result (**Figure 8C**) and was used for all subsequent analyses (referred to as mIMCD-3 cells). HeLa cells were also heterogeneous and the majority of cells did not show a primary cilium. mAFB and mEFB were more homogeneous and their nuclei did not overlap and almost every cell displayed a primary cilium. In all further studies, I used mAFBs, mEFBs, and the clone mIMCD-3 MCA3.

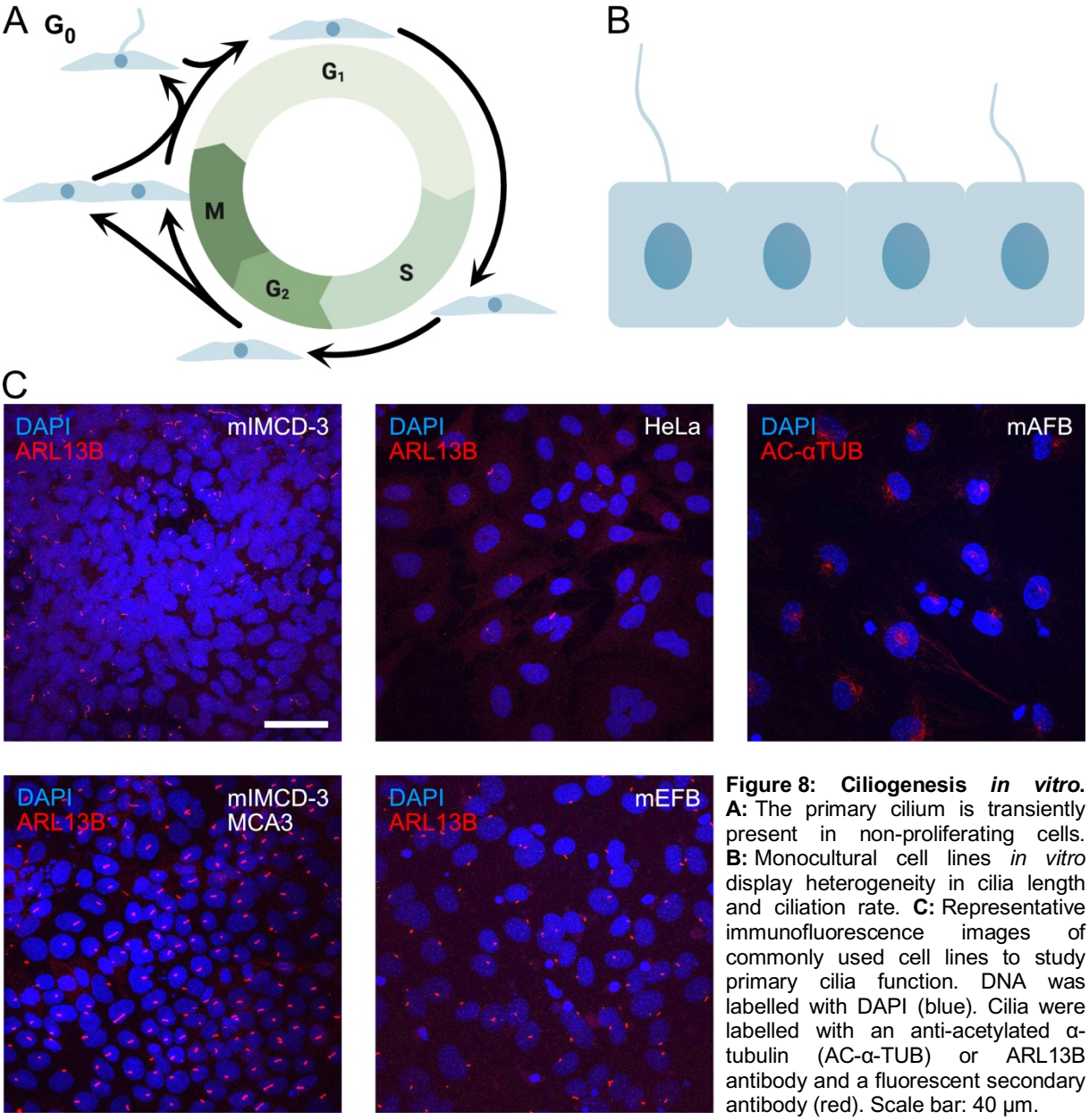

Figure 8: Ciliogenesis *in vitro*. **A:** The primary cilium is transiently present in non-proliferating cells. **B:** Monocultural cell lines *in vitro* display heterogeneity in cilia length and ciliation rate. **C:** Representative immunofluorescence images of commonly used cell lines to study primary cilia function. DNA was labelled with DAPI (blue). Cilia were labelled with an anti-acetylated α-tubulin (AC-α-TUB) or ARL13B antibody and a fluorescent secondary antibody (red). Scale bar: 40 µm.

3.2 Analysis of the ciliary membrane lipid-environment using the environment-sensitive, solvatochromic dyes Di-4-ANEPPDHQ and Pro12A

Unlike most other cellular organelles, the primary cilium membrane does not entirely enclose the organelle but is continuous with the plasma membrane. Nonetheless, the primary cilium maintains a unique lipid and protein identity, whose dynamic regulation is crucial for ciliary function (Garcia et al., 2018; Nachury and Mick, 2019; Rohatgi and Snell, 2010; Verhey and Yang, 2016). So far, the ciliary lipid identity and molecular

mechanisms that maintain its homeostasis remain largely unknown (Kaiser et al., 2020; Nechipurenko, 2020). The membrane order is a key feature of the plasma membrane lipid identity: The more efficient lipids are packed, the more polar water molecules are excluded from the nonpolar cell membrane and vice versa. This can be quantified by environment-sensitive dyes that insert into the lipid bilayers of cells (Owen et al., 2011). Solvatochromic dyes change their emission spectrum in response to polarity changes by intramolecular charge transfer and are, therefore, widely used to quantify membrane order (Klymchenko, 2017). Laurdan and di-4-ANEPPDHQ are well-characterized examples (Dinic et al., 2011; Owen et al., 2011): Di-4-ANEPPDHQ has two positive charges to reduce the likelihood to flip-flop from the outer into the inner leaflet of the plasma membrane and subsequently into intracellular membranes. Its emission peaks at 570 nm in the liquid-ordered (L_o) phase and shifts to 630 nm in the liquid-disordered (L_d) phase (**Figure 9 A**) (Jin et al., 2005). In contrast, Laurdan rapidly flips between membranes and is, therefore, not suited to study the plasma or ciliary membrane (PM and CM, respectively) (Mazeres et al., 2014). However, the recently developed Laurdan relative, Pro12A, contains a linker with a negative charge, which anchors into the lipid bilayer and drastically reduces flip-flop. Pro12A emission peaks at 438 nm in the L_o phase and shifts to 555 nm in the L_d phase (**Figure 9 D**) (Danylchuk et al., 2020). Compared to di-4-ANEPPDHQ, Pro12A has a lower photostability (Danylchuk et al., 2020; Jin et al., 2005; Obaid et al., 2004). Moreover, Laurdan, and thus likely its relative Pro12A, probe different plasma membrane properties than di-4-ANEPPDHQ: Pro12A is likely more sensitive to temperature changes, whereas di-4-ANEPPDHQ is more sensitive to changes in cholesterol content in well-defined lipid-phase systems (Amaro et al., 2017). Thus, using di-4-ANEPPDHQ or Pro12A to probe the PM or CM membrane order might lead to different results. Therefore, I used both dyes and compared the results.

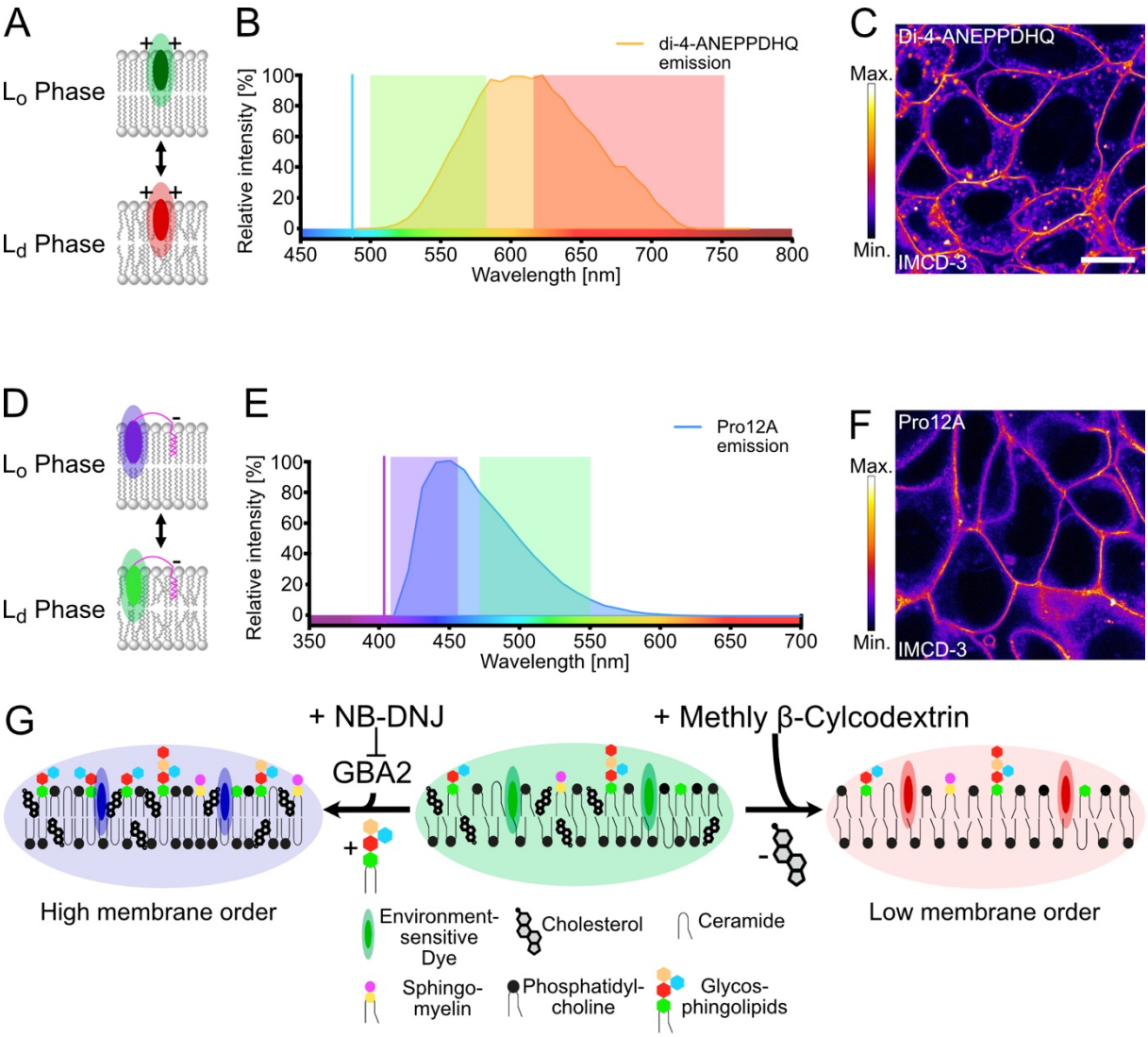

Figure 9: The environment-sensitive membrane dyes Di-4-ANEPPDHQ and Pro12A. A: The emission spectrum of Di-4-ANEPPDHQ shifts towards the green spectrum in a lipid ordered (L_o) and towards the red spectrum in a lipid disordered (L_d) phase membrane. Two positive charges drastically reduce flipping of the extracellular applied dye. **B:** Emission spectrum of mIMCD-3 cells loaded with 5 µM Di-4-ANEPPDHQ (Leica SP8 confocal laser scanning microscope, 488 nm excitation). Green and red columns depict the emission windows for ratiometric dye measurement (500-580 nm and 630-750 nm, respectively). The cyan line depicts laser excitation wavelength (488 nm). **C:** Confocal image of mIMCD-3 cells loaded with Di-4-ANEPPDHQ (488 nm excitation, 500-580 nm emission). Scale bar: 10 µm. **D:** The emission spectrum of Pro12A shifts towards the purple spectrum in a lipid ordered (L_o) and towards the green spectrum in a lipid disordered (L_d) phase membrane. A membrane-inserted linker with a negative charge more drastically reduces flipping of the extracellular applied dye. **E:** Emission spectrum of mIMCD-3 cells loaded with 800 nM Pro12A (Leica SP8 confocal laser scanning microscope, 405 nm excitation). violet and green columns depict the emission windows for ratiometric dye measurement (410-455 nm and 470-550 nm, respectively). The purple line depicts laser excitation wavelength (405 nm). **F:** Confocal image of mIMCD-3 cells loaded with Pro12A (405 nm excitation, 410-455 nm emission). **G:** Both dyes are shifted in their respective emission spectra to a more blue or more red spectrum in L_d or L_o phase membranes, respectively. Cellular membranes are known to be shifted towards the L_d or L_o phase after extraction of cholesterol or addition of glycosphingolipids, respectively.

Loading of cells with either dye did not allow to distinguish between PM and CM (data not shown). To differentiate between labeled PM and CM without using a ciliary marker, I considered the orientation of primary cilia in 3D. *In vitro*, primary cilia from mAFB and mEFB are shorter than from mIMCD-3 cells. They tend to lay almost flat on the PM,

making it impossible to identify cilia with the narrowest optical resolution being 956 nm in the z-axis using the 60x NA 1.40 oil objective of the Leica SP8 confocal microscope (see “Di-4-ANEPPDHQ and Pro12A live cell imaging and analysis”). Hence, I first used mIMCD-3 cells to establish the imaging approach and analyze the ciliary lipid environment using di-4-ANEPPDHQ and Pro12A. To characterize the dyes, I loaded mIMCD-3 with 5 µM di-4-ANEPPDHQ or 800 nM Pro12A and recorded the emission spectrum at 488 or 405 nm, respectively (**Figure 9 B & E**). Generalized polarization (GP) allows quantifying the relative proportion of the L_o/L_d phase and, thereby, the membrane order using ratiometric imaging (Parasassi et al., 1990). In detail, the dye is excited with the respective wavelength (488 nm for di-4-ANEPPDHQ and 405 nm for Pro12A), and emission is simultaneously recorded in two emission windows left and right of the emission peak. Thus, the lower wavelength emission window represents the L_o phase and the higher wavelength emission window the L_d phase. The two columns in each emission spectrum depict these selected emission windows (**Figure 9B & E**). Representative intensity images of mIMCD-3 cells loaded with the respective dyes and recorded with L_o emission windows showed predominant plasma membrane staining. The intracellular membranes were only labeled by di-4-ANEPPDHQ, but not by Pro12A (**Figure 9C & F**). An increase in the GSL content results in a more ordered membrane, whereas extraction of cholesterol using methyl-β-cyclodextrin (M-β-CD) results in a lower ordered membrane, which I can follow using either di-4-ANEPPDHQ or Pro12A (**Figure 9G)** (Hamzeh, 2017; Owen et al., 2011; Raju et al., 2015; Zidovetzki and Levitan, 2007). Here, I aimed to analyze GSL-dependent changes in the order of the ciliary membrane.

3.2.1 GP imaging and analysis

Owen and colleagues published a well-written protocol with a corresponding Fiji/ImageJ (Fiji Version 2.3.0) (Schindelin et al., 2012) macro to quantify the membrane lipid order in cells and organisms using confocal imaging (Owen et al., 2011). I adapted this protocol and used the Leica SP8 confocal laser scanning microscope, which contains a spectral detector that splits the emission light to allow continuous, tunable detection within the visible spectrum by up to 5 light sensors (Borlinghaus, 2017). Simplified, a prism splits the emission light into its spectrum. A

motorized spectrometer slits block undesired light from the detector and reflect the blocked light onto the next slit-detector pair (**Figure 10A**).

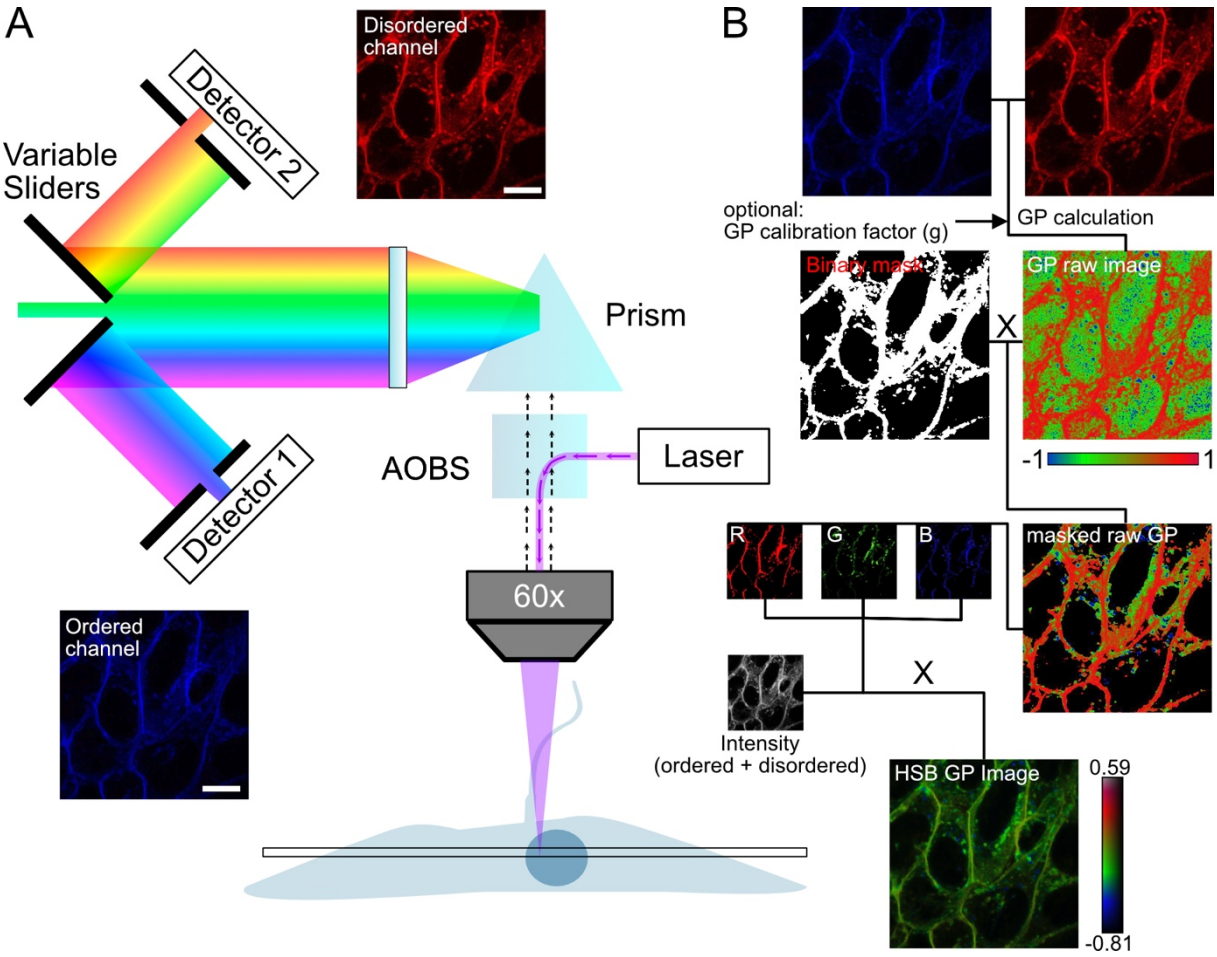

Figure 10: **Schematic overview of environment-sensitive dye measurements and analysis.** In the Leica SP8 confocal laser scanning microscope, the laser passes through an Acousto-Optical Beam Splitter (AOBS) to be directed into the objective and focused on the probe. Emission light passes back through the objective and the AOBS into a prism, which refracts the emission light. It is then directed via variable sliders and mirrors onto the desired detectors. This system allows to freely adjust the captured emission light windows. Captured images are then processed as depicted by the workflow scheme. Scale bar: 10 µm.

I used two detectors to record the emission light (**Figure 10B & E**): the lower emission wavelength (colored in blue) represents the ordered membrane, while the higher emission wavelength (red) represents the disordered membrane. Using both images, I calculated the GP value for every pixel according to **Equation 1**, which generates a raw RGB GP image.

$$GP\,(x,y) = \frac{L_o(x,y) - g\,L_d(x,y)}{L_o(x,y) + g\,L_d(x,y)}$$

Equation 1: Formula to calculate the GP value. The GP value is calculated for every pixel, defined by the position (x,y), where I_o is the intensity value of the ordered channel, I_d is the intensity value of the disordered channel, and g is the (optional) correction factor, which is set to 1 if unknown or -1 to estimate it.

When calibrated using the g factor, a high GP value corresponds to a high membrane order, whereas a low GP value defines a low membrane order. If not calibrated, I can use the GP value to compare measurements in relative terms: if the membrane from measurement A has a higher GP value than the membrane from measurement B, this demonstrates that membrane A has a higher membrane order than membrane B.

Next, I generated a thresholded image from the intensity sum of both channels to mask undesired pixel values on the raw GP image, which I can use for a GP histogram analysis. For visual presentation, I generated a hue-saturation-brightness (HSB) image to de-emphasize low signal pixels: The masked GP image was split into the respective red, green, and blue channels and merged with the summed intensity images from the ordered and disordered channels. The HSB image contained the membrane order and structural information, in which the GP value was set to hue, the saturation was assigned to 1, and the summed intensity of the ordered and disordered channel was set to brightness (**Figure 10B**).

Having a higher photostability, I started to establish the imaging approach using d-4-ANEPPDHQ. In contrast to imaging a single plane of the cell body, I had to image primary cilia in several planes to fully capture them (**Figure 11A**). Before analyzing the CM in a single plane like the PM, I needed to trace each cilium into a maximum z-projection. HSB analysis of the PM and processed CM revealed no noticeable differences (**Figure 11B**). Thus, I analyzed the GP histogram to quantify differences and normalized it to the pixel count (**Figure 11C**). The GP histogram of the CM was shifted to higher GP values, and the left flank (representing a lower membrane order) was a lot wider in the PM histogram. This was due to di-4-ANEPPDHQ also staining inner membranes with a much lower membrane order (de Duve, 1971; Lange et al., 1989; Owen et al., 2011; Ray et al., 1969). To compare the results of the GP histograms, I plotted the peak GP value of each histogram (**Figure 11D**): the GP value for the CM was higher compared to the PM, demonstrating that the CM is more ordered than the PM.

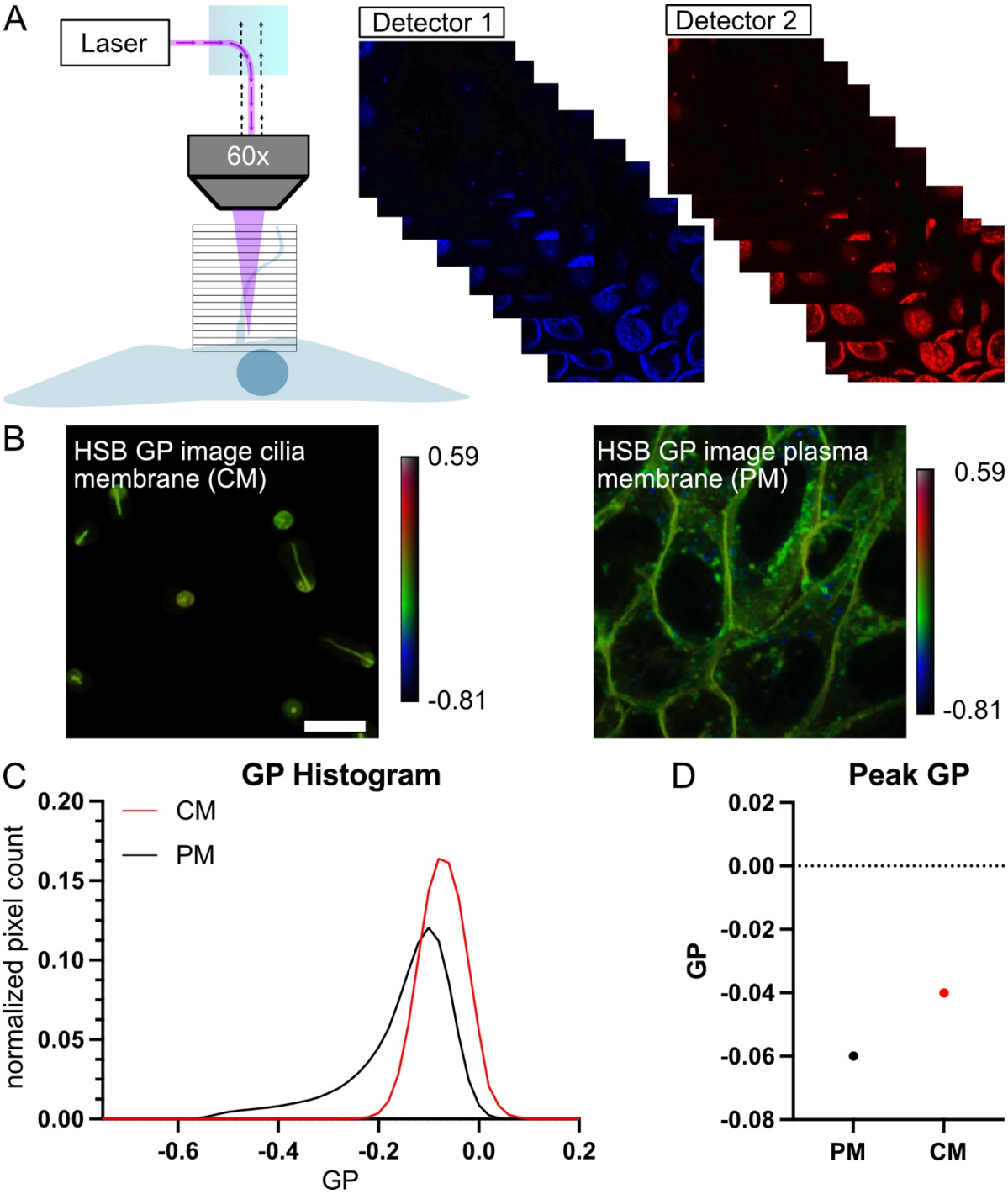

Figure 11: Analysis pipeline to determine the membrane order. A: Cilia have to be imaged in several optical planes. **B:** After manual cropping of cilia from the combined optical sections, cilia membrane (CM) and plasma membrane (PM) images are both processed as single optical plane images Scale bar: 10 µm. **C:** GP values are plotted to the normalized pixel count of each image. **D:** The maxima of the respective histograms can be plotted as representative values for comparison. Higher GP values correspond to a higher ordered membrane and vice versa.

As described in the introduction, loss or dysfunction of GBA2 leads to the accumulation of glucosylceramide and, thereby, accumulation of glycosphingolipids in the PM (Hamzeh, 2017; Yildiz et al., 2006). We hypothesized that GBA2 also regulates the GSL content in the CM (**Figure 12A**). I tested this hypothesis using pharmacological inhibition of GBA2 by the iminosugar N-butyldeoxynojirimycin (NB-DNJ). NB-DNJ

specifically blocks GBA2 activity (IC_{50}: 5-300 nM, *in vitro*), but also inhibits glucosylceramide synthase (GCS) at higher concentrations (IC_{50}: 20.4-50 µM, *in vitro*) (Ashe et al., 2011; Ridley et al., 2013). I seeded mIMCD-3 cells, induced ciliogenesis, treated them for 48 h with 2 µM NB-DNJ, and stained them with di-4-ANEPPDHQ and Pro12A. However, using my approach, I got contradictory results. Both, di-4-ANEPPDHQ and Pro12A GP values displayed a huge variety amongst the technical replicates and in 6 out of 12 measurements, the GP values shifted in the opposite direction compared to what we expected from our previous findings (**Figure 12B & C**).

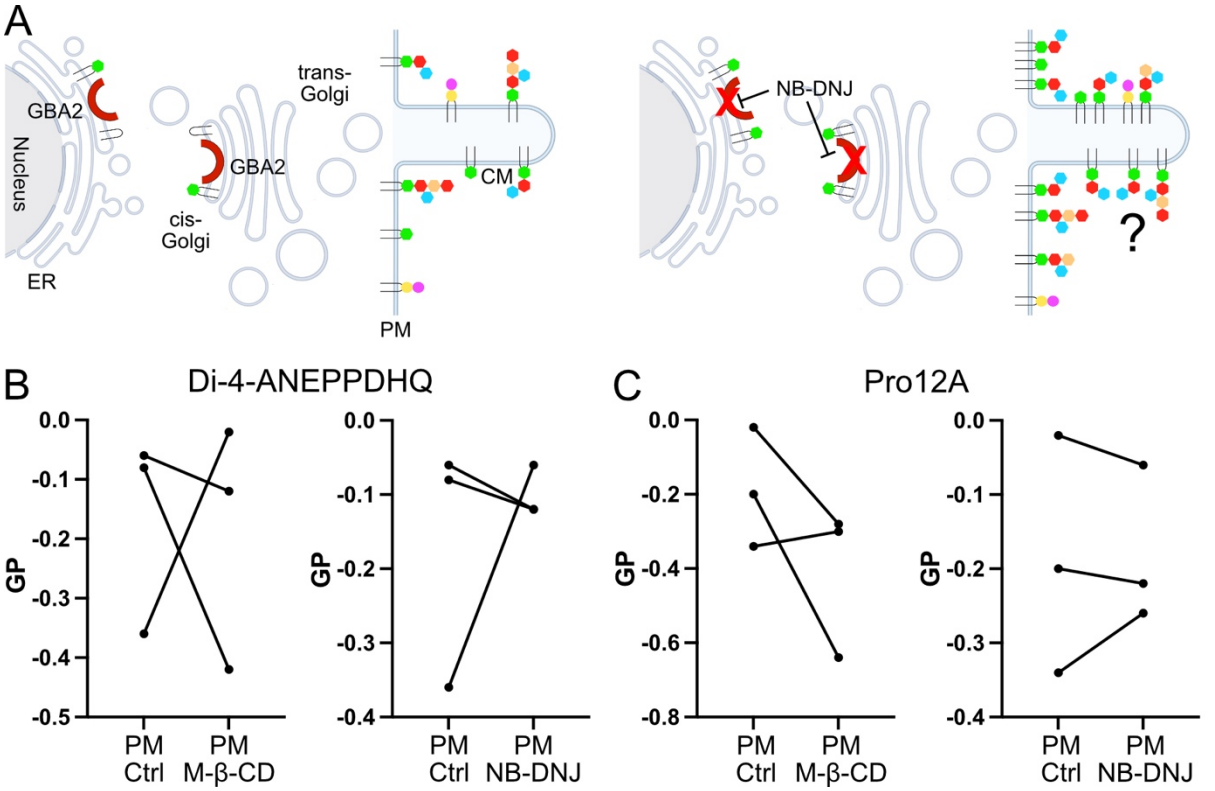

Figure 12: Analysis of PM with Di-4-ANEPPDHQ and Pro12A. A: Scheme illustrating that GBA2 resides at the luminal sides of the ER and cis-Golgi, where it degrades the central building block of higher GSL, glucosylceramide, into glucose and ceramide. Absence or inhibition of GBA2 leads to an increase of GSLs in the PM, but whether this affects the GSL homeostasis in the CM is affected is not known. **C:** The addition of Methyl β-Cyclodextrin (M-β-CD) extracts cholesterol from the membrane and results in a shift towards the L_d phase, whereas the addition of the GBA2 specific blockers NB-DNJ or MZ-21 lead to GSL accumulation and a shift towards the L_o phase. **D:** GP values plotted as points and lines diagram for the PM of non-treated (Ctrl), 10 mM Methyl-β-Cyclodextrin (M-β-CD), or 2 µM NB-DNJ treated cells of n = 3 independent experiments.

I hypothesized that the GP value shift is due to photoselection, which describes the probability of a chromophores electron to absorb a photon, dependent on the excited state dipole orientation (Albrecht, 1961). Unlike most fluorescent molecules in biological systems, the membrane dyes are drastically limited in their excited state dipole orientation in the cellular membrane, as their backbone aligns in parallel to the acyl chain of the membranes phospholipid (**Figure 13A**). When the excited state dipole

orientation differs from the incident polarized light, electrons will less likely resonate with the light, and a transition of the electron to the excited state is less likely to happen (Albrecht, 1961). Thus, photoselection is more pronounced in L_o phase membranes, as dye movement is even more restricted there (**Figure 13A**). The probability of photons from a polarized light source to excite an electron depends on the angle of the incident photons by $\cos^2$ ($\cos^2\theta_A$) (**Figure 13B**). Photoselection using linearly or circularly polarized light on a spherical object (representing a cell) with either an L_d or L_o phase lipid bilayer is illustrated in **Figure 13C & D**: With linearly polarized light, there is an equal probability in the polar plane of L_d and L_o phase lipid bilayers to excite di-4-ANEPPDHQ or Pro12A, because their excited state dipole orientation towards the vector of the incident light will be almost the same in any position of the polar plane. In the equatorial plane, excitation varies drastically. It is more pronounced in the L_o phase because the excited state dipole orientation differs towards the incident light vector in almost every equatorial plane position. Using circularly-polarized light, the observed effects between the polar and equatorial planes are switched. The dyes are equally excited in the equatorial plane and variously in the polar plane. Thus, I have to use circularly-polarized light because I measure in the equatorial plane.

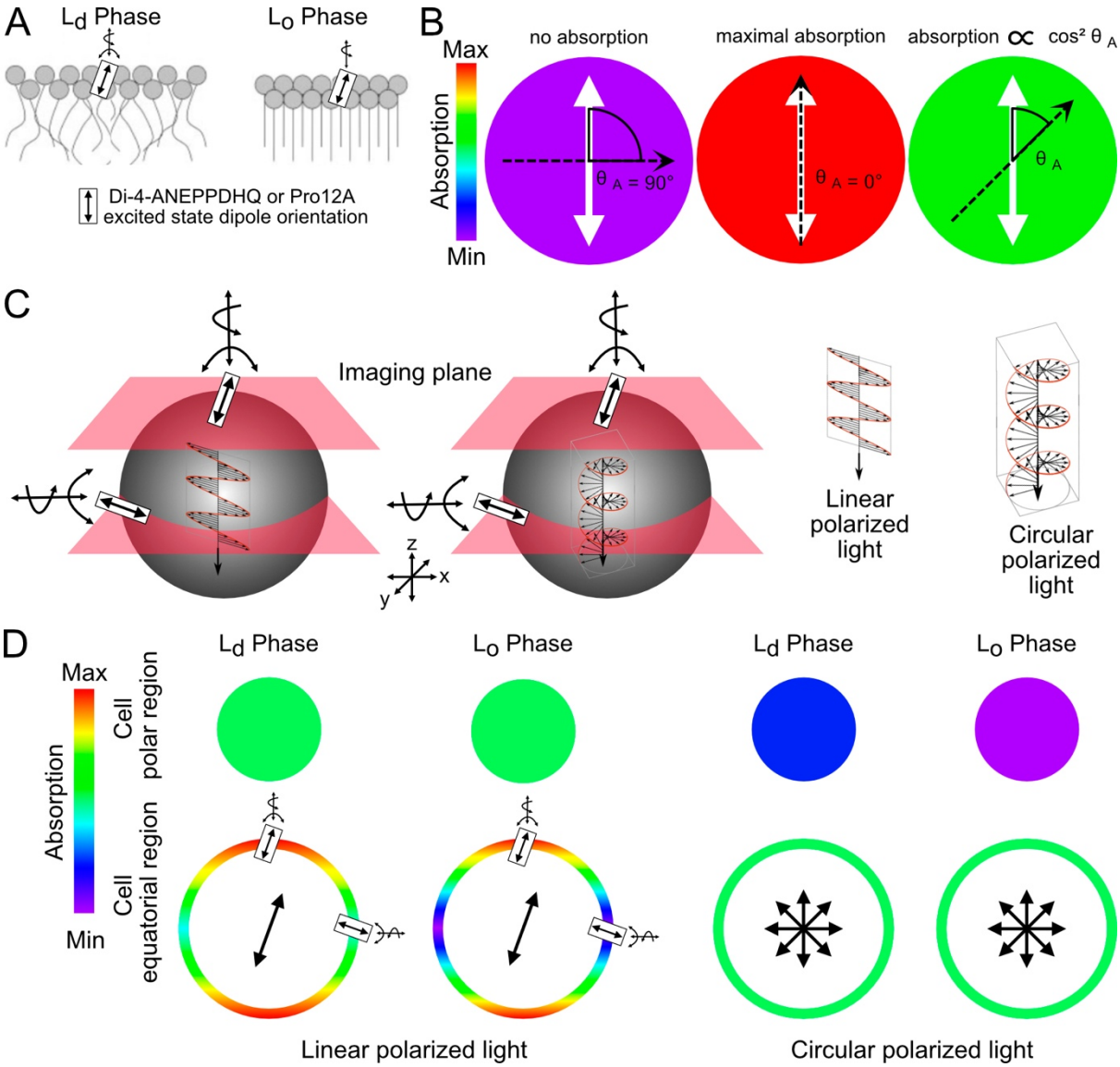

Figure 13: Photoselection with polarized light. A: Di-4-ANEPPDHQ and Pro12A excited state dipole orientation is restricted when anchored into a lipid membrane. The degree of movement restriction depends on the membrane phase. Modified from (Fidorra et al., 2006). **B:** The probability of the fluorophore absorbing photons and thus being excited is proportional to the degree of the electric field vector of the incident polarized light (black arrow) to the fluorophore´s excited state dipole orientation (white arrow). Modified from (Yip, 2016). **C:** Scheme of linearly and circularly polarized light orientation with respect to the imaging plane and dipole orientation of the dyes in a cell. Modified from (Fidorra et al., 2006). **D:** Scheme of expected fluorescence emission in the polar and equatorial region of cells. Modified from (Bagatolli and Gratton, 2000). **E:** A quarter-wave plate transforms linearly polarized light into circularly polarized light.

To transform the linearly polarized light at the confocal microscope into circularly polarized light, I used a quarter-wave plate. When the incident linearly polarized light passes the quarter-wave plate with a 45° angle with respect to the quarter-wave plate fast axis, it is transformed into circularly polarized light (**Figure 14A**). The Leica SP8 allows inserting a quarter-wave plate by mounting it onto a carrier to easily insert it into the light path (**Figure 14B)**. In turn, the linearly polarized light from the light source is circularly polarized before reaching the probe for excitation (**Figure 14C**). However,

information about the orientation of the linear polarized light from the light source could not be obtained from Leica. Thus, I used the Leica SP8s Abbe-Koenig field rotator to solve this problem. It rotates the scan field before hitting the quarter-wave plate and allows to rotate the linear polarized light instead of the quarter-wave plate position to set up the desired 45° position. I recorded images of the same cell in the equatorial plane with 5° rotation steps from a zero position (defined as 0°) to a 90° position (**Figure 14D**). Using the Fiji Rainbow RGB lookup table (LUT) to identify intensity differences more efficiently, the equatorial plane showed the most homogenous emission at an Abbe-Koenig field rotation of 35° with the inserted quarter-wave plate (**Figure 14B).** In the following, I recorded the same cell in the equatorial plane with and without the quarter-wave plate to verify the compensation for photoselection in the equatorial plane. Indeed, the intensity of perpendicular directions varied greatly without the quarter-wave plate, whereas it appeared equally distributed with the quarter-wave plate at 35° Abbe-Koenig field rotation (**Figure 14E**). Next, I re-measured my probes with circularly polarized light.

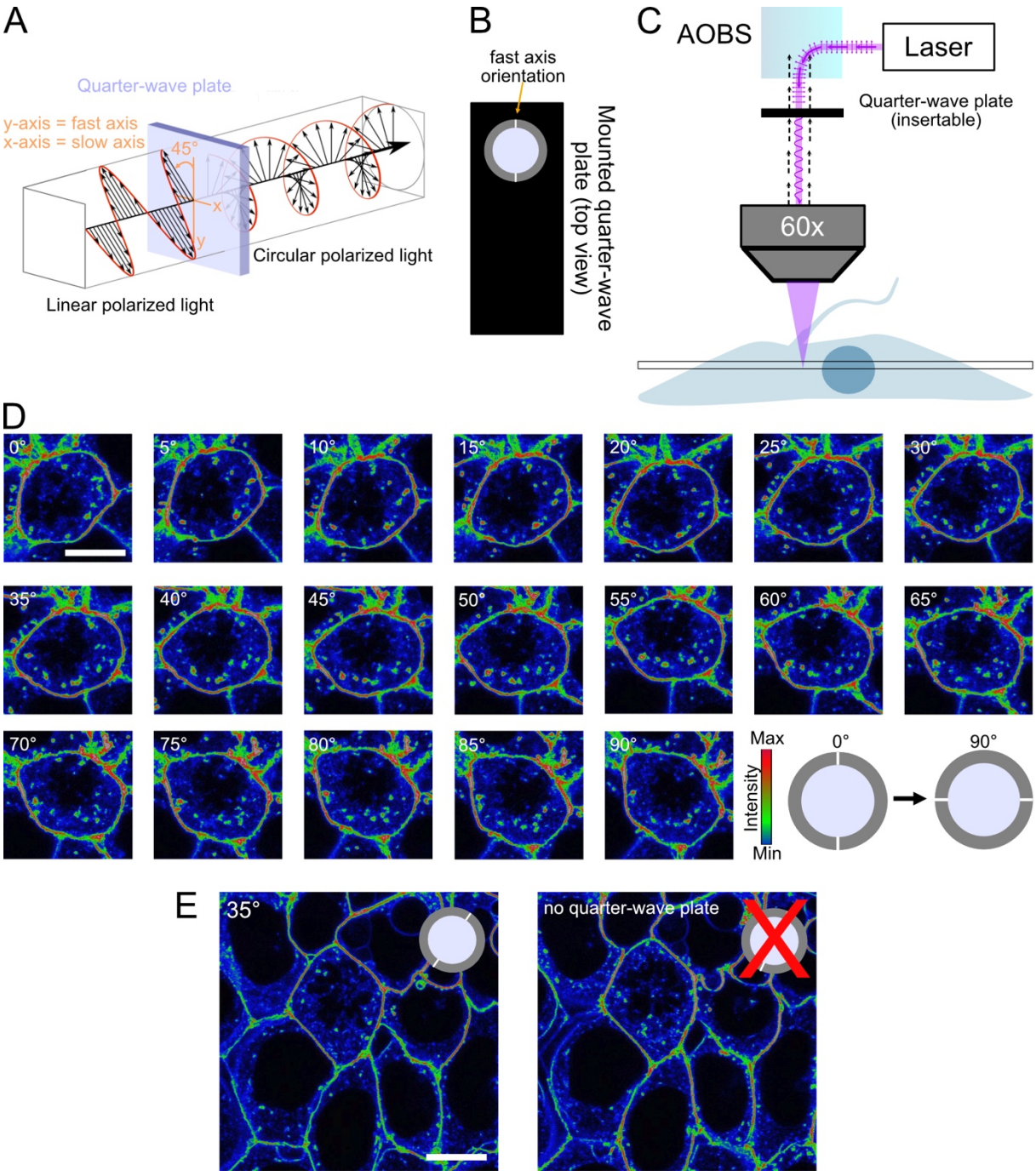

Figure 14: Set-up to compensate for photoselection in the LEICA SP8 confocal laser scanning microscope. **A:** Correct positioning of the quarter-wave plate to transform linearly into circularly polarized light. **B:** Orientation of the mounted quarter-wave plate. **C:** Positioning of the mounted quarter-wave plate in the optical path of the microscope. **D:** Imaging series of the same field of view rotated using the Abbe-König scan field rotator to compensate for the unknown angle of linearly polarized light. **E:** Images with and without the quarter-wave plate to demonstrate the efficient compensation of photoselection in the equatorial plane at 35° angle of the Abbe-König scan field rotator. All scale bars: 10 µm.

Di-4-ANEPPDHQ imaging of the PM revealed that treating the cells with 10 mM M-β-CD significantly reduced the mean GP value by 0.144 (**Figure 15A**), while the GP value after treatment of Pro12A labeled, M-β-CD treated cells was not significantly reduced (**Figure 15F**) compared to non-treated cells. Previous studies have shown

that di-4-ANEPPDHQ is more sensitive to changes in cholesterol content than the Pro12A relative Laurdan (Amaro et al., 2017). This might explain the different outcomes using the two different dyes. After treatment with 2 µM NB-DNJ, the GP values remained unchanged for cells labeled with either dye (**Figure 15B & G**). Thus, I observed the expected changes in membrane order for the different conditions when using circularly polarized light, but the results were mostly not significant. Next, I compared the GP values of the PM and CM in untreated cells using di-4-ANEPPDHQ and Pro12A imaging: for both dyes, the GP value of the CM was significantly higher compared to the PM, demonstrating a higher membrane order in the CM compared to the PM (**Figure 15C & H**). This is in line with results showing that primary cilia contain high cholesterol and GSL (GM3 and GM1) content (Janich and Corbeil, 2007; Kinnebrew et al., 2019). To verify whether I could change the CM order by depleting cholesterol, I treated the cells with 10 mM M-β-CD. Indeed, for both di-4-ANEPPDHQ and Pro12A, the GP value was reduced compared to non-treated cells (**Figure 15D & I**). However, the changes were not significant. Furthermore, as observed for the PM, the GP values of the CM remained unchanged after treatment with 2 µM NB-DNJ (**Figure 15E & J**). Missing significance might be due to the low number of replicates, which could be solved in the future by performing more experiments and evaluating single cells/cilia from one recording instead of taking the whole histogram of one recording for determining the peak GP value on the other side.

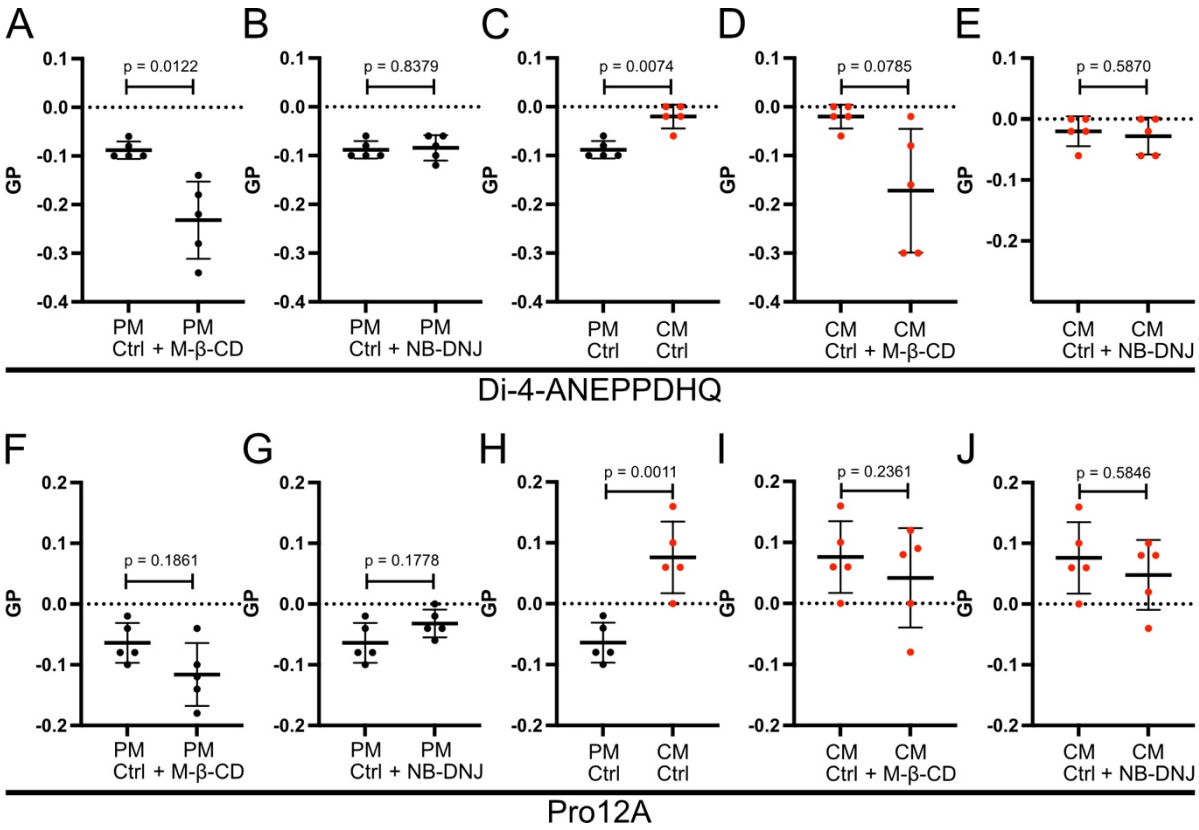

Figure 15: Analysis of the lipid order in the plasma membrane (PM) and ciliary membrane (CM) by Di-4-ANEPPDHQ and Pro12A imaging using circularly polarized light. A-B: GP values plotted scatter-plot diagrams of mean ± S.D. for the PM of non-treated (Ctrl), 10 mM Methyl-β-Cyclodextrin (M-β-CD), or 2 µM NB-DNJ (NB-DNJ) treated cells loaded with Di-4-ANEPDHQ (A) or Pro12A (B). Statistical differences were calculated using paired t-tests. P-values are indicated. Data points shown as the mean of peak GP values of n = 5 independent experiments with n = 6 to 12 cells or 4 to 12 cilia per condition per experiment.

3.3 Analyzing GSL function in primary cilia signaling using GBA2

Hh signaling is the best studied ciliary signaling pathway. Thus, I analyzed Hh signaling as a read-out to study the impact of GSL homeostasis on ciliary signaling. In particular, the state-dependent localization of the different Hh signaling proteins, the second messenger dynamics, and the evoked changes in gene expression offer a wide range of parameters to analyze. In the previous chapter, I showed that 1. the ciliary membrane has a significantly higher order than the plasma membrane, and 2. that accumulation of GSLs, after blocking GBA2 did not further increase the membrane order in the range that the environment-sensitive dyes are able to report. Thus, to analyze the direct impact on ciliary signaling, I investigated whether changing the GSL homeostasis by inhibiting GBA2 activity has an effect on ciliary Hh signaling.

3.3.1 Adapting CiliaQ analysis for unbiased quantification of ciliary immunofluorescence

I used the ciliary SMO localization upon Hh pathway activation as a read-out. I hypothesized that disturbing ciliary GSL homeostasis by loss of GBA2 activity might alter ciliary protein localization (**Figure 16A**): To this end, I performed immunocytochemistry to label SMO using an anti-SMO antibody (Ocbina et al., 2011) in combination with ciliary marker proteins using antibodies AC-α-TUB or the ARL13B (Caspary et al., 2007; LeDizet and Piperno, 1991). AC-α-TUB labels microtubules, which form the ciliary axoneme, whereas ARL13B is associated with the ciliary membrane (**Figure 16B**).

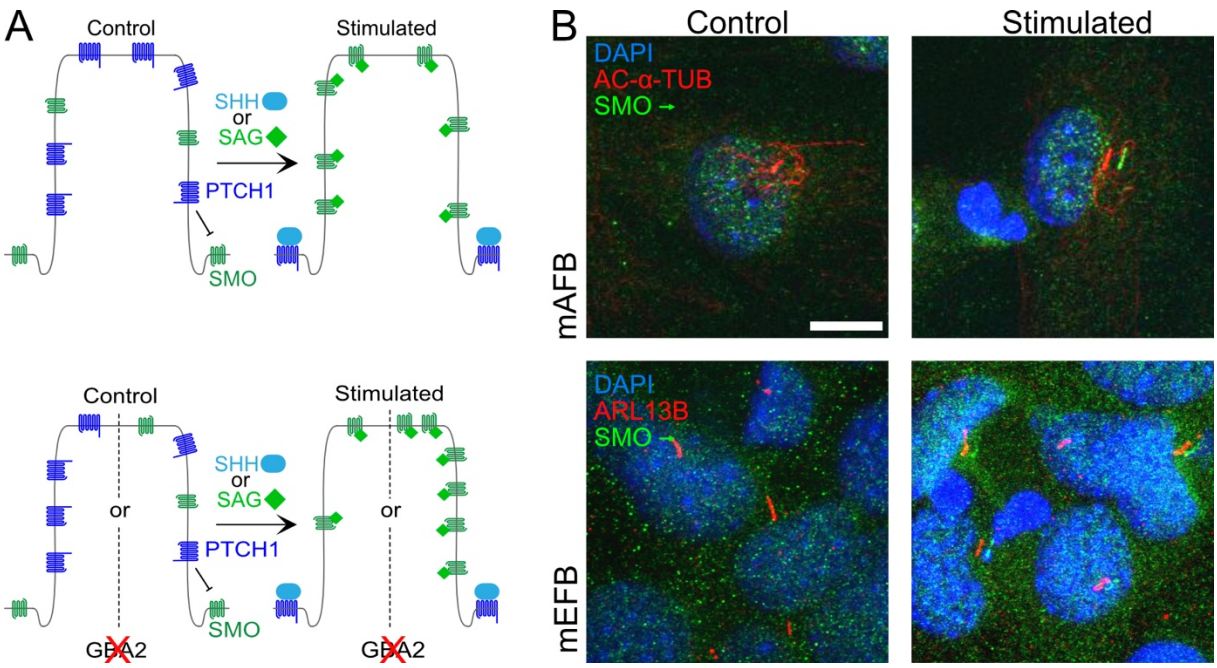

Figure 16: Analyzing ciliary Hedgehog signaling using the subcellular localization of Smoothened (SMO) as a read-out. A: Scheme depicting ciliary Patched1 (PTCH1) and Smoothened (SMO) distribution in control and stimulated conditions (upper row) as well as a model depicting how the distribution might change after altered lipid packaging of the ciliary and plasma membrane. **B:** Representative image of a ciliated mouse adult fibroblast (mAFB) cells under control (+ 1:1000 DMSO and stimulated (+ 3 µM SAG) conditions. Cells have been labeled with DAPI (DNA, blue), with an anti-acetylated α tubulin antibody (AC-α-TUB, cilia, red) and an anti SMO antibody (green, channel pixel shifted as indicated). Scale bar: 10 µm.

To analyze the fluorescence images in an unbiased and reproducible way, I used CiliaQ (Hansen et al., 2021). CiliaQ is an open-source software, which has been developed in our lab and allows to quantify ciliary fluorescence. The CiliaQ workflow consists of three steps (**Figure 17A**): First, the CiliaQ preparator segments the ciliary marker image into cilia and background. The second and optional step is to use CiliaQ Editor to scrutinize and correct errors (not shown and not used, i.e., allows deletion of false-positive identified cilia or connect two halves of a cilium that CiliaQ placed as two cilia). Alternatively, false-positive identified cilia can be excluded from data evaluation later via their cilium ID. In the third and last step, CiliaQ quantifies and visualizes cilia and allows to study protein localization in the cilium. Here, I quantified the ciliary SMO localization using the average SMO immunofluorescence intensity (average intensity), the average SMO immunofluorescence intensity of the 10% highest voxels in the cilium (highest 10% voxel intensity), and the colocalized volume compared to the background of SMO immunofluorescence (colocalization) (**Figure 17B**). Each of those parameters is prone to different detection biases: the average ciliary intensity is a less stable parameter because it is sensitive to variation of the ciliary mask during the segmentation process under a low signal-to-noise ratio. The average intensity is a very

common parameter when analyzing ciliary proteins by immunolabeling and reflects all voxels in the ciliary mask. However, the intensity of the 10% highest voxels in the cilium is a more robust read-out and less error-prone to a low signal-to-noise ratio. Still, it depends on a uniform ciliary intensity distribution and takes only the brightest voxel into account. Colocalization compared to background indicates the volumetric ciliary protein enrichment with respect to the cell soma. This parameter is thus less error-prone to an unspecific background signal. Still, it might induce artifacts when the protein of interest varies in the ciliary and somatic detection (Hansen et al., 2021). Furthermore, there is also a bias depending on the ciliary marker, i.e., B or ARL13B: Compared to ARL13B, AC-α-TUB has reduced detection in resorbing cilia as these have reduced tubulin acetylation, but reconstruction can incompletely capture ciliary localization of a membrane protein (Malicki and Johnson, 2017). Hence, AC-α-TUB detection might exclude cilia in the state of resorption, whereas ARL13B might perform better in capturing the ciliary membrane (Hansen et al., 2020). Exclusion of resorbing cilia might be helpful because they might not be in a representative Hh signaling state, whereas better capturing of the ciliary membrane might be more sensitive when analyzing localization of SMO as a protein in the ciliary membrane.

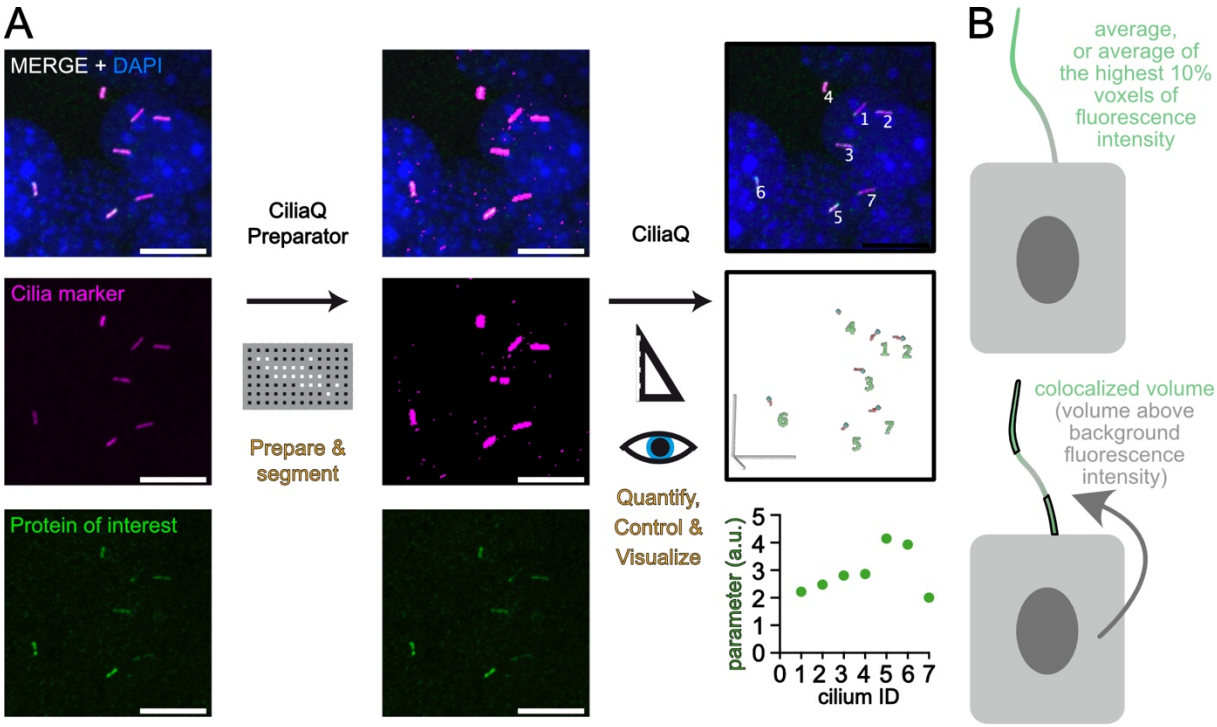

Figure 17: CiliaQ simplified workflow. A: CiliaQ and CiliaQ Preparator are open-source software for automated quantification of ciliary morphology and fluorescence in 2D, 3D, and 4D images. Scale bars: 10 µm. **B:** Scheme of parameters used in this thesis. Figure modified from (Hansen et al., 2021).

3.3.2 Analyzing GBA2-dependent ciliary Hh signaling using SMO labeling

I analyzed the ciliary SMO localization under different conditions using mouse adult and embryonic fibroblasts (mAFB and mEFB) with the following time-course (**Figure 18**): I seeded cells and let them grow for 24 h to proliferate until confluence. Subsequently, I induced ciliation for 24 h in the presence or absence of either 2 µM NB-DNJ or 30 nM MZ-21 (alias AMP-DNM), which both reversibly inhibit GBA2 but with different IC_{50} (18-21 nM vs. 1.7-4.8 pM, *in vitro,* respectively) (Körschen et al., 2013; Woeste, 2018). After 24 h, in the presence or absence of either blocker, I stimulated Hh signaling for 24 h before analysis.

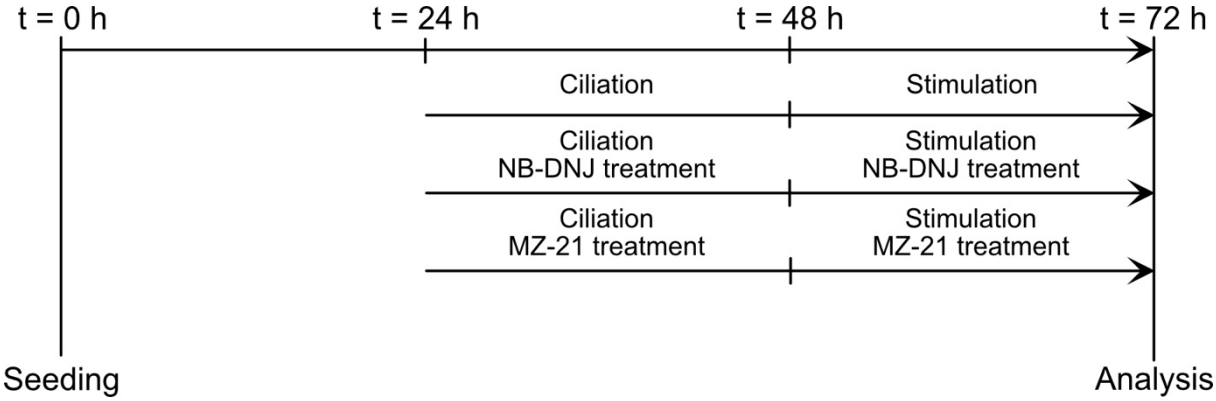

Figure 18: **Time course for the treatment of fibroblasts to analyze Hh signaling.** Cells were seeded at t = 0 h. After 24 h of growth, the medium was changed to 0.5% instead of 10% FCS (Ciliation). Additionally, cells were treated with 2 µM NB-DNJ (NB-DNJ treatment), or 30 nM MZ-21 (MZ-21 treatment). After another 24 h of incubation, cells were stimulated. NB-DNJ and MZ-21 were also present during stimulation.

Stimulation of mAFB with SAG resulted in a significant increase of ciliary SMO localization, as detected by all three parameters (**Figure 19A**). Treatment with NB-DNJ significantly reduced the SAG-dependent ciliary SMO localization, whereas MZ-21 did not change the ciliary SMO localization (**Figure 19B**). Of note, the effect of NB-DNJ was only observed in 2 out of the 3 parameters: SMO colocalization was not significantly different compared to the control, but several data points were in saturation (depicted by 100% colocalization). Thus, the information on the actual values was lost, rendering it difficult to detect changes in ciliary SMO. My results indicate that increasing the membrane order affects ciliary Hh signaling by reducing the SAG-dependent translocation of SMO into the cilium. However, this effect was only observed in the presence of NB-DNJ and not MZ-21, although both inhibit GBA2 activity. One explanation for this discrepancy could be that the applied MZ-21 concentration also inhibits glucosylceramide synthase (GCS) activity, which in turn could change GSL levels differently compared to NB-DNJ-treated cells.

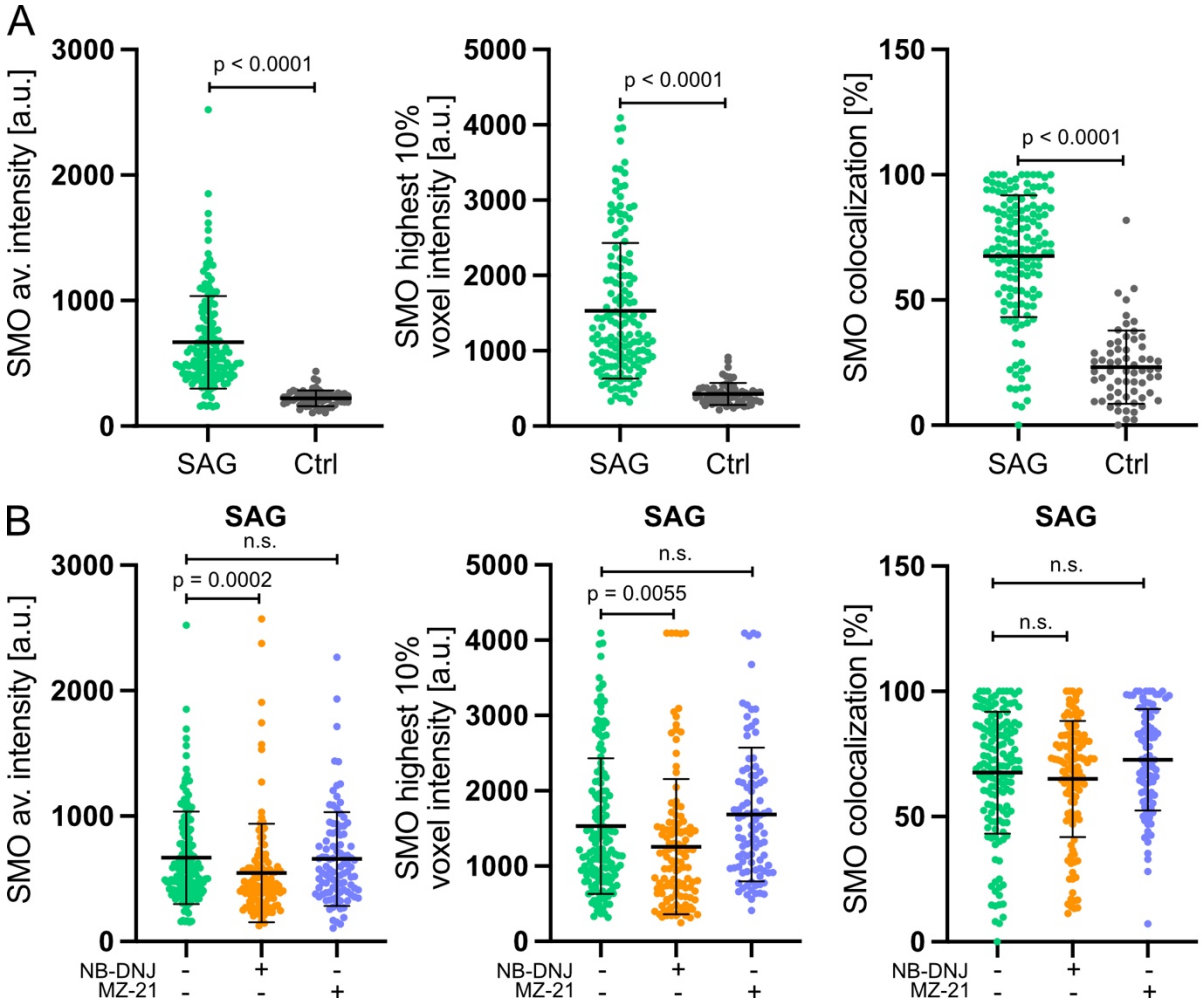

Figure 19: Analysis of ciliary Hh signaling using Smo labeling in mAFB. A: Smo quantification in ciliated mAFB treated with 3 µM SAG (SAG) or DMSO (Control) for 24 h. As datasets were not normality distributed, statistical differences were calculated using a Mann-Whitney test, p-values are indicated. **B:** Smo quantification in ciliated mAFB treated with 3 µM SAG (SAG) for 24 h and SAG for 24 h + 2 µM NB-DNJ (NB-DNJ) for 48 or 30 nM MZ-21 (MZ-21) for 48 h. As datasets were not normality distributed, statistical differences were calculated using a Kruskal-Wallis test and Dunn´s multiple comparison posthoc test, p-values are indicated, non-significant (n.s.). All data are shown as individual data points with mean ± S.D. from 3 independent experiments.

Although SAG induces Hh signaling, its activating mechanism differs from the endogenous ligand, SHH, as SAG binds to SMO and not to the SHH receptor PTCH1 (Chen et al., 2002; Gigante and Caspary, 2020; Petrov et al., 2021). Hence, SMO localization into the primary cilium after SAG stimulation might not reflect Hh pathway activity like SMO localization after SHH stimulation might do. Therefore, I compared SAG to SHH stimulation in my assay. In addition, I included *Gba2* knockout cells in my experimental set-up. Loss of GBA2 in G*ba2* knockout (*Gba2*$^{-/-}$) mouse lines was initially verified using a GBA2 activity assay (Woeste, 2018) and by genotyping. To this end, I first had to obtain SHH. The biological active morphogen SHH is a 19 kDa protein that originates from a 45 kDa precursor. After autoproteolytic cleavage, the 27 kDa C-terminal part cholesteroylates the N-terminal 19 kDa SHH and, thereby, anchors it to

the cell membrane (Bumcrot et al., 1995; Porter et al., 1996b). Thus, I chose to generate SHH in HEK293 cells without the cholesterol moiety. The Beachy lab cloned a cDNA (*ShhN*, addgene ID: 37680, unpublished), which lacks the C-terminal part of the SHH precursor protein at the position where it autoproteolytically cleaves itself (**Figure 20A**). As a result, cells transfected with *ShhN* produce biological active SHH (referred to ShhN in the following), as determined *in vitro* and *in vivo* studies, which is secreted instead of anchored to the membrane (**Figure 20B**) (Li et al., 2006; Porter et al., 1996a; Zeng et al., 2001).

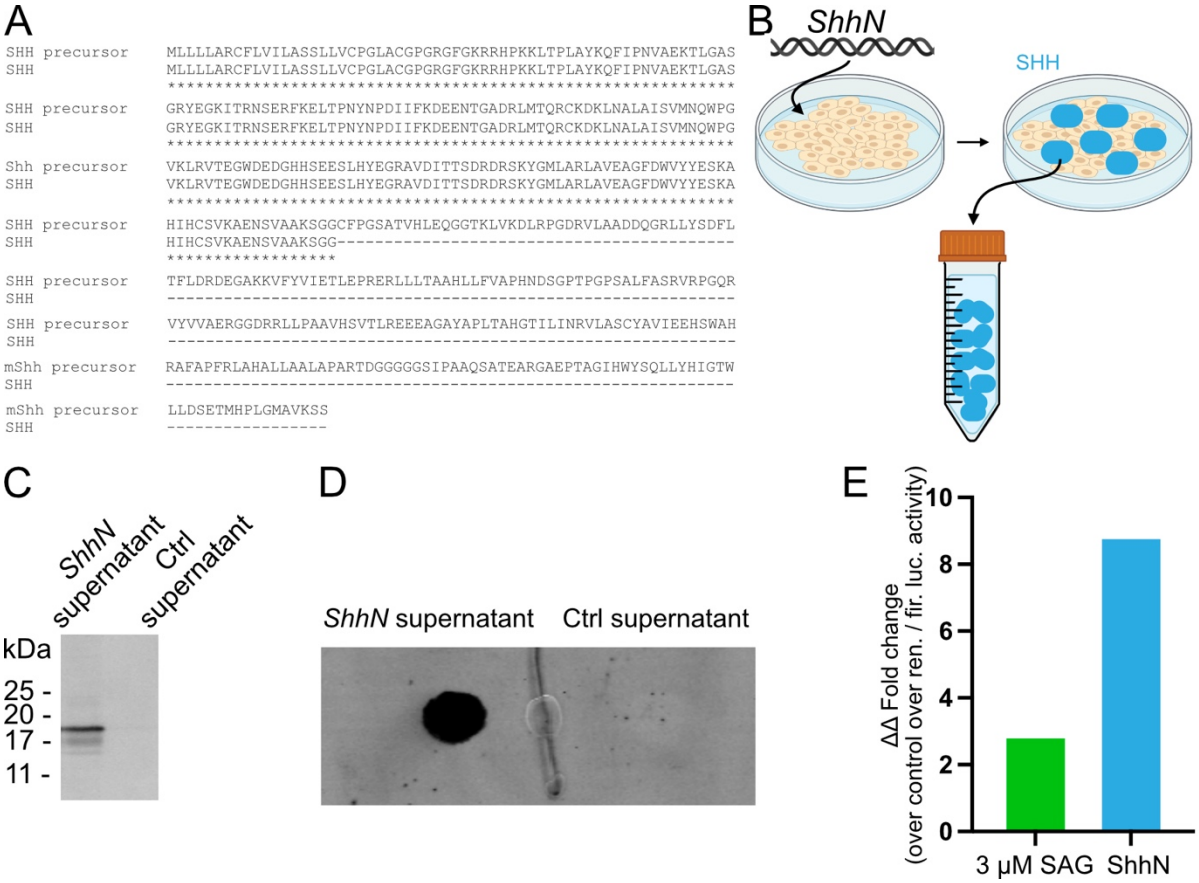

Figure 20: Establishing the generation of soluble Sonic Hedgehog (SHH) ligand. A: Comparison of the mouse SHH precursor protein and the final SHH protein. The precursor protein has an autoproteolytic cleavage site that cleaves the precursor in the 19 kDa N-terminal part, which is the SHH ligand, and a 25 kDa C-terminal part with accompanying cholesterol modification. The cholesterol modification anchors SHH to the plasma membrane after secretion. **B:** Transfection of cells with ShhN leads to the production of the SHH ligand, but without cholesterol modification. That leads to the secretion of the protein in the supernatant. **C:** Western blot analysis of cell supernatant from ShhN and non-transfected (Ctrl supernatant) cells. **D:** Dot blot of ShhN and Ctrl supernatant to verify SHH expression. **E:** SHH activity assay to compare the activity between SAG and ShhN supernatant. Data are shown as mean of one experiment with duplicates.

I transfected HEK293 cells with *ShhN* and harvested the supernatant 24 h after transfection (**Figure 20B**). Compared to the supernatant of mock-transfected cells, Western blot analysis using an anti-SHH antibody showed a prominent, specific band at around19 kDa (**Figure 20C**), verifying the presence of ShhN in *ShhN* supernatant.

For every experiment in which I used *ShhN* supernatant, I confirmed its expression by dot blot analysis (**Figure 20D**). Next, I determined SHHN activity using a Hh reporter activity assay. Here, Hh pathway activation drives the expression of a *firefly luciferase* under the control of eight consecutive GREs (Zhao, 2014). In a single experiment measured in duplicates, SHHN from *ShhN* supernatant induced luciferase activity by 8-fold compared to a 3-fold induction after 3 µM SAG stimulation (**Figure 20E**). Consequently, I decided to dilute the supernatant 3-fold for stimulation. Diluting the supernatant also has the advantagethat the fibroblast-medium composition is only changed by ca. 33% as it differs from the HEK293 medium.

Like SAG, stimulation of mAFB with ShhN resulted in a significant increase of ciliary SMO localization, as detected by all three parameters (**Figure 21 A-C**). Furthermore, the ciliary SMO localization was significantly reduced after NB-DNJ treatment, but no changes were observed after MZ-21 treatment, in line with the results after SAG stimulation. Strikingly, the ciliary SMO localization was also reduced in *Gba2*$^{-/-}$ compared to *Gba2*$^{+/+}$ mAFB (**Figure 21 D-F**), confirming the results after NB-DNJ treatment. To test whether loss of GBA2 function might also affect Hh signaling in the unstimulated state, I compared ciliary SMO levels between *Gba2*$^{-/-}$ and *Gba2*$^{+/+}$ mAFB under control conditions. In two of the three parameters, I saw a significant increase of ciliary SMO in *Gba2*$^{-/-}$ cells (**Figure 21 G-I**). I conclude that in the absence of GBA2-activity, GSL levels, and in turn, the membrane order increase, which might hinder the dynamic shuttling of SMO in and out of the cilium and, thereby, prolong the residence time of SMO in the cilium.

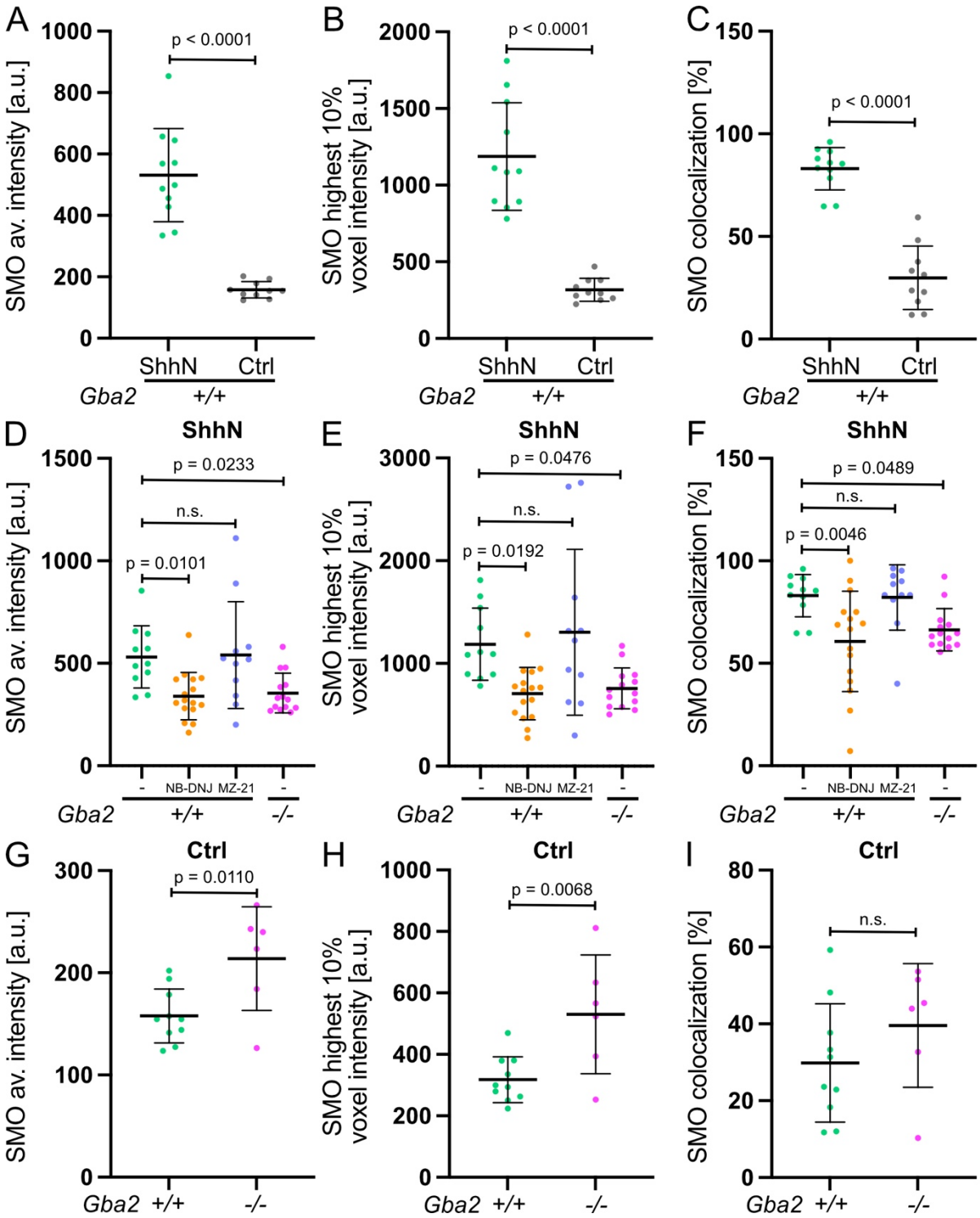

Figure 21: Analysis of ciliary Hh signaling using Smo labeling in ciliated mAFB and SHH stimulation. **A-C:** Smo quantification in ciliated GBA2$^{+/+}$ mAFB treated with 3-fold diluted SHH supernatant (SHH) or control supernatant (Ctrl) for 24 h. As datasets were normal distributed, statistical differences were calculated and unpaired t-test, p-values are indicated. **D-F:** Smo quantification in ciliated GBA2$^{+/+}$ and GBA2$^{-/-}$ mAFB SHH stimulated cells that were treated with 2 µM NB-DNJ or 30 nM MZ-21 when indicated (+). As datasets were normal distributed, statistical differences were calculated using Dunnett´s multiple comparison test, p-values are indicated. Non-significant (n.s.). **G-I:** Smo quantification in ciliated GBA2$^{+/+}$ and GBA2$^{-/-}$ mAFB non-stimulated cells that were. As datasets were normal distributed, statistical differences were calculated using Dunnett´s multiple comparison test, p-values are indicated. Non-significant (n.s.) All data are shown as individual data points of fold changes to their respective control, which was only treated with control supernatant instead of Shh supernatant, with mean ± S.D. from 1 experiment.

In summary, my results demonstrate that increasing the membrane order by abolishing GBA2 activity alters ciliary Hh signaling by increasing the ciliary SMO localization under basal conditions and reducing further translocation upon pathway activation.

Other studies have shown that the dynamics of Hh signaling differ among cell types (Cohen et al., 2015; Taipale et al., 2000). Thus, I analyzed whether my results can be recapitulated in another cell type, i.e., embryonic fibroblasts that I generated from *Gba2*$^{-/-}$ and *Gba2*$^{+/+}$ mice (mEFB) (see Materials and Methods). Furthermore, as the concentration of ShhN in *ShhN* supernatant might vary from one experiment to the other, I also used the rather expensive but purified, recombinant human SHH (hSHH) that I could apply in defined concentration. Because I wanted to use hSHH on mouse cells, I verified hSHH activity using the Hh activity assay (**Figure 22**): 1 nM hSHH induced a 1.5-fold increase, and I observed the highest activity (8.4-fold) with 10 nM hSHH, which is in line with the half-maximal activity determined by the manufacturer (between 263 pM and 1.05 nM). Of note, 50 nM hSHH displayed less activity (2.1-fold increase), not reported by the manufacturer or others. The stock concentration of hSHH was 100 nM in H_2O; thus, these adverse effects could be due to osmotic changes.

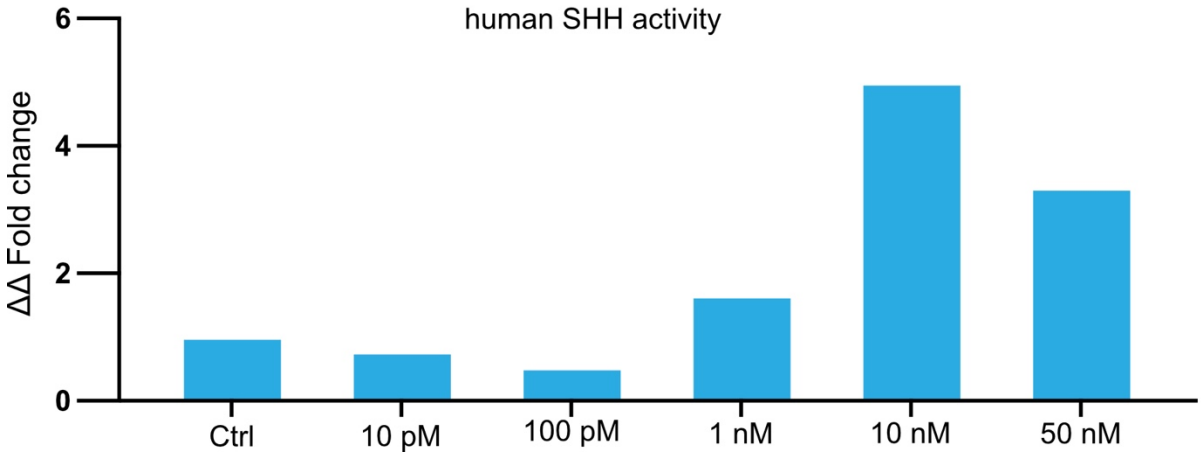

Figure 22: Hh activity assay to determine a non-saturating concentration of hSHH. Data are shown as mean of one experiment with duplicates. Data are plotted to ΔΔ fold changes to housekeeping signal and to the non-stimulated control (Ctrl). For details, see Hh activity assay

Based on my results, I decided to use 2 nM hSHH for the following experiments. In addition, I used ARL13B as a ciliary marker in all experiments instead of AC-α-TUB, as ARL13B labeling seems to be more specific in mEFB.

Stimulation of mEFB with hSHH resulted in a significant increase in ciliary SMO localization, reported by all three parameters (**Figure 23A-C**). Subsequently, I compared the response in hSHH-stimulated *Gba2*$^{+/+}$ and *Gba2*$^{-/-}$ mEFB to hSHH-stimulated *Gba2*$^{+/+}$ cells treated with NB-DNJ or MZ-21. Strikingly, I observed significantly increased ciliary SMO levels in stimulated *Gba2*$^{-/-}$ cells in all three parameters, which was neither recapitulated by NB-DNJ nor MZ-21 treatment in *Gba2*$^{+/+}$ cells (**Figure 23D-F**). However, SMO localization was significantly reduced in the presence of MZ-21 (**Figure 23F**), which I also observed in stimulated, MZ-21 treated *Gba2*$^{-/-}$ mEFB, indicating an off-target effect. SMO localization did not change under basal conditions: neither *Gba2*$^{-/-}$ nor *Gba2*$^{+/+}$ mEFB treated with NB-DNJ showed significant differences compared to non-treated *Gba2*$^{+/+}$ mEFB (**Figure 23G-I**). Of note, *Gba2*$^{+/+}$ treated MZ-21 cells in the highest 10 % voxel intensity parameter displayed a significant difference. Still, I omitted this result again as an off-target effect because it also appeared in MZ-21 treated *Gba2*$^{-/-}$ cells (**Figure 23H**). These results suggest that the GSL homeostasis is either differentially regulated in mEFB compared to mAFB or that Hh signaling is less prone to changes in the GSL homeostasis in mEFB compared to mAFB.

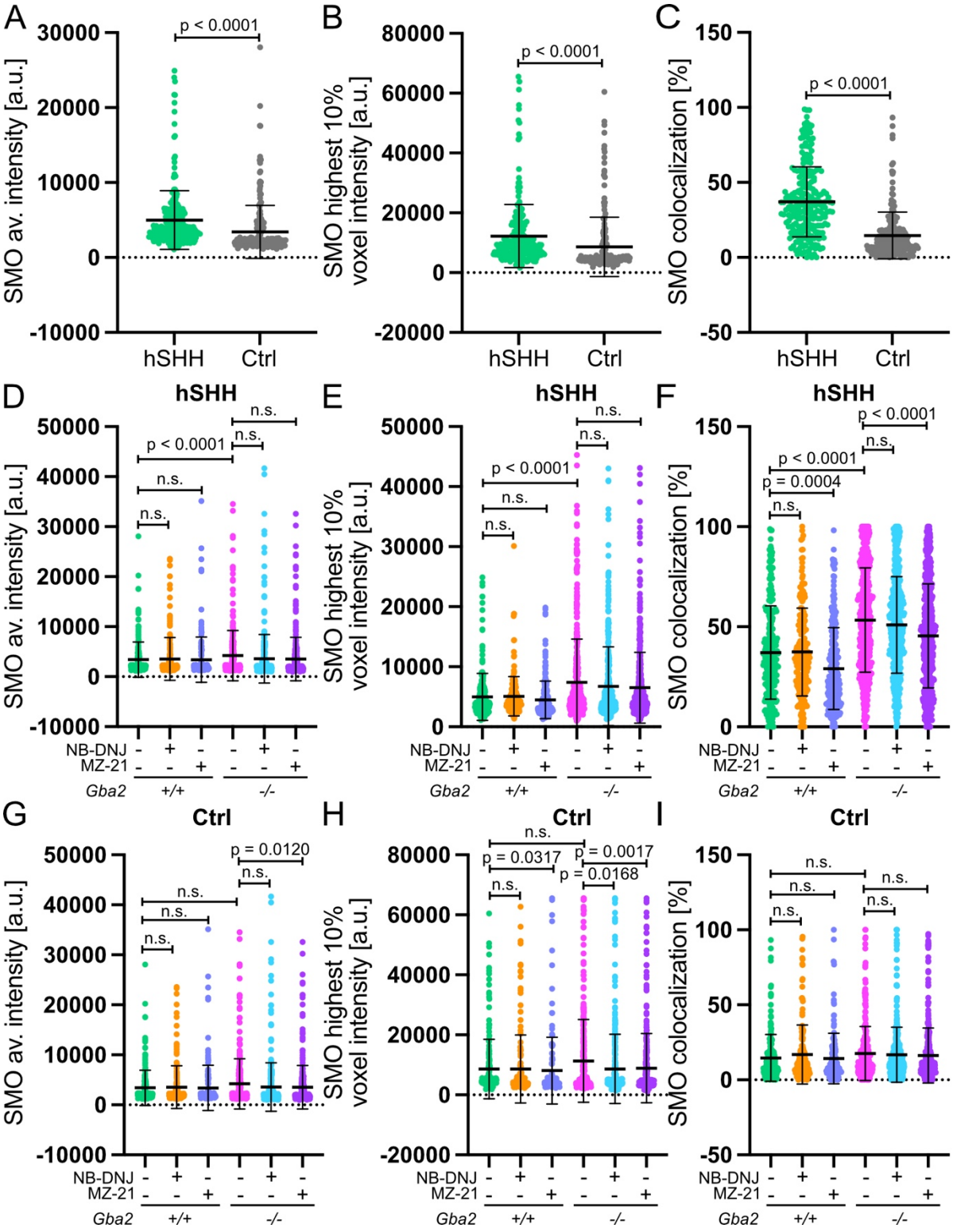

Figure 23: Analysis of ciliary Hh signaling using Smo labeling in ciliated GBA2 mEFB and hSHH stimulation. **A-C:** Smo quantification in ciliated GBA2$^{+/+}$ mEFB treated with 2 nM hShh (hSHH) or H_2O (Ctrl). As datasets were not normality distributed, statistical differences were calculated using a Mann-Whitney test, p-values are indicated. **D-F:** Smo quantification in ciliated GBA2$^{+/+}$ and GBA2$^{-/-}$ mEFB hSHH stimulated cells that were treated with 2 µM NB-DNJ or 30 nM MZ-21 when indicated (+). As datasets were not normality distributed statistical differences were calculated using Dunn´s multiple comparison test, p-values are indicated, n.s. = non-significant **G-I:** Smo quantification in ciliated GBA2$^{+/+}$ and GBA2$^{-/-}$ mEFB non-stimulated cells that were treated with 2 µM NB-DNJ or 30 nM MZ-21 when indicated (+). As datasets were not normality distributed statistical differences were calculated using Dunn´s multiple comparison test, p-values are indicated, n.s. = non-significant. All data are shown as individual data points, with mean ± S.D. from n = 3 independent experiments.

3.3.3 Analyzing Hedgehog downstream signaling using *Ptch1* and *Gli1* expression

To investigate whether the differences in ciliary SMO localization also affect Hh downstream signaling, I analyzed Hh gene expression using reverse-transcription quantitative PCR (RT-qPCR). Amongst others, Hh pathway activity induces *Ptch1* and *Gli1* expression, and based on the SMO localization data, I hypothesized that loss of GBA2 function could result in a change of *Ptch1 or Gli1* expression after Hh stimulation or even under basal conditions (**Figure 24A**) (Goodrich et al., 1996; Harfe et al., 2004; Niewiadomski et al., 2014).

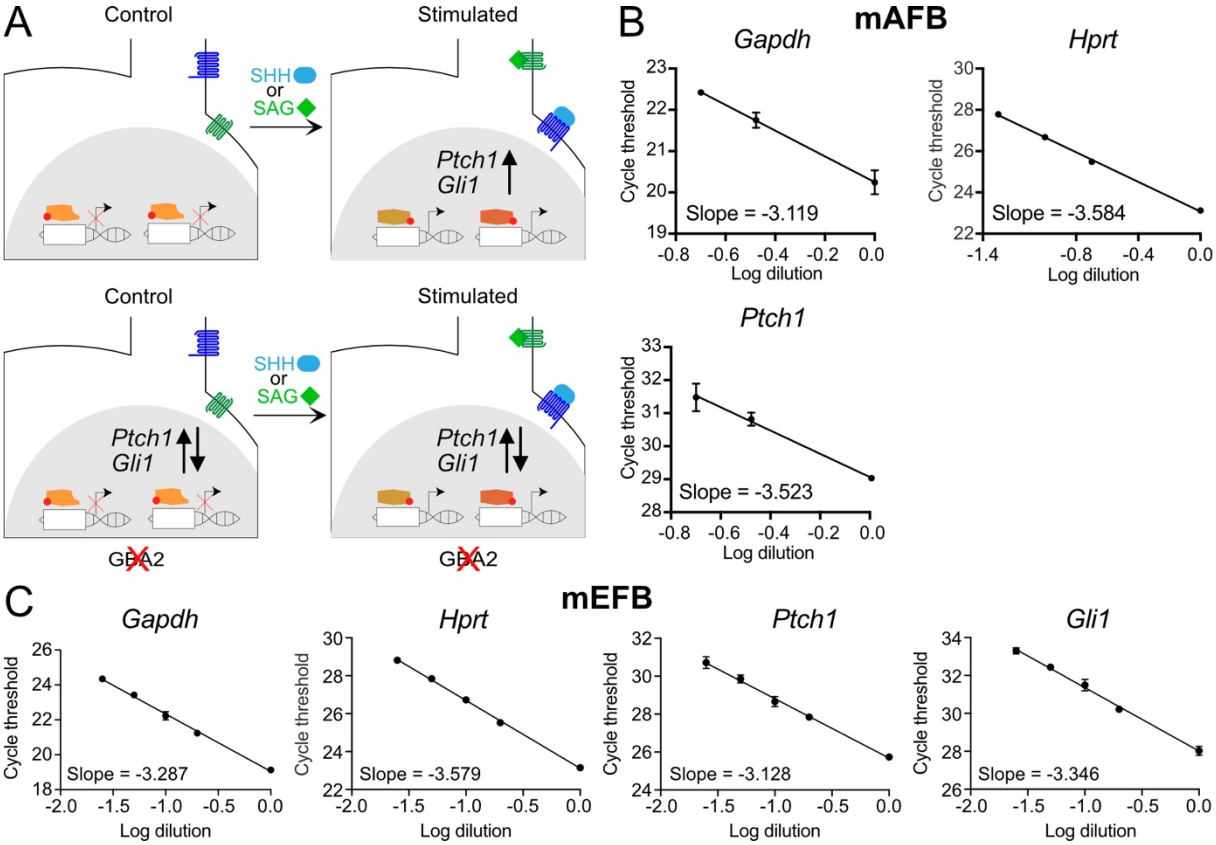

Figure 24: Analyzing ciliary Hedgehog signaling using *Ptch1* and *Gli1* gene expression. A: Scheme depicting regulation of *Ptch1* and *Gli1* gene expression in ciliated cells under control or stimulated conditions (upper row) and a model depicting how the expression might change after GBA2 altered lipid packaging of the ciliary and plasma membrane. **B:** Primer efficiency test (PET) for the used housekeeper genes Gapdh and Hprt, as well as the analyzed gene of interest, Ptch1, using the Bio-Rad iQ5 real-time PCR detection system and mAFB. **C:** Primer efficiency test (PET) for the used housekeeper genes Gapdh and Hprt, as well as the analyzed genes of interest, *Ptch1* and *Gli1*, using the QS6Pro real-time PCR detection system and mEFB. Data are shown as mean ± S.D. of triplicates with a calculated linearly regression line. Primer efficiencies are calculated with the slope of the regression line.

To compare *Ptch1* and *Gli1* expression in the different states, I normalized to the two housekeeping genes (HKGs), *Gapdh* and *Hprt*. Furthermore, to accurately quantify differences in gene expression, I determined the primer efficiency (E) for every primer pair (VanGuilder et al., 2008) using a serial dilution of mAFB or mEFB cDNA. I plotted

the measured cycle threshold (cT) values in a logarithmic scale to their concentrations and calculated the respective regression line to get a primer-pair specific slope (**Figure 24B % C**). The efficiency was then calculated using E [%] = 100 * (-1+$10^{-1/slope}$). The results for mAFB were as follows: E (*Gapdh)* = 109%, E (*Hprt)* = 90%, and E (*Ptch1)* = 92% and for mEFB cDNA: E (*Gapdh)* = 101%, E (*Hprt)* = 90%, E (*Ptch1)* = 100%, and E (*Gli1)* = 99%, which were all in the desired range between 90% and 110.

I analyzed Hh-dependent gene expression for *Ptch1* (mAFB) or *Ptch1* and *Gli1* (mEFB). Both cell types respond with a robust change in gene expression after stimulation for either *Ptch1* (mAFB: 3.4 ± 1.2; mEFB: 3.9 ± 2.2) or *Gli1* (mEFB: 7.0 ± 7.3) (**Figure 25A & E**). Notably, statistical analysis showed no significant changes for Hh-dependent gene expression for mEFB, probably due to the high variability. Nevertheless, in every experiment, hSHH increased the expression of both genes as the individual values after stimulation were always higher in the respective experiment compared to *Gba2*$^{+/+}$ mEFB non-stimulated controls, depicted by the green dotted line (**Figure 25E**). Next, I compared the Hh-dependent gene expression in *Gba2*$^{+/+}$ mAFB to the gene expression in *Gba2*$^{+/+}$ mAFB in the presence or absence of NB-DNJ or MZ-21, as well as to *Gba2*$^{-/-}$ mAFB: Hh-dependent *Ptch1* expression remained unchanged, both when blocking GBA2 activity or after the loss of GBA2 after normalization to non-stimulated *Gba2*$^{+/+}$ (**Figure 25B**) or non-stimulated *Gba2*$^{-/-}$ mAFB (**Figure 25D**). Additionally, *Ptch1* expression in non-stimulated *Gba2*$^{-/-}$ mAFB was slightly, although not significantly, decreased compared to non-stimulated *Gba2*$^{+/+}$ mAFB (**Figure 25C**). Next, I verified this response in mEFB by analyzing *Gli1* and *Ptch1* expression. Comparing NB-DNJ- or MZ-21-treated *Gba2*$^{+/+}$ mEFB and *Gba2*$^{-/-}$ mEFB to *Gba2*$^{+/+}$ mEFB under non-stimulated conditions revealed no significant differences (**Figure 25F & G**), except for *Ptch1* expression in MZ-21-treated *Gba2*$^{-/-}$ mEFB (**Figure 25F**). Because MZ-21 cannot act on GBA2 in *Gba2*$^{-/-}$ cells, I concluded that this result presents an off-target effect. Likewise, comparing NB-DNJ- or MZ-21-treated *Gba2*$^{+/+}$ mEFB and *Gba2*$^{-/-}$ mEFB to *Gba2*$^{+/+}$ mEFB under Hh-dependent gene expression revealed no significant differences, either (**Figure 25H & I**). In summary, both cell types appear to compensate on the transcriptional output level for the GBA2-dependent changes in ciliary SMO localization.

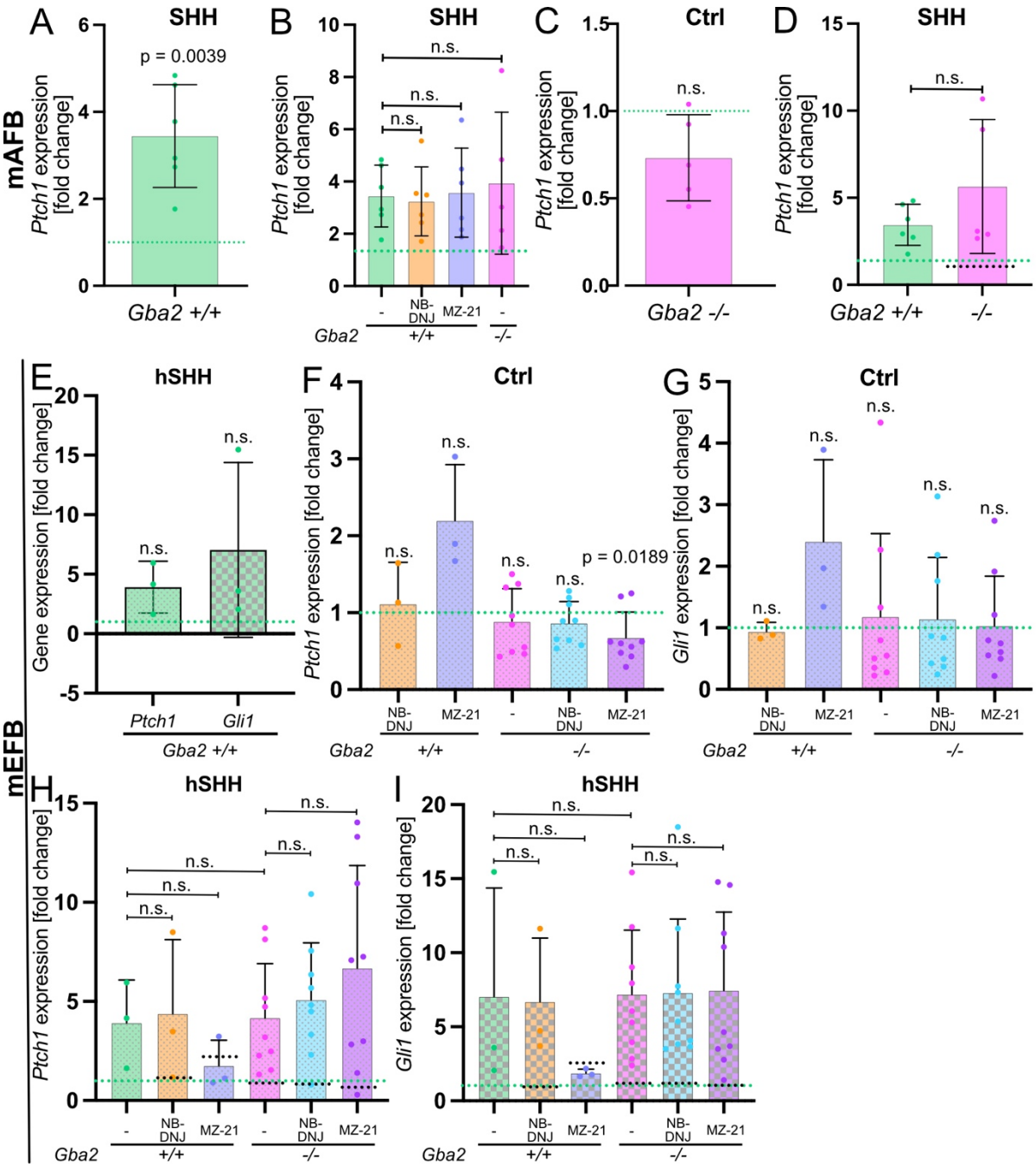

Figure 25: Analyzing ciliary Hedgehog signaling using Hh target gene expression in *Gba2* mAFB and mEFB. **A:** *Ptch1* expression in *Gba2*$^{+/+}$ mAFB after SHH supernatant stimulation normalized to non-stimulated *Gba2*$^{+/+}$ mAFB (depicted by the green-dotted line). **B:** *Ptch1* expression after SHH supernatant stimulation normalized to non-stimulated *Gba2*$^{+/+}$ mAFB (depicted by the green-dotted line) in *Gba2*$^{+/+}$ and *Gba2*$^{-/-}$ mAFB that were treated with 2 µM NB-DNJ or 30 nM MZ-21 when indicated (+). **C:** *Ptch1* expression in non-stimulated *Gba2*$^{-/--}$ mAFB normalized to non-stimulated *Gba2*$^{+/+}$ cells (depicted by the green-dotted line). **D:** *Ptch1* expression after SHH supernatant stimulation in *Gba2*$^{+/+}$ and *Gba2*$^{-/-}$ cells, each normalized to their respective non-stimulated control (depicted by the green- and black-dotted lines, respectively). **E:** *Ptch1* and *Gli1* expression in *Gba2*$^{+/+}$ mEFB after hSHH stimulation normalized to non-stimulated *Gba2*$^{+/+}$ mEFB (depicted by the green-dotted line). **F-G:** *Ptch1* and *Gli1* expression in non-stimulated *Gba2*$^{-/-}$ and *Gba2*$^{+/+}$ mEFB that were treated with 2 µM NB-DNJ or 30 nM MZ-21 when indicated (+) and normalized to non-stimulated *Gba2*$^{+/+}$ mEFB (depicted by the green-dotted line). **H-I:** *Ptch1* and *Gli1* expression in hSHH-stimulated *Gba2*$^{-/-}$ and *Gba2*$^{+/+}$ mEFB that were treated with 2 µM NB-DNJ or 30 nM MZ-21 when indicated (+) and normalized to their respective non-stimuated control (depicted by the green- and black-dotted lines). As data were either normal distributed or too small for normality testing, statistical differences were calculated using a one sample t test or Dunnett's multiple comparison test. Data are shown as column diagrams with mean ± S.D. of 3-6 independent experiments with individual data points, p-values are indicated, n.s. = non-significant.

3.4 Analyzing GSL function in primary cilia signaling using GBA1

Our lab has previously shown that preferably loss of GBA2 changes the order of the plasma membrane (Hamzeh, 2017; Raju et al., 2015). However, not only GBA2, but also GBA1 controls cellular GSL levels. Loss of GBA1 activity leads to accumulation of GlcCer in fibroblasts, mainly in the lysosome and endosomes, but not the plasma membrane or the ER (Fuller et al., 2008; Schonauer, 2017).

3.4.1 Analyzing GBA1-dependent ciliary Hh signaling using SMO labeling and Hh-dependent gene expression

To test whether GBA1-dependent changes in GSL homeostasis alter Hh signaling, I analyzed the SMO localization and Hh-dependent gene expression. The ciliary SMO localization was significantly increased after hSHH stimulation in *Gba1*$^{+/+}$ mEFB (**Figure 26A-C**). However, in *Gba1*$^{-/-}$ mEFB, the ciliary SMO localization was significantly reduced compared to *Gba1*$^{+/+}$ mEFB after hSHH stimulation, as depicted by all the three parameters (**Figure 26D-E**). Comparing non-stimulated *Gba1*$^{-/-}$ mEFB to non-stimulated *Gba1*$^{+/+}$ mEFB revealed a significant reduction in ciliary SMO in two of the three parameters (**Figure 26F-H**), demonstrating that under both basal and stimulated conditions, the ciliary SMO localization was reduced in the absence of GBA1. Milenkovic and colleagues have demonstrated that SMO can enter the cilium laterally through the plasma membrane and internally through recycling endosomes (Milenkovic et al., 2009). As loss of GBA1 activity might immediately increase endosomal GlcCer levels and, in turn, GSL levels, the ciliary SMO dynamics seem to be affected by both, changes in GSL levels in the plasma membrane and in the endosomal system.

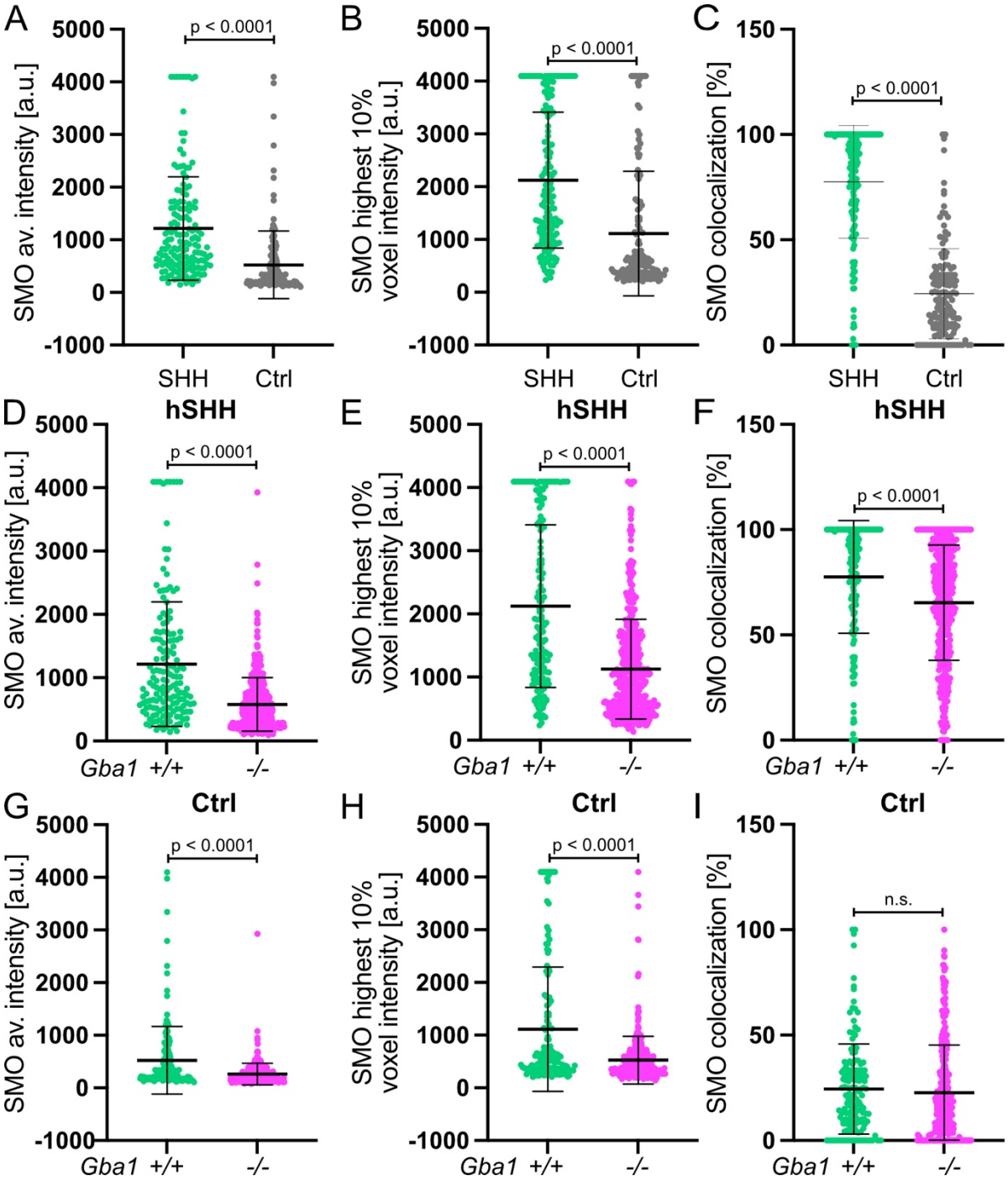

Figure 26: Analysis of ciliary Hh signaling using Smo labeling in ciliated *Gba1* mEFB and hSHH stimulation. **A-C:** Smo quantification in ciliated *Gba1*$^{+/+}$ mEFB treated with 2 nM hShh (hSHH) or H_2O (Ctrl). As datasets were not normality distributed, statistical differences were calculated using a Mann-Whitney test, p-values are indicated. **D-F:** Smo quantification in ciliated *Gba1*$^{+/+}$ and *Gba1*$^{-/-}$ mEFB hSHH stimulated cells. As datasets were not normality distributed statistical differences were calculated using Dunn´s multiple comparison test, p-values are indicated, n.s. = non-significant **G-I:** Smo quantification in ciliated *Gba1*$^{+/+}$ and *Gba1*$^{-/-}$ mEFB non-stimulated cells. As datasets were not normality distributed statistical differences were calculated using Dunn´s multiple comparison test, p-values are indicated, n.s. = non-significant. All data are shown as individual data points, with mean ± S.D. from n = 3 independent experiments.

To reveal whether loss of GBA1 also affects Hh target gene expression, I compared *Ptch1* and *Gli1* expression: in *Gba1*$^{+/+}$ mEFB, I observed a 4.0 ± 3.6 and 15.7 ± 18.3-fold increase in *Ptch1* and *Gli1* expression, respectively that was, however, not significant (**Figure 27A**). *Ptch1* and *Gli1* expression in *Gba1*$^{-/-}$ compared to *Gba1*$^{+/+}$ mEFB under basal conditions was significantly reduced (**Figure 27B**). However, Hh-dependent changes in *Ptch1* and *Gli1* expression were not different between *Gba1*$^{+/+}$ and *Gba1*$^{-/-}$ mEFB (**Figure 27C-D**).

In summary, GBA1-dependent GSL accumulation in mEFB altered the ciliary SMO localization, by reducing SMO levels in the basal and Hh-stimulated state, which translated into a reduced *Ptch1* and *Gli1* expression under basal, but not Hh-stimulated conditions.

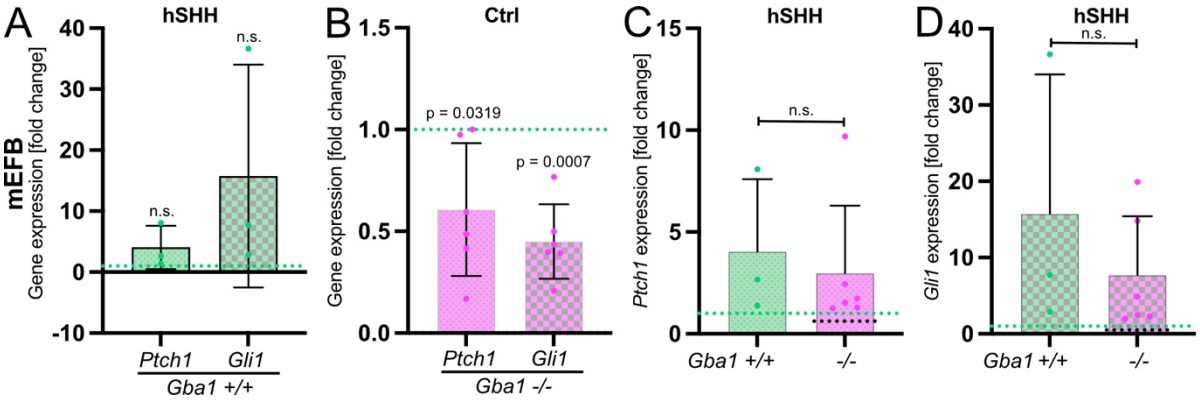

Figure 27: Analyzing ciliary Hedgehog signaling using Hh target gene expression in *Gba1* mEFB. A: *Ptch1* and *Gli1* expression after hSHH stimulation normalized to non-stimulated *Gba1*$^{+/+}$ cells (depicted by the green-dotted line). Dataset numbers were too low for normality testing and statistical differences were calculated using a one sample t test against 1. **B:** *Ptch1* and *Gli1* expression in non-stimulated *Gba1*$^{-/-}$ cells normalized to non-stimulated *Gba1*$^{+/+}$ cells (green-dotted line). As datasets were normal distributed, statistical differences were calculated using a one sample t test against 1. **C:** *Ptch1* expression after hSHH stimulation in *Gba1*$^{+/+}$ and *Gba1*$^{-/-}$ cells normalized to their respective control (depicted by the green- and black-dotted lines). *Gba1*$^{+/+}$ mEFB dataset number was too low for normality testing and statistical differences were calculated using an unpaired t-test. **D:** *Gli1* expression after hSHH stimulation in *Gba1*$^{+/+}$ and *Gba1*$^{-/-}$ cells normalized to their respective control (depicted by the green- and black-dotted lines). *Gba1*$^{+/+}$ mEFB dataset number was too low for normality testing and statistical differences were calculated using an unpaired t-test. Data are shown as column diagrams with mean ± S.D. (in C and D only + S.D.) of 3 independent experiments with individual data points, p-values are indicated, n.s. = non-significant.

Thus, these results indicate that mEFB appear to compensate partly on the transcriptional output level for GBA1-dependent changes in ciliary SMO localization. This is in contrast to the apparent full compensation for GBA2-dependent changes in mEFB and mAFB. Loss of GBA1 activity leads to endosomal GSL accumulation (Fuller et al., 2008), while loss of GBA2 activity increase GSL levels in the plasma membrane (Raju et al., 2015). SMO trafficking occurs through both compartments (Milenkovic et al., 2009), but might not do so in equal terms, which could explain differences in ciliary SMO localization under the absence of either β-glucosidase. Moreover, changes in

ciliary GSL membrane composition might affect SMO function as GSLs were shown to modulate GPCR function in the plasma membrane (Jafurulla and Chattopadhyay, 2015), which points to another cause in the observed differences as GBA1 most likely does not change the GSL membrane composition of primary cilia.

3.5 Analyzing ciliary cAMP signaling

To investigate how cells compensate for the disturbed ciliary protein dynamics, I aimed to analyze Hh pathway activity downstream of SMO re-localization and upstream of target gene expression. I aimed to establish measuring ciliary cAMP dynamics. To this end, I used genetically-encoded, fluorescent cAMP biosensors (hereafter simply referred to as cAMP biosensors) (Kim et al., 2021; Klausen et al., 2019). Using these tools, cAMP signaling has already been studied in the primary cilium by us and others (Jiang et al., 2019; Marley et al., 2013; Moore et al., 2016; Mukherjee et al., 2016; Sherpa et al., 2019; Truong et al., 2021). In general, there are two different categories of cAMP biosensors: 1. Förster Resonance Energy Transfer (FRET)- based biosensors and 2. single fluorescent protein (FP)-based biosensors. Both display intrinsic advantages and disadvantages: FRET is inversely proportional to the sixth power of the distance between donor and acceptor fluorophore (Förster, 1946), whereby it is very sensitive to report on subtle changes. Moreover, FRET-based biosensors are intrinsically ratiometric, which normalizes cell-to-cell and measurement variations and allows to infer absolute cAMP concentrations after calibration (Borner et al., 2011; Correa and Schultz, 2009). However, FRET imaging requires correcting for bleed-through and cross-excitation, resulting in a more complicated set-up than single FPs. In addition, FRET sensors often suffer from low signal-to-noise ratios, majorly only work with donor-acceptor pairs near the blue light spectrum, and cover a broader light spectrum by using two FP (Klausen et al., 2019). Thus, combinations with other fluorescent or optogenetic tools are limited. Single FP-based biosensors are not intrinsically ratiometric but can be fused to another fluorophore to add this feature, whereby they lose the advantage of only having one wavelength for imaging. Still, their set-up remains less complicated as they do not require bleed-through and cross-excitation correction. In my studies, I tried to establish two FRET-based and two single-FP-based biosensors: the mICNBD-FRET (Mukherjee et al., 2016) and AKAR4 (Depry

et al., 2011) FRET-based biosensors and the ratiometric 5-HT_6-mCherry-cADDIS (Moore et al., 2016) and R-FlincA (Ohta et al., 2018) single FP-based biosensors.

3.5.1 Characteristics of the mlCNBD-FRET and AKAR4 FRET-based cAMP biosensors

The mlCNBD-FRET biosensor directly measures cAMP dynamics using the cyclic nucleotide-binding domain (CNBD) of the cyclic nucleotide-gated K^+ channel from *Mesorhizobium loti.* Here, the FRET pair Cerulean (CER) and Citrine (CIT) sandwich the CNBD, whereby donor (CER) illumination results in acceptor (CIT) emission via FRET. The binding of cAMP to the CNBD induces a conformational change, which increases the proximity between the two FP, thereby decreasing FRET (**Figure 28A**) (Mukherjee et al., 2016).

Notably, mlCNBD-FRET has an extraordinarily high affinity for cAMP (K_D = 66 ± 15 nM (Mukherjee et al., 2016)), making it more sensitive than other cAMP biosensors and, thus, favorable to study cAMP dynamics in subcellular compartments. mlCNBD-FRET has already been demonstrated to function in sperm flagella and primary cilia by fusion to the ciliary-localized somatostatin receptor 3 (SSTR3) (Mukherjee et al., 2016). However, SSTR3 as a G_i-coupled GPCR might influence ciliary cAMP dynamics. Thus, we targeted mlCNBD-FRET to the primary cilium using another targeting strategy, which I also adapted for the AKAR4 biosensor. The AKAR4 biosensor is an A-kinase activity reporter that indirectly measures cAMP dynamics by reporting PKA activity (Depry et al., 2011). The Zhang lab designed AKAR4 with the FRET pair CER and circularly permuted (cp) Venus, of which the latter is an improved CIT variant. Circular permutation re-locates the amino- and carboxyl termini to alternative locations on the surface of the protein's 3-dimensional structure without changing the formation of the GFP beta-barrel (Baird et al., 1999; Topell et al., 1999). This preserves its fluorescence but can change the orientation of the fluorescent dipole into a position more favorable for FRET interaction with the donor (van der Krogt et al., 2008). The AKAR4 FRET pair flanks a phosphoamino acid-binding domain and an artificial PKA substrate, which reports a cAMP-dependent increase in PKA phosphorylation by a FRET increase (**Figure 28B**) (Depry et al., 2011). The differences between spectral properties of Venus and CIT are very similar (**Figure 28C**), which is why I established the FRET imaging set-up once for both biosensors.

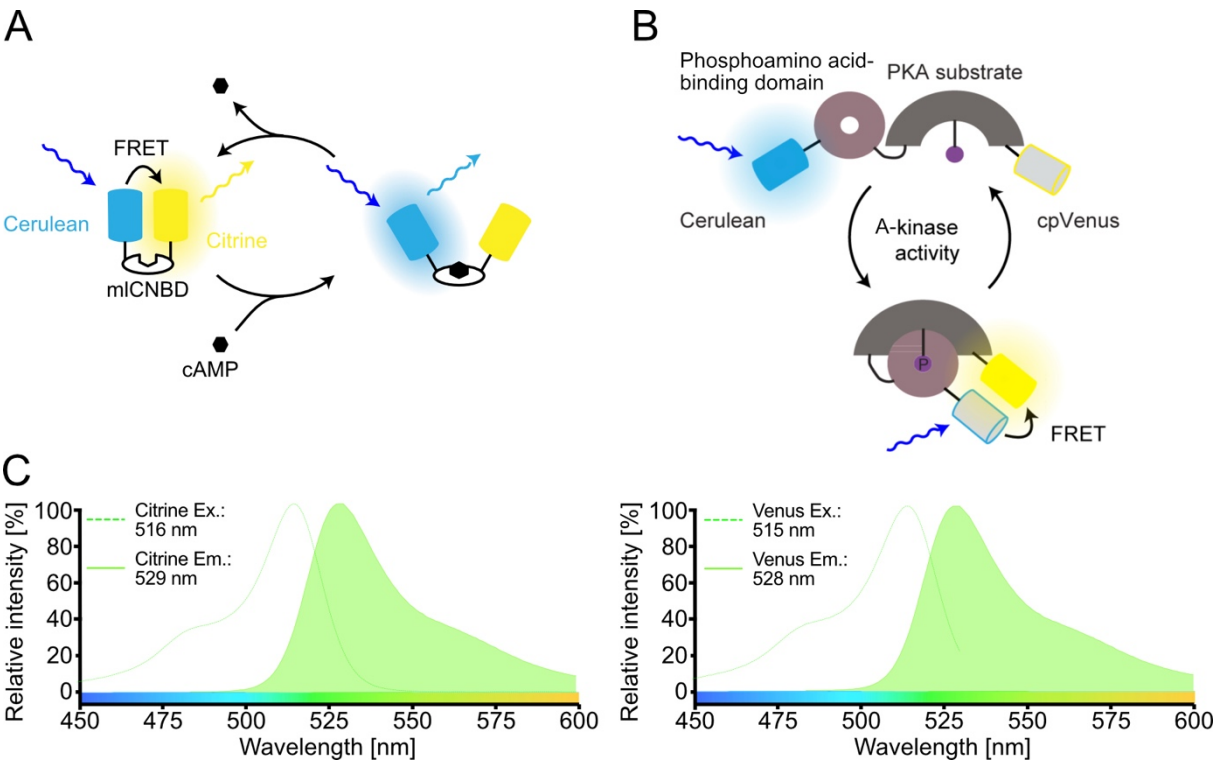

Figure 28: Working principle of the direct cAMP biosensor mICNBD-FRET and the indirect cAMP biosensor AKAR4. A: Binding of cyclic AMP (cAMP) to the cyclic nucleotide-binding domain (CNBD) reduces FRET between the FRET pair Cerulean (donor) and Citrine (acceptor). **B:** cAMP activates PKA (A-kinase) activity, leading to phosphorylation of an artificial PKA substrate by the phosphoamino acid-binding domain, which increases FRET between the donor (Cerulean) and the circularly permutated (cp) acceptor Venus (cpVenus). **C:** Comparison between the spectral properties of Citrine and Venus (graphs adapted from fpbase.org)

3.5.2 Setting up FRET imaging for mICNBD-FRET and AKAR4 using three-cube imaging

For FRET to occur, the donor emission and the acceptor excitation spectra have to overlap. (Förster, 1946). However, in microscopy systems, it is rather difficult to separate the spectral overlap of donor and acceptor (**Figure 29A**). Thus, different measures have to be applied (Erickson et al., 2001; Gordon et al., 1998). "Three-cube FRET" imaging is the method of choice to correct a measured FRET signal: it measures the FRET signal (donor excitation, acceptor emission), as well as the donor (donor excitation donor emission) and the acceptor signal (acceptor excitation acceptor emission) (**Figure 29B**).

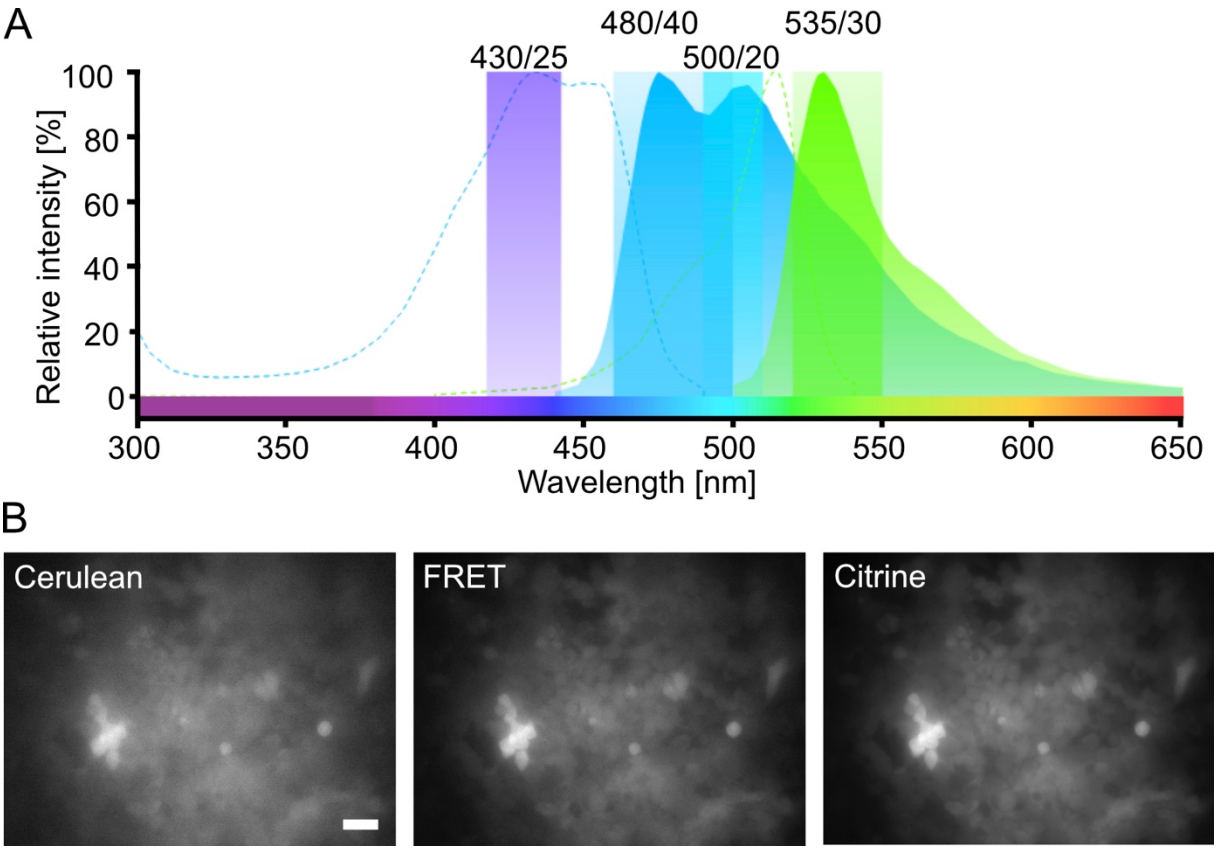

Figure 29: Measuring FRET using three-cube imaging. A: Excitation and emission spectra of Cerulean and Citrine with the corresponding filter set at the CellR imaging system. Blue: Cerulean, green: Citrine, dotted lines: excitation spectra, solid lines: emission spectra. Numbered bars: Excitation and emission filters with the corresponding band-path numbering. **B:** Three-cube imaging in HEK293 cells transfected with mICNBD-FRET. The donor excitation/donor emission channel (Cerulean), donor excitation/acceptor emission channel (FRET), and acceptor excitation/emission channel (Citrine) are shown. Scale bar: 40 µm.

The intensity values of the donor and acceptor channel are then used to calculate a corrected FRET signal (**Equation 2**).

$$\text{Corrected FRET} = \text{FRET} - \alpha \times \text{Cerulean} - \beta \times \text{Citrine}$$

Equation 2: Formula to correct the FRET value using "three-cube FRET" measurement. α x Cerulean represents the bleed-through of donor emission into the FRET channel upon donor excitation and β x Citrine represents the bleed-through of acceptor emission into the FRET channel upon donor excitation.

To obtain the α (donor bleed-through) and β (acceptor cross-excitation) values, I used cells only expressing either CER or CIT. I established three-cube imaging at two set-ups: The widefield Olympus CellR imaging system (see "Live cell imaging" in the Materials and Methods for details) that is easy to handle and allows to characterize biosensors in a whole cell, and the confocal Andor Spinning Disk microscope (see "Live cell imaging" in the Materials and Methods for details) that allows measuring ciliary cAMP dynamics. At the CellR, CER displayed a high bleed-through signal in the FRET channel (**Figure 30A**) whereas CIT showed a low cross-excitation signal in the FRET channel (**Figure 30B**). In turn, the calculated bleed-through value α was 0.76 for the exemplary image and 0.75 as the determined average value from three independent experiments, and the cross-excitation value β was 0.02 for the exemplary image and the determined average value (**Figure 30C**).

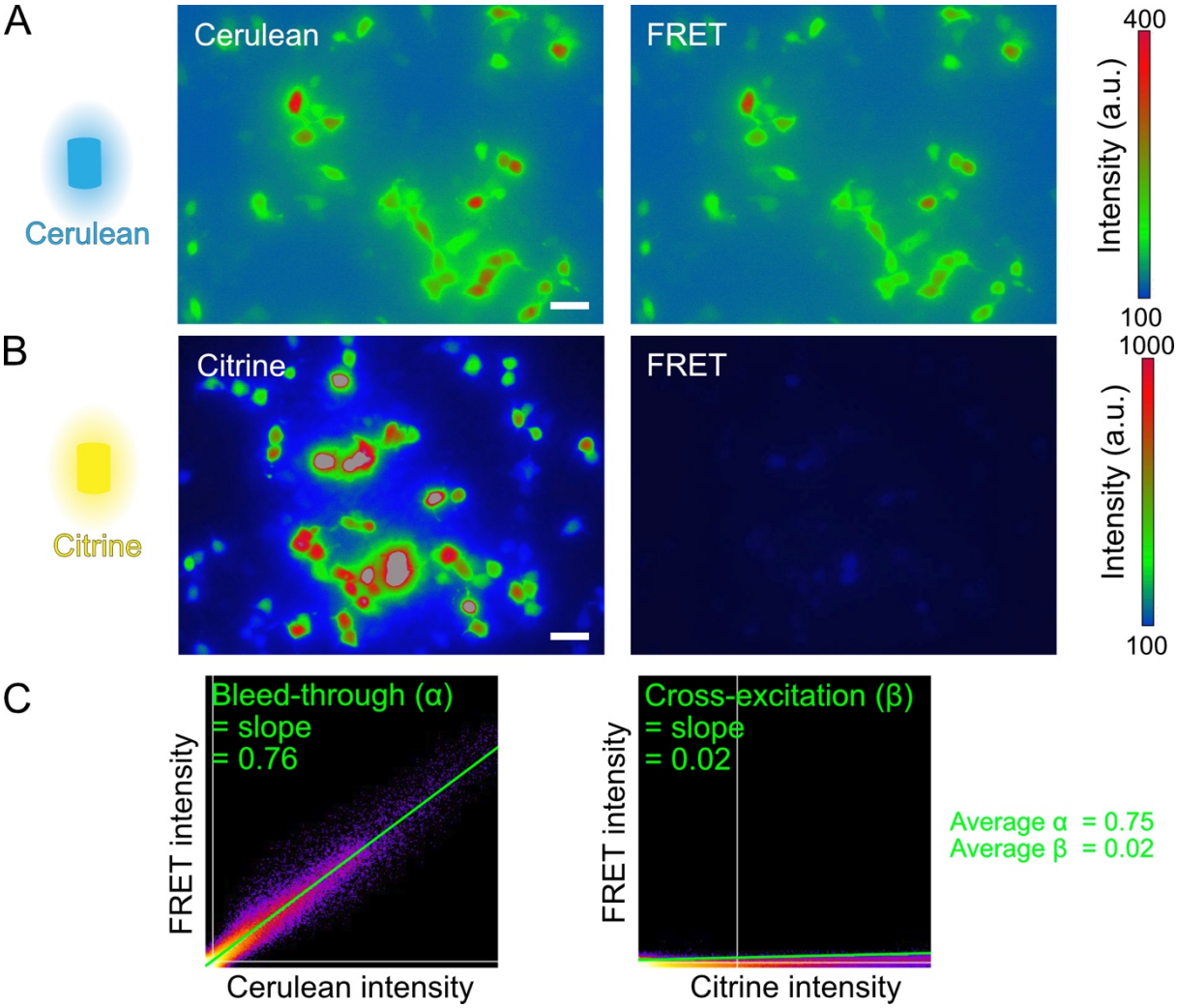

Figure 30: FRET correction at the CellR imaging system. A: HEK293 cells transfected with donor only (Cerulean). Fluorescent levels were measured in the Cerulean (excitation: 430/25 nm, emission: 480/40 nm) and FRET (excitation 430/25 nm, emission: 535/30 nm) channel. Scale bar: 40 µm. **B:** HEK293 cells transfected with acceptor only (Citrine). Fluorescent levels were measured in the Citrine (excitation: 500/20 nm) and FRET channel. Scale bar: 40 µm. **C:** Correction values for bleed through (α) and cross-excitation (β) were determined by the slope of the regression lines that was calculated according to the co-localization of the indicated channels. For images shown in (A) and (B), the values were 0.76 and 0.02, respectively. The average values determined for α and β were 0.75 and 0.02, respectively (n = 6 technical replicates from 3 independent experiments).

We decided to use the Andor Spinning Disk microscope (ref mat-met) as fast image acquisition is crucial for ciliary imaging: Although the primary cilium is immotile, it moves during image acquisition in live-cell imaging due to Brownian motion in the solution of the extracellular space. At the Spinning Disk, I determined the α and β values using ciliary targeted CER and CER (mNphp3(201)-Cerulean, and mNphp3(201)-Citrine, respectively) and CiliaQ 3D analysis (**Figure 31**). Analysis of the α value showed a bleed-through value α of 0.70 (**Figure 31A**). For the β value, I measured no specific signal, leading to the conclusion that cross-excitation is vanishingly low, and, therefore, I omitted measuring the Citrine channel for FRET correction at the Spinning Disk microscope (**Figure 31B**).

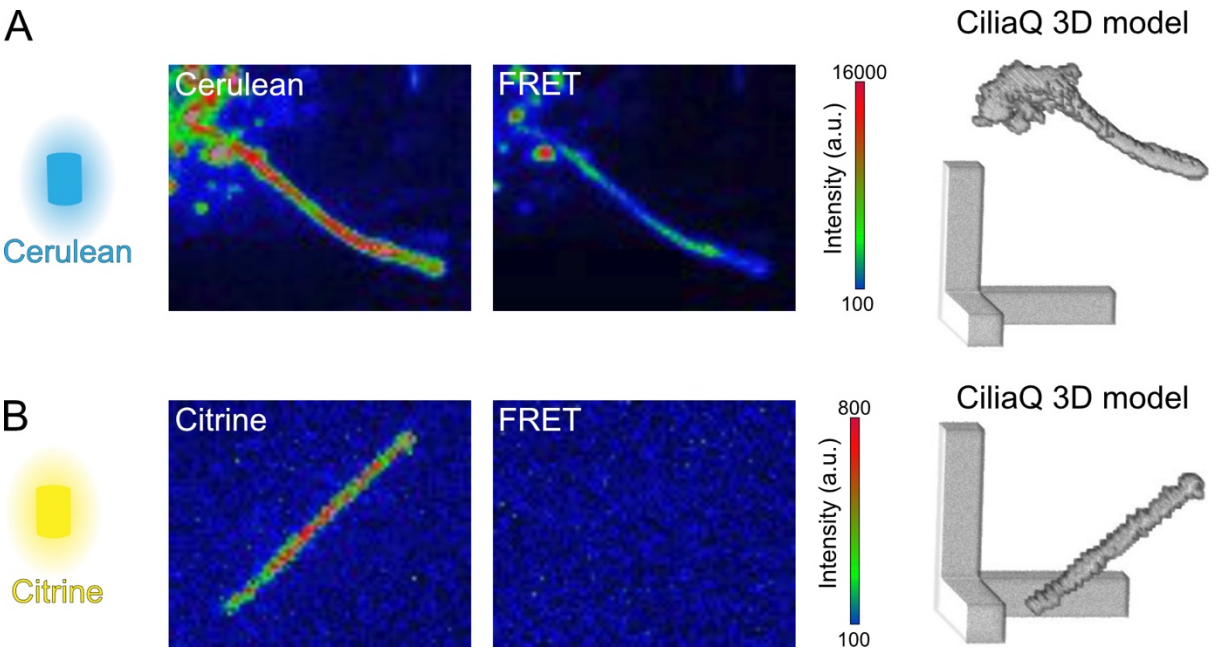

Figure 31: FRET correction values at the Andor Spinning Disk imaging system. A: mIMCD-3 cells transfected with the donor only (mNphp3-Cerulean). Fluorescent levels were measured in the Cerulean (excitation: 445 nm, emission: 475/25 nm) and FRET (excitation: 445 nm, emission: 550/49 nm). Scale bar: 10 µm. The average bleed through factor was determined with α = 0.70 (n = 2 replicates from one experiment). **B:** mIMCD-3 cells transfected with the acceptor only (mNPHP3-Citrine). Fluorescent levels were measured in the Citrine (excitation: 515 nm, emission: 550/49 nm) and FRET channel. The cross-excitation factor was determined with β = 0, as there was no signal above background level detectable in the FRET channel. Scale bar: 10 µm.

3.5.3 Functional characterization of mICNBD-FRET and AKAR4 targeting strategy using HEK293 cells

Targeting biosensors to subcellular localizations is challenging, and protein fusion to targeting sequences often alters the biosensor properties (Surdo et al., 2017). Thus, I first verified whether our targeting strategy does not impair mICNBD-FRET or AKAR4 function using HEK293 cells on the CellR imaging system. It has been shown that the first 201 amino acids of the mouse nephrocystin 3 protein (mNPHP3(201)) are sufficient for ciliary localization (Nakata et al., 2012). Thus, we fused mNPHP3(201) to the N-terminus of mICNBD-FRET or AKAR4-NES, a variant of AKAR4 bearing a nuclear export signal (NES) at the C-terminus, to generate the ciliary-targeted mNphp3(201)-mICNBD-FRET and mNphp3(201)-AKAR4-NES cAMP biosensors. To verify their performance, I also measured the non-targeted mICNBD-FRET and AKAR4-NES in HEK293 cells. After increasing cAMP levels by stimulating with 20 µM of the selective β-adrenergic agonist Isoproterenol Hydrochloride (Isoproterenol) (**Figure 32A&C**), the CER intensity increased, whereas FRET decreased for mICNBD-FRET and vice versa for AKAR4, which is best seen in the CER / FRET (mICNBD-

FRET) or FRET / CER (AKAR4) ratio (**Figure 32B&D**). I used these different ratios to correlate increasing cAMP levels with an increased ratio for both sensors.

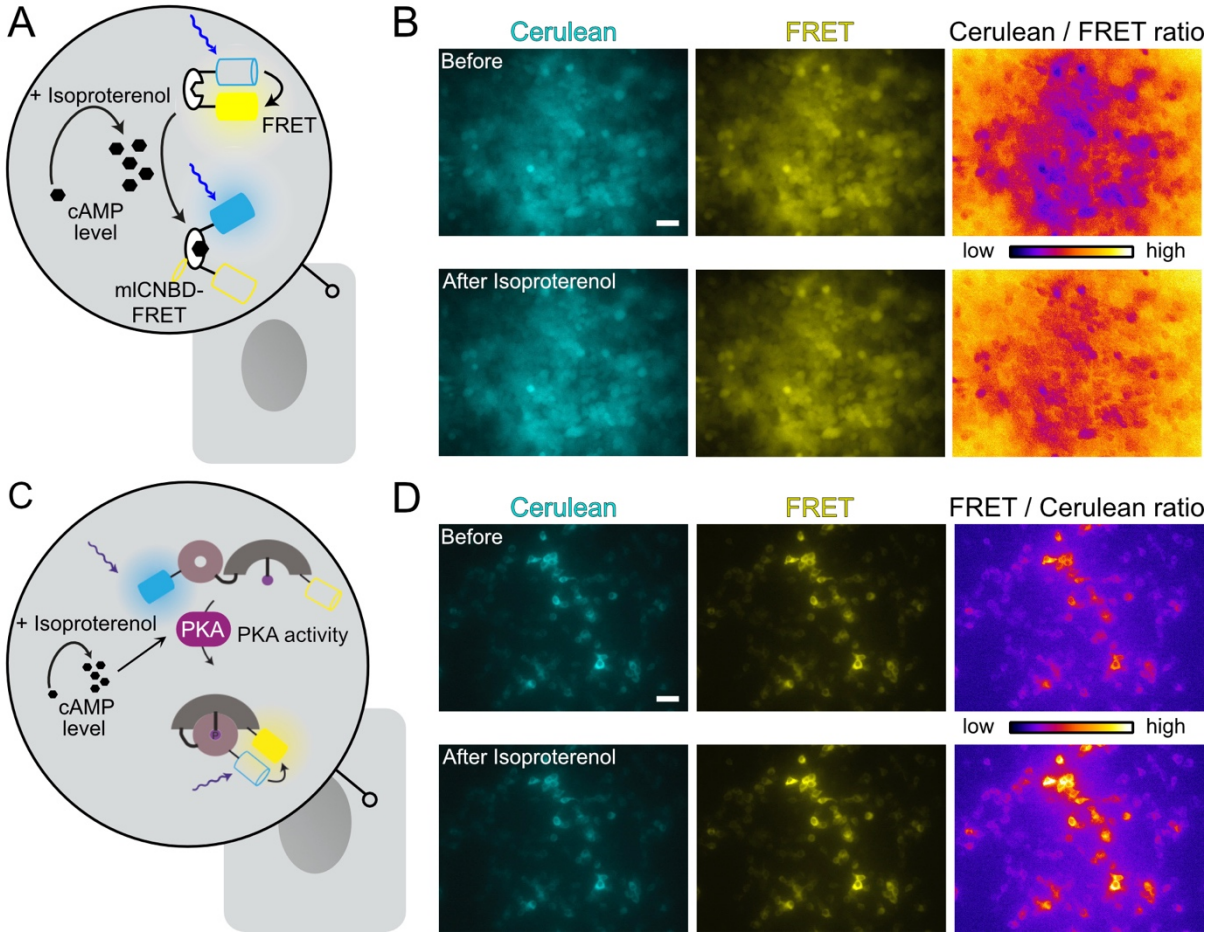

Figure 32: Set-up to characterize mICNBD-FRET and AKAR4 in non-ciliated HEK293 cells. A: Schematic overview of the functional assay in non-ciliated HEK293 cells. **B:** FRET imaging in the cytosol of HEK293 mICNBD-FRET cells. **C:** Schematic overview of AKAR4 imaging in non-ciliated HEK293 cells. **B:** FRET imaging in HEK293 cells transfected with *AKAR4-NES*. Cerulean and FRET are shown before and after stimulation with 20 µM Isoproterenol. Scale bars: 40 µm.

For time-course quantification, I extracted the intensity values of single cells using Fiji and calculated the corrected FRET value according to **Equation 2**, followed by baseline normalization and plotting the data as a ratio to the CER signal (for details, see “FRET imaging at the CellR System”). The mICNBD-FRET biosensor reported an Isoproterenol-induced cAMP increase, which was absent in the control (buffer) (**Figure 33A**). The AKAR4-NES sensor reported a transient increase in PKA phosphorylation, which was absent in the control (**Figure 33C**). In contrast, the mNphp3(201)-mICNBD-FRET did not show a change in FRET upon Isoproterenol stimulation (**Figure 33B**), and the FRET response for the mNPHP3(201)-AKAR4-NES after Isoproterenol stimulation was also reduced (**Figure 33D**). In line with my results, Mukherjee and colleagues reported a 40% increase in the ratio for the untargeted

mlCNBD-FRET sensor, which was reduced to 25% after N-terminal SSTR3 fusion (Mukherjee et al., 2016). Furthermore, we observed and tackled similar problems for other proteins, i.e., optogenetic tools, whose functions were also diminished upon N-terminal fusion to a ciliary targeting sequence (Hansen et al., 2020). (Moore et al., 2016).

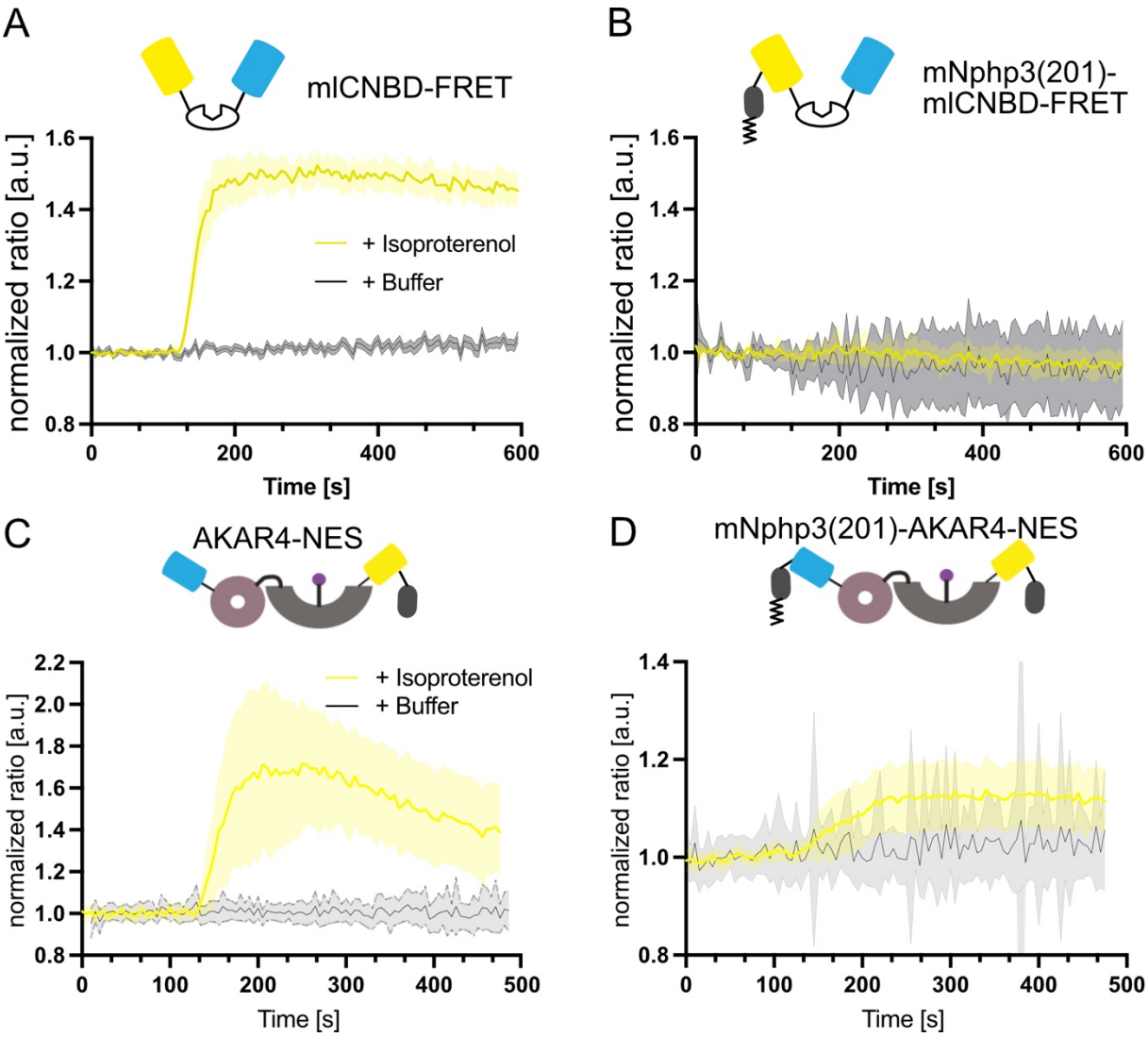

Figure 33: Functional characterization of the mNPHP3(201) ciliary-targeting strategy for FRET-based cAMP biosensors. A-B: FRET imaging under control (+ Buffer) conditions or after stimulation with 20 µM Isoproterenol (+ Isoproterenol) in HEK293 mlCNBD-FRET cells (C) or in HEK293 cells transfected with mNphp3(201)-mlCNBD-FRET of n = 3 independent experiments. Figures modified from (Hansen et al., 2020) **C-D:** FRET imaging under control (+ Buffer) or after stimulation with 20 µM Isoproterenol (+ Isoproterenol) in HEK293 mlCNBD-FRET cells transiently expressing AKAR4-NES (B) or mNPHP3(201)-AKAR4-NES (C). Data are shown as mean (solid line) ± S.D. (dotted line) of n = 3 independent experiments, 30-90 cells per experiment. Stimulus addition at 120 s.

3.5.4 Functional characterization of R-FlincA targeting strategy using HEK293 cells and optogenetics

Single FP biosensors depict a different topology. I wondered whether N-terminal mNPHP3(201) fusion also interferes with R-FlincA function, as the cADDis sensor was well characterized to not show alteration upon N-terminal 5-HT_6 fusion (Moore et al., 2016). R-FlincA consists of the PKA RIα subunit and cpmApple, inserted between amino acid positions 218 and 219 (in PKA RIα). Upon cAMP binding, the cpmApple fluorescence increases (**Figure 34A**) (Ohta et al., 2018). R-FlincA operates in the yellow- to red-light spectrum with a peak excitation at 567 nm and peak-emission at 592 nm (**Figure 34B**). In turn, R-FlincA can be combined with optogenetic tools that operate in the blue light range, i.e., the bacterial photoactivated adenylyl cyclase (bPAC), which synthesizes cAMP from adenosine triphosphate (ATP) after exposure to blue light stimulation (Stierl et al., 2011). In contrast to pharmacological stimuli, bPAC allows to increase cAMP in a spatially and temporally controlled manner. To test whether R-FlincA can monitor cAMP changes evoked by photo-activation of bPAC, I co-expressed R-FlincA and GFP-tagged bPAC (bPAC-GFP) in HEK293 cells (**Figure 34C**). I imaged the R-FlincA fluorescence on the CellR set-up before and after exposing the cells to a white-light stimulus. At the end of the experiment, I identified the cells based on the cpmApple and GFP fluorescence to determine cells co-expressing R-FlincA and bPAC-GFP. Indeed, the R-FlincA fluorescence increased after light exposure in cells expressing both constructs (**Figure 34D**). Interestingly, in cells displaying a high GFP fluorescence and, therefore, putatively high bPAC-GFP expression, R-FlincA did not show a response (data not shown). This might be due to the bPAC "dark" activity in the absence of light (Stierl et al., 2011): The more bPAC-GFP is expressed in the cell, the more cAMP is produced even in the absence of light, increasing the intracellular cAMP concentration and saturating the sensor. R-FlincA has a dissociation constant for cAMP of 300 nM with a dynamic range of 100 µM (Ohta et al., 2018). In resting cells, the free intracellular cAMP has been estimated at around 1 µM, but bPAC dark activity in cells with high expression levels might very well exceed the dynamic range of R-FlincA (Koschinski and Zaccolo, 2017). Thus, I only analyzed R-FlincA intensity values in single cells with low bPAC-GFP expression and did a baseline normalization (for details, see “R-FlincA imaging at the CellR System”). As a control, I used an R-FlincA mutant (R-FlincA_mut), which does not bind cAMP (Ohta

et al., 2018). R-FlincA reported a transient increase in cAMP levels after light-stimulation of bPAC at 120 s, which was absent in R-FlincA_mut measurements (**Figure 34E**). Although I observed prominent photobleaching of R-FlincA_mut fluorescence after light exposure (**Figure 34E**), my results demonstrate that I combine optogenetic manipulation of intracellular cAMP levels with measuring cAMP dynamics using a single FP cAMP biosensor R-FlincA. Next, to target R-FlincA to primary cilia, I fused it to mNPHP3(201) to generate the ciliary-targeted mNphp3(201)_R-FlincA. I verified its performance as described above for R-FlincA: mNphp3(201)_R-FlincA fluorescence was stable at baseline without showing photobleaching but dropped instantaneously at 120 s upon white-light exposure and then showed an increase over time to reach a steady-state (**Figure 34F**). Of note, the drop in fluorescence right after white light exposure was most likely a measuring artifact. In conclusion, N-terminal mNPHP3(201) fusion also alters R-FlincA characteristics but does not fully impair sensor function as observed for the mICNBD-FRET sensor.

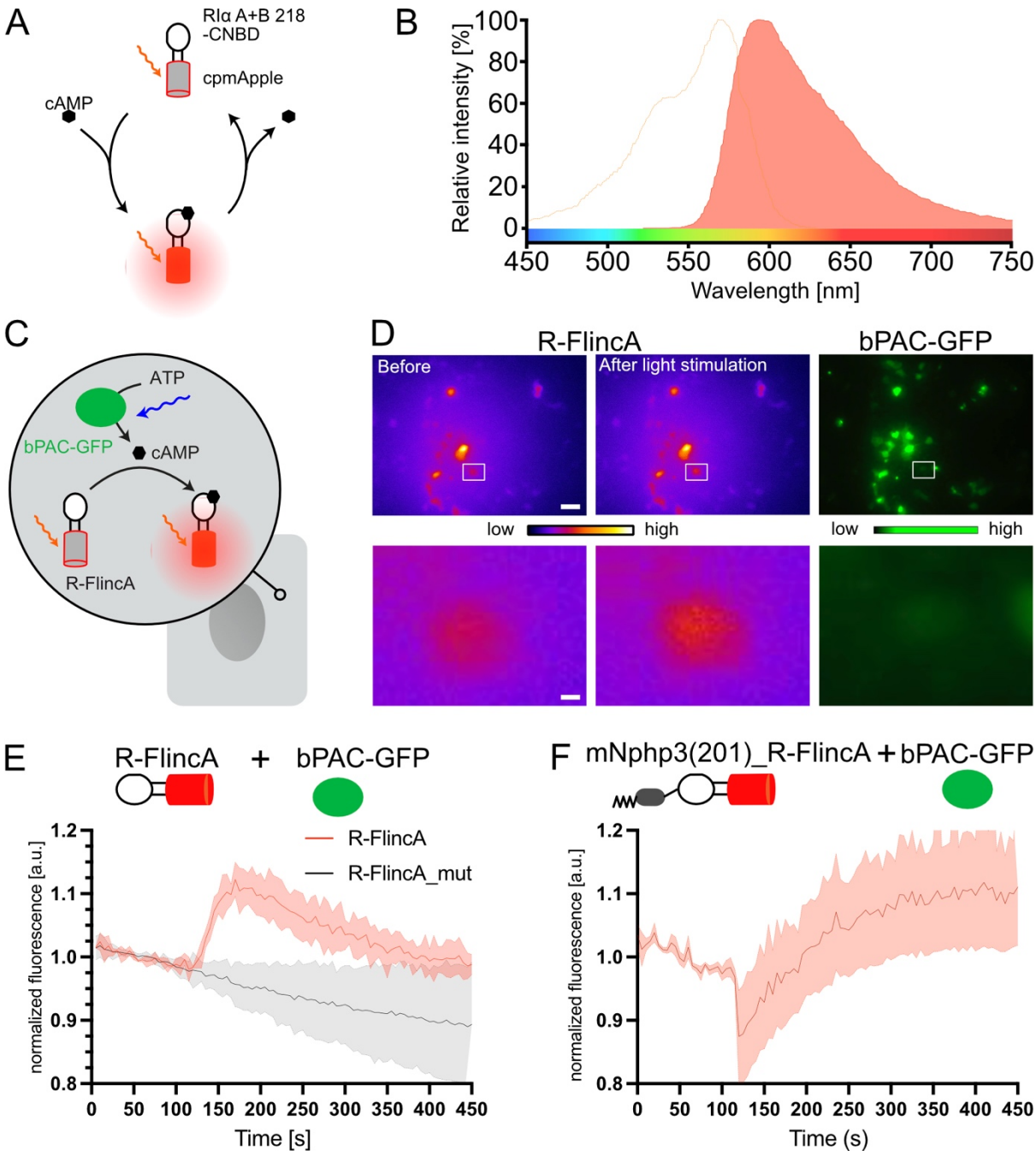

Figure 34: Functional characterization of the single fluorescent protein (FP) cAMP biosensor R-FlincA in non-ciliated HEK293 cells. A: Conformational changes of the RIα CNBD subunit after cAMP binding lead to changes in mApple fluorescence. **B:** Excitation and emission spectrum of mApple (graph adapted from fpbase.org). **C:** Schematic overview of R-FlincA imaging in non-ciliated HEK293 cells transfected with R-FlincA and bPAC-GFP. **D:** Single FP imaging in HEK293 cells transfected with R-FlincA and bPAC-GFP. Cells have been stimulated with a 1 second white-light pulse. Lower row shows the inset depicted in the upper row. Only some cells showed a change in fluorescence after light stimulation, also both constructs were expressed at the same time. Scale bars: 40 µm (upper panels) and 4 µm (lower panels). **E-F:** Time course of the normalized mean change in R-FlincA fluorescence (solid line) ± S.D. (dotted line) in HEK293 cells transfected with bPAC-GFP and R-FlincA, or the cAMP insensitive mutant R-FlincA_mut (E), or bPAC-GFP and cilia-targeted mNphp3(201)_R-FlincA (F). Only cells with putative low bPAC-GFP expression were analyzed. White-light stimulation at 120 s. Data shown of n = 1 experiment with 3-12 cells per experiment.

3.5.5 Nanobody-directed ciliary targeting to preserve sensor function

To circumvent the problems observed after N-terminal fusion, I teamed up with Jan Hansen in our lab and together, we developed an alternative targeting strategy based on ciliary-targeted nanobodies, which we published as shared co-first authors in *eLife* (Hansen et al., 2020). We co-expressed ciliary-targeted nanobodies, which bind fluorescent proteins (i.e., mCherry or CER and CIT as in mICNBD-FRET) in the cytosol and drag them into the cilium. Thereby, we avoid N-terminal fusion of the target protein (**Figure 35A**).

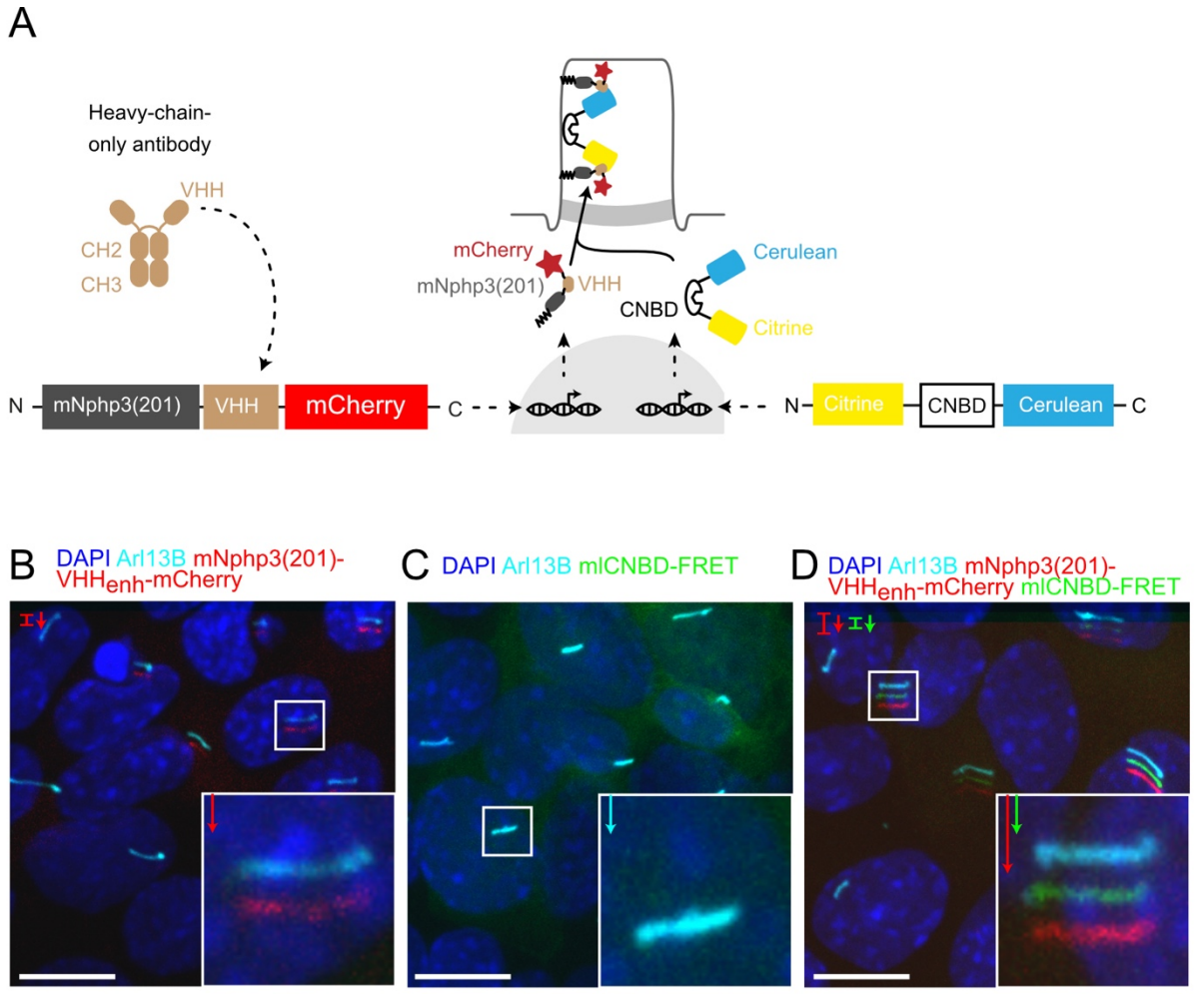

Figure 35: Targeting mICNBD-FRET to the primary cilium using nanobodies. A: Schematic overview of the targeting approach. The VHH was fused to the C terminus of mNphp3(201) for ciliary localization and to the N terminus of mCherry for detection. mICNBD-FRET is co-expressed and recognized by the VHH domain via its fluorophores Cerulean and Citrine. Binding of the nanobody to mICNBD-FRET is expected to result in ciliary localization. **B:** Localization of the mNPHP3(201)-$VHH_{enhancer}$-mCherry anti GFP (mNPHP3(201)-VHH_{enh}-mCherry) to primary cilia. **C-D:** Localization of mICNBD-FRET in the absence (C) or presence (D) of mNphp3(201)-VHH_{enh}-mCherry. DNA is labeled with DAPI (blue), cilia are labelled with Arl13b (Cyan), mNphp3(201)-VHH_{enh}-mCherry fluorescence (red), and mICNBD-FRET fluorescence (green) is shown. Scale bar: 10 µm. Arrows and colored scale bars depict a pixel shift of the respective colored channel. The white inset in the corner shows a magnified view of the small white box. Figure modified from (Hansen et al., 2020).

First, we verified the localization of the ciliary-targeted nanobody recognizing CER and CIT (mNphp3(201)-VHH$_{enh}$-mCherry) in primary cilia of mIMCD-3 cells using ICC (**Figure 35B)**: In the absence of the ciliary-targeted nanobody, mICNBD-FRET was evenly distributed throughout the cell soma and was absent from primary cilia (**Figure 35C**). Co-expression of the ciliary-targeted nanobody with mICNBD-FRET resulted in both proteins being localized in primary cilia with a concomitant loss of mICNBD-FRET localization in the cytoplasm (**Figure 35D**).

Next, I verified mICNBD-FRET sensor function in the presence of mNphp3(201)-VHH$_{enh}$-mCherry in HEK293 cells after increasing cAMP levels by stimulating with 20 µM Isoproterenol (**Figure 36A**).

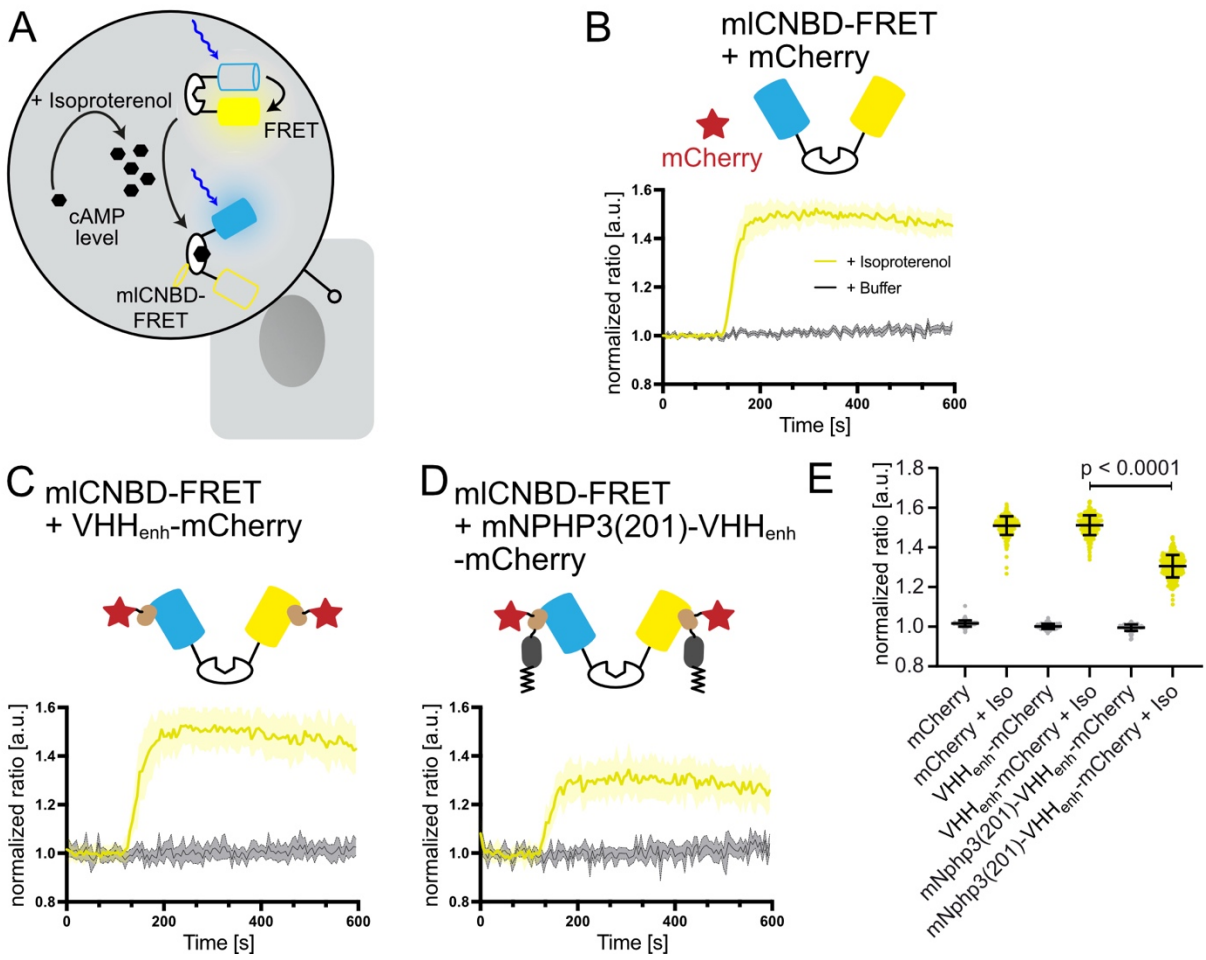

Figure 36: Functional characterization of the cilia-targeted mICNBD-FRET biosensor in non-ciliated cells. A: Schematic overview of the mICNBD-FRET biosensor in non-ciliated HEK293 cells**. B-E:** FRET imaging under control (+ Buffer) or after stimulation with 20 µM Isoproterenol (+ Isoproterenol) in HEK293 mICNBD-FRET cells co-transfected with mCherry (B), in HEK293 mICNBD-FRET cells co-transfected with mNPHP3(201)-Vhh$_{enh}$-mCherry (C), or in HEK293 mICNBD-FRET cells co-transfected with Vhh$_{enh}$-mCherry (D). Data are shown as mean (solid line) ± S.D. (dotted line) of n = 3 independent experiments, 30-90 cells per experiment. Stimulus addition at 120 s. F: Comparison of maximal change for data shown in (B-E). Data are presented as individual data points and mean ± S.D.; p-value calculated using an unpaired, two-tailed Mann-Whitney test as indicated. Figure modified from (Hansen et al., 2020).

As a first control, I analyzed mICNBD-FRET function in the presence of mCherry only and observed a robust increase in the FRET ratio upon stimulation with Isoproterenol (**Figure 36B**). As a second control, I analyzed mICNBD-FRET function in the presence of a non-ciliary targeted nanobody, VHH_{enh}-mCherry and saw the same response (**Figure 36C**). Strikingly, co-expression with mNphp3(201)-VHH_{enh}-mCherry only marginally decreased the change in FRET of mICNBD-FRET (**Figure 36D-F**). In conclusion, nanobody-directed targeting of mICNBD-FRET to cilia circumvents loss of protein function occurring after direct mNPHP3(201) N-terminal fusion and is therefore ideally suited to measure ciliary cAMP dynamics.

3.5.6 Establishing FRET imaging for ciliary imaging

Besides determining bleed-through and cross-excitation values for the Andor Spinning Disk microscope that I did before, ciliary FRET imaging requires further establishment for proper analysis: For further establishing the set-up, I used our nanobody-directed ciliary targeting for mICNBD-FRET (**Figure 37A**). A Spinning Disk microscope is a confocal microscope that uses several fixed pinholes on a fast-spinning disk instead of one adjustable pinhole in front of a detector. As a consequence, image acquisition is faster. However, more light exposes the probe, leading to photobleaching, and the fixed pinholes result in larger optical sections with more out-of-focus light (**Figure 37B**). I used CiliaQ to analyze cAMP biosensor fluorescence: CiliaQ failed to reconstruct cilia with a low signal-to-noise ratio due to too low laser intensities (**Figure 37C**), but using too high laser intensities resulted in donor photobleaching over time, which led to measuring artifacts (**Figure 37D**). In the end, 18 % laser intensity resulted in a sufficient signal-to-noise ratio for CER and FRET intensity reconstruction without photobleaching (data not shown) and was used for subsequent FRET-based cAMP biosensors measurements on this instrument.

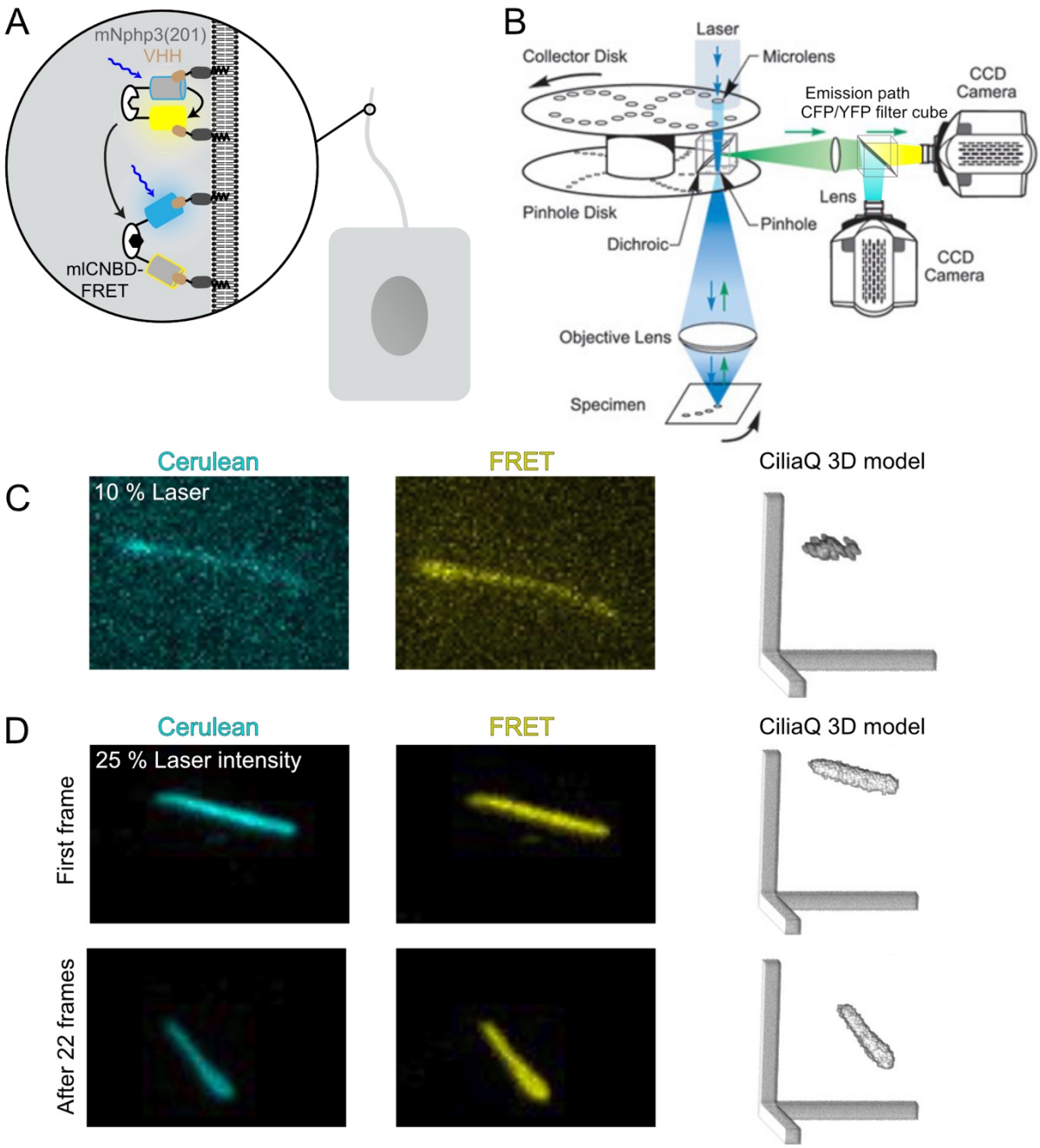

Figure 37: Establishing live cell imaging of the cilary-targeted mICNBD-FRET sensor in ciliated mIMCD-3 cells. A: Schematic overview of the imaging conditions. **B:** Schematic overview of the Spinning Disk confocal microscopy system. The system allows for fast 2 channel confocal imaging of large volumes. Imaged modified from (Nelson et al., 2010). **C-D:** For fast imaging, the exposure time is limited and signal quality has mainly to be adjusted with laser intensity. Choosing a laser intensity too low does not allow to record cilia with sufficient intensity for 3D modeling (C), which is necessary for proper signal evaluation.Laser intensity too strong leads to bleaching over time (D). Scale bars: 10 µm. 18% laser intensity was determined to be the optimal setting for subsequent imaging.

3.5.7 Functional characterization of ciliary-targeted cAMP biosensors

It has already been proposed that the R-FlincA sensor might not be feasible to measure cAMP dynamics in subcellular compartments because it is too dim (Ohta et al., 2018). Still, ciliary-targeted proteins accumulate in the cilium, thereby increasing their local

concentration. Indeed, recently, Truong and colleagues recently measured cAMP dynamics in primary cilia using the even dimmer predecessor of R-FlincA, pink-Flamindo (Truong et al., 2021). I first verified the performance of mICNBD-FRET in the presence of mNphp3(201)-VHH$_{enh}$-mCherry in mIMCD-3 cells on the Spinning Disk set-up after stimulation with 250 µM of the broad phosphodiesterase-inhibitor 3-Isobutyl-1-methylxanthine (IBMX) (**Figure 38A**). Stimulation with IBMX increased the Cerulean / FRET ratio, while control stimulation with buffer did not change the ratio (**Figure 38B & C**). However, I could not measure changes in mNPHP3(201)_R-FlincA fluorescence in ciliated mIMCD-3 cells (data not shown).

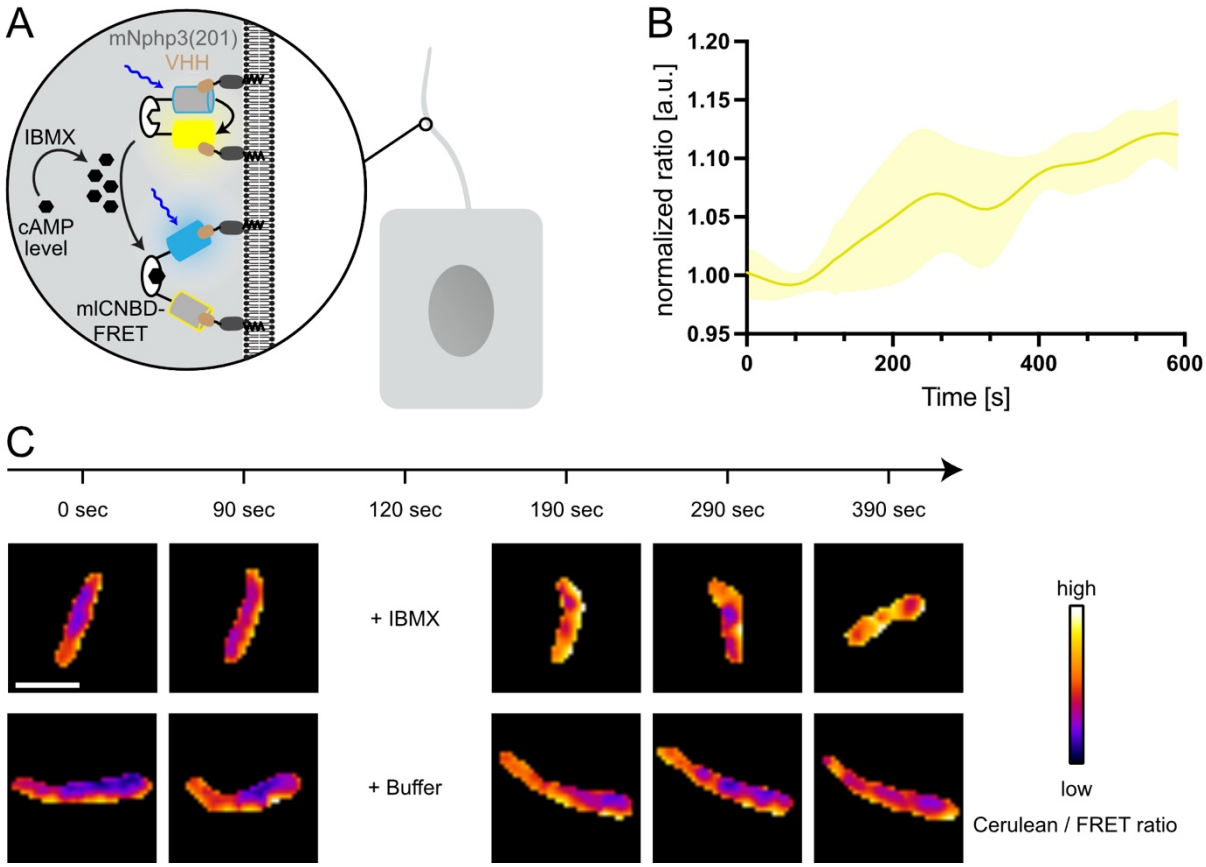

Figure 38: Functional characterization of the nanobody-targeted mICNBD-FRET biosensor in ciliated cells. **A:** Schematic overview of mICNBD-FRET imaging in the primary cilium of mIMCD-3 cells. **B:** FRET imaging in primary cilia of mIMCD-3 cells expressing mICNBD-FRET and mNPHP3(201)-VHH$_{enh}$-mCherry. Cells have been stimulated with 250 µM IBMX. Cerulean and Citrine are shown before and after addition. The change of Cerulean/Citrine ratio is shown in the lowest row (color sheme indicated at the bottom). Scale bar: 2 µm. **C:** Time course of mean change in FRET (solid yellow line) ± S.D. (dotted yellow line) for the data set exemplary shown in C of n = 5 individual cilia. Stimulus addition at 120 s. Figure modified from (Hansen et al., 2020)

To measure changes in PKA activity in the primary cilium, I expressed mNphp3(201)-AKAR4-NES sensor in ciliated mIMCD-3 cells and stimulated them with 250 µM IBMX or 40 µM of the water-soluble Forskolin derivative NKH477, which activates ACs and

increases cAMP levels (**Figure 39A**). Unfortunately, I could not observe a change in PKA-based FRET in the cilium using either stimulus compared to stimulation with a control (buffer) (**Figure 39B & C**).

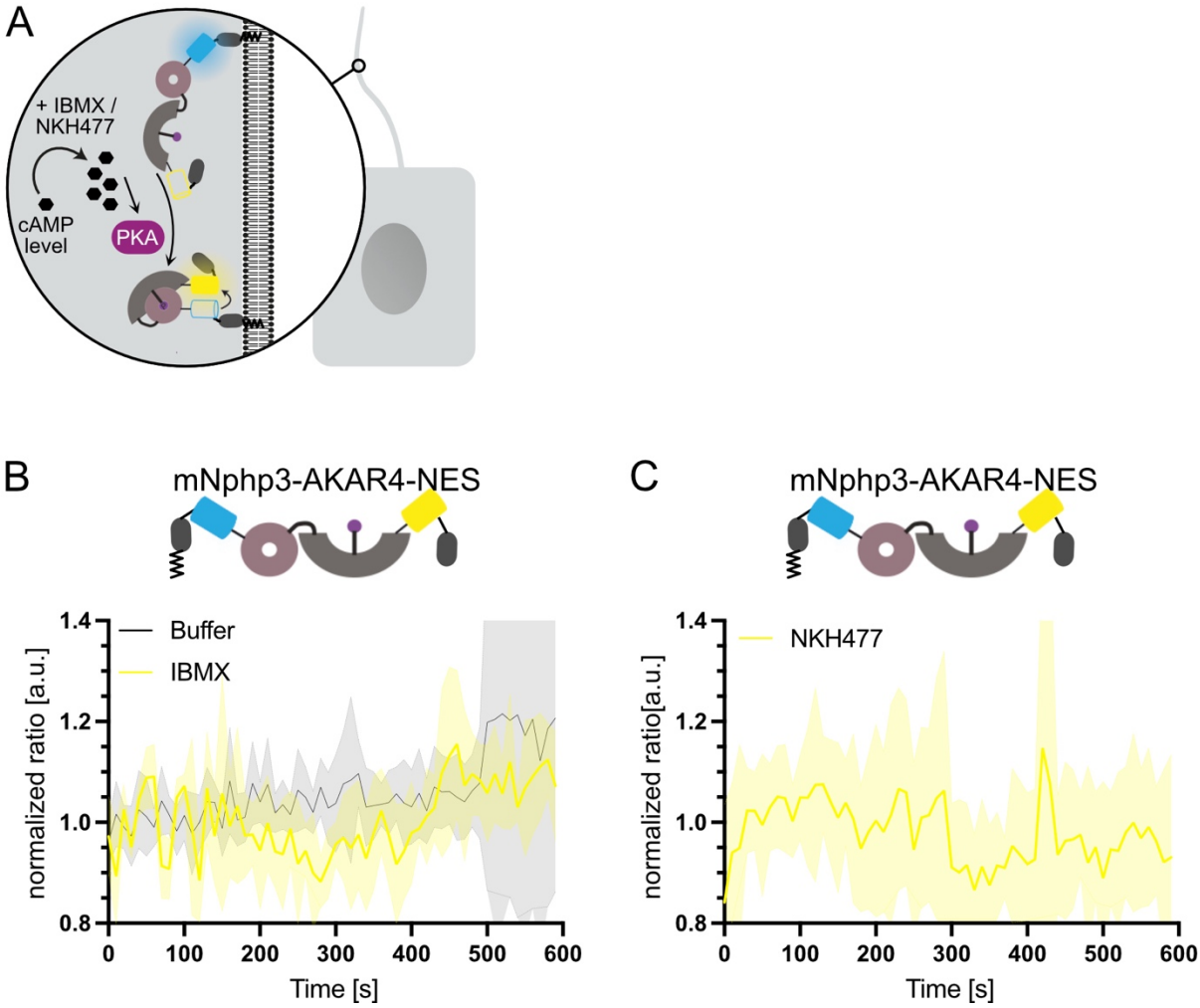

Figure 39: Functional characterization of the cilia-targeted mNPHP3(201)-AKAR4-NES biosensor in ciliated mIMCD-3 cells. A: Schematic overview of AKAR4 imaging in the primary cilium of mIMCD-3 cells. **B-C:** FRET imaging under control (+ Buffer) condition or after stimulation (+ 250 µM IBMX (B) or + 40 µM NKH477 (C)) conditions in ciliated mIMCD-3 cells transiently expressing mNPHP3(201)-AKAR4-NES. Data are shown as mean (solid line) ± S.D. (dotted line) of n = 1 experiment, 4-10 cilia per experiment. Stimulus addition at 120 s.

One explanation why I did not observe an increase in ciliary PKA activity could be that basal PKA activity in the cilium was already sufficient to saturate the sensor. Thereby, the basal ciliary PKA activity exceeds the dynamic range, in which the sensor can report increased PKA activity. I will test this in a future experiment by reducing PKA activity via ciliary Hh stimulation or using a reversible PKA inhibitor. Another possibility could be that the change in PKA activity is smaller than the noise in my measurements. If this is the case, the quality of my measurements needs to be improved and measuring more cilia could unmask putative changes in PKA-based FRET from the

noise. Last but not least, alternative nanobody-directed targeting might also improve AKAR4 sensor response in the primary cilium. Interestingly, Moore and colleagues measured ciliary PKA activity using AKAR4 with N-terminal fusion to the Gαs protein-coupled 5-hydroxytryptamine receptor subtype 6 (5-HT_6) (Moore et al., 2016). However, they did not show temporal changes in PKA dynamics but only end-point measurements, depicting a higher ciliary PKA activity than the cytosol. Nevertheless, they followed up their observation by measuring ciliary cAMP dynamics using the commercially available 5-HT_6-cADDis-mCherry (Montana Molecular, #D0211G), which I also obtained to measure ciliary cAMP dynamics.

The 5-HT_6-cADDis-mCherry biosensor consists of the cpmNeonGreen (cpmNG) fluorescent protein, the Epac2 CNBD, and the 5-HT6 receptor at its N-terminus. 5-HT_6 targets the sensor to the cilium, while mCherry allows performing ratiometric measurements. 5-HT_6-cADDis-mCherry reports increasing cAMP levels with decreasing cpmNG fluorescence upon cAMP binding to the Epac2 CNBD, which can be normalized to mCherry fluorescence (**Figure 40A**). The sensor is supposed to report cAMP concentrations from 300 nM to 100 µM (Moore et al., 2016). Although cpmNG and mCherry display spectral overlap, cpmNG shows a peak excitation at 504 nm and emission at 517 nm, whereas mCherry excitation peaks at 587 nm and it emits at 610 nm. Thus, FRET does not occur between the two FP in this sensor (**Figure 40B**). To verify the results obtained by others (Moore et al., 2016), I expressed 5-HT_6-cADDis-mCherry in ciliated mIMCD-3 cells and measured sensor fluorescence at the Andor Spinning Disk before and after stimulation with 100 nM of the 5-HT_6 agonist, 2-methyl-5-hydroxytryptamine (2M5HT) (**Figure 40C**). The cpmNG fluorescence was reduced upon 2M5HT stimulation, whereas the mCherry fluorescence remained constant, resulting in an increase of the a mCherry/cpmNG ratio (**Figure 40D**).

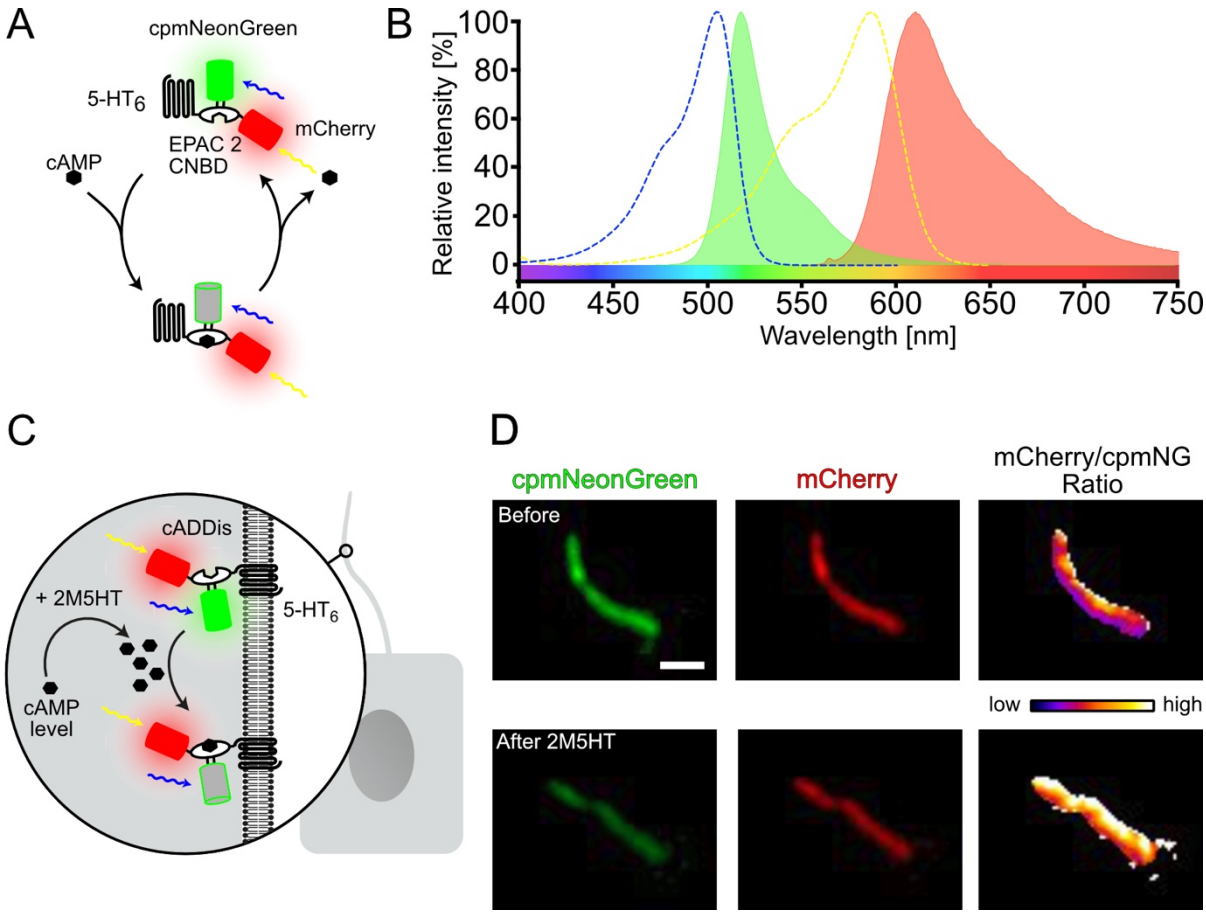

Figure 40: Functional characterization of the cilia-targeted, ratiometric 5-HT$_6$-cADDis-mCherry cAMP biosensor in ciliated cells. A: Schematic overview of the 5-HT$_6$-cADDis-mCherry cAMP biosensor. Cp of mNeonGreen allows the insertion into the hinge region of EPAC2 near the chromophore. Binding of cAMP to the CNBD of EPAC2 results in a conformational change of the hinge region, which leads to change in mNeonGreen fluorescence. N terminal fusion to the full length GPCR 5-HT$_6$ results in cilia localization. C terminal fusion to mCherry allows ratiomerization of the fluorescence values. **B:** Excitation (dotted lines) and emission (solid lines) spectra of mNeonGreen (blue and green) and mCherry (yellow and red). **C:** Schematic overview of 5-HT$_6$-cADDis-mCherry imaging in ciliated mIMCD-3 cells. **D:** Ratiometric imaging of ciliated mIMCD-3 cells transduced with 5-HT$_6$-cADDis-mCherry. Stimulation with 100 nM 2M5HT results in mNeonGreen fluorescence quenching, while mCherry fluorescence is not affected. After stimulation, the mCherry / mNeonGreen ratio increases.

To further analyze 5-HT$_6$-cADDis-mCherry, I used various compounds to increase cAMP levels in primary cilia. I extracted the ciliary fluorescence intensity values using CiliaQ followed by baseline normalization and plotting the data as normalized mCherry/cpmNeonGreen ratio (for details, see “cADDis imaging at the Andor Spinning Disk ”). Treating cells with 250 µM IBMX, 40 µM Forskolin, or 40 µM NKH477, a Forskolin derivative, increased the biosensor fluorescence ratio and, thereby, ciliary cAMP levels (**Figure 41A-D**). While I cannot determine absolute cAMP levels without calibrating the sensor, I can interpret the sensor response kinetics: The sensor reported the slowest cAMP dynamics after stimulation with IBMX, while 2M5HT showed the fastest response, as I would expect for GPCR activation. Forskolin and NKH477 first have to pass the lipid bilayer of the plasma membrane before acting on

the intracellular side of ACs, which was slower than inducing AC activity via a stimulatory GPCR. Overall, 5-HT$_6$-cADDis-mCherry looks to be the most promising cAMP biosensor to analyze Hh-dependent cAMP analysis.

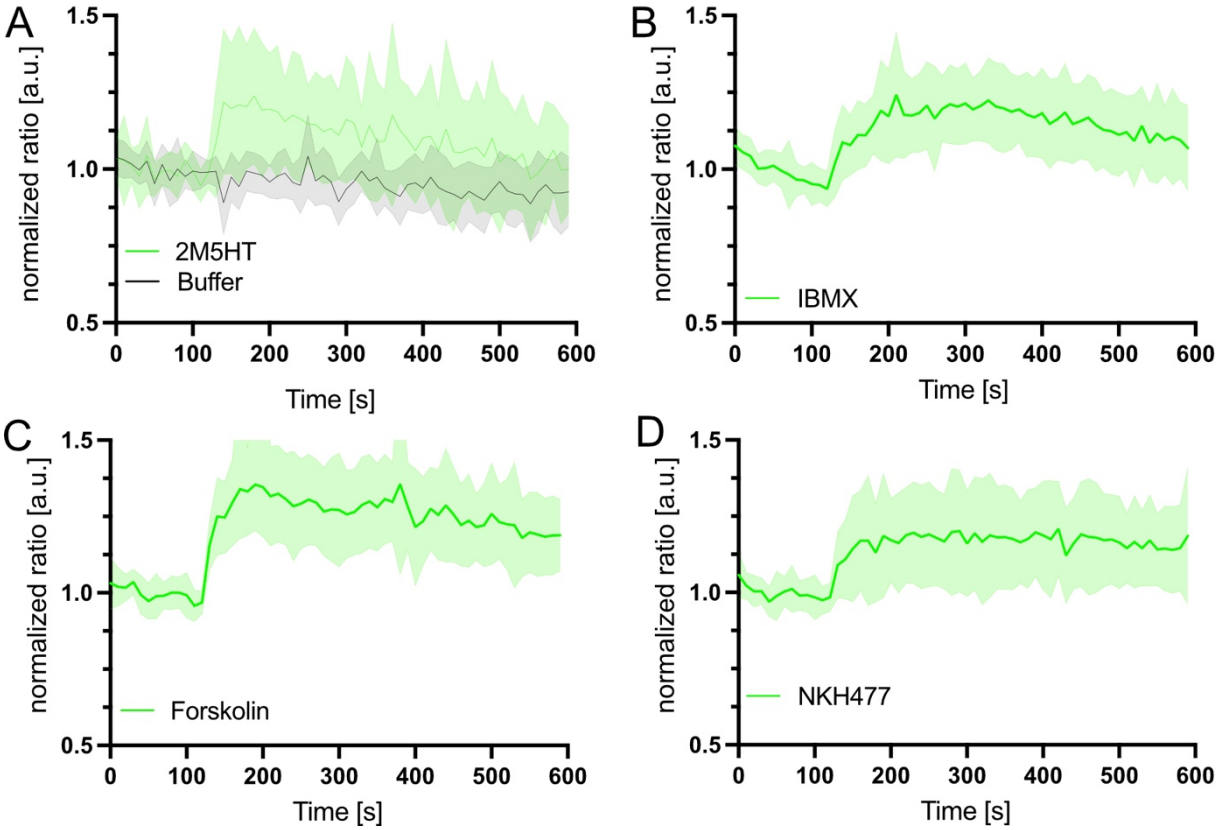

Figure 41: Functional characterization of the cilia-targeted, ratiometric 5-HT$_6$-cADDis-mCherry biosensor in ciliated mIMCD-3 cells. A-D: Ratiometric single FP imaging under control (+ Buffer) or after stimulation with 100 nM 2M5HT (A), 250 µM IBMX (B), 40 µM Forskolin (C), or 40 µM NKH477 (D) in ciliated mIMCD-3 cells transiently expressing *5-HT$_6$-cADDis-mCherry*. Data are shown as normalized mean (solid line) ± S.D. (dotted line) of n = 3-5 independent experiments, 2-14 cilia per experiment. Stimulus addition at 120 s.

3.5.8 Analyzing ciliary Hh-dependent cAMP signaling using ciliary-targeted cADDis-mCherry

In the current Hh signaling model, intraciliary cAMP levels are reduced when SMO enters into the cilium, as it acts via an inhibitory G-protein subunit and inhibits AC activity. In addition, GPR161 leaves the cilium upon Hh stimulation, whereby AC activity is no longer stimulated (May et al., 2021). I analyzed Hh-dependent changes in ciliary cAMP levels using 5-HT$_6$-cADDis-mCherry. To this end, I measured the fluorescence changes before and after adding 100 nM hSHH at 120 s after beginning the recording. However, the sensor did not report a change in fluorescence after hSHH stimulation, demonstrating that cAMP levels remained unchanged (**Figure 42A**).

However, due to the changes in protein localization in and out of the cilium, the process of altering ciliary cAMP levels upon Hh pathway activation might occur on the longer time scale outside my recording window. Therefore, I expressed the sensor in cells that I treated for 24 h with 10 nM hSHH before recording sensor fluorescence. Without further normalization, I plotted the average mCherry fluorescence intensity divided by the cpmNG ratio from the first 120 s of recording and statistically compared the ratio to untreated cells (**Figure 42B**). In contrast to what I expected, the ratio in hSHH treated cells was significantly higher than in untreated cells, which indicates an increased intraciliary cAMP concentration.

My results contrast the findings from others, who reported a significant decrease in the

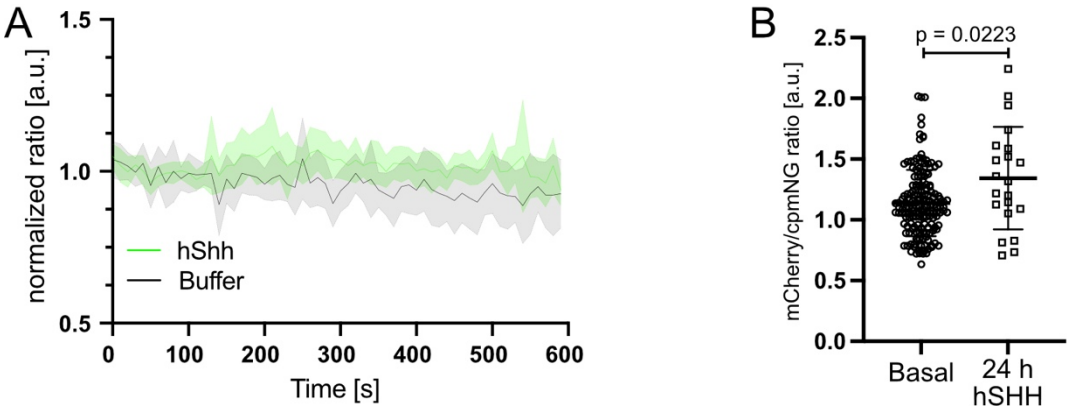

Figure 42: Analyzing ciliary Hh-dependent cAMP dynamics using 5-HT$_6$-cADDis-mCherry. A: Ratiometric single FP imaging under control (+ Buffer) or after stimulation with 100 nM hSHH in ciliated mIMCD-3 cells transiently expressing 5-HT$_6$-cADDis-mCherry. Data are shown as normalized mean (solid line) ± S.D. (dotted line) of n = 4-5 independent experiments, 2-5 cilia per experiment. Stimulus addition at 120 s. **B:** Comparison of mean mCherry / cpmNG ratio of cilia that are non-treated (basal) or treated with 100 nM hSHH for 24 h before measuring. Each dot represents the mean ratio of a single cilium from 3-5 independent experiments. Basal values passed tests for normal distributions, whereas hSHH values did not. Statistical differences were calculated using a Mann-Whitney test, p-value is indicated above.

ciliary cAMP concentration upon Hh stimulation (Moore et al., 2016). However, they measured ciliary cAMP levels in mEFB, whereas I used mIMCD-3 cells. Another group directly visualized cAMP signaling in mIMCD-3 and mEFB primary cilia using another sensor but co-expressed the 5-HT$_6$ receptor in their measurements, which I used for ciliary cADDis-mCherry localization (Jiang et al., 2019). Using direct visualization of ciliary cAMP signaling, they revealed up-regulation of ciliary GPCR activity following Hh activation that was different in mIMCD-3 compared to mEFB cells. This indicates that different cells might regulate ciliary cAMP levels differently. In addition, they verified well-known constitutive activity of 5-HT$_6$ (Jiang et al., 2019; Kohen et al., 2001). Thus, the higher ciliary cAMP concentration I measured might be due to elevated

cAMP levels caused by constitutive 5-HT_6 activity, which likely masked the hSHH-dependent changes in mIMCD-3 cells.

Therefore, I decided to exchange the 5-HT_6 with the mNPHP3(201) ciliary-localization tag to generate the mNphp3(201)-cADDis-mCherry cAMP biosensor (**Figure 43A**). Subsequently, I expressed mNphp3(201)-cADDis-mCherry in ciliated mIMCD-3 cells and measured sensor fluorescence at the Andor Spinning Disk before and after stimulation with 40 µM NKH477 (**Figure 43B**). Treating cells with 40 µM NKH477 depicted an increase in normalized mCherry/cpmNG ratio, whereas treatment with buffer showed no effect (**Figure 43C**). As seen before, mNPHP3 fusion slowed down sensor response but reported a higher increase in the normalized ratio than the response of the 5-HT_6-cADDIs-mCherry (**Figure 41D**). The peak mCherry/cpmNG ratios was significantly higher for the mNphp3(201)-cADDis-mCherry sensor, compared to the 5-HT_6-cADDIs-mCherry (**Figure 43D**). While the mNphp3(201)-cADDis-mCherry data only results from one experiment, they indicate that 5-HT_6 expression increases basal ciliary cAMP levels in mIMCD-3 cells.

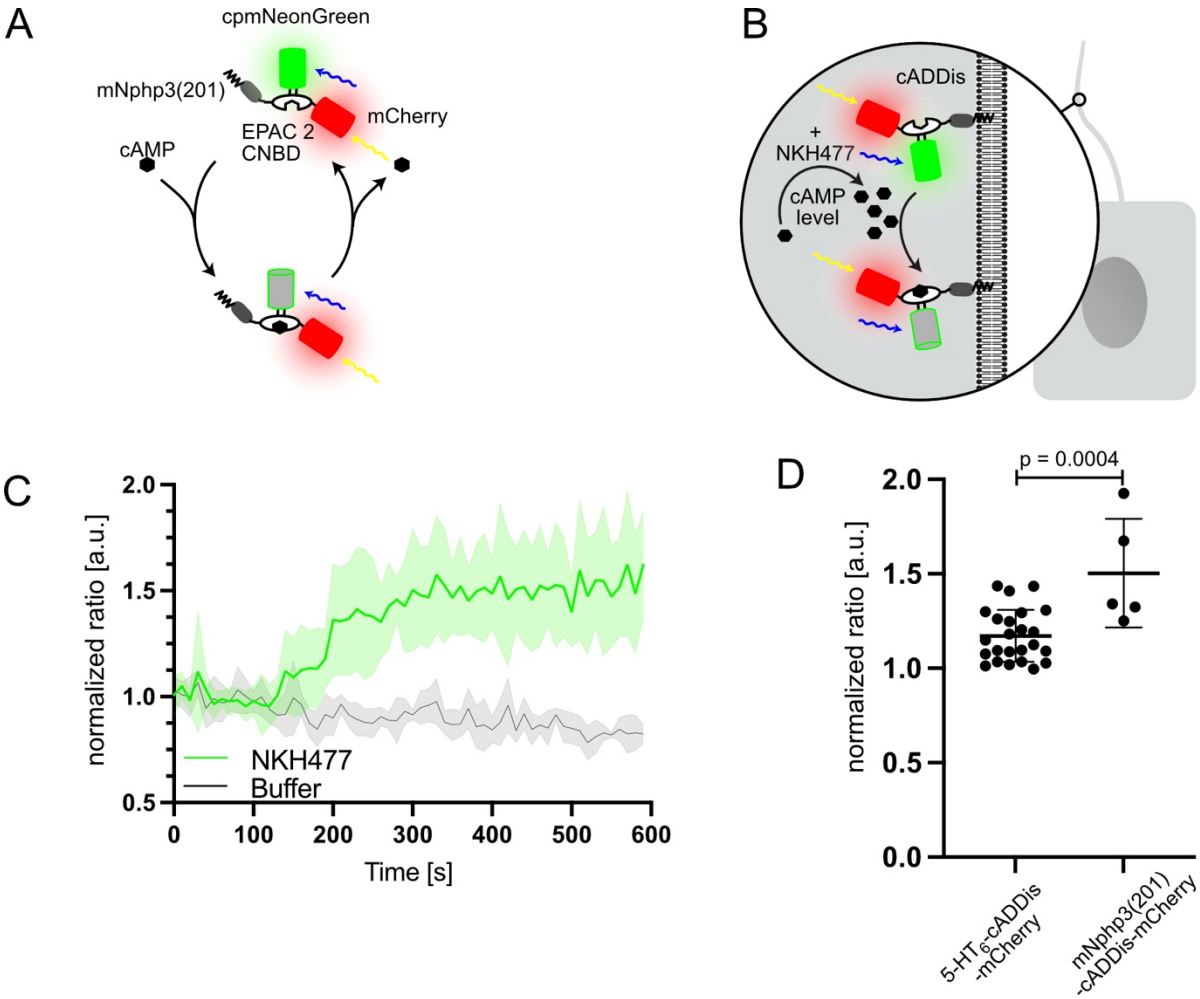

Figure 43: Functional characterization of the cilia-targeted, ratiometric mNphp3(201)-cADDis-mCherry biosensor in ciliated mIMCD-3 cells. A: Schematic overview of mNphp3(201)-cADDis-mCherry. mNphp3(201) was fused to the N terminus of cADDis-mCherry for ciliary localization. **B:** Schematic overview of cADDis imaging in the primary cilium of mIMCD-3 cells. **C:** Ratiometric single FP imaging under control (+ Buffer) or after stimulation 40 µM NKH477 (NKH477) in ciliated mIMCD-3 cells transiently expressing mNphp3(201)-cADDis-mCherry. Data are shown as mean (solid line) ± S.D. (dotted line) of n = 1 experiment, 5 cilia per experiment. Stimulus addition at 120 s. **D:** Comparison of maximal change of data shown in (C) and figure Figure 42D. Data are presented as individual data points with mean ± S.D.; Datasets passed a normality test and statistical differences were calculated using an unpaired t-test, p-value is indicated.

In summary, mNphp(201)-cADDis-mCherry appears the most suitable ciliary-targeted cAMP biosensor to analyze ciliary cAMP dynamics. I established this biosensor in ciliated mIMCD-3 cells, and I will now be able to analyze putative changes in Hh-dependent cAMP dynamics in a GBA2-dependent manner.

3.6 Establishing knockout cells of the 5´inositol phosphatase INPP5E to study its role in ciliary cAMP signaling

PI(4)P is the predominant PIP species in the primary cilium, which is mainly maintained by INPP5E (Chavez et al., 2015; Garcia-Gonzalo et al., 2015). Loss of INPP5E results in ciliary PI(4,5)P_2 enrichment, which is accompanied by ciliary GPR161 enrichment and inhibition of ciliary GPR161 exit after Hh pathway stimulation (Chavez et al., 2015; Garcia-Gonzalo et al., 2015). Downstream, on the transcriptional level, the expression of Hh target genes under basal conditions in *Inpp5e*-KO cells is not changed upon ciliary GPR161 enrichment, but the induction of *Ptch1* and *Gli1* is diminished after Hh pathway stimulation, when GPR161 would exit the cilium in wild-type cells (Chavez et al., 2015; Garcia-Gonzalo et al., 2015).

Ciliary GPR161 has been proposed to regulate the Hh pathway signaling via changing cAMP levels through the action of their $G\alpha_s$-coupled proteins. I hypothesized that loss of INPP5E increases ciliary cAMP levels due to GPR161 being enriched in the cilium. After establishing a suitable cAMP biosensor to analyze ciliary cAMP dynamics, I also aimed to generate *Inpp5e*-KO cells and delineate downstream signaling after INPP5E loss in terms of cAMP signaling.

To this end, I generated *Inpp5e*-KO cells using CRISPR-Cas9 and aimed to measure ciliary cAMP levels.

3.7 Generation of *Inpp5e* knockout cells using CRISPR-Cas9

To knockout *Inpp5e* in mIMCD-3 cells, I used the RNA-guided Cas9 nuclease from the microbial clustered regularly interspaced short palindromic repeats (CRISPR) adaptive immune system (CRISPR-Cas9) (Garneau et al., 2010; Gasiunas et al., 2012; Jinek et al., 2012). Small RNA sequences, typically of 20 base pairs (bps) in length, precisely guide the Cas9 to the desired genomic locus through Watson-Crick base pairing, where the Cas9 induces a double-strand break (DSB). In the absence of a repair template, the cell repairs the DSB through the non-homologous end joining (NHEJ). However, the Cas9 will cleave the repaired locus as long as it is present, or the NHEJ generates an error in the repair process. Preferably, the error results in a nonsense mutation, an insert or deletion, or both (indel), causing a frameshift and, thereby, a knockout of the target gene (Ran et al., 2013).

3.7.1 CRISPR-Cas9 targeting design

To genetically ablate *Inpp5e*, I identified all splice variants using the ensemble gene database (Hunt et al., 2018): there are seven splice variants, of which four are protein-coding, but only two translate into functional proteins with a length of 647 and 605 amino acids (AA) (transcript IDs: ENSMUST00000145701.8; *mInpp5e-205*, and ENSMUST00000114090.8; *mInpp5e-202*). The shorter variant lacks parts of the last exon, exon 10, which encodes a CAAX motif for C-terminal farnesylation and parts of the predicted catalytic phosphatase domain. Otherwise, the coding sequences of the two variants are identical (**Figure 44A**).

Figure 44: CRISR-Cas9 target design and characteristics of *Inpp5e*. A: Alignment of the coding sequences of the two variants that translate into functional proteins. The two proteins only differ in the last amino acids at the 3´-end. **B:** Sequences predicted to encode for the phosphatase domain and CAAX motif are downstream of guide RNA target sites. Guide RNA target sites are indicated with background coloring of the respective sequences. Overlapping sequence of guide RNA #2 and #3 is depicted in yellow.

Consequently, the longer variant is predicted to be membrane-anchored, whereas the shorter variant is putatively soluble and could potentially have phosphatase activity. The predicted catalytic phosphatase domain (ranging from AA 277 to 633) is encoded by exons 3 to 10. I decided to induce a mutation before exon 3. Blasting exon 2 to the whole mouse genome revealed that it is unique for *Inpp5e*. Thus, I used a CRISPR-Cas9 guide design tool to design three guide RNAs in exon 2 (http://crispr.mit.edu/, recently shut down) (**Figure 44B**). Blasting of the guide RNAs showed no other sequence alignment other than to *Inpp5e*. Finally, I cloned the guide RNAs into the PX459 V2.0 CRISPR-Cas9 vector (Ran et al., 2013), which additionally bears a puromycin resistance cassette.

3.7.2 *Inpp5e*-directed CRISPR-Cas9 targeting and identification of *Inpp5e*-KO candidate cell lines

I transiently transfected mIMCD-3 cells with two PX459 V2.0 vectors, combining either guide RNAs #1/2 or #1/3 to increase the likelihood of inducing a frameshift in the *Inpp5e* locus. Furthermore, I selected cells for Cas9 expression using puromycin. Of note, I only performed the selection until mock-transfected control cells started to die to avoid stable Cas9 expression. This might cause functional artifacts and increase the chance of off-target effects.

Next, I performed monoclonal propagation of cells without puromycin selection and isolated genomic DNA from each clone for PCR amplification of a 201 bp fragment covering the targeted locus. Sanger sequencing is commonly used to determine small nucleotide sequences of up to 1000 bps. Interestingly, the Sanger sequencing chromatogram can be used to identify and quantify differences in DNA (Brinkman et al., 2014). Indeed, the chromatogram of wild-type cells showed only single peaks (**Figure 45**). In contrast, a mixed population of cells exposed to the *Inpp5e*-targeted Cas9 displayed various different peaks, starting around the position where guide RNA #2 targets (**Figure 45**). The various peaks could also result from the mutation of only one instead of both alleles (heterozygous mutation). By analyzing the Sanger sequencing chromatogram of the generated PCR fragments, I tried to answer the following questions: 1.) Does the candidate cell line carry a mutation in the *Inpp5e* gene compared to the wild-type sequence? 2.) Is the mutation homo- or heterozygous, or do we have mixed populations instead of a monoclonal cell line? And 3.) If the

mutation is homozygous and appears to be from a monoclonal cell line, is it a nonsense mutation or results in a frameshift?

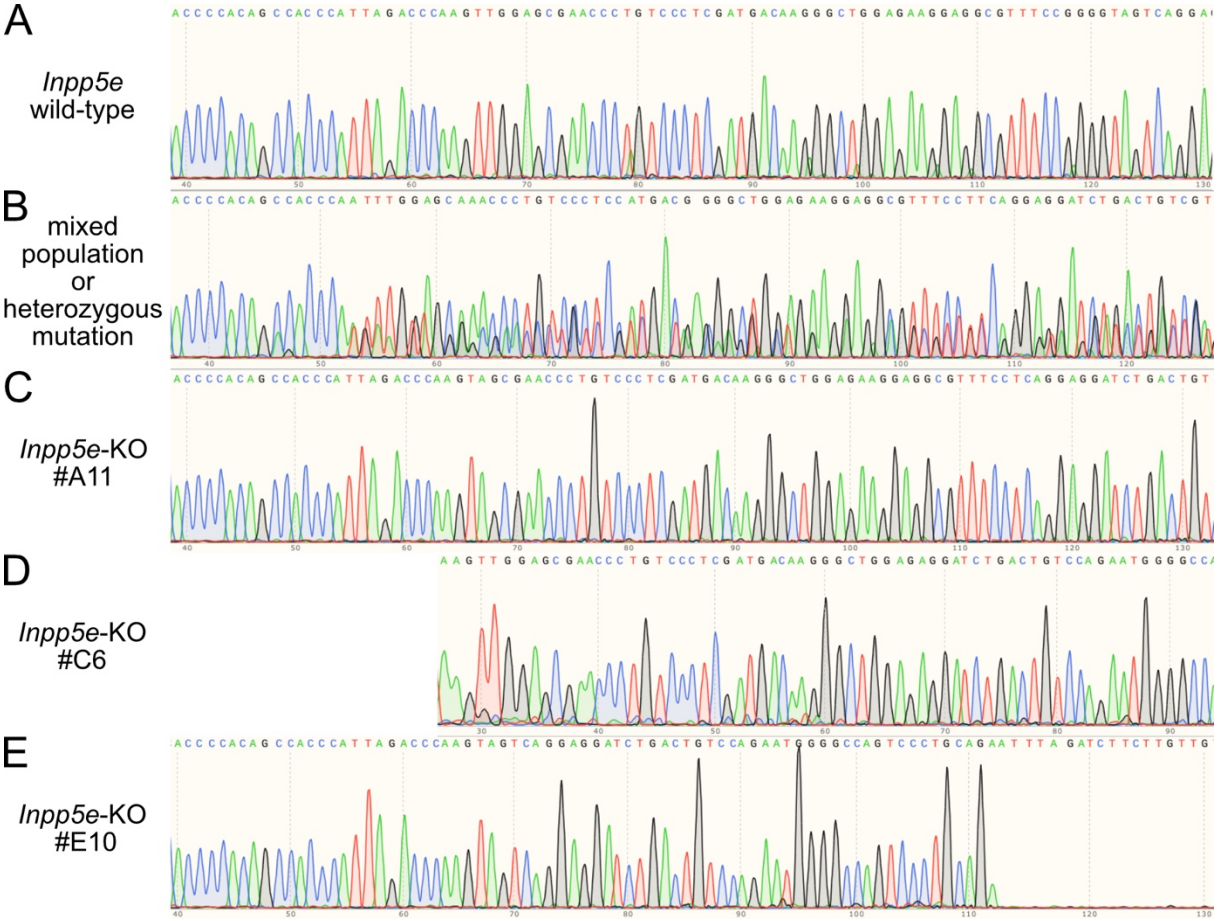

Figure 45: Sanger sequencing chromatograms. A-E: Chromatograms A and C-E show single peaks, indicating a single cell population being homozygous for the sequenced genomic locus, whereas chromatogram B depicts either a mixed population or a heterozygous mutation.

Using this approach, I identified three clones, mIMCD-3 *Inpp5e-KO* #A11, #C6, and #E10 with the following characteristics: The Sanger sequencing chromatograms of the three candidate cell lines displayed single peaks for the different nucleotides (**Figure 45C-E**), but differed from the wild type (**Figure 46A**): Compared to the wild-type sequence, Clone #A11 contained a three bp deletion in the region targeted by guide RNA #3 and a seven bp deletion targeted by guide RNA #1. Clone #C6 contained a 26 bp deletion in the region targeted by guide RNA #2, while Clone #E10 contained a 56 bp deletion in the region targeted by guide RNAs #1 and #3. Notably, none of these genomic sequences align with the respective guide RNAs they were exposed to. All mutations would result in a frameshift, resulting in alternative AA sequences compared to the wild type. Furthermore, all frameshifts lead to early stop codons

(**Figure 46B**). Thus, I concluded that I generated three independent mIMCD-3 *Inpp5e*-KO cell lines using CRISPR-Cas9.

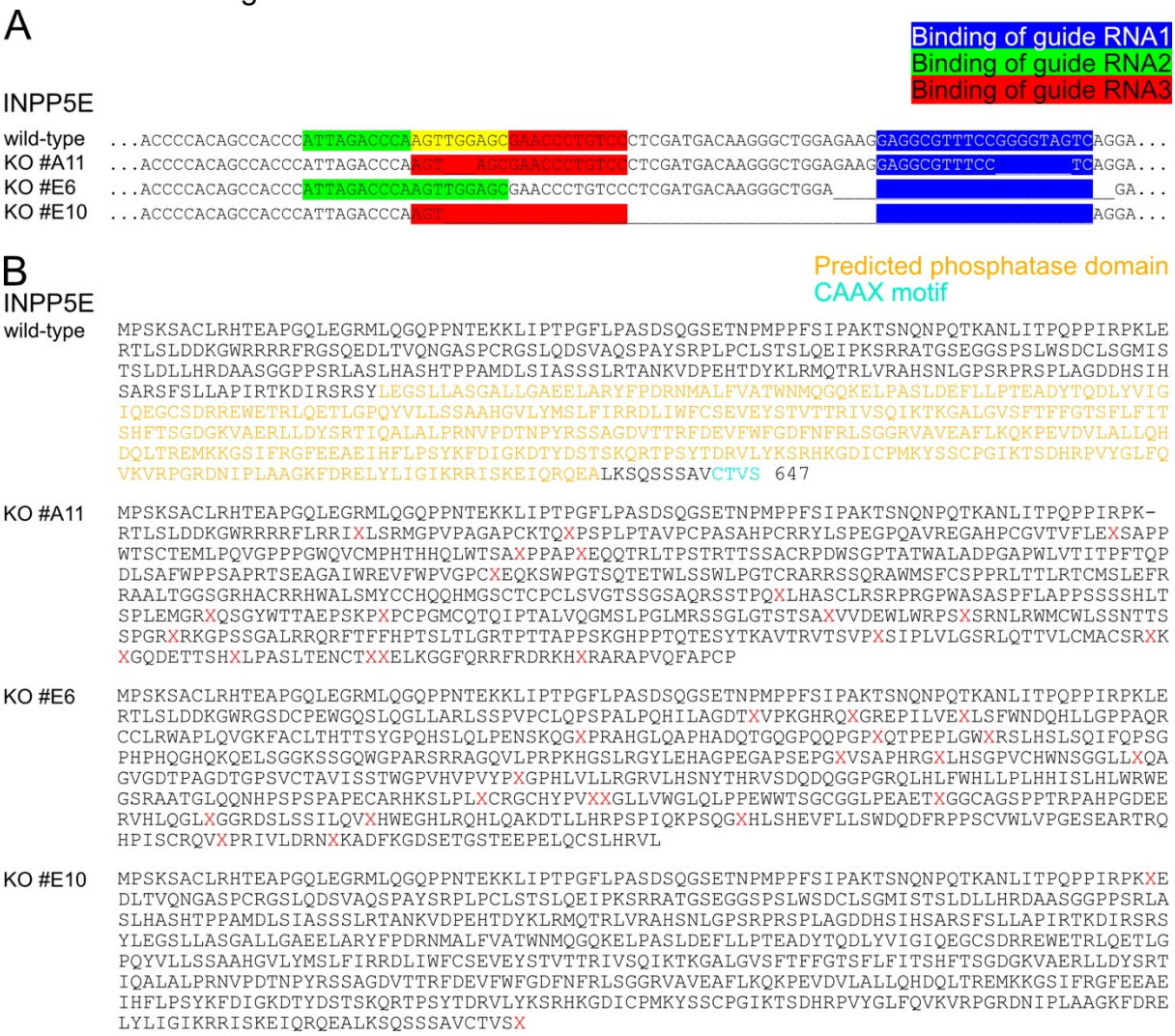

Figure 46: Interpretation of the Sanger sequencing data. A: Sanger sequencing revealed deletions of several nucleotides in the region of guide RNA target sites. **B:** Translating the putative nucleotides with the sequenced mutations would result in a frame shift and stop codons in all *Inpp5e*-KO candidate cell lines (indicated with a red X in the AA code), before the predicted phosphatase domain.

3.7.3 Verification of *Inpp5e*-KO candidate cell lines using Western Blot analysis and immunocytochemistry

To verify the absence of INPP5E in the *Inpp5e*-KO cell lines, I analyzed the presence of the protein. The calculated sizes of the membrane-anchored INPP5E and putative soluble variant are 72 and 71 kDa, respectively. Western Blot analysis of total cell lysates did not detect a specific band in this size range in any of my samples (**Figure 47A**). However, ciliary proteins are usually underrepresented in total cell lysates. Thus, I also analyzed INPP5E expression using immunocytochemistry.

However, labeling ciliated mIMCD-3 wild-type cells with an anti INPP5E antibody did not show a specific signal colocalizing with the ciliary marker (**Figure 47B**).

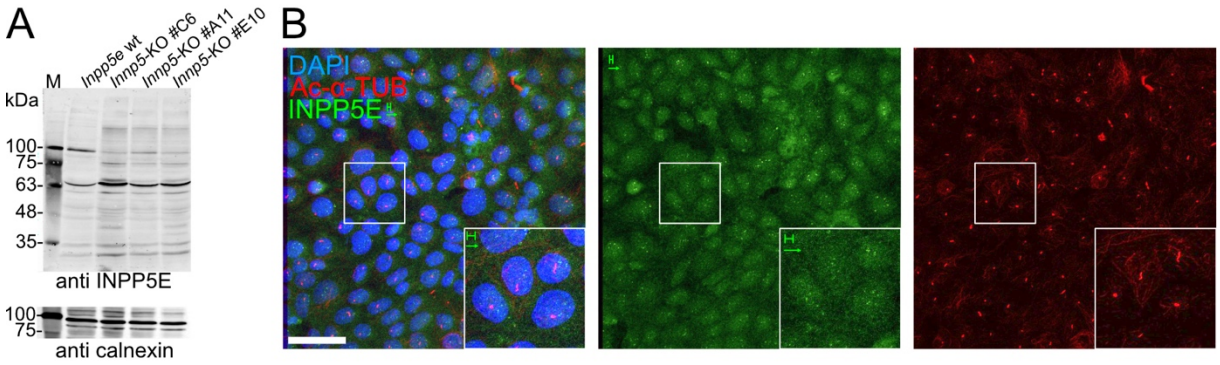

Figure 47: Immunodetection of INPP5E. A: Western blot analysis of total lysates from mIMCD-3 wild-type cells and the mIMCD-3 *Inpp5e*-KO candidate cell lines. The calculated size of INPP5E is 72 and 71 kDa for the long and short variant, respectively. Calnexin was used as a loading control. **B:** Characterization of ciliary INPP5E in mIMCD-3 wild-type cells using ICC and confocal microscopy. Cells were stained with DAPI (blue) to label DNA, and antibodies against INPP5E (green) and Ac-α-TUB (red). Scale bar: 40 µm. Pixels of the green channel are shifted to the right as indicated by the green scalebar and arrow. The white inset in the corner shows a magnified view of the small white box.

Thus, I applied an indirect approach and performed immunolabeling of PIPs. I hypothesized that PI(4)P levels should be high in cilia of mIMCD-3 wild-type cells, whereas *Inpp5e*-KO cell lines would show PI(4,5)P_2 in cilia. For PIP immunolabeling, I used 0.2% glutaraldehyde together with 4% PFA for fixing the cells, which leads to a tighter crosslinking of proteins, whereby the PIP species should also remain in place for immunolabeling. Moreover, I enhanced the fluorescence by using a secondary antibody coupled to biotin and a streptavidin coupled to a fluorophore. However, I did not observe specific PIP labeling in either of the cell lines (**Figure 48**).

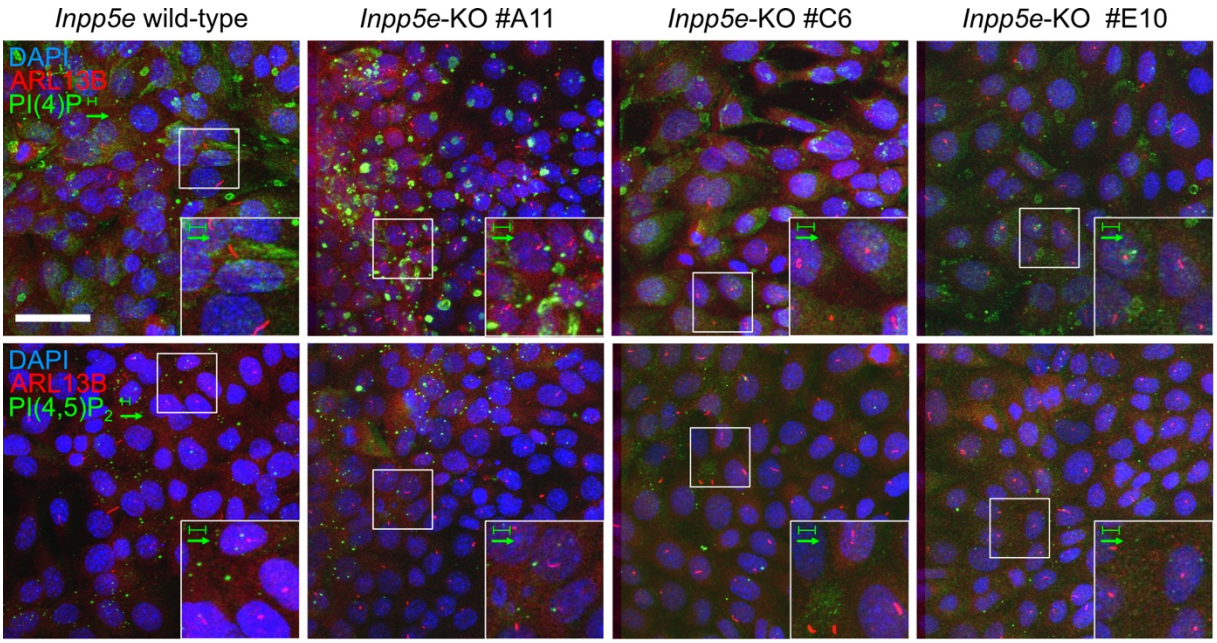

Figure 48: Characterization of mIMCD-3 wild-type and mIMCD-3 *Inpp5e*-KO candidate cell lines using immunofluorescent labeling. Ciliated cells were stained with DAPI (blue) to label DNA and antibodies against PI(4)P (upper row) or PI(4,5)P_2 (lower row)(green), and ARL13B (red). Scale bar: 40 µm. Pixels of the green channel are shifted to the right as indicated by the green scalebar and arrow. The white inset in the corner shows a magnified view of the small white box.

In summary, I generated three independent mIMCD-3 CRISPR-Cas9 clones, which appear to be homozygous knockouts for *Inpp5e* on the DNA level. However, I could not verify the loss of INPP5E on the protein level or functionally by changes of PIP species in the ciliary membrane using immunolabeling. These protocols will have to be optimized in future experiments. Similarly, due to time constraints, I did not manage to measure cAMP dynamics in the putative *Inpp5e*-KO cell lines.

3.8 Isolation and purification of primary cilia for lipid extraction and mass-spectrometric analysis of the ciliary membrane lipid composition

Tight control of the ciliary lipid and protein homeostasis is crucial for maintaining ciliary function (Garcia et al., 2018; Rohatgi and Snell, 2010). However, while there have been several unbiased approaches to characterize the ciliary proteome, a similar strategy to unravel the ciliary lipidome is lacking (Garcia et al., 2018; May et al., 2021; Mick et al., 2015; Nachury and Mick, 2019). A common, unbiased approach to analyze lipid content qualitatively and quantitatively is "shotgun lipidomics". Here, lipids are extracted from the biological sample, processed by various methods, and analyzed by mass-spectrometry (Hsu, 2018). The main requirement for analyzing the ciliary lipidome using this approach is to exclusively isolate the primary cilium from the rest of the cell, which is exceptionally challenging. During recent years, only a few groups have reported strategies to isolate primary cilia. However, none of them performed proteomic or lipidomic analysis on the isolated samples (Huang et al., 2006; Mitchell et al., 2004; Monaco et al., 2018; Raychowdhury et al., 2005; Raychowdhury et al., 2009; Sherpa et al., 2019; Wang and Brautigan, 2008). Reasons for not performing proteomic or lipidomic analysis are unclear, but might be a lack of purity, sufficient amount of cilia, or both. Here, I combined two approaches to maximize the amount of isolated primary cilia while minimizing cell damage and contamination with other subcellular compartments. This protocol includes the isolation of primary cilia using shear stress and isolation of primary cilia using a Ca^{2+}-shock (Mitchell et al., 2004; Raychowdhury et al., 2005).

3.8.1 Establishing specific isolation of primary cilia using shearing-forces and Ca^{2+} shock

Both methods that I combined in my protocol have some drawbacks: While the shearing-force method likely works better for very long cilia, i.e., for primary cilia on *Xenopus* A6 kidney cells with a length of 23 µm, the Ca^{2+}-shock method requires cells to be in solution, i.e., by scrapping the cells, which resulted in contamination with other cellular compartments (Mitchell et al., 2009). In addition, the shearing-force method needed four confluent 150 mm dishes of *Xenopus* A6 cells to yield 6-20 µg primary

cilia fraction. I aimed to analyze the lipid content of primary cilia from mIMCD-3 cells, which is a renal cell line like *Xenopus* A6, but with shorter cilia length of 2-5 µm (Hansen et al., 2021; Sun et al., 2019). I set out to solve all these challenges by combining the two methods with collagen-coated dextran beads (Cytodex® 3 microcarrier beads, Sigma-Aldrich). These beads allow to grow adherent cells on a large scale in solution and are, according to the manufacturer, optimized for epithelial cell lines. (**Figure 49A**). First, I tested the growth and proliferation of mIMCD-3 cells on the microcarrier. Indeed, using DIC light microscopy, I observed adherent mIMCD-3 cells on microcarriers, which proliferated from one microcarrier to another (**Figure 49B,** illustration for clarification on the right side). Growing cells on microcarriers in a suspension requires constant shaking, which exposes cells to more mechanical stress than growth on plastic dishes. To test whether primary cilia form and are maintained under these conditions, I performed ICC to label cilia. Strikingly, I observed primary cilia on a confluent microcarrier using ARL13B as a ciliary marker (**Figure 49C**).

Next, I established the workflow for primary cilia isolation and purification (**Figure 49D**): I transferred the microcarrier-cell suspension into a 50 mL vessel and extracted some microcarriers for ICC to verify the presence of primary cilia. Subsequently, I exchanged the supernatant with a buffer containing a high Ca^{2+} concentration (10 mM) and incubated the microcarriers while shaking to generate shearing forces together with the Ca^{2+}-shock. Again, I also extracted some microcarriers from this step for ICC. I then performed a low-speed centrifugation step to separate cell debris from the detached cilia in the supernatant. I isolated proteins for Western-Blot analysis from this cell pellet and subjected the supernatant containing primary cilia to high-speed centrifugation. In turn, I also isolated proteins from this pellet for Western-Blot analysis. The Western blot was performed using 60 and 1 µg total protein from the first and 1 µg total protein from the second pellet and stained with an anti-AC-α-TUB antibody as a ciliary marker and an anti-calnexin (CNX) antibody as an endoplasmic reticulum (ER) marker, which should be absent from primary cilia. My results demonstrate that i) I have ciliated cells on a confluent microcarrier, as observed by fluorescent labeling of primary cilia (**Figure 49D**); ii) The isolation protocol removes primary cilia from the cells, as the number of ciliated cells was reduced and a more punctual ARL13B staining was observed after exposure to mechanical forces and a Ca^{2+}-shock (**Figure 49D**); iii) the pellet after high-speed fraction seems to contain primary cilia, as

indicated by the presence of AC-α-TUB, and is rather free of cellular contaminates, as indicated by the absence of CNX (**Figure 49D**).

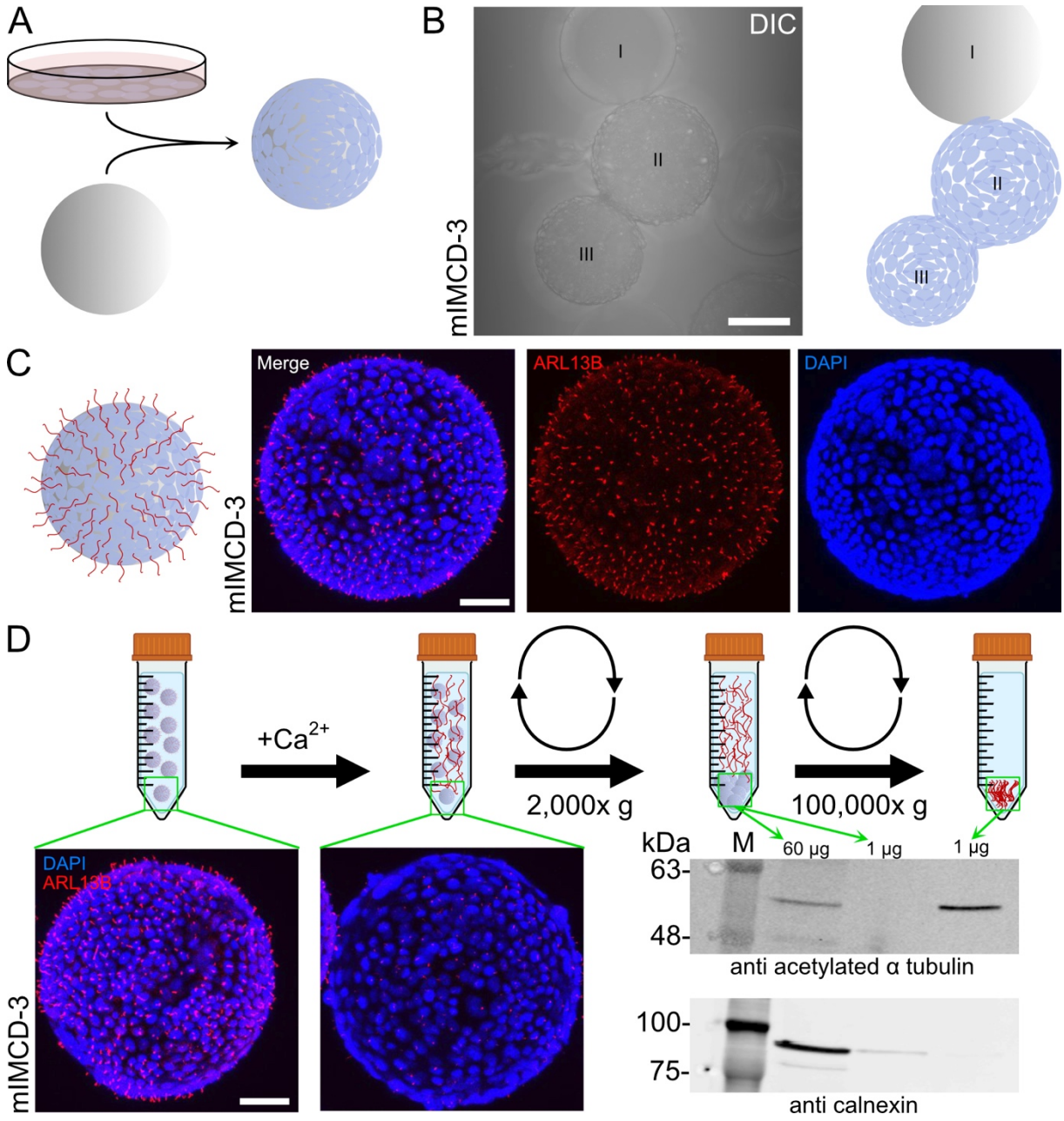

Figure 49: Establishing adherent cell growth on microcarrier for primary cilia isolation. A: Adherent cell lines can be seeded and grown on collagen-coated microcarriers. **B:** Representative DIC image of mIMCD-3 cells growing in a tissue culture from one (II) to another (III) microcarrier, while a third microcarrier is not yet occupied (I). Scheme depicting the three described microcarriers from the DIC image shown on the right side. Scale bar: 40 µm. **C:** Scheme and confocal microscopy image of ciliated mIMCD-3 cells on a microcarrier. Cilia have been stained with an anti-Arl13b antibody (red) and DNA was labeled with DAPI (blue). Scale bar: 40 µm. **D:** Scheme to illustrate deciliation using ciliated mIMCD-3 cells on microcarriers using a Calcium (Ca^{2+}) shock, followed by low- and high-speed centrifugation steps. Confocal microscopy images show mIMCD-3 cells labeled with an anti ARL13B antibody (red) and DAPI (blue) on microcarrier from the indicated steps during cilia isolation. Scale bar: 40 µm. Western blot analysis was performed from the pellets of the indicated steps using acetylated α tubulin (55 kDa) as a ciliary marker and calnexin (90 kDa) as a marker for the endoplasmic reticulum.

3.8.2 Preliminary lipidomic analysis of isolated mIMCD-3 primary cilia

To analyze the lipid content of the primary cilia fraction after isolation, we analyzed the ciliary lipidome in cooperation with Christoph Thiele (Life & Medical Sciences Institute (LIMES), Group for Biochemistry and Cell Biology of Lipids, University of Bonn, Germany). To this end, we chose a liquid-liquid extraction protocol based on chloroform/methanol mixtures that are commonly used for lipid extraction when intending an untargeted lipid analysis (Aldana et al., 2020). Specifically, I prepared samples using protocols established by the Thiele group (Thiele et al., 2019) with the modification to omit the described click reactions and only using 5 µL internal standard (IS) for the primary cilia fraction and in parallel 10 µL IS for 1 x 10^6 deciliated cells that I collected after the second step of the isolation process (**Figure 49D**).

To compare the lipid content, I normalized the different lipids to the total level of phosphatidylcholine (PC) in the sample, assuming that the relative PC levels in the whole cell ("Whole-Cell") and ciliary ("Cilia") lipid extraction are equal (**Figure 50**). So far, I only once managed to isolate a primary cilia fraction once that was free of contamination with other subcellular compartments, indicating that I still had to optimize the procedure (see chapter 3.8.3). Thus, I only show here lipidomics data for one experiment. Compared to the whole-cell lipid extract, the ether-linked phosphatidylcholine (PC-O) and triacylglycerides (TAGs) levels were slightly increased in the cilia fraction (**Figure 50A**). In contrast, the levels of phosphatidylinositol (PI) were slightly decreased. Strikingly, SM levels were increased in the cilia fraction, which is in line with a recent report by the Rohatgi lab (**Figure 50A**) (Kinnebrew et al., 2019), showing enriched ciliary SM levels using fluorescent probes and confocal microscopy. The ganglioside species GM2 was reduced in the cilia fraction, whereas GM3 levels were increased (**Figure 50B**). Levels of GM1 were below the detection limit in both whole-cell and ciliary lipid extracts (**Figure 50B**). At least for GM3, this is in line with other reports, demonstrating an enrichment in primary cilia of MDCK cells using fluorescent probes (Janich and Corbeil, 2007).

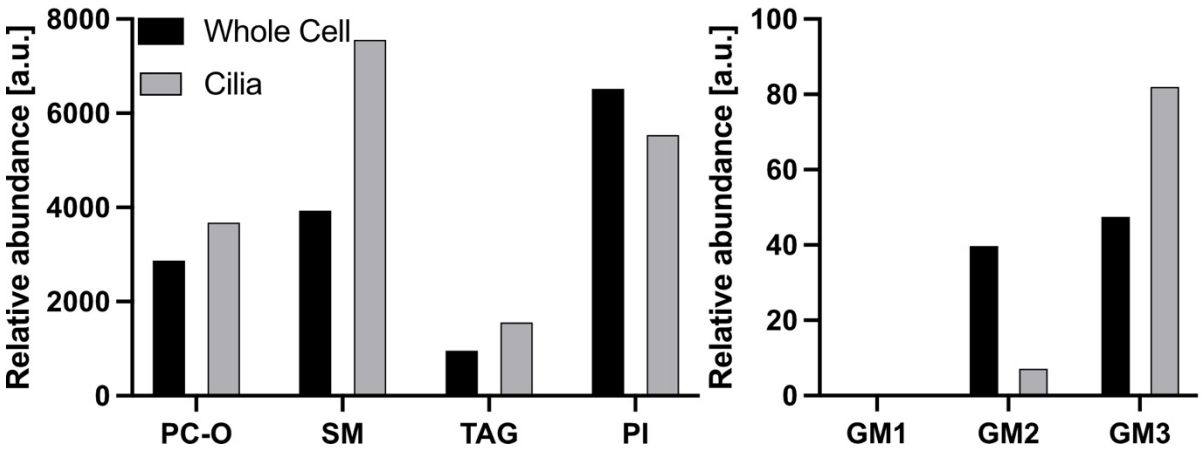

Figure 50: Mass spectrometric analysis of isolated cilia and whole-cell samples from mIMCD-3 cells. Lipids were extracted from isolated cilia of a confluent 100 mg microcarrier culture or $1x10^6$ de-ciliated cells. Quantified lipids were normalized to the total level of phosphatidylcholine in each sample. Ether phosphatidylcholine (PC-O), sphingomyelin (SM), triacylglycerides (TAG), phosphatidylinositol (PI), gangliosides 1-3 (GM1-3).

Overall, my results demonstrate that ciliary lipidomic analysis is feasible and recapitulates current knowledge.

To identify differences in other lipid species between the ciliary and plasma membrane and verify my approach, I aimed to introduce a ciliary tag that allows me for more efficient and consistent isolation and purification of primary cilia.

3.8.3 Establishing the ALFA-tag for cilia-specific pull-down

To further optimize my isolation approach, I aimed to introduce a ciliary tag that isolates and purifies primary cilia more efficiently and consistently. Recently, the ALFA-tag has been published, which outperforms established tags like the HA-, FLAG-, or myc-tag: The ALFA-tag epitope forms irrespectively of its position in the tagged protein, is detected in living and fixed specimen, and allows pull-down of entire living cells (Gotzke et al., 2019). In more detail concerning the last characteristic, ALFA-tag expression on the cellular surface has been shown to allow cellular enrichment, e.g., of $CD62L^+$ lymphocytes (Gotzke et al., 2019). I aimed to introduce the ALFA-Tag on the extracellular side of SMO, which is localized to the primary cilium in a Hh-dependent manner. I inserted the ALFA-tag into the first extracellular domain of SMO near the N-terminus (ALFA-SMO). This approach has previously been used for YFP (Milenkovic et al., 2009) (**Figure 51A**). I expect ALFA-SMO only to be localized in the ciliary membrane after Hh stimulation. This would allow to specifically capture isolated primary cilia using anti-ALFA nanobodies coupled to a matrix (Muyldermans, 2013) (**Figure 51B**). ALFA-Smo protein that is shuttled in endosomes or is present in the

ER/Golgi (Milenkovic et al., 2009) does not expose the tag to the extracellular environment, while I expect the concentration of ALFA-SMO to be vanishingly low in the PM like it is for endogenous SMO (Milenkovic et al., 2009). After generating the *ALFA-Smo* plasmid, as a proof-of-principle, I heterologously expressed it in HEK293 cells and analyzed ALFA-Smo expressing by Western Blot (**Figure 51C**). I observed specific bands using an anti-ALFA-tag antibody in *ALFA-Smo* transfected cells but not in mock-transfected HEK293 cells. However, the bands appeared at the upper part of the stacking gel, indicating that the ALFA-SMO protein aggregated and did not enter the sodium-dodecyl polyacrylamide gel. In contrast, the loading control, β-tubulin, appeared at the calculated molecular weight of around 50 kDa in transfected and mock-transfected cells. Thus, ALFA-SMO seems to be expressed, but I could not verify whether a full-length protein is expressed. Next, I analyzed ALFA-SMO, expressed in HE293 cells, which I could isolate using anti-ALFA-tag nanobodies bound to magnetic beads (**Figure 51D**). To reduce protein aggregation, I incubated the samples with SDS sample buffer containing 8% instead of 4% β-mercaptoethanol for 1 h instead of 10 min at RT before loading. Indeed, ALFA-SMO bound to the beads as I observed two specific bands around the expected molecular weight of ALFA-SMO (60 kDa). Thus, I generated stable cell mIMCD-3 cell lines with the *ALFA-Smo* construct.

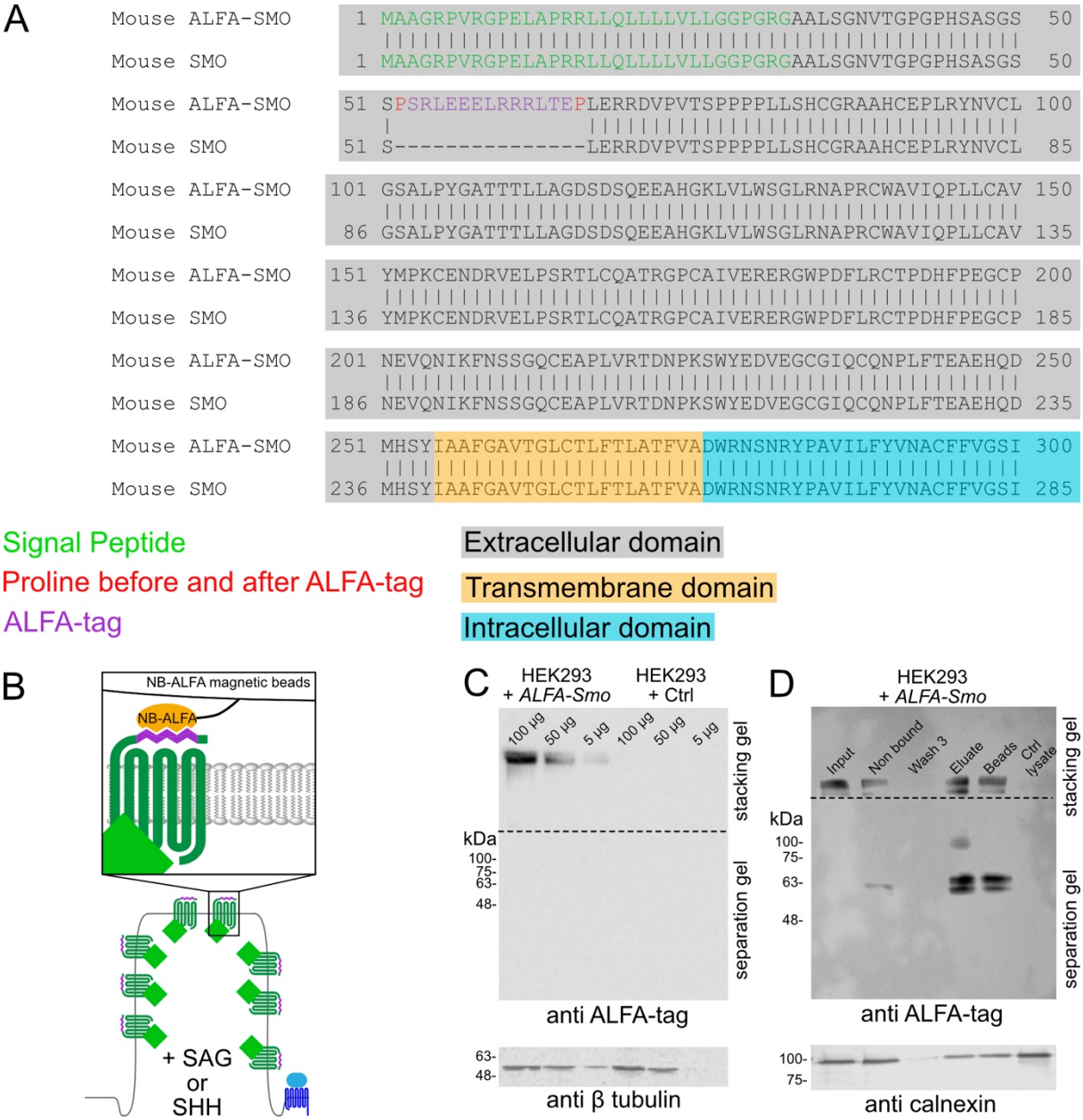

Figure 51: Generating extracellular ALFA tagged SMO to improve accuracy and reproducibility of primary cilia isolation. A: Partial alignment of translated *ALFA-Smo* plasmid sequencing results (ALFA-SMO AA1-300) with mouse SMO (AA1-285, UniProt ID P56726). **B:** Illustration to depict how the ALFA-SMO can be used for affinity purification of the ciliary membrane from SAG or SHH stimulated cells using NB-ALFA magnetic beads. **C:** Western blot analysis of *ALFA-SMO* transfected HEK293 cells from total lysates (left side) or mechanical lysates, where ALFA-SMO and attached endoplasmic reticulum membrane was pulled down using anti-ALFA magnetic beads.

As the ALFA-tag insertion seems to work for SMO, I also engineered the ALFA-tag into the first extracellular domain of PTCH1, again based on a strategy shown for insertion of YFP (Rohatgi et al., 2007) (**Figure 52A**). In contrast to ALFA-SMO, ALFA-PTCH1 should allow me to pull-down primary cilia from cells without Hh stimulation (**Figure 52B**). For ALFA-PTCH1, I generated stable mIMCD-3 cell lines as well.

A

```
Mouse ALFA-PTCH1   1  MASAGNAAGALGRQAGGGRRRRTGGPHRAAPDRDYLHRPSYCDAAFALEQ  50
                      ||||||||||||||||||||||||||||||||||||||||||||||||||
Mouse PTCH1        1  MASAGNAAGALGRQAGGGRRRRTGGPHRAAPDRDYLHRPSYCDAAFALEQ  50

Mouse ALFA-PTCH1  51  ISKGKATGRKAPLWLRAKFQRLLFKLGCYIQKNCGKFLVVGLLIFGAFAV 100
                      ||||||||||||||||||||||||||||||||||||||||||||||||||
Mouse PTCH1       51  ISKGKATGRKAPLWLRAKFQRLLFKLGCYIQKNCGKFLVVGLLIFGAFAV 100

Mouse ALFA-PTCH1  101 GLKAANLETNVEELWVEVGGRVSRELNYTRQKIGEEAMFNPQLMIQTPKE 150
                      |||||||||||||||||||||||||||||||||||||||||||||||||||
Mouse PTCH1       101 GLKAANLETNVEELWVEVGGRVSRELNYTRQKIGEEAMFNPQLMIQTPKE 150

Mouse ALFA-PTCH1  151 EGANVLTTEALLQHLDSALQASRVHVYMYNRQWKLEHLCYKSGELITETG 200
                      ||||||||||||||||||||||||||||||||||||||||||||||||||||
Mouse PTCH1       151 EGANVLTTEALLQHLDSALQASRVHVYMYNRQWKLEHLCYKSGELITETG 200

Mouse ALFA-PTCH1  201 YMDQIIEYLYPCLIITPLDCFWEGAKLQSGTAYLLPSRLEEELRRRLTEP 250
                      ||||||||||||||||||||||||||||||||||
Mouse PTCH1       201 YMDQIIEYLYPCLIITPLDCFWEGAKLQSGTAYLL---------------- 235

Mouse ALFA-PTCH1  251 GKPPLRWTNFDPLEFLEELKKINYQVDSWEEMLNKAEVGHGYMDRPCLNP 300
                      ||||||||||||||||||||||||||||||||||||||||||||||||||||
Mouse PTCH1       236 GKPPLRWTNFDPLEFLEELKKINYQVDSWEEMLNKAEVGHGYMDRPCLNP 285
```

Proline before and after ALFA-tag

ALFA-tag

Extracellular domain

Transmembrane domain

Intracellular domain

B

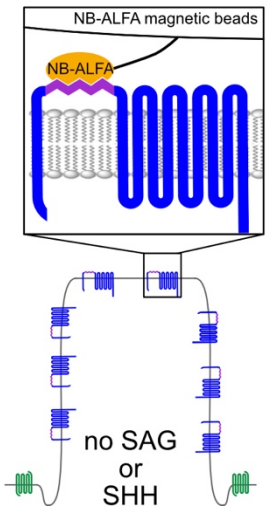

Figure 52: Generating extracellular ALFA tagged PTCH1 to improve accuracy and reproducibility of primary cilia isolation. A: Partial alignment of translated *ALFA-Ptch1* plasmid sequencing result (ALFA-PTCH1 AA1-300) with mouse PTCH1 (AA1-285, UniProt ID Q61115). **B:** Illustration to depict how the ALFA-PTCH1 can be used for affinity purification of the ciliary membrane from non-stimulated cells using NB-ALFA magnetic beads. **C:** Western blot analysis of *ALFA-Ptch1* transfected HEK293 cells from total lysates (left side).

I transduced mIMCD-3 cells with either the *ALFA-Smo* or *ALFA-Ptch1* construct using an HIV-based lentiviral transduction system for stably integrating each construct into the cell's genome. Six passages after transduction, I analyzed the cells by ICC before and after Hh pathway stimulation (**Figure 53**). To this end, I used mIMCD-3 wild-type (WT) cells as a control and exposed all cell lines to DMSO (ctrl) or 3 µM SAG for 24 h to analyze the localization of the ALFA-tag proteins under basal or stimulated Hh

signaling (**Figure 53A**). As a control for Hh activity, I also labeled cells with an anti-SMO antibody, which detects both endogenous and ALFA-SMO. WT cells were only positive for SMO after Hh stimulation but not for the ALFA-tag (**Figure 53B**). In mIMCD-3 *ALFA-Smo* cells, I detected ALFA-specific signals in primary cilia, but I could not observe differences between ctrl or SAG conditions (**Figure 53C**). Moreover, the anti-SMO antibody only labeled cilia that were also positive for ALFA-SMO, but I could not detect endogenous SMO labeling. This observation is likely due to the SMO labeling of heterologously expressed *ALFA-Smo* being too strong to observe the endogenous signal by eye. In mIMCD-3 *ALFA-Ptch1* cells, I could observe endogenous SMO labeling that was more pronounced in the SAG stimulated cells. However, similar to mIMCD-3 *ALFA-Smo* cells, the ALFA-specific signal was present in both ctrl and SAG stimulated cells (**Figure 53B & C**). Thus, either overexpression or the ALFA-tag itself causes accumulation in the primary cilium in a Hh-independent manner.

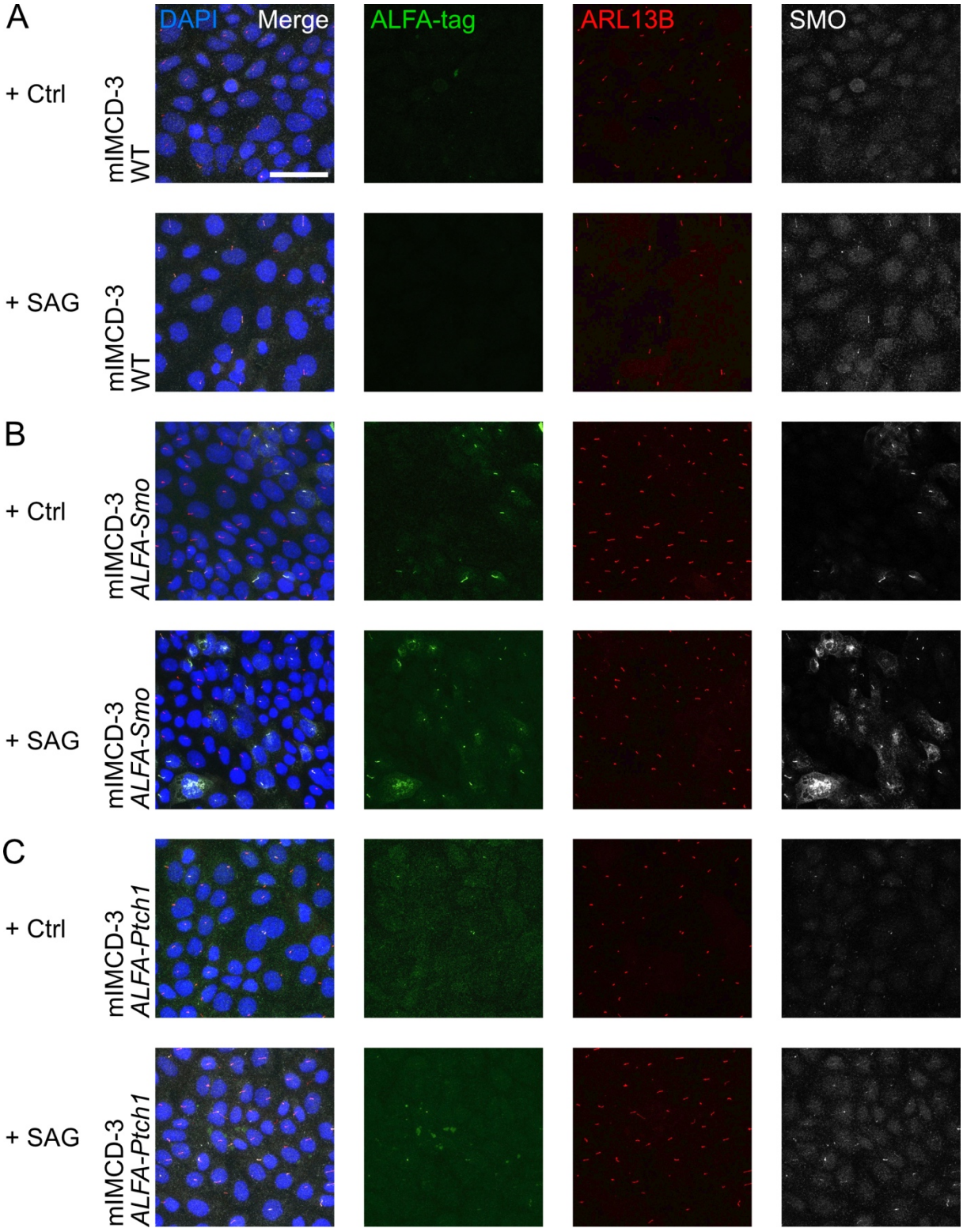

Figure 53: Characterization of mIMCD-3 cells with stable ALFA-tagged protein expression using ICC and confocal microscopy. A-C: Ciliated mIMCD-3 WT (A), mIMCD-3 *ALFA-Smo* (B), and mIMCD-3 *ALFA-Ptch1* cells were treated with 3 µm SAG or 1:1000 DMSO (+ Ctrl) as indicated and stained with DAPI (blue) to label DNA, and antibodies against the ALFA-tag (green), ARL13B (red), and SMO (grey). Scale bar: 40 µm.

As the expression in the different cell lines was also heterogenous, I performed fluorescent-assisted cell sorting (FACS) to generate monoclonal cell lines.

To this end, I labeled ciliated mIMCD-3 WT, mIMCD-3 *ALFA-Smo,* and mIMCD-3 *ALFA-Ptch1* cells using an Alexa Fluor 488 (A488)-coupled anti-ALFA nanobody (anti-ALFA A488) and subjected them to FACS. Compared to mIMCD-3 WT cells, mIMCD-3 *ALFA-Smo* and mIMCD-3 *ALFA-Ptch1* displayed a specific anti-ALFA A488 signal, which I separated into a high and low signal (**Figure 54A**).

I propagated single cells from each of the mIMCD-3 *ALFA-Smo* and mIMCD-3 *ALFA-Ptch1* to generate monoclonal cell lines and characterized these cell lines using ICC and SAG-induced Hh pathway stimulation. The cell line mIMCD-3 *ALFA-Smo* D2 showed SAG-dependent accumulation of ALFA-SMO in the ciliary membrane and the majority of cells being positive for ciliary ALFA-SMO (**Figure 54B**). Of note, I labeled cells with the anti-ALFA nanobody before fixation or permeabilization, thereby exclusively labeling extracellularly accessible ALFA-tag. For ALFA-PTCH1, the cell line mIMCD-3 *ALFA-Ptch1* B2 appeared most promising, showing a specific ALFA-PTCH1 signal in the majority of cilia. Although the signal appeared to be more pronounced in the ctrl, I also observed ALFA-PTCH1 in cilia of SAG stimulated cells (**Figure 54C**). Nevertheless, I continued using this cell clone. In summary, these two cell lines provide the following: mIMCD-3 *ALFA-Ptch1* B2 allows to pull-down non-stimulated primary cilia, while mIMCD-3 *ALFA-Smo* D2 allows enriching cilia with active Hh signaling. In future experiments, I can now combine the established cilia isolation with the ALFA-specific pull-down to achieve a sufficient and constant probe quality for lipidome analysis.

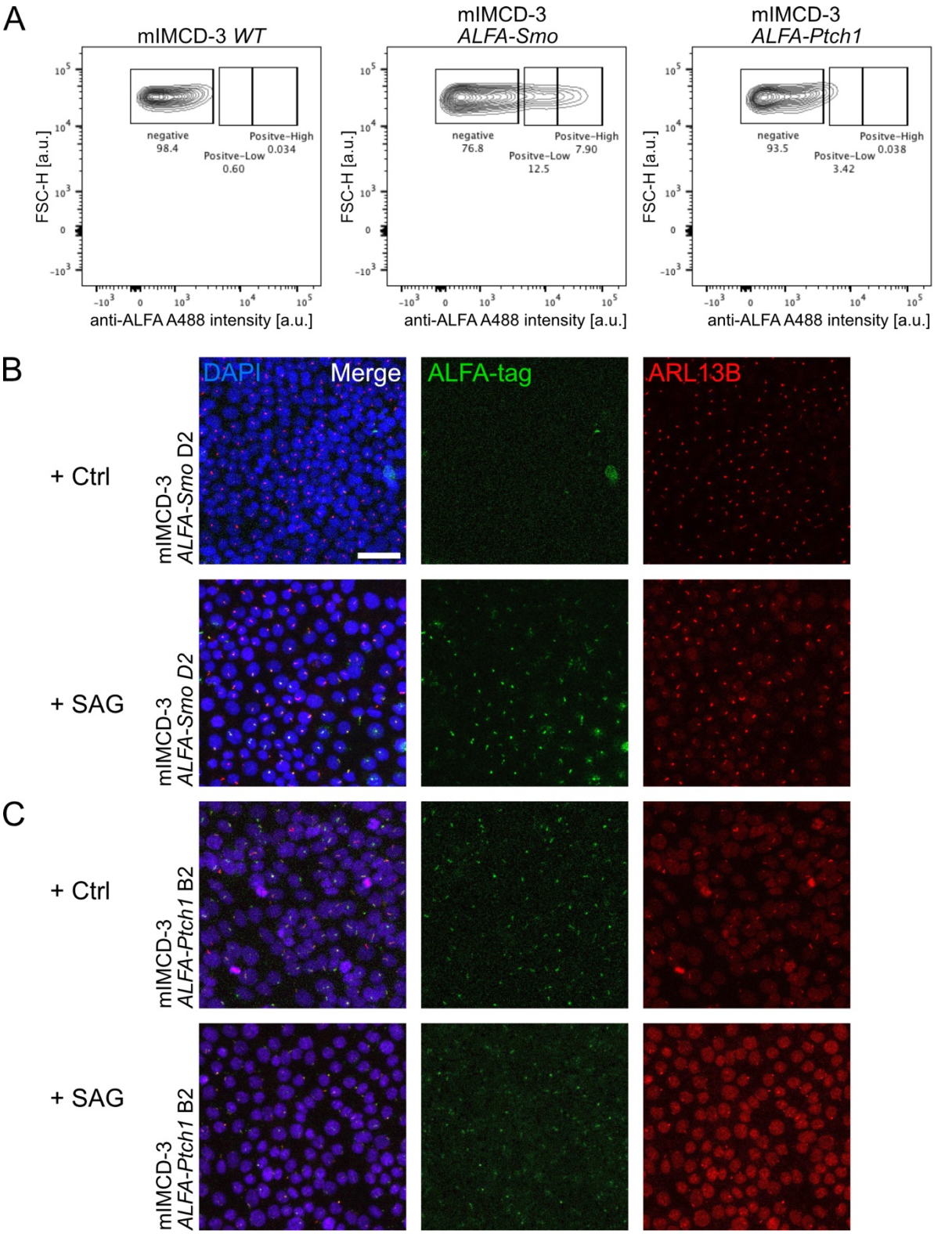

Figure 54: Generation and characterization of stable ALFA-SMO or ALFA-PTCH1 expressing monoclonal cell lines using fluorescent-activated cell sorting (FACS) and immunolabeling with confocal microscopy. **A:** Stable low expressing mIMCD-3 ALFA-SMO or ALFA-PTCH1 single cells were selected via FACS based on fluorescent intensity, and propagated. **B:** Ciliated monoclonal cell lines mIMCD-3 *ALFA-Smo* D2 and mIMCD-3 *ALFA-Ptch1* B2 were treated with 3 µm SAG or 1:1000 DMSO (+ Ctrl) as indicated and stained with DAPI (blue) to label DNA, and antibodies against the ALFA-tag (green), and Arl13b (red). Scale bar: 40 µm.

4 Discussion

In my thesis, I demonstrated that primary cilia depict a higher-ordered membrane compared to the PM. This fits into the model of the CM being enriched in SPLs and lipid rafts, which has been proposed based on the identification of the lipid raft-specific gangliosides GM3 and GM1, lipid raft marker proteins, and SM in the CM. Furthermore, whereas the PM order could be further increased by increasing GSL levels, the CM was inert to these changes, which underlines that even at basal conditions, the CM order is already so high that it cannot be increased any further. To specifically delineate the lipid composition of the CM, I established a method to isolate and purify primary cilia for mass-spectrometric lipid analysis. My preliminary data also depicted a higher SM and GM3 content in the CM compared to the PM.

Although the CM could not be further increased upon increasing GSL levels, I observed differences in ciliary Hh signaling. These differences were cell-type specific, which suggests that GSL homeostasis is either differentially regulated in different cell types or that Hh signaling is regulated in a cell type-specific manner. In my Ph.D. thesis, I have established all the techniques to now perform quantitative analyses and determine changes of the membrane order in a cell-type and signaling state-specific manner, as well as quantify lipid species from isolated and purified primary cilia in a signaling state-specific manner.

Furthermore, as I have established different biosensors for imaging ciliary cAMP dynamics, it is now possible to delineate the molecular mechanisms underlying ciliopathies that might lead to the development of curative therapies instead of symptomatic treatments.

4.1 Analyzing ciliary cAMP dynamics using cAMP biosensors to delineate ciliary signaling and function

My thesis results demonstrated that increasing GSL levels using GBA2 altered the dynamic ciliary shuttling of the $G\alpha_i$ coupled receptor SMO. However, the apparent changes in the altered SMO localization, which is a key mediator of Hh signal transduction, did not result in significant differences of Hh target gene expression. An essential step between SMO translocation to the cilium and the downstream transcriptional response is signal transduction via second messengers, in particular

cAMP. Thus, analyzing ciliary cAMP dynamics under the studied conditions would be the first step in unraveling how the cell might compensate on the molecular level.

After the release of SMO inhibition from PTCH1, SMO mediates the activation of Hh signaling via re-structuring the multisite-phosphorylation landscape of GLI transcription factors, thereby, turning them from repressor (GLI-R) into activators (GLI-A) for Hh gene expression (Han et al., 2019; Kong et al., 2019). The balance between repressor and activator forms (GLI-R and GLI-A, respectively) determines the activity of the Hh pathway, which is controlled by GLI multisite phosphorylation via PKA and atypical protein kinase C (aPKC) (Atwood et al., 2013; Niewiadomski et al., 2014). PKA has been shown to be the master regulator in this process, as pharmacological inhibition of PKA completely blocks Hh activation and genetic ablation of PKA strongly shifts the balance to GLI-A (Niewiadomski et al., 2014). Results from several studies suggest that $G\alpha_s$ activity of GPR161 increases (Mukhopadhyay et al., 2013), whereas the $G\alpha_i$ activity of SMO decreases cAMP levels (Shen et al., 2013) to control PKA activity in the primary cilium (Mick et al., 2015; Moore et al., 2016). Taking my results into account, altered ciliary SMO localization would then alter ciliary cAMP levels; however, these changes could be compensated by altered ciliary GPR161 localization, which would likewise be changed. Although the mechanisms underlying SMO and GPR161 trafficking to the primary cilium are different, results by other studies support the hypothesis that re-balancing ciliary SMO and GPR161 levels can rescue dysfunctional Hh signaling (Chavez et al., 2015; Dyson et al., 2016; Garcia-Gonzalo et al., 2015): Underlying ciliary cAMP dynamics have, also there, not been analyzed. These studies focused on the *Inpp5e*-KO model, in which GPR161 is enriched in the cilium and does not exit upon Hh pathway activation. In parallel, ciliary SMO enrichment is reduced upon Hh pathway activation, which results in decreased Hh target gene expression after SAG stimulation. Interestingly, the heterologously expressed, constitutively active, PTCH1-independent mutant SMOM2 localizes to primary cilia in *Inpp5e*-KO mEFB and partly rescue the *Inpp5e*-KO phenotype *in vivo* (Dyson et al., 2016): *Inpp5e*-KO mice expressing SMOM2 (*Inpp5e*$^{-/-}$*, CMVCre; SmoM2*) show a complete rescue of *Ptch1* mRNA levels, the bilateral anophthalmia and exencephaly, and partial rescue of the edema, hindlimb polydactyly, and cleft palate. I hypothesize that this might be due to the reduction of ciliary cAMP levels via SMOM2 activity, which counteracts the constitutive activity of GPR161 in the cilium. Noteworthy, Dyson and colleagues were

the only ones reporting reduced ciliary SMO levels after SAG stimulation in *Inpp5e*-KO mEFBs, while Chavez and Garcia-Gonzalo did not identify changes in ciliary SMO localization (Chavez et al., 2015; Dyson et al., 2016; Garcia-Gonzalo et al., 2015). These discrepancies might be due to the cell model used: similar to my approach, Chavez and Garcia-Gonzalo both performed their experiments using SV40-transformed mEFB (Chavez et al., 2015; Garcia-Gonzalo et al., 2015), whereas Dyson and colleagues performed their experiments using primary mEFB at low passage numbers (Dyson et al., 2016). Dyson and colleagues pointed out that SV40 activates Hh and other signaling pathways, which increases the expression of Hh components, including SMO (Ali-Seyed et al., 2006). Additionally, the survival of SV40-transformed cells relies on active Hh signaling (Ali-Seyed et al., 2006). Thus, using primary cells of low passage numbers might be the method of choice to analyze ciliary Hh signaling in future studies. This needs to be combined with measuring ciliary cAMP dynamics to understand the molecular mechanisms underlying disease development.

To measure ciliary cAMP dynamics, cAMP biosensors need to be targeted to the primary cilium. Most targeting strategies are based on fusion to full-length and functional GPCRs (Marley et al., 2013; Moore et al., 2016; Mukherjee et al., 2016) or other ciliary proteins, like ARL13B (Jiang et al., 2019) or constitutive active RAB23 Q68L (Truong et al., 2021). Constitutive GPCR activity is a common phenomenon (Seifert and Wenzel-Seifert, 2002) and overexpression of a GPCR in the cilium to target a cAMP biosensor, thus, likely alters ciliary cAMP levels and subsequently, results in changes of ciliary cAMP dynamics. Comparing the measurements in my thesis using the ratiometric cADDis-mCherry cAMP biosensors, targeted to the cilium using 5-HT_6 receptor fusion, compared to the mNPHP3(201) targeting strategy underlines this hypothesis as the maximal fold-change upon increasing cAMP levels was significantly reduced for cADDis-mCherry. For targeting using ARL13B, the situation might be somehow similar: ARL13B regulates ciliary INPP5E levels and the transport of ciliary proteins (Fujisawa et al., 2021). Although ciliary Hh signaling remained unchanged upon ARL13B exclusion from primary cilia (Gigante et al., 2020), ARL13B seemed to exert its function on Hh signaling in the cytoplasm in endosomes (Gigante et al., 2020). Endosomal trafficking is one way SMO enters the cilium besides lateral trafficking through the PM. Thus, using functional ARL13B as a ciliary targeting strategy might change the ciliary proteome and, thereby, also alter ciliary cAMP

dynamics. Last but not least, RAB23-dependent targeting appears even less suited to analyze ciliary cAMP dynamics during Hh signaling: RAB23 is a well-characterized antagonist of SHH and regulates ciliary SMO levels (Boehlke et al., 2010; Eggenschwiler et al., 2006; Eggenschwiler et al., 2001; Evans et al., 2005). In summary, mNPHP3(201) provides the only ciliary targeting strategy used to date for analyzing cAMP dynamics without altering ciliary cAMP dynamics itself.

Unfortunately, we also demonstrated that the N-terminal fusion of mNPHP3(201) can diminish the function of optogenetic tools and fluorescent biosensors, particularly the light-dependent activation (Hansen et al., 2020). However, we developed a targeting strategy using nanobodies, which not only preserves protein function upon ciliary targeting, but also provides a new toolbox to target any protein to a subcellular compartment and analyze cellular functions *in vitro* and *in vivo* in different microdomains (Hansen et al., 2020).

A general question that remains is how a cell generates a signaling pathway-specific output when using cAMP as a second messenger. Cellular functions controlled by intracellular cAMP signaling are very diverse, ranging from gene expression (Wang et al., 2000; Yamamoto et al., 1988), cell migration (Howe, 2004; Zimmerman et al., 2015), to cell proliferation and cell death (Insel et al., 2012). One approach to tackle this problem is to compartmentalize cAMP signaling using protein scaffolds combined with compartment-specific phosphodiesterase (PDE) isoforms to restrict cAMP diffusion out of these compartments (Lefkimmiatis and Zaccolo, 2014). So far, this concept has only been developed for cAMP signaling in the cytoplasm.

The primary cilium is a signaling hub for various GPCRs and ACs (Wachten and Mick, 2021). We and others have recently shown that cAMP signaling in the primary cilium and cytoplasm differentially control cellular functions (Guo et al., 2019; Hansen et al., 2020; Truong et al., 2021).

To investigate the signaling pathways that are regulated by ciliary cAMP signaling, we analyzed gene expression using RNA-sequencing in cells expressing the bacterial, photoactivated adenylyl cyclase (bPAC) either in the cilium or the cell soma after light stimulation. bPAC is an optogenetic tool produces cAMP upon blue light stimulation (Stierl et al., 2011). Targeting bPAC exclusively to subcellular compartments or restricted pattern illumination allows controlling cAMP synthesis with spatio-temporal precision. We applied this approach in primary cilia and demonstrated that ciliary cAMP

levels in cells expressing bPAC in the primary cilium (cilia-bPAC) are higher compared to cells expression bPAC in the cytoplasm (cyto-bPAC) after light stimulation. Vice versa, cytosolic but not ciliary bPAC increased total cAMP levels after light stimulation (**Figure 55**).

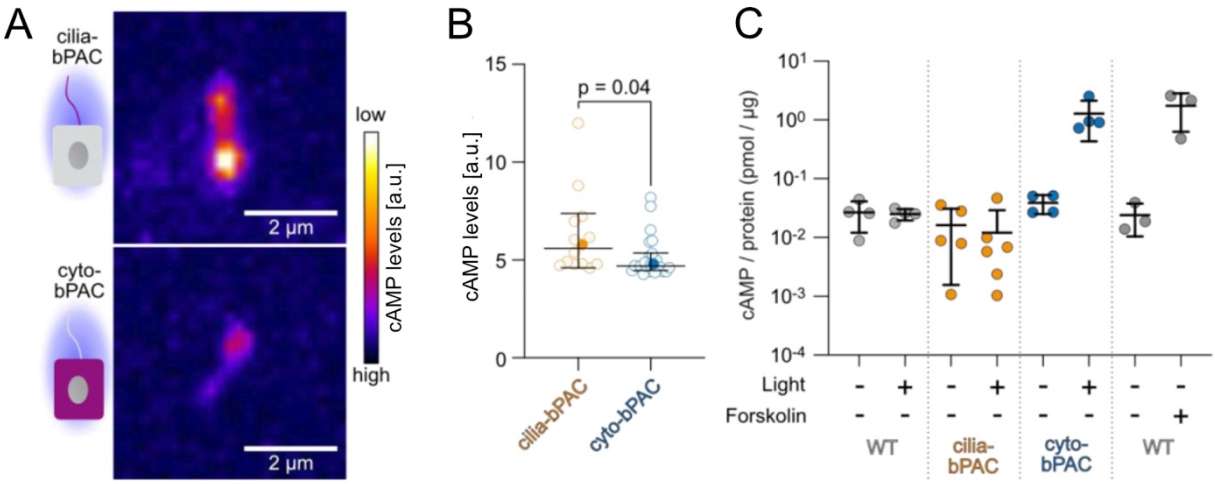

Figure 55: Spatial manipulation of ciliary cAMP using optogenetics. A-B: Measuring ciliary cAMP levels depicts higher ciliary cAMP levels in cells expressing cilia-bPAC compared to cells expressing cyto-bPAC after the exposure to blue light. **C:** ELISA-based measurements of total cAMP levels from wild-type (WT), cilia-bPAC, or cyto-bPAC mIMCD-3 cells kept in the dark or light-stimulated (1 h, 465 nm, 38.8 µW/cm²) and WT cells stimulated with DMSO (as control) or 10 µM of Forskolin (1 h). Figure and legend adapted from (Hansen et al., in revision)

Strikingly, increasing ciliary cAMP levels evoked a distinct gene expression that is different from the changes evoked by increasing cAMP levels in the cytoplasm (**Figure 56**) (Hansen et al., *in revision*).

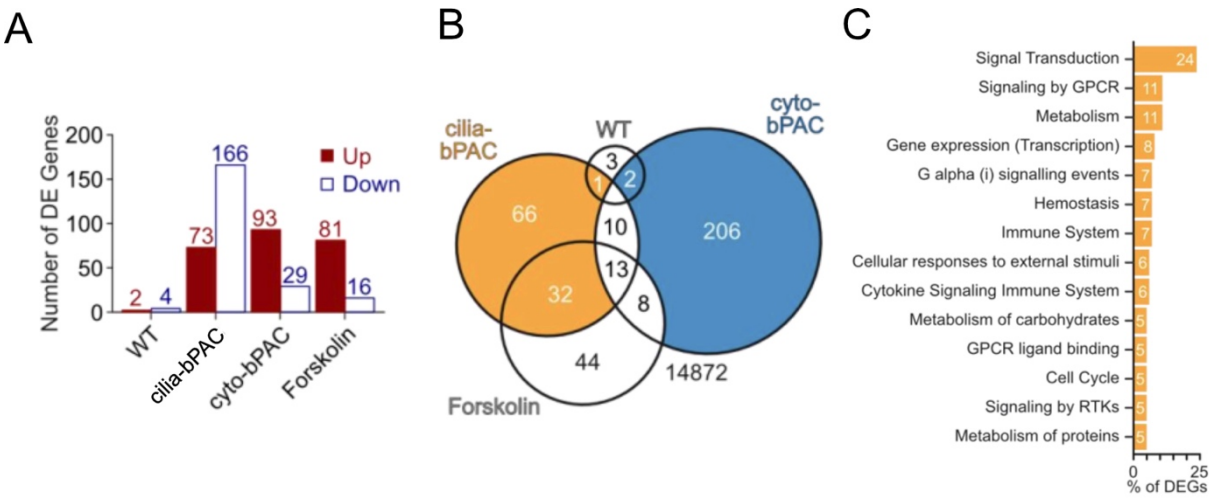

Figure 56: Ciliary cAMP signaling evokes a specific gene expression signature compared to somatic cAMP signaling. A: Differentially expressed (DE) genes unraveled by RNASequence analysis of mIMCD-3 cells with the indicated conditions. Wild-type (WT), cilia-bPAC, and cyto-bPAC: light-stimulated cells were compared to cells kept in the dark. Forskolin: WT cells stimulated with 10 µM of Forskolin were compared to WT cells incubated with DMSO (control). **B:** Venn diagram of the DE genes. **C:** Participation of the DE genes identified in cilia-bPAC cells in specific reactomes; for more details, see (Hansen et al., *in revision*). Figure and legend taken from (Hansen et al., *in revision*).

Our results nicely underline how the primary cilium evokes a specific cellular output using cAMP signaling. In line with what has been shown for subcellular compartments in the cytosol, we hypothesized that PDEs also compartmentalize cAMP signaling in the primary cilium. Indeed, our results demonstrated that PDEs in general and specifically the PDE4C isoform, which localizes to primary cilia (Choi et al., 2011), maintains the ciliary cAMP compartment in our cell system.

However, the question remains how a cell generates a pathway-specific cellular response using cAMP as a second messenger when several cAMP-dependent pathways are localized to the same compartment, i.e., the primary cilium. In terms of cAMP signaling, I can imagine a model where ciliary signaling pathways are localized in nanodomains within the cilium (**Figure 57**):

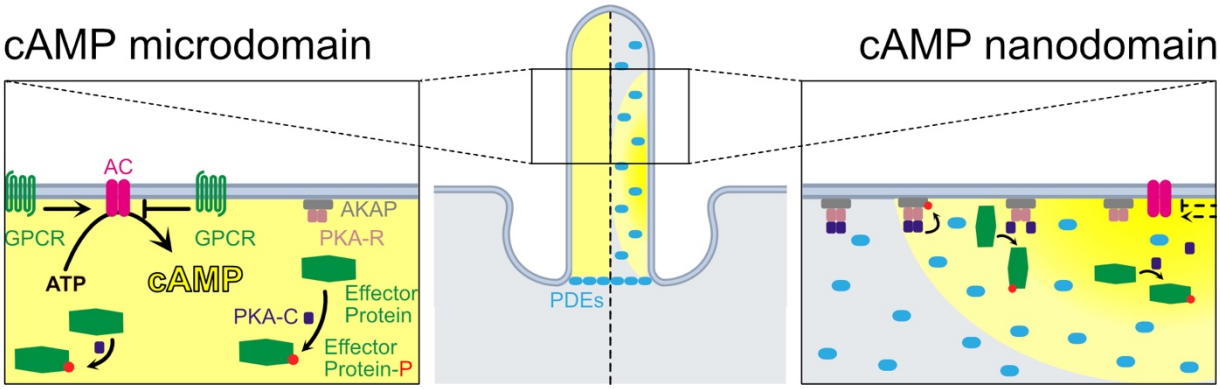

Figure 57: Putative model of further ciliary cAMP compartmentalization into nanodomains. The spatial organization of the following proteins play a key role in the nanodomain compartmentalization: G protein-coupled receptor (GPCR), transmembrane adenylyl cyclase (AC), A-kinase anchoring protein (AKAP), protein kinase A (PKA) regulatory (PKA-R) and catalytic (PKA-C) subunit, and phosphodiesterase (PDE). For details see text.

Here, ciliary PDEs would restrict cAMP to nanodomains within the cilium and the target proteins which PKA phosphorylates depends in the cAMP concentration, i.e., at very high cAMP concentrations around the activated ACs, the PKA-C subunits dissociate from the PKA-R subunits and phosphorylate all target proteins around the origin of cAMP production. At lower cAMP levels, the PKA-C and PKA-R subunits stay together. Still, they could proceed with phosphorylation as an intact holoenzyme in the "open state" of targets in close proximity, like other proteins in a scaffold complex, or in the "closed state" of targets in immediate proximity, like AKAPs.

The findings of several studies support the more localized model of cAMP signaling in nanodomains. First of all, studies stated that an almost 5-fold higher cAMP concentration is required for the half-maximal activation (EC_{50}) of membrane-associated PKA (Koschinski and Zaccolo, 2017), compared to *in vitro* measurements

that determined an EC_{50} of 100-300 nM cAMP (Adams et al., 1991; Mongillo et al., 2004). Basal intracellular cAMP concentrations are estimated to range from 100 nM to almost 1 µM and basal ciliary cAMP levels are supposed to be similar (Borner et al., 2011; Jiang et al., 2019). Of note, the latter statement is under debate in the field as another group reported higher ciliary cAMP levels compared to the cytosol (Moore et al., 2016). Nonetheless, a consequence of the higher PKA EC_{50} is that PDEs would restrict PKA-activating cAMP concentrations more locally and possibly, only the PKA-C subunits near the site of cAMP concentration would be able to dissociate. Second, in line with these findings is the discovery that PKA can proceed its activity as an intact holoenzyme that can phosphorylate targets within 250 ångström (Å) in an "open state" and within 150 Å in a "closed state" (Smith et al., 2017). Third, scaffolds for local cAMP signaling axis proteins are also present in the primary cilium, e.g., GPR161 functions as an AKAP for PKA (Bachmann et al., 2016), while PDE4C localizes to primary cilia as part of a multi-protein complex including another AKAP (Choi et al., 2011). Fourth, accumulation and PKA-independent processing of GLI at the most distal part of the primary cilium after Hh pathway activation demonstrates that signaling occurs within nanodomains in the ciliary compartment (Wen et al., 2010). Finally, earlier findings of the Wachten lab already demonstrated that cAMP signaling is compartmentalized into smaller domains within motile cilia, i.e., sperm flagella (Mukherjee et al., 2016; Raju et al., 2019). In addition to this model, a study by Truong and colleagues suggested that the geometric shape of the cilium, which results in a greater surface to volume ratio compared to the cell body, leads to much more efficient activation of PKA and, thereby, another layer of possible compartmentalization of ciliary cAMP signaling (Truong et al., 2021). Further studies of ciliary cAMP dynamics, improving data analysis and progress in the implementation of optogenetic tools will allow testing this and other models in the near future.

Progress in the analysis of ciliary cAMP signaling *in vivo* or *ex vivo* in tissue from ciliopathy patients might also improve therapeutic approaches: if ciliary cAMP signaling in the respective ciliopathy is dysregulated, unraveling the tissue specificity would allow treatment with PDE isoform-specific activators or inhibitors. This could provide a curative therapy at best.

Likewise, the analysis of ciliary cAMP signaling *in* or *ex vivo* of cancerous tissue might also improve therapeutic approaches: Dysregulation of Hh signaling is the cause of

approximately 25% of all human cancer, including basal cell carcinoma (BBC), and SMO has become a promising drug target (Ruat et al., 2014; Skoda et al., 2018). In BBC therapy, SMO antagonists, like Vismodegib or Sonidegib, are used, but 50% of patients show no response, some show worsening of cancer progression, and 20% develop drug resistance during treatment (Habashy et al., 2021). On the one hand, analysis of the ciliary cAMP signaling in the respective tissue might unravel whether or not it is dysregulated and therapies might focus on rescuing it. On the other hand, manipulation of the ciliary cAMP levels might balance the dysregulated Hh signaling. More specifically, SMO hyperactivation and uncoupling from PTCH1 inhibition, which strongly shifts the balance to GLI-A production is the underlying cause in some cancers. In line with this, another study showed that loss of ciliary ACs, and thereby ciliary cAMP production, also results in a complete shift to GLI-A production while GLI-R processing is lost (Somatilaka et al., 2020). Consequently, increasing PKA activity by elevated cAMP levels to generate more GLI-R in a tissue-specific manner could, therefore, be of great benefit to rescue the dysregulated Hh signaling.

4.2 The role of GSLs in ciliary cAMP signaling

Before discussing the role of GSLs in ciliary cAMP signaling, I want to briefly highlight that the membrane lipid cholesterol also plays an essential role by direct modulation of GPCR activity. To date, roughly 15 GPCRs exhibit cholesterol-dependent function (Paila and Chattopadhyay, 2010; Paila et al., 2011; Pydi et al., 2016) and around 50 GPCRs are candidates to exhibit a cholesterol-dependent function (Sarkar and Chattopadhyay, 2020). For ciliary Hh signaling, SMO has shown to be activated by ciliary cholesterol from the outer leaflet, controlled by PTCH1, which transports cholesterol from the outer to the inner leaflet of the lipid bilayer (Kinnebrew et al., 2019; Kinnebrew et al., 2021). The binding of SHH to PTCH1 blocks its transport function and results in ciliary PTCH1 exit, whereby the increased outer leaflet cholesterol activates SMO to drive Hh pathway activity via several mechanisms, one of which is the $G\alpha_i$ subunit activation of SMO, thereby, reducing cAMP levels (Kinnebrew et al., 2019; Kinnebrew et al., 2021). Thus, the cell regulates ciliary GPCR activity via redistribution of a membrane lipid, cholesterol, which could be a general mechanism for the cells to regulate receptor activity using other lipids that have the ability also to modulate protein activity: GSLs.

The cilium contains high concentrations of SPLs and lipid raft domains seem to be ideal to regulate GPCR activity via GSLs and, thereby, ciliary cAMP. Although no study, except my thesis, analyzed ciliary signaling with respect to ciliary GSLs, one recent study demonstrated that primary cilia could regulate the activity of the downstream target of RTKs, the serine/threonine kinase Akt, by modulating lipid raft dynamics outside of the cilium (Yamakawa et al., 2021). I hypothesize that the cell could also modulate lipid raft dynamics inside primary cilia. In line with this hypothesis, another recent study compared the activity of ciliary GPCRs in primary cilia and the plasma membrane in ciliated and non-ciliated cells (Jiang et al., 2019): Except for the GPCR dopamine D1 receptor (D1R), which has a cholesterol-binding domain for localization in cholesterol-based lipid rafts (Tiu et al., 2020), none of the other analyzed GPCRs, 5-HT_6, SSTR3, prostaglandin E_2 receptor 4 (EP4), and vasopressin receptor 2 (V2R) have been connected to cholesterol. Surprisingly, Jiang and colleagues found these receptors to exhibit different activities, depending on whether the cell was ciliated or not. In more detail, this study demonstrated that ciliary GPCR activity appears to be diminished or even abolished in or by primary cilia, while Hh pathway stimulation relieved this mechanism and up-regulated ciliary GPCR activity (Jiang et al., 2019). Jiang and colleagues could not provide an underlying molecular mechanism, while cholesterol is an unlikely candidate to regulate activity of all these receptors, except D1R. In speculation, the primary cilium-regulated lipid raft dynamics outside of the cilium that Yamakawa and colleagues observed (Yamakawa et al., 2021) were the cause of different GPCR activities in the study of Jiang and colleagues (Jiang et al., 2019). Consequently, the likewise observed differences in GPCR activity in primary cilia would have been caused by lipid raft dynamics in the primary cilium.

Thus, in addition to cholesterol-dependent regulation of GPCR signaling, cells likely employ GSLs to regulate GPCR signaling in cilia. On the molecular level, this is supported by the following findings: lipid rafts, consisting of cholesterol, GSLs and SM, as well as lipid raft-associated proteins, have been documented in the ciliary membrane, and my results demonstrated that the order of the ciliary membrane is particularly high. GSLs might dynamically determine the lipid identity of ciliary lipid rafts and, thereby, alter the composition of lipid raft-associated proteins, which, in turn, regulates ciliary signaling. One example in this is the following: G protein-coupling of the Takeda G protein-coupled receptor 5 (TGR5) switches from $G\alpha_s$- to $G\alpha_i$-coupling

upon translocation to the primary cilium (Masyuk et al., 2013). I hypothesize that this switch is facilitated by the membrane order determined by the GSL composition in the ciliary membrane. Furthermore, it has been demonstrated that regulation of the biophysical properties of the membrane surrounding a GPCR by GSLs modulates its ligand affinity (Szlenk et al., 2019). Last but not least, GSLs have been shown to directly induce protein conformational changes, leading to, e.g., activation of RTKs (Coskun et al., 2011) or modulate the activity of GPCRs like the glucagon receptor (GCGR) and serotonin receptor 1A (5-HT_{1A}) (Ansell et al., 2020). Vice versa, depletion of GSLs has been shown to impair ligand binding to 5-HT_{1A} (Singh et al., 2012). Finally, the study of Jiang and colleagues observed cell-type-specific differences for the activity of GPCRs (Jiang et al., 2019): in primary cilia of mIMCD-3 cells, GPCR activity was abolished and Hh pathway activation allowed their activity, whereas in cilia of mEFB, GPCR activity was diminished and Hh pathway activation up-regulated GPCR activity, which points to a cell-type-specific regulation of ciliary GPCR signaling.

In summary, there are several potential mechanisms that, so far, have only been demonstrated for GPCRs outside of cilia, by which GSLs might regulate GPCR activity and, in turn, ciliary cAMP dynamics. Moreover, there is evidence that the regulation of these mechanisms is cell-type specific. My study forms the basis for addressing all these exciting questions and unraveling molecular mechanisms underlying the interaction between protein and lipid components regulating ciliary signaling.

4.3 How are ciliary GSLs regulated?

The ciliary protein and lipid identities are tightly regulated but how the cell regulates GSLs in the ciliary membrane is unknown. The three 5´-phosphatases that regulate the ciliary PIP homeostasis, INPP5E, INPP5B, and OCRL localize to microdomains within primary cilia (Conduit and Vanhaesebroeck, 2020), whereas no GSL metabolizing enzyme has yet been identified in primary cilia. While GSL metabolizing enzymes might still be detected in the ciliary membrane in future studies, the focus of the following discussion is built on potential transport mechanisms and metabolizing enzymes outside the cilium that control ciliary GSL homeostasis.

The first candidate that we considered to play a pivotal role in controlling the ciliary GSL homeostasis was GBA2, based on our own studies demonstrating that GBA2 regulates GSL homeostasis in the plasma membrane and is crucial for the function of

sperm cells (Raju et al., 2015; Yildiz et al., 2006). GBA2 degrades GlcCer into glucose and Cer at the ER and cis-Golgi (Körschen et al., 2013). Using confocal fluorescence microscopy, I could confirm that loss of GBA2 function results in a higher PM order. The spatial resolution using confocal microscopy also allowed me for the first time to investigate the CM order, which was significantly higher than the PM order. Supposedly, the CM order could not be further increased after loss of GBA2, but I still observed dysregulation of ciliary SMO localization.

SMO localizes to primary cilia via three transport mechanisms (Milenkovic et al., 2009): The first is direct trafficking of SMO from the Golgi to the cilium via vesicles. A second mechanism is the recycling pathway, which traffics PM-residing SMO to the cilium via endocytosis. A third mechanism is the trafficking of SMO from the Golgi to the plasma membrane, followed by lateral transport through the PM to the cilium. I hypothesize that loss of GBA2 dysregulates lateral transport of SMO. My results further suggest that the ciliary SMO transport mechanisms are cell type-specific: mAFB seem to use direct trafficking, lateral trafficking, and the recycling route for SMO to a different extent than mEFBs and loss of GBA2 likely affects one trafficking pathway more than the other. To quantify the changes in lipid composition upon loss of GBA2, future studies need to perform mass spectrometry from purified cilia as an independent and more quantitative measure compared to the environment-sensitive dyes.

Strikingly, my results demonstrated that also loss of GBA1 altered the ciliary SMO localization. Loss of GBA1 results in GSL accumulation mainly in lysosomes and endosomes (Fuller et al., 2008). Thus, alteration of SMO trafficking through the recycling pathway by endosomal GSL enrichment might have caused this phenotype.

In contrast to GBA2, which regulates the GSL homeostasis at the PM by GlcCer degradation, the glycolipid transfer protein (GLTP) plays a key role in the regulation of GSL homeostasis at the PM by facilitating non-vesicular transport of GSLs (Mishra et al., 2020). Analyzing ciliary signaling and CM order in cells that lack GLTP might reveal a potential role in the regulation of the ciliary lipid homeostasis.

Interestingly, a loss-of-function CRISPR screen using a custom library of 1244 lipid-related genes was performed to identify positive and negative regulators of Hh signaling (Kinnebrew et al., 2019): In detail, a GLI1-GFP Cas9 reporter cell line was transfected with a CRISPR guide RNA library and stimulated with SHH. Afterwards, cells were sorted according to their GFP signal using FACS. The idea behind this is

that when knocking-out a gene whose protein is a positive regulator for Hh signaling, the cell would show a weaker GFP signal in FACS after SHH stimulation and vice versa. Interestingly, genes encoding for proteins that participate in SPL metabolism, i.e., *Cers5, Cers6, Sptlc1 and 2, Sgppl1,* and *Sgms1,* have been identified as negative regulators for Hh signaling. It is now known whether this is due to changes in SPL homeostasis or due to loss of cholesterol depletion in the CM. These findings underline that ciliary Hh signaling might only be regulated by cholesterol and SM in terms of lipids and also shows the limitations of this CRISPR screen: Other ciliary pathways and functions might still depend on the regulation by ciliary GSLs, but genes participating in GSL metabolism that affect these pathways would not show up in a Hh-specific screen. Employing a different cilia-specific pathway using this type of screening would provide further insides.

One model of ciliary compartmentalization proposes restriction of lateral diffusion from proteins and lipids between the PM and CM (Breslow and Nachury, 2011) through action of a "picket fence". The "picket fence" model for primary cilia proposes anchorage of transmembrane proteins to actin networks around the membrane of the ciliary base, the periciliary space, which also depicts a gel-like high membrane order, thereby, abolishing lateral diffusion of lipids and proteins (Kiesel et al., 2020; Kusumi et al., 2012). The periciliary space also invaginates in many cell types, like fibroblasts, and is then referred to as the ciliary pocket. The ciliary pocket enriches in clathrin-coated pits, whereby this region becomes a hub for endocytosis and exocytosis to manage im- and export of ciliary membrane components (Pedersen et al., 2016). Endo- and exocytosis at the ciliary pocket could be one mechanism of the cell to control ciliary GSL homeostasis. This is underlined by findings in cilia of the nematode *Caenorhabditis elegans*, which suggests that the endosomal maturation factors Rabenosyn-5/VPS45 and CAV1 regulate the ciliary lipid homeostasis (Scheidel et al., 2018). As the morphology of the periciliary membrane differs between different cell type, and the lipid composition is a key player in membrane shape (Frolov et al., 2011), one would assume that the regulation of the ciliary GSL homeostasis is cell-type-specific.

Although there are no studies investigating morphological differences between adult and embryonic fibroblasts, these differences could also explain the cell-type specific differences that I observed. The combination of imaging techniques to characterize

and compare morphological differences of the periciliary space from different cell types with spatially resolved mass spectrometry would be ideal. While the latter method has not yet been established, imaging the periciliary space with specific markers has already been established (Garcia et al., 2018).

The cilium uses the release of membrane vesicles from the ciliary tip, termed ectosomes, which is a mechanism for protein-turnover and putative extracellular signaling (Nager et al., 2017; Phua et al., 2017; Wood and Rosenbaum, 2015). As an outlook, enriching these ectosomes with specific lipid species could be another key step in how the cell regulates the ciliary lipid homeostasis. Established protocols for the isolation of extracellular vesicles (Brennan et al., 2020) could be applied for ciliated tissues *in vitro* to compare their lipidome to the lipidome of primary cilia and follow this hypothesis.

5 References

Adams, S.R., A.T. Harootunian, Y.J. Buechler, S.S. Taylor, and R.Y. Tsien. 1991. Fluorescence ratio imaging of cyclic AMP in single cells. *Nature*. 349:694-697.

Albrecht, A.C. 1961. Polarizations and assignments of transitions: The method of photoselection. *J. Mol. Spectrosc.* 6:84-108.

Aldana, J., A. Romero-Otero, and M.P. Cala. 2020. Exploring the Lipidome: Current Lipid Extraction Techniques for Mass Spectrometry Analysis. *Metabolites*. 10:231.

Ali-Seyed, M., N. Laycock, S. Karanam, W. Xiao, E.T. Blair, and C.S. Moreno. 2006. Cross-platform expression profiling demonstrates that SV40 small tumor antigen activates Notch, Hedgehog, and Wnt signaling in human cells. *BMC Cancer*. 6:54.

Amaro, M., F. Reina, M. Hof, C. Eggeling, and E. Sezgin. 2017. Laurdan and Di-4-ANEPPDHQ probe different properties of the membrane. *J. Phys. D. Appl. Phys.* 50:134004.

Anderson, R.G. 1972. The three-dimensional structure of the basal body from the rhesus monkey oviduct. *J. Cell Biol.* 54:246-265.

Ansell, T.B., W. Song, and M.S.P. Sansom. 2020. The Glycosphingolipid GM3 Modulates Conformational Dynamics of the Glucagon Receptor. *Biophys. J.* 119:300-313.

Anvarian, Z., K. Mykytyn, S. Mukhopadhyay, L.B. Pedersen, and S.T. Christensen. 2019. Cellular signalling by primary cilia in development, organ function and disease. *Nat. Rev. Nephrol.* 15:199-219.

Arveseth, C.D., J.T. Happ, D.S. Hedeen, J.F. Zhu, J.L. Capener, D. Klatt Shaw, I. Deshpande, J. Liang, J. Xu, S.L. Stubben, I.B. Nelson, M.F. Walker, K. Kawakami, A. Inoue, N.J. Krogan, D.J. Grunwald, R. Huttenhain, A. Manglik, and B.R. Myers. 2021. Smoothened transduces Hedgehog signals via activity-dependent sequestration of PKA catalytic subunits. *PLoS Biol.* 19:e3001191.

Ashe, K.M., D. Bangari, L. Li, M.A. Cabrera-Salazar, S.D. Bercury, J.B. Nietupski, C.G. Cooper, J.M. Aerts, E.R. Lee, D.P. Copeland, S.H. Cheng, R.K. Scheule, and J. Marshall. 2011. Iminosugar-based inhibitors of glucosylceramide synthase increase brain glycosphingolipids and survival in a mouse model of Sandhoff disease. *PLoS One*. 6:e21758.

Atwood, S.X., M. Li, A. Lee, J.Y. Tang, and A.E. Oro. 2013. GLI activation by atypical protein kinase C ι/λ regulates the growth of basal cell carcinomas. *Nature*. 494:484-488.

Azbazdar, Y., M. Karabicici, E. Erdal, and G. Ozhan. 2021. Regulation of Wnt Signaling Pathways at the Plasma Membrane and Their Misregulation in Cancer. *Front. Cell Dev. Biol.* 9.

Bachmann, V.A., J.E. Mayrhofer, R. Ilouz, P. Tschaikner, P. Raffeiner, R. Rock, M. Courcelles, F. Apelt, T.W. Lu, G.S. Baillie, P. Thibault, P. Aanstad, U. Stelzl, S.S. Taylor, and E. Stefan. 2016. Gpr161 anchoring of PKA consolidates GPCR and cAMP signaling. *Proc. Natl. Acad. Sci. U.S.A*. 113:7786-7791.

Bagatolli, L.A., and E. Gratton. 2000. A Correlation between Lipid Domain Shape and Binary Phospholipid Mixture Composition in Free Standing Bilayers: A Two-Photon Fluorescence Microscopy Study. *Biophys. J.* 79:434-447.

Baird, G.S., D.A. Zacharias, and R.Y. Tsien. 1999. Circular permutation and receptor insertion within green fluorescent proteins. *Proc. Natl. Acad. Sci. U.S.A.* 96:11241-11246.

Balla, T. 2013. Phosphoinositides: tiny lipids with giant impact on cell regulation. *Physiol. Rev.* 93:1019-1137.

Bielas, S.L., J.L. Silhavy, F. Brancati, M.V. Kisseleva, L. Al-Gazali, L. Sztriha, R.A. Bayoumi, M.S. Zaki, A. Abdel-Aleem, R.O. Rosti, H. Kayserili, D. Swistun, L.C. Scott, E. Bertini, E. Boltshauser, E. Fazzi, L. Travaglini, S.J. Field, S. Gayral, M. Jacoby, S. Schurmans, B. Dallapiccola, P.W. Majerus, E.M. Valente, and J.G. Gleeson. 2009. Mutations in INPP5E, encoding inositol polyphosphate-5-phosphatase E, link phosphatidyl inositol signaling to the ciliopathies. *Nat. Genet.* 41:1032-1036.

Bishop, G.A., N.F. Berbari, J. Lewis, and K. Mykytyn. 2007. Type III adenylyl cyclase localizes to primary cilia throughout the adult mouse brain. *J. Comp. Neurol.* 505:562-571.

Bloodgood, R.A. 2009. From central to rudimentary to primary: the history of an underappreciated organelle whose time has come. The primary cilium. *Methods Cell Biol.* 94:3-52.

Bloom, G. 1954. Studies on the olfactory epithelium of the frog and the toad with the aid of light and electron microscopy. *Z. Zellforsch. Mikrosk. Anat.* 41:89-100.

Boehlke, C., M. Bashkurov, A. Buescher, T. Krick, A.K. John, R. Nitschke, G. Walz, and E.W. Kuehn. 2010. Differential role of Rab proteins in ciliary trafficking: Rab23 regulates smoothened levels. *J. Cell. Sci.* 123:1460-1467.

Borlinghaus, R.T. 2017. The White Confocal : Microscopic Optical Sectioning in all Colors. Springer International Publishing : Imprint: Springer,, Cham. 1 online resource (XIII, 115 pages 173 illustrations in color.

Borner, S., F. Schwede, A. Schlipp, F. Berisha, D. Calebiro, M.J. Lohse, and V.O. Nikolaev. 2011. FRET measurements of intracellular cAMP concentrations and cAMP analog permeability in intact cells. *Nat. Protoc.* 6:427-438.

Brady, R.O., J.N. Kanfer, and D. Shapiro. 1965. Metabolism of Glucocerebrosides. Ii. Evidence of an Enzymatic Deficiency in Gaucher's Disease. *Biochem. Biophys. Res. Commun.* 18:221-225.

Brennan, K., K. Martin, S.P. FitzGerald, J. O'Sullivan, Y. Wu, A. Blanco, C. Richardson, and M.M. Mc Gee. 2020. A comparison of methods for the isolation and separation of extracellular vesicles from protein and lipid particles in human serum. *Sci. Rep.* 10:1039.

Breslow, David K., and Maxence V. Nachury. 2011. Primary Cilia: How to Keep the Riff-Raff in the Plasma Membrane. *Curr. Biol.* 21:R434-R436.

Brinkman, E.K., T. Chen, M. Amendola, and B. van Steensel. 2014. Easy quantitative assessment of genome editing by sequence trace decomposition. *Nucleic Acids Res.* 42:e168-e168.

Bumcrot, D.A., R. Takada, and A.P. McMahon. 1995. Proteolytic processing yields two secreted forms of sonic hedgehog. *Mol. Cell. Biol.* 15:2294-2303.

Caspary, T., C.E. Larkins, and K.V. Anderson. 2007. The graded response to Sonic Hedgehog depends on cilia architecture. *Dev. Cell.* 12:767-778.

Chailley, B., and E. Boisvieux-Ulrich. 1985. Detection of plasma membrane cholesterol by filipin during microvillogenesis and ciliogenesis in quail oviduct. *J. Histochem. Cytochem.* 33:1-10.

Chavez, M., S. Ena, J. Van Sande, A. de Kerchove d'Exaerde, S. Schurmans, and S.N. Schiffmann. 2015. Modulation of Ciliary Phosphoinositide Content Regulates Trafficking and Sonic Hedgehog Signaling Output. *Dev. Cell.* 34:338-350.

Chen, J.K., J. Taipale, K.E. Young, T. Maiti, and P.A. Beachy. 2002. Small molecule modulation of Smoothened activity. *Proc. Natl. Acad. Sci. U.S.A*. 99:14071-14076.

Choi, Y.H., A. Suzuki, S. Hajarnis, Z. Ma, H.C. Chapin, M.J. Caplan, M. Pontoglio, S. Somlo, and P. Igarashi. 2011. Polycystin-2 and phosphodiesterase 4C are components of a ciliary A-kinase anchoring protein complex that is disrupted in cystic kidney diseases. *Proc. Natl. Acad. Sci. U.S.A*. 108:10679-10684.

Cockcroft, S., and P. Raghu. 2018. Phospholipid transport protein function at organelle contact sites. *Curr. Opin. Cell Biol.* 53:52-60.

Cohen, M., A. Kicheva, A. Ribeiro, R. Blassberg, K.M. Page, C.P. Barnes, and J. Briscoe. 2015. Ptch1 and Gli regulate Shh signalling dynamics via multiple mechanisms. *Nat. Commun.* 6:6709.

Conduit, S.E., and B. Vanhaesebroeck. 2020. Phosphoinositide lipids in primary cilia biology. *Biochem. J.* 477:3541-3565.

Corbit, K.C., P. Aanstad, V. Singla, A.R. Norman, D.Y. Stainier, and J.F. Reiter. 2005. Vertebrate Smoothened functions at the primary cilium. *Nature*. 437:1018-1021.

Correa, A., and C. Schultz. 2009. Chapter 6 Small molecule-based FRET probes. *Laboratory Techniques in Biochemistry and Molecular Biology*. 33.

Coskun, Ü., M. Grzybek, D. Drechsel, and K. Simons. 2011. Regulation of human EGF receptor by lipids. *Proc. Natl. Acad. Sci. U.S.A*. 108:9044-9048.

D'Angelo, G., S. Capasso, L. Sticco, and D. Russo. 2013. Glycosphingolipids: synthesis and functions. *Febs J.* 280:6338-6353.

Danylchuk, D.I., E. Sezgin, P. Chabert, and A.S. Klymchenko. 2020. Redesigning Solvatochromic Probe Laurdan for Imaging Lipid Order Selectively in Cell Plasma Membranes. *Anal. Chem.* 92:14798-14805.

de Duve, C. 1971. Tissue fraction-past and present. *J. Cell Biol.* 50:20.

de Graaf, M., I.C. van Veen, I.H. van der Meulen-Muileman, W.R. Gerritsen, H.M. Pinedo, and H.J. Haisma. 2001. Cloning and characterization of human liver cytosolic beta-glycosidase. *Biochem. J.* 356:907-910.

De Robertis, E. 1956. Electron microscope observations on the submicroscopic organization of the retinal rods. *J. Biophys. Biochem. Cytol.* . 2:319-330.

Depry, C., M.D. Allen, and J. Zhang. 2011. Visualization of PKA activity in plasma membrane microdomains. *Mol. Biosyst.* 7:52-58.

Deshpande, I., J. Liang, D. Hedeen, K.J. Roberts, Y. Zhang, B. Ha, N.R. Latorraca, B. Faust, R.O. Dror, P.A. Beachy, B.R. Myers, and A. Manglik. 2019. Smoothened stimulation by membrane sterols drives Hedgehog pathway activity. *Nature*. 571:284-288.

Dickson, E.J., and B. Hille. 2019. Understanding phosphoinositides: rare, dynamic, and essential membrane phospholipids. *Biochem. J.* 476:1-23.

Dinic, J., H. Biverstahl, L. Maler, and I. Parmryd. 2011. Laurdan and di-4-ANEPPDHQ do not respond to membrane-inserted peptides and are good probes for lipid packing. *Biochim. Biophys. Acta.* 1808:298-306.

Dubreuil, V., A.M. Marzesco, D. Corbeil, W.B. Huttner, and M. Wilsch-Bräuninger. 2007. Midbody and primary cilium of neural progenitors release extracellular

membrane particles enriched in the stem cell marker prominin-1. *J. Cell Biol.* 176:483-495.

Dyson, J.M., S.E. Conduit, S.J. Feeney, S. Hakim, T. DiTommaso, A.J. Fulcher, A. Sriratana, G. Ramm, K.A. Horan, R. Gurung, C. Wicking, I. Smyth, and C.A. Mitchell. 2016. INPP5E regulates phosphoinositide-dependent cilia transition zone function. *J. Cell Biol.* 216:247-263.

Eagle, H., and E.M. Levine. 1967. Growth regulatory effects of cellular interaction. *Nature*. 213:1102-1106.

Eggenschwiler, J.T., O.V. Bulgakov, J. Qin, T. Li, and K.V. Anderson. 2006. Mouse Rab23 regulates hedgehog signaling from smoothened to Gli proteins. *Dev. Biol.* 290:1-12.

Eggenschwiler, J.T., E. Espinoza, and K.V. Anderson. 2001. Rab23 is an essential negative regulator of the mouse Sonic hedgehog signalling pathway. *Nature*. 412:194-198.

Enquist, I.B., E. Nilsson, A. Ooka, J.-E. Månsson, K. Olsson, M. Ehinger, R.O. Brady, J. Richter, and S. Karlsson. 2006. Effective cell and gene therapy in a murine model of Gaucher disease. *Proc. Natl. Acad. Sci. U.S.A.* 103:13819-13824.

Erickson, M.G., B.A. Alseikhan, B.Z. Peterson, and D.T. Yue. 2001. Preassociation of calmodulin with voltage-gated Ca(2+) channels revealed by FRET in single living cells. *Neuron*. 31:973-985.

Evans, T.M., F. Simpson, R.G. Parton, and C. Wicking. 2005. Characterization of Rab23, a negative regulator of sonic hedgehog signaling. *Meth. Enzymol.* 403:759-777.

Fidorra, M., L. Duelund, C. Leidy, A.C. Simonsen, and L.A. Bagatolli. 2006. Absence of fluid-ordered/fluid-disordered phase coexistence in ceramide/POPC mixtures containing cholesterol. *Genes. Dev.* 90:4437-4451.

Förster, T. 1946. Energiewanderung und Fluoreszenz. *Naturwissenschaften*. 33:166-175.

Frolov, V.A., A.V. Shnyrova, and J. Zimmerberg. 2011. Lipid polymorphisms and membrane shape. *Cold Spring Harb. Perspect.* 3:a004747.

Fujisawa, S., H. Qiu, S. Nozaki, S. Chiba, Y. Katoh, and K. Nakayama. 2021. ARL3 and ARL13B GTPases participate in distinct steps of INPP5E targeting to the ciliary membrane. *Biology. Open.* 10.

Fuller, M., T. Rozaklis, M. Lovejoy, K. Zarrinkalam, J.J. Hopwood, and P.J. Meikle. 2008. Glucosylceramide accumulation is not confined to the lysosome in fibroblasts from patients with Gaucher disease. *Mol. Genet. Metab.* 93:437-443.

Garcia, G., 3rd, D.R. Raleigh, and J.F. Reiter. 2018. How the Ciliary Membrane Is Organized Inside-Out to Communicate Outside-In. *Curr. Biol.* 28:R421-R434.

Garcia-Gonzalo, F.R., S.C. Phua, E.C. Roberson, G. Garcia, 3rd, M. Abedin, S. Schurmans, T. Inoue, and J.F. Reiter. 2015. Phosphoinositides Regulate Ciliary Protein Trafficking to Modulate Hedgehog Signaling. *Dev. Cell.* 34:400-409.

Garneau, J.E., M.-È. Dupuis, M. Villion, D.A. Romero, R. Barrangou, P. Boyaval, C. Fremaux, P. Horvath, A.H. Magadán, and S. Moineau. 2010. The CRISPR/Cas bacterial immune system cleaves bacteriophage and plasmid DNA. *Nature*. 468:67-71.

Gasiunas, G., R. Barrangou, P. Horvath, and V. Siksnys. 2012. Cas9–crRNA ribonucleoprotein complex mediates specific DNA cleavage for adaptive immunity in bacteria. *Proc. Natl. Acad. Sci. U.S.A.* 109:E2579.

Gerhardt, C. 2019. Treatment of Ciliopathies: Current Perspectives. *Curr. Med. Chem.* 26:3080-3080.

Gigante, E.D., and T. Caspary. 2020. Signaling in the primary cilium through the lens of the Hedgehog pathway. *Wiley Interdiscip. Rev. Dev. Biol.* 9:e377.

Gigante, E.D., M.R. Taylor, A.A. Ivanova, R.A. Kahn, and T. Caspary. 2020. ARL13B regulates Sonic hedgehog signaling from outside primary cilia. *eLife*. 9:e50434.

Gilpin, W., M.S. Bull, and M. Prakash. 2020. The multiscale physics of cilia and flagella. *Nat. Rev. Phys.* 2:74-88.

Gilula, N.B., and P. Satir. 1972. The ciliary necklace. A ciliary membrane specialization. *J. Cell Biol.* 53:494-509.

Goodrich, L.V., R.L. Johnson, L. Milenkovic, J.A. McMahon, and M.P. Scott. 1996. Conservation of the hedgehog/patched signaling pathway from flies to mice: induction of a mouse patched gene by Hedgehog. *Genes. Dev.* 10:301-312.

Gordon, G.W., G. Berry, X.H. Liang, B. Levine, and B. Herman. 1998. Quantitative fluorescence resonance energy transfer measurements using fluorescence microscopy. *Biophys. J.* 74:2702-2713.

Gotzke, H., M. Kilisch, M. Martinez-Carranza, S. Sograte-Idrissi, A. Rajavel, T. Schlichthaerle, N. Engels, R. Jungmann, P. Stenmark, F. Opazo, and S. Frey. 2019. The ALFA-tag is a highly versatile tool for nanobody-based bioscience applications. *Nat. Commun.* 10:4403.

Guo, J., J.M. Otis, S.K. Suciu, C. Catalano, L. Xing, S. Constable, D. Wachten, S. Gupton, J. Lee, A. Lee, K.H. Blackley, T. Ptacek, J.M. Simon, S. Schurmans, G.D. Stuber, T. Caspary, and E.S. Anton. 2019. Primary Cilia Signaling Promotes Axonal Tract Development and Is Disrupted in Joubert Syndrome-Related Disorders Models. *Dev. Cell*. 51:759-774.e755.

Habashy, S., A. Jafri, H.O. Osman, N.E. Thomas, S. Udekwe, and S.E. Heindl. 2021. Hedgehog Pathway Inhibitors: Clinical Implications and Resistance in the Treatment of Basal Cell Carcinoma. *Cureus*. 13:e13859-e13859.

Hahn, H., J. Christiansen, C. Wicking, P.G. Zaphiropoulos, A. Chidambaram, B. Gerrard, I. Vorechovsky, A.E. Bale, R. Toftgard, M. Dean, and B. Wainwright. 1996. A mammalian patched homolog is expressed in target tissues of sonic hedgehog and maps to a region associated with developmental abnormalities. *J. Biol. Chem.* 271:12125-12128.

Hamzeh, H. 2017. Organization and function of signaling molecules in sperm. *In* Group of Molecular Physiology. Rheinische Friedrich-Wilhelms-Universität Bonn, Bonn. 185.

Han, Y., B. Wang, Y.S. Cho, J. Zhu, J. Wu, Y. Chen, and J. Jiang. 2019. Phosphorylation of Ci/Gli by Fused Family Kinases Promotes Hedgehog Signaling. *Dev. Cell*. 50:610-626.e614.

Hansen, J.N., F. Kaiser, C. Klausen, B. Stuven, R. Chong, W. Bonigk, D.U. Mick, A. Moglich, N. Jurisch-Yaksi, F.I. Schmidt, and D. Wachten. 2020. Nanobody-directed targeting of optogenetic tools to study signaling in the primary cilium. *eLife*. 9.

Hansen, J.N., S. Rassmann, B. Stuven, N. Jurisch-Yaksi, and D. Wachten. 2021. CiliaQ: a simple, open-source software for automated quantification of ciliary morphology and fluorescence in 2D, 3D, and 4D images. *Eur. Phys. J. E. Soft Matter*. 44:18.

Harfe, B.D., P.J. Scherz, S. Nissim, H. Tian, A.P. McMahon, and C.J. Tabin. 2004. Evidence for an expansion-based temporal Shh gradient in specifying vertebrate digit identities. *Cell*. 118:517-528.

He, Q., G. Wang, S. Dasgupta, M. Dinkins, G. Zhu, and E. Bieberich. 2012. Characterization of an apical ceramide-enriched compartment regulating ciliogenesis. *Mol. Biol. Cell.* 23:3156-3166.

He, Q., G. Wang, S. Wakade, S. Dasgupta, M. Dinkins, J.N. Kong, S.D. Spassieva, and E. Bieberich. 2014. Primary cilia in stem cells and neural progenitors are regulated by neutral sphingomyelinase 2 and ceramide. *Mol. Biol. Cell.* 25:1715-1729.

Hedger, G., M.S.P. Sansom, and H. Koldsø. 2015. The juxtamembrane regions of human receptor tyrosine kinases exhibit conserved interaction sites with anionic lipids. *Sci. Rep.* 5:9198.

Herzog, R., D. Schwudke, K. Schuhmann, J.L. Sampaio, S.R. Bornstein, M. Schroeder, and A. Shevchenko. 2011. A novel informatics concept for high-throughput shotgun lipidomics based on the molecular fragmentation query language. *Genome Biol.* 12:1-25.

Howe, A.K. 2004. Regulation of actin-based cell migration by cAMP/PKA. *Biochim. Biophys. Acta. Mol. Cell. Res.* 1692:159-174.

Hsu, F.F. 2018. Mass spectrometry-based shotgun lipidomics - a critical review from the technical point of view. *Anal. Bioanal. Chem.* 410:6387-6409.

Huang, B.Q., T.V. Masyuk, M.A. Muff, P.S. Tietz, A.I. Masyuk, and N.F. Larusso. 2006. Isolation and characterization of cholangiocyte primary cilia. *Am. J. Physiol. Gastrointest. Liver Physiol.* 291:G500-509.

Huangfu, D., and K.V. Anderson. 2005. Cilia and Hedgehog responsiveness in the mouse. *Proc. Natl. Acad. Sci. U.S.A.* 102:11325-11330.

Huangfu, D., A. Liu, A.S. Rakeman, N.S. Murcia, L. Niswander, and K.V. Anderson. 2003. Hedgehog signalling in the mouse requires intraflagellar transport proteins. *Nature*. 426:83-87.

Humke, E.W., K.V. Dorn, L. Milenkovic, M.P. Scott, and R. Rohatgi. 2010. The output of Hedgehog signaling is controlled by the dynamic association between Suppressor of Fused and the Gli proteins. *Genes. Dev.* 24:670-682.

Hunt, S.E., W. McLaren, L. Gil, A. Thormann, H. Schuilenburg, D. Sheppard, A. Parton, I.M. Armean, S.J. Trevanion, P. Flicek, and F. Cunningham. 2018. Ensembl variation resources. *Database*. 2018.

Ikeda, M., A. Kihara, and Y. Igarashi. 2006. Lipid asymmetry of the eukaryotic plasma membrane: functions and related enzymes. *Biol. Pharm. Bull.* 29:1542-1546.

Ingham, P.W., and A.P. McMahon. 2001. Hedgehog signaling in animal development: paradigms and principles. *Genes. Dev.* 15:3059-3087.

Insel, P.A., L. Zhang, F. Murray, H. Yokouchi, and A.C. Zambon. 2012. Cyclic AMP is both a pro-apoptotic and anti-apoptotic second messenger. *Acta. Physiol. (Oxf)*. 204:277-287.

Jacoby, M., J.J. Cox, S. Gayral, D.J. Hampshire, M. Ayub, M. Blockmans, E. Pernot, M.V. Kisseleva, P. Compère, S.N. Schiffmann, F. Gergely, J.H. Riley, D. Pérez-Morga, C.G. Woods, and S. Schurmans. 2009. INPP5E mutations cause primary cilium signaling defects, ciliary instability and ciliopathies in human and mouse. *Nat. Genet.* 41:1027-1031.

Jafurulla, M., and A. Chattopadhyay. 2015. Sphingolipids in the function of G protein-coupled receptors. *Eur. J. Pharmacol.* 763:241-246.

Janich, P., and D. Corbeil. 2007. GM1 and GM3 gangliosides highlight distinct lipid microdomains within the apical domain of epithelial cells. *FEBS Lett.* 581:1783-1787.

Jiang, J.Y., J.L. Falcone, S. Curci, and A.M. Hofer. 2019. Direct visualization of cAMP signaling in primary cilia reveals up-regulation of ciliary GPCR activity following Hedgehog activation. *Proc. Natl. Acad. Sci. U.S.A.* 116:12066-12071.

Jiang, K., Y. Liu, J. Fan, J. Zhang, X.A. Li, B.M. Evers, H. Zhu, and J. Jia. 2016. PI(4)P Promotes Phosphorylation and Conformational Change of Smoothened through Interaction with Its C-terminal Tail. *PLoS Biol.* 14:e1002375.

Jin, L., A.C. Millard, J.P. Wuskell, H.A. Clark, and L.M. Loew. 2005. Cholesterol-enriched lipid domains can be visualized by di-4-ANEPPDHQ with linear and nonlinear optics. *Biophys J.* 89:L04-06.

Jinek, M., K. Chylinski, I. Fonfara, M. Hauer, J.A. Doudna, and E. Charpentier. 2012. A programmable dual-RNA-guided DNA endonuclease in adaptive bacterial immunity. *Science*. 337:816-821.

Julien, S., M. Bobowski, A. Steenackers, X. Le Bourhis, and P. Delannoy. 2013. How Do Gangliosides Regulate RTKs Signaling? *Cells*. 2:751-767.

Kaiser, F., M. Huebecker, and D. Wachten. 2020. Sphingolipids controlling ciliary and microvillar function. *FEBS Lett.* 594:3652-3667.

Kaneshiro, E.S., D.F. Matesic, and K. Jayasimhulu. 1984. Characterizations of six ethanolamine sphingophospholipids from Paramecium cells and cilia. *J. Lipid Res.* 25:369-377.

Kaupp, U.B. 2010. Olfactory signalling in vertebrates and insects: differences and commonalities. *Nat. Rev. Neurosci.* 11:188-200.

Kiesel, P., G.A. Viar, N. Tsoy, R. Maraspini, P. Gorilak, V. Varga, A. Honigmann, and G. Pigino. 2020. The molecular structure of mammalian primary cilia revealed by cryo-electron tomography. *Nat. Struct. Mol. Biol.* 27:1115-1124.

Kim, J., M. Kato, and P.A. Beachy. 2009. Gli2 trafficking links Hedgehog-dependent activation of Smoothened in the primary cilium to transcriptional activation in the nucleus. *Proc. Natl. Acad. Sci. U.S.A.* 106:21666-21671.

Kim, N., S. Shin, and S.W. Bae. 2021. cAMP Biosensors Based on Genetically Encoded Fluorescent/Luminescent Proteins. *Biosensors (Basel)*. 11.

Kinnebrew, M., E.J. Iverson, B.B. Patel, G.V. Pusapati, J.H. Kong, K.A. Johnson, G. Luchetti, K.M. Eckert, J.G. McDonald, D.F. Covey, C. Siebold, A. Radhakrishnan, and R. Rohatgi. 2019. Cholesterol accessibility at the ciliary membrane controls hedgehog signaling. *eLife*. 8.

Kinnebrew, M., G. Luchetti, R. Sircar, S. Frigui, L.V. Viti, T. Naito, F. Beckert, Y. Saheki, C. Siebold, A. Radhakrishnan, and R. Rohatgi. 2021. Patched 1 reduces the accessibility of cholesterol in the outer leaflet of membranes. *eLife*. 10:e70504.

Klausen, C., F. Kaiser, B. Stuven, J.N. Hansen, and D. Wachten. 2019. Elucidating cyclic AMP signaling in subcellular domains with optogenetic tools and fluorescent biosensors. *Biochem. Soc. Trans.* 47:1733-1747.

Klymchenko, A.S. 2017. Solvatochromic and Fluorogenic Dyes as Environment-Sensitive Probes: Design and Biological Applications. *Acc. Chem. Res.* 50:366-375.

Kohen, R., L.A. Fashingbauer, D.E. Heidmann, C.R. Guthrie, and M.W. Hamblin. 2001. Cloning of the mouse 5-HT6 serotonin receptor and mutagenesis studies of the third cytoplasmic loop. *Brain. Res. Mol. Brain. Res.* 90:110-117.

Kong, J.H., C. Siebold, and R. Rohatgi. 2019. Biochemical mechanisms of vertebrate hedgehog signaling. *Development*. 146.

Körschen, H.G., Y. Yildiz, D.N. Raju, S. Schonauer, W. Bonigk, V. Jansen, E. Kremmer, U.B. Kaupp, and D. Wachten. 2013. The non-lysosomal beta-glucosidase GBA2 is a non-integral membrane-associated protein at the endoplasmic reticulum (ER) and Golgi. *J. Biol. Chem.* 288:3381-3393.

Koschinski, A., and M. Zaccolo. 2017. Activation of PKA in cell requires higher concentration of cAMP than in vitro: implications for compartmentalization of cAMP signalling. *Sci. Rep.* 7:14090.

Kusumi, A., T.K. Fujiwara, R. Chadda, M. Xie, T.A. Tsunoyama, Z. Kalay, R.S. Kasai, and K.G. Suzuki. 2012. Dynamic organizing principles of the plasma membrane that regulate signal transduction: commemorating the fortieth anniversary of Singer and Nicolson's fluid-mosaic model. *Annu. Rev. Cell. Dev. Biol.* 28:215-250.

Lange, Y., M.H. Swaisgood, B.V. Ramos, and T.L. Steck. 1989. Plasma membranes contain half the phospholipid and 90% of the cholesterol and sphingomyelin in cultured human fibroblasts. *J. Biol. Chem.* 264:3786-3793.

LeDizet, M., and G. Piperno. 1991. Detection of acetylated alpha-tubulin by specific antibodies. *Meth. Enzymol.* 196:264-274.

Lefkimmiatis, K., and M. Zaccolo. 2014. cAMP signaling in subcellular compartments. *Pharmacol. Ther.* 143:295-304.

Li, Y., H. Zhang, Y. Litingtung, and C. Chiang. 2006. Cholesterol modification restricts the spread of Shh gradient in the limb bud. *Proc. Natl. Acad. Sci. U.S.A.* 103:6548-6553.

Luo, N., A. Kumar, M. Conwell, R.N. Weinreb, R. Anderson, and Y. Sun. 2013. Compensatory Role of Inositol 5-Phosphatase INPP5B to OCRL in Primary Cilia Formation in Oculocerebrorenal Syndrome of Lowe. *PLoS One*. 8:e66727.

Luo, N., C.C. West, C.A. Murga-Zamalloa, L. Sun, R.M. Anderson, C.D. Wells, R.N. Weinreb, J.B. Travers, H. Khanna, and Y. Sun. 2012. OCRL localizes to the primary cilium: a new role for cilia in Lowe syndrome. *Hum. Mol. Genet.* 21:3333-3344.

Malicki, J.J., and C.A. Johnson. 2017. The Cilium: Cellular Antenna and Central Processing Unit. *Trends Cell. Biol.* 27:126-140.

Mandel, M., and A. Higa. 1970. Calcium-dependent bacteriophage DNA infection. *J. Mol. Biol.* 53:159-162.

Marini, K.D., B.J. Payne, D.N. Watkins, and L.G. Martelotto. 2011. Mechanisms of Hedgehog signalling in cancer. *Growth Factors*. 29:221-234.

Marley, A., R.W. Choy, and M. von Zastrow. 2013. GPR88 reveals a discrete function of primary cilia as selective insulators of GPCR cross-talk. *PLoS One*. 8:e70857.

Masyuk, A.I., B.Q. Huang, B.N. Radtke, G.B. Gajdos, P.L. Splinter, T.V. Masyuk, S.A. Gradilone, and N.F. LaRusso. 2013. Ciliary subcellular localization of TGR5 determines the cholangiocyte functional response to bile acid signaling. *Am. J. Physiol. Gastrointest. Liver Physiol.* 304:G1013-1024.

May, E.A., M. Kalocsay, I.G. D'Auriac, P.S. Schuster, S.P. Gygi, M.V. Nachury, and D.U. Mick. 2021. Time-resolved proteomics profiling of the ciliary Hedgehog response. *J. Cell Biol.* 220.

Mazeres, S., E. Joly, A. Lopez, and C. Tardin. 2014. Characterization of M-laurdan, a versatile probe to explore order in lipid membranes. *F1000Res.* 3:172.

Mazloumi Gavgani, F., V. Smith Arnesen, R.G. Jacobsen, C. Krakstad, E.A. Hoivik, and A.E. Lewis. 2018. Class I Phosphoinositide 3-Kinase PIK3CA/p110α and PIK3CB/p110β Isoforms in Endometrial Cancer. *Int. J. Mol. Sci.* 19:3931.

Mick, D.U., R.B. Rodrigues, R.D. Leib, C.M. Adams, A.S. Chien, S.P. Gygi, and M.V. Nachury. 2015. Proteomics of Primary Cilia by Proximity Labeling. *Dev. Cell.* 35:497-512.

Milenkovic, L., M.P. Scott, and R. Rohatgi. 2009. Lateral transport of Smoothened from the plasma membrane to the membrane of the cilium. *J. Cell Biol.* 187:365-374.

Mishra, S.K., Y.G. Gao, X. Zou, D.J. Stephenson, L. Malinina, E.H. Hinchcliffe, C.E. Chalfant, and R.E. Brown. 2020. Emerging roles for human glycolipid transfer protein superfamily members in the regulation of autophagy, inflammation, and cell death. *Prog. Lipid. Res.* 78:101031.

Mitchell, K.A., B.C. Gallagher, G. Szabo, and S. Otero Ade. 2004. NDP kinase moves into developing primary cilia. *Cell motil. cytoskelet.* 59:62-73.

Mitchell, K.A., G. Szabo, and S. Otero Ade. 2009. Methods for the isolation of sensory and primary cilia--an overview. *Methods Cell Biol.* 94:87-101.

Mitchison, H.M., and E.M. Valente. 2017. Motile and non-motile cilia in human pathology: from function to phenotypes. *J. Pathol.* 241:294-309.

Monaco, S., K. Baur, A. Hellwig, G. Holzl-Wenig, C. Mandl, and F. Ciccolini. 2018. A Flow Cytometry-Based Approach for the Isolation and Characterization of Neural Stem Cell Primary Cilia. *Front. Cell. Neurosci.* 12:519.

Mongillo, M., T. McSorley, S. Evellin, A. Sood, V. Lissandron, A. Terrin, E. Huston, A. Hannawacker, M.J. Lohse, T. Pozzan, M.D. Houslay, and M. Zaccolo. 2004. Fluorescence resonance energy transfer-based analysis of cAMP dynamics in live neonatal rat cardiac myocytes reveals distinct functions of compartmentalized phosphodiesterases. *Circ. Res.* 95:67-75.

Montesano, R. 1979. Inhomogeneous distribution of filipin-sterol complexes in the ciliary membrane of rat tracheal epithelium. *Am. J. Anat.* 156:139-145.

Moore, B.S., A.N. Stepanchick, P.H. Tewson, C.M. Hartle, J. Zhang, A.M. Quinn, T.E. Hughes, and T. Mirshahi. 2016. Cilia have high cAMP levels that are inhibited by Sonic Hedgehog-regulated calcium dynamics. *Proc. Natl. Acad. Sci. U.S.A.* 113:13069-13074.

Mukherjee, S., V. Jansen, J.F. Jikeli, H. Hamzeh, L. Alvarez, M. Dombrowski, M. Balbach, T. Strunker, R. Seifert, U.B. Kaupp, and D. Wachten. 2016. A novel biosensor to study cAMP dynamics in cilia and flagella. *eLife*. 5.

Mukhopadhyay, S., X. Wen, B. Chih, C.D. Nelson, W.S. Lane, S.J. Scales, and P.K. Jackson. 2010. TULP3 bridges the IFT-A complex and membrane phosphoinositides to promote trafficking of G protein-coupled receptors into primary cilia. *Genes Dev.* 24:2180-2193.

Mukhopadhyay, S., X. Wen, N. Ratti, A. Loktev, L. Rangell, S.J. Scales, and P.K. Jackson. 2013. The ciliary G-protein-coupled receptor Gpr161 negatively regulates the Sonic hedgehog pathway via cAMP signaling. *Cell*. 152:210-223.

Muyldermans, S. 2013. Nanobodies: natural single-domain antibodies. *Annu. Rev. Biochem.* 82:775-797.

Nachury, M.V. 2018. The molecular machines that traffic signaling receptors into and out of cilia. *Curr. Opin. Cell. Biol.* 51:124-131.

Nachury, M.V., and D.U. Mick. 2019. Establishing and regulating the composition of cilia for signal transduction. *Nat. Rev. Mol. Cell. Biol.* 20:389-405.

Nager, A.R., J.S. Goldstein, V. Herranz-Pérez, D. Portran, F. Ye, J.M. Garcia-Verdugo, and M.V. Nachury. 2017. An Actin Network Dispatches Ciliary GPCRs into Extracellular Vesicles to Modulate Signaling. *Cell*. 168:252-263.e214.

Nakada-Tsukui, K., N. Watanabe, T. Maehama, and T. Nozaki. 2019. Phosphatidylinositol Kinases and Phosphatases in Entamoeba histolytica. *Front. Cell. Infect. Microbiol.* 9.

Nakata, K., D. Shiba, D. Kobayashi, and T. Yokoyama. 2012. Targeting of Nphp3 to the primary cilia is controlled by an N-terminal myristoylation site and coiled-coil domains. *Cytoskeleton (Hoboken)*. 69:221-234.

Nauli, S.M., F.J. Alenghat, Y. Luo, E. Williams, P. Vassilev, X. Li, A.E. Elia, W. Lu, E.M. Brown, S.J. Quinn, D.E. Ingber, and J. Zhou. 2003. Polycystins 1 and 2 mediate mechanosensation in the primary cilium of kidney cells. *Nat. Genet.* 33:129-137.

Nechipurenko, I.V. 2020. The Enigmatic Role of Lipids in Cilia Signaling. *Front Cell Dev Biol*. 8:777.

Nelson, M., J. Ledoux, M. Taylor, A. Bonev, R. Hannah, V. Solodushko, B. Shui, Y. Tallini, and M. Kotlikoff. 2010. Spinning Disk Confocal Microscopy of Calcium Signalling in Blood Vessel Walls. *Microsc. Anal. (Am. Ed.)*. 24:5-8.

Niewiadomski, P., J.H. Kong, R. Ahrends, Y. Ma, E.W. Humke, S. Khan, M.N. Teruel, B.G. Novitch, and R. Rohatgi. 2014. Gli protein activity is controlled by multisite phosphorylation in vertebrate Hedgehog signaling. *Cell Rep.* 6:168-181.

Nusslein-Volhard, C., and E. Wieschaus. 1980. Mutations affecting segment number and polarity in Drosophila. *Nature*. 287:795-801.

Obaid, A.L., L.M. Loew, J.P. Wuskell, and B.M. Salzberg. 2004. Novel naphthylstyryl-pyridium potentiometric dyes offer advantages for neural network analysis. *J. Neurosci. Meth.* 134:179-190.

Ocbina, P.J., J.T. Eggenschwiler, I. Moskowitz, and K.V. Anderson. 2011. Complex interactions between genes controlling trafficking in primary cilia. *Nat. Genet.* 43:547-553.

Ohta, Y., T. Furuta, T. Nagai, and K. Horikawa. 2018. Red fluorescent cAMP indicator with increased affinity and expanded dynamic range. *Sci. Rep.* 8:1866.

Oude Weernink, P.A., L. Han, K.H. Jakobs, and M. Schmidt. 2007. Dynamic phospholipid signaling by G protein-coupled receptors. *Biochim. Biophys. Acta. Biomembr.* 1768:888-900.

Owen, D.M., C. Rentero, A. Magenau, A. Abu-Siniyeh, and K. Gaus. 2011. Quantitative imaging of membrane lipid order in cells and organisms. *Nat. Protoc.* 7:24-35.

Paila, Y.D., and A. Chattopadhyay. 2010. Membrane cholesterol in the function and organization of G-protein coupled receptors. *Subcell. Biochem.* 51:439-466.

Paila, Y.D., E. Jindal, S.K. Goswami, and A. Chattopadhyay. 2011. Cholesterol depletion enhances adrenergic signaling in cardiac myocytes. *Biochim. Biophys. Acta.* 1808:461-465.

Pal, K., S.H. Hwang, B. Somatilaka, H. Badgandi, P.K. Jackson, K. DeFea, and S. Mukhopadhyay. 2016. Smoothened determines β-arrestin-mediated removal of the G protein-coupled receptor Gpr161 from the primary cilium. *J. Cell Biol.* 212:861-875.

Parasassi, T., G. De Stasio, A. d'Ubaldo, and E. Gratton. 1990. Phase fluctuation in phospholipid membranes revealed by Laurdan fluorescence. *Biophys. J.* 57:1179-1186.

Pedersen, L.B., J.B. Mogensen, and S.T. Christensen. 2016. Endocytic Control of Cellular Signaling at the Primary Cilium. *Trends Biochem. Sci.* 41:784-797.

Petrov, K., T. de Almeida Magalhaes, and A. Salic. 2021. Mechanism and ultrasensitivity in Hedgehog signaling revealed by Patched1 disease mutations. *Proc. Natl. Acad. Sci. U.S.A.* 118.

Petrova, R., and A.L. Joyner. 2014. Roles for Hedgehog signaling in adult organ homeostasis and repair. *Development (Cambridge, England)*. 141:3445-3457.

Phua, S.C., S. Chiba, M. Suzuki, E. Su, E.C. Roberson, G.V. Pusapati, S. Schurmans, M. Setou, R. Rohatgi, J.F. Reiter, K. Ikegami, and T. Inoue. 2017. Dynamic Remodeling of Membrane Composition Drives Cell Cycle through Primary Cilia Excision. *Cell*. 168:264-279.e215.

Porter, J.A., S.C. Ekker, W.J. Park, D.P. von Kessler, K.E. Young, C.H. Chen, Y. Ma, A.S. Woods, R.J. Cotter, E.V. Koonin, and P.A. Beachy. 1996a. Hedgehog patterning activity: role of a lipophilic modification mediated by the carboxy-terminal autoprocessing domain. *Cell*. 86:21-34.

Porter, J.A., K.E. Young, and P.A. Beachy. 1996b. Cholesterol modification of hedgehog signaling proteins in animal development. *Science*. 274:255-259.

Prosseda, P.P., N. Luo, B. Wang, J.A. Alvarado, Y. Hu, and Y. Sun. 2017. Loss of OCRL increases ciliary PI(4,5)P2 in Lowe oculocerebrorenal syndrome. *J. Cell Sci.* 130:3447-3454.

Pydi, S.P., M. Jafurulla, L. Wai, R.P. Bhullar, P. Chelikani, and A. Chattopadhyay. 2016. Cholesterol modulates bitter taste receptor function. *Biochim. Biophys. Acta.* 1858:2081-2087.

Raju, D., S. Schonauer, H. Hamzeh, K.C. Flynn, F. Bradke, K. Vom Dorp, P. Dormann, Y. Yildiz, C. Trotschel, A. Poetsch, B. Breiden, K. Sandhoff, H.G. Korschen, and D. Wachten. 2015. Accumulation of glucosylceramide in the absence of the beta-glucosidase GBA2 alters cytoskeletal dynamics. *PLoS Genet.* 11:e1005063.

Raju, D.N., J.N. Hansen, S. Rassmann, B. Stüven, J.F. Jikeli, T. Strünker, H.G. Körschen, A. Möglich, and D. Wachten. 2019. Cyclic Nucleotide-Specific Optogenetics Highlights Compartmentalization of the Sperm Flagellum into cAMP Microdomains. *Cells*. 8:648.

Ran, F.A., P.D. Hsu, J. Wright, V. Agarwala, D.A. Scott, and F. Zhang. 2013. Genome engineering using the CRISPR-Cas9 system. *Nat. Protoc.* 8:2281-2308.

Ray, T.K., V.P. Skipski, M. Barclay, E. Essner, and F.M. Archibald. 1969. Lipid composition of rat liver plasma membranes. *J. Biol. Chem.* 244:5528-5536.

Raychowdhury, M.K., M. McLaughlin, A.J. Ramos, N. Montalbetti, R. Bouley, D.A. Ausiello, and H.F. Cantiello. 2005. Characterization of single channel currents from primary cilia of renal epithelial cells. *J. Biol. Chem.* 280:34718-34722.

Raychowdhury, M.K., A.J. Ramos, P. Zhang, M. McLaughin, X.Q. Dai, X.Z. Chen, N. Montalbetti, M. Del Rocio Cantero, D.A. Ausiello, and H.F. Cantiello. 2009. Vasopressin receptor-mediated functional signaling pathway in primary cilia of renal epithelial cells. *Am. J. Physiol. Renal. Physiol.* 296:F87-97.

Reiter, J.F., O.E. Blacque, and M.R. Leroux. 2012. The base of the cilium: roles for transition fibres and the transition zone in ciliary formation, maintenance and compartmentalization. *EMBO Rep.* 13:608-618.

Reiter, J.F., and M.R. Leroux. 2017. Genes and molecular pathways underpinning ciliopathies. *Nat. Rev. Mol. Cell Biol.* 18:533-547.

Ridley, C.M., K.E. Thur, J. Shanahan, N.B. Thillaiappan, A. Shen, K. Uhl, C.M. Walden, A.A. Rahim, S.N. Waddington, F.M. Platt, and A.C. van der Spoel. 2013. beta-

Glucosidase 2 (GBA2) activity and imino sugar pharmacology. *J. Biol. Chem.* 288:26052-26066.

Rieder, C.L., C.G. Jensen, and L.C. Jensen. 1979. The resorption of primary cilia during mitosis in a vertebrate (PtK1) cell line. *J. Ultrastruct. Res.* 68:173-185.

Riobo, N.A. 2014. Canonical and Non-Canonical Hedgehog Signaling Pathways: Role of G Proteins. *In* The Smoothened Receptor in Cancer and Regenrative Medicine. Springer Cham. 13-42.

Riobo, N.A. 2015. Canonical and Non-Canonical Hedgehog Signaling Pathways: Role of G Proteins. *In* The Smoothened Receptor in Cancer and Regenerative Medicine. M. Ruat, editor. Springer International Publishing, Cham. 13-42.

Rohatgi, R., L. Milenkovic, R.B. Corcoran, and M.P. Scott. 2009. Hedgehog signal transduction by Smoothened: pharmacologic evidence for a 2-step activation process. *Proc. Natl. Acad. Sci. U.S.A.* . 106:3196-3201.

Rohatgi, R., L. Milenkovic, and M.P. Scott. 2007. Patched1 regulates hedgehog signaling at the primary cilium. *Science*. 317:372-376.

Rohatgi, R., and M.P. Scott. 2007. Patching the gaps in Hedgehog signalling. *Nat. Cell. Biol.* 9:1005-1009.

Rohatgi, R., and W.J. Snell. 2010. The ciliary membrane. *Curr. Opin. Cell. Biol.* 22:541-546.

Rosenbaum, J.L., and G.B. Witman. 2002. Intraflagellar transport. *Nat. Rev. Mol. Cell. Biol.* 3:813-825.

Ruat, M., L. Hoch, H. Faure, and D. Rognan. 2014. Targeting of Smoothened for therapeutic gain. *Trends Pharmacol. Sci.* 35:237-246.

Sandhoff, K., and T. Kolter. 2003. Biosynthesis and degradation of mammalian glycosphingolipids. *Philos. Trans. R. Soc. Lond. B. Biol. Sci.* 358:847-861.

Sarkar, P., and A. Chattopadhyay. 2020. Cholesterol interaction motifs in G protein-coupled receptors: Slippery hot spots? *Wiley Interdiscip. Rev. Syst. Biol. Med.* 12:e1481.

Satir, P., and S.T. Christensen. 2007. Overview of structure and function of mammalian cilia. *Annu. Rev. Physiol.* 69:377-400.

Scheidel, N., J. Kennedy, and O.E. Blacque. 2018. Endosome maturation factors Rabenosyn-5/VPS45 and caveolin-1 regulate ciliary membrane and polycystin-2 homeostasis. *EMBO J.* 37:e98248.

Schindelin, J., I. Arganda-Carreras, E. Frise, V. Kaynig, M. Longair, T. Pietzsch, S. Preibisch, C. Rueden, S. Saalfeld, B. Schmid, J.Y. Tinevez, D.J. White, V. Hartenstein, K. Eliceiri, P. Tomancak, and A. Cardona. 2012. Fiji: an open-source platform for biological-image analysis. *Nat. Methods*. 9:676-682.

Schnaar, R.L., and T. Kinoshita. 2015. Glycosphingolipids. *In* Essentials of Glycobiology. rd, A. Varki, R.D. Cummings, J.D. Esko, P. Stanley, G.W. Hart, M. Aebi, A.G. Darvill, T. Kinoshita, N.H. Packer, J.H. Prestegard, R.L. Schnaar, and P.H. Seeberger, editors, Cold Spring Harbor (NY). 125-135.

Schonauer, S. 2017. Investigating the GBA1-dependent regulation of GBA2 activity in Gaucher disease. *In* Mathematisch-Naturwissenschaftliche Fakultät. Vol. Dr. rer. nat. Rheinische Friedrich-Wilhelms-Universität, Bonn.

Schou, K.B., J.B. Mogensen, S.K. Morthorst, B.S. Nielsen, A. Aleliunaite, A. Serra-Marques, N. Fürstenberg, S. Saunier, A.A. Bizet, and I.R. Veland. 2017. KIF13B establishes a CAV1-enriched microdomain at the ciliary transition zone to promote Sonic hedgehog signalling. *Nat. Commun.* 8:1-15.

Seifert, R., and K. Wenzel-Seifert. 2002. Constitutive activity of G-protein-coupled receptors: cause of disease and common property of wild-type receptors. *Naunyn-Schmiedeberg's Arch. Pharmacol.* 366:381-416.

Seo, S., L.M. Baye, N.P. Schulz, J.S. Beck, Q. Zhang, D.C. Slusarski, and V.C. Sheffield. 2010. BBS6, BBS10, and BBS12 form a complex with CCT/TRiC family chaperonins and mediate BBSome assembly. *Proc. Natl. Acad. Sci. U.S.A.* . 107:1488-1493.

Sezgin, E., I. Levental, S. Mayor, and C. Eggeling. 2017. The mystery of membrane organization: composition, regulation and roles of lipid rafts. *Nat. Rev. Mol. Cell Biol.* 18:361-374.

Shen, F., L. Cheng, A.E. Douglas, N.A. Riobo, and D.R. Manning. 2013. Smoothened is a fully competent activator of the heterotrimeric G protein G(i). *Mol. Pharmacol.* 83:691-697.

Sherpa, R.T., A.M. Mohieldin, R. Pala, D. Wachten, R.S. Ostrom, and S.M. Nauli. 2019. Sensory primary cilium is a responsive cAMP microdomain in renal epithelia. *Sci Rep*. 9:6523.

Singh, P., Y.D. Paila, and A. Chattopadhyay. 2012. Role of glycosphingolipids in the function of human serotonin1A receptors. *J. Neurochem.* 123:716-724.

Skoda, A.M., D. Simovic, V. Karin, V. Kardum, S. Vranic, and L. Serman. 2018. The role of the Hedgehog signaling pathway in cancer: A comprehensive review. *Bosn. J. Basic. Med. Sci.* 18:8-20.

Smith, F., J. Esseltine, P. Nygren, D. Veesler, D. Byrne, M. Vonderach, I. Strashnov, C. Eyers, P. Eyers, L. Langeberg, and J. Scott. 2017. Local protein kinase A action proceeds through intact holoenzymes. *Science*. 356:1288-1293.

Somatilaka, B.N., S.-H. Hwang, V.R. Palicharla, K.A. White, H. Badgandi, J.M. Shelton, and S. Mukhopadhyay. 2020. Ankmy2 Prevents Smoothened-Independent Hyperactivation of the Hedgehog Pathway via Cilia-Regulated Adenylyl Cyclase Signaling. *Dev. Cell*. 54:710-726.e718.

Stierl, M., P. Stumpf, D. Udwari, R. Gueta, R. Hagedorn, A. Losi, W. Gartner, L. Petereit, M. Efetova, M. Schwarzel, T.G. Oertner, G. Nagel, and P. Hegemann. 2011. Light modulation of cellular cAMP by a small bacterial photoactivated adenylyl cyclase, bPAC, of the soil bacterium Beggiatoa. *J. Biol. Chem.* 286:1181-1188.

Stirnemann, J., N. Belmatoug, F. Camou, C. Serratrice, R. Froissart, C. Caillaud, T. Levade, L. Astudillo, J. Serratrice, A. Brassier, C. Rose, T. Billette de Villemeur, and M.G. Berger. 2017. A Review of Gaucher Disease Pathophysiology, Clinical Presentation and Treatments. *Int. J. Mol. Sci.* 18.

Sun, S., R.L. Fisher, S.S. Bowser, B.T. Pentecost, and H. Sui. 2019. Three-dimensional architecture of epithelial primary cilia. *Proc. Natl. Acad. Sci. U.S.A.* . 116:9370-9379.

Surdo, N.C., M. Berrera, A. Koschinski, M. Brescia, M.R. Machado, C. Carr, P. Wright, J. Gorelik, S. Morotti, E. Grandi, D.M. Bers, S. Pantano, and M. Zaccolo. 2017. FRET biosensor uncovers cAMP nano-domains at beta-adrenergic targets that dictate precise tuning of cardiac contractility. *Nat. Commun.* 8:15031.

Szlenk, C.T., J.B. Gc, and S. Natesan. 2019. Does the Lipid Bilayer Orchestrate Access and Binding of Ligands to Transmembrane Orthosteric/Allosteric Sites of G Protein-Coupled Receptors? *Mol. Pharmacol.* 96:527-541.

Taipale, J., J.K. Chen, M.K. Cooper, B. Wang, R.K. Mann, L. Milenkovic, M.P. Scott, and P.A. Beachy. 2000. Effects of oncogenic mutations in Smoothened and Patched can be reversed by cyclopamine. *Nature*. 406:1005-1009.

Taipale, J., M.K. Cooper, T. Maiti, and P.A. Beachy. 2002. Patched acts catalytically to suppress the activity of Smoothened. *Nature*. 418:892-897.

Thiele, C., K. Wunderling, and P. Leyendecker. 2019. Multiplexed and single cell tracing of lipid metabolism. *Nat. Methods*. 16:1123-1130.

Tiu, A., J. Yang, L. Asico, P. Konkalmatt, X. Zheng, S. Cuevas, X. Wang, H. Lee, M. Mazhar, R. Felder, P. Jose, and V. Villar. 2020. Lipid rafts are required for effective renal D1 dopamine receptor function. *FASEB J.* 34.

Topell, S., J. Hennecke, and R. Glockshuber. 1999. Circularly permuted variants of the green fluorescent protein. *FEBS Lett.* 457:283-289.

Truong, M.E., S. Bilekova, S.P. Choksi, W. Li, L.J. Bugaj, K. Xu, and J.F. Reiter. 2021. Vertebrate cells differentially interpret ciliary and extraciliary cAMP. *Cell*. 184:2911-2926 e2918.

Tucker, R.W., A.B. Pardee, and K. Fujiwara. 1979. Centriole ciliation is related to quiescence and DNA synthesis in 3T3 cells. *Cell*. 17:527-535.

van der Krogt, G.N., J. Ogink, B. Ponsioen, and K. Jalink. 2008. A comparison of donor-acceptor pairs for genetically encoded FRET sensors: application to the Epac cAMP sensor as an example. *PLoS One*. 3:e1916.

van Weely, S., M. Brandsma, A. Strijland, J.M. Tager, and J.M. Aerts. 1993. Demonstration of the existence of a second, non-lysosomal glucocerebrosidase that is not deficient in Gaucher disease. *Biochim. Biophys. Acta.* 1181:55-62.

VanGuilder, H.D., K.E. Vrana, and W.M. Freeman. 2008. Twenty-five years of quantitative PCR for gene expression analysis. *Biotechniques*. 44:619-626.

Verhey, K.J., and W. Yang. 2016. Permeability barriers for generating a unique ciliary protein and lipid composition. *Curr. Opin. Cell. Biol.* 41:109-116.

Vieira, O.V., K. Gaus, P. Verkade, J. Fullekrug, W.L. Vaz, and K. Simons. 2006. FAPP2, cilium formation, and compartmentalization of the apical membrane in polarized Madin-Darby canine kidney (MDCK) cells. *Proc. Natl. Acad. Sci. U.S.A.* 103:18556-18561.

Vuolo, L., A. Herrera, B. Torroba, A. Menendez, and S. Pons. 2015. Ciliary adenylyl cyclases control the Hedgehog pathway. *J. Cell Sci.* 128:2928-2937.

Wachten, D., and D.U. Mick. 2021. Signal transduction in primary cilia - analyzing and manipulating GPCR and second messenger signaling. *Pharmacol. Ther.* 224:107836.

Walden, C.M., R. Sandhoff, C.C. Chuang, Y. Yildiz, T.D. Butters, R.A. Dwek, F.M. Platt, and A.C. van der Spoel. 2007. Accumulation of glucosylceramide in murine testis, caused by inhibition of beta-glucosidase 2: implications for spermatogenesis. *J. Biol. Chem.* 282:32655-32664.

Wang, B., J.F. Fallon, and P.A. Beachy. 2000. Hedgehog-regulated processing of Gli3 produces an anterior/posterior repressor gradient in the developing vertebrate limb. *Cell*. 100:423-434.

Wang, W., and D.L. Brautigan. 2008. Phosphatase inhibitor 2 promotes acetylation of tubulin in the primary cilium of human retinal epithelial cells. *BMC Cell Biol.* 9:62.

Waters, A.M., and P.L. Beales. 2011. Ciliopathies: an expanding disease spectrum. *Pediatr. Nephrol.* 26:1039-1056.

Wen, X., C.K. Lai, M. Evangelista, J.A. Hongo, F.J. de Sauvage, and S.J. Scales. 2010. Kinetics of hedgehog-dependent full-length Gli3 accumulation in primary cilia and subsequent degradation. *Mol. Cell Biol.* 30:1910-1922.

Wheatley, D.N. 2018. The primary cilium - once a "rudimentary" organelle that is now a ubiquitous sensory cellular structure involved in many pathological disorders. *J. Cell Commun. Signal.* 12:211-216.

Wheway, G., L. Nazlamova, and J.T. Hancock. 2018. Signaling through the Primary Cilium. *Front. Cell Dev. Biol.* 6.

Wingfield, J.L., K.F. Lechtreck, and E. Lorentzen. 2018. Trafficking of ciliary membrane proteins by the intraflagellar transport/BBSome machinery. *Essays Biochem.* 62:753-763.

Woeste, M.A. 2018. The role of GBA2 in controlling locomotor activity. *In* Mathematisch-Naturwissenschaftliche Fakultät. Vol. Dr. rer. nat. Rheinische Friedrich-Wilhelms-Universität Bonn, Bonn.

Wood, C.R., and J.L. Rosenbaum. 2015. Ciliary ectosomes: transmissions from the cell's antenna. *Trends Cell Biol.* 25:276-285.

Yamaji, T., and K. Hanada. 2015. Sphingolipid metabolism and interorganellar transport: localization of sphingolipid enzymes and lipid transfer proteins. *Traffic*. 16:101-122.

Yamakawa, D., D. Katoh, K. Kasahara, T. Shiromizu, M. Matsuyama, C. Matsuda, Y. Maeno, M. Watanabe, Y. Nishimura, and M. Inagaki. 2021. Primary cilia-dependent lipid raft/caveolin dynamics regulate adipogenesis. *Cell Rep.* 34:108817.

Yamamoto, K.K., G.A. Gonzalez, W.H. Biggs, and M.R. Montminy. 1988. Phosphorylation-induced binding and transcriptional efficacy of nuclear factor CREB. *Nature*. 334:494-498.

Ye, F., A.R. Nager, and M.V. Nachury. 2018. BBSome trains remove activated GPCRs from cilia by enabling passage through the transition zone. *J. Cell Biol.* 217:1847-1868.

Yildiz, Y., H. Matern, B. Thompson, J.C. Allegood, R.L. Warren, D.M. Ramirez, R.E. Hammer, F.K. Hamra, S. Matern, and D.W. Russell. 2006. Mutation of beta-glucosidase 2 causes glycolipid storage disease and impaired male fertility. *J. Clin. Invest.* 116:2985-2994.

Yip, P. 2016. Nanometrology using Time-Resolved Fluorescence. University of Strathclyde.

Zeng, X., J.A. Goetz, L.M. Suber, W.J. Scott, Jr., C.M. Schreiner, and D.J. Robbins. 2001. A freely diffusible form of Sonic hedgehog mediates long-range signalling. *Nature*. 411:716-720.

Zhao, C. 2014. Hedgehog (Hh) Reporter Activity Assay. *Bio Protoc.* 4:e1182.

Zidovetzki, R., and I. Levitan. 2007. Use of cyclodextrins to manipulate plasma membrane cholesterol content: evidence, misconceptions and control strategies. *Biochim. Biophys. Acta.* 1768:1311-1324.

Zimmerman, N.P., I. Roy, A.D. Hauser, J.M. Wilson, C.L. Williams, and M.B. Dwinell. 2015. Cyclic AMP regulates the migration and invasion potential of human pancreatic cancer cells. *Mol. Carcinog.* 54:203-215.

Zimmermann, K.W. 1898. Beiträge zur Kenntniss einiger Drüsen und Epithelien. *Arch. Für Mikrosk. Anat.* 52:552-706.

6 Appendix

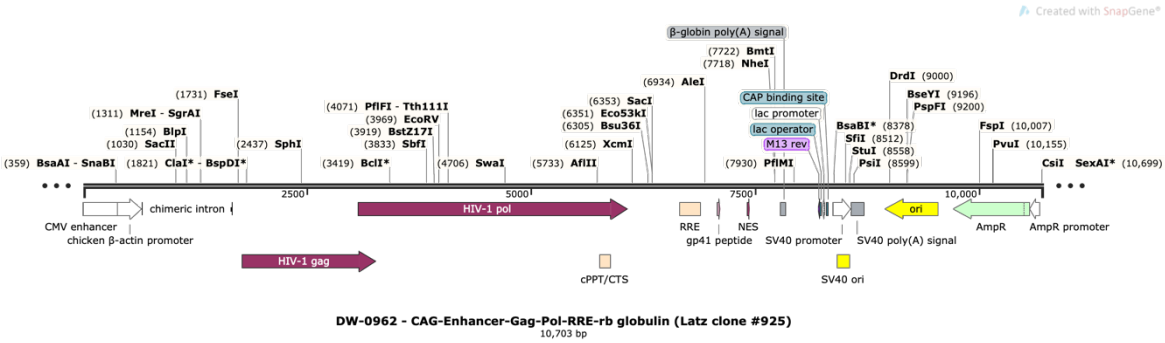

Figure 58: Plasmid map of CAG-Enhancer-Gag-Pol-RRE-rb globulin. The figure has been created with SnapGene Viewer.

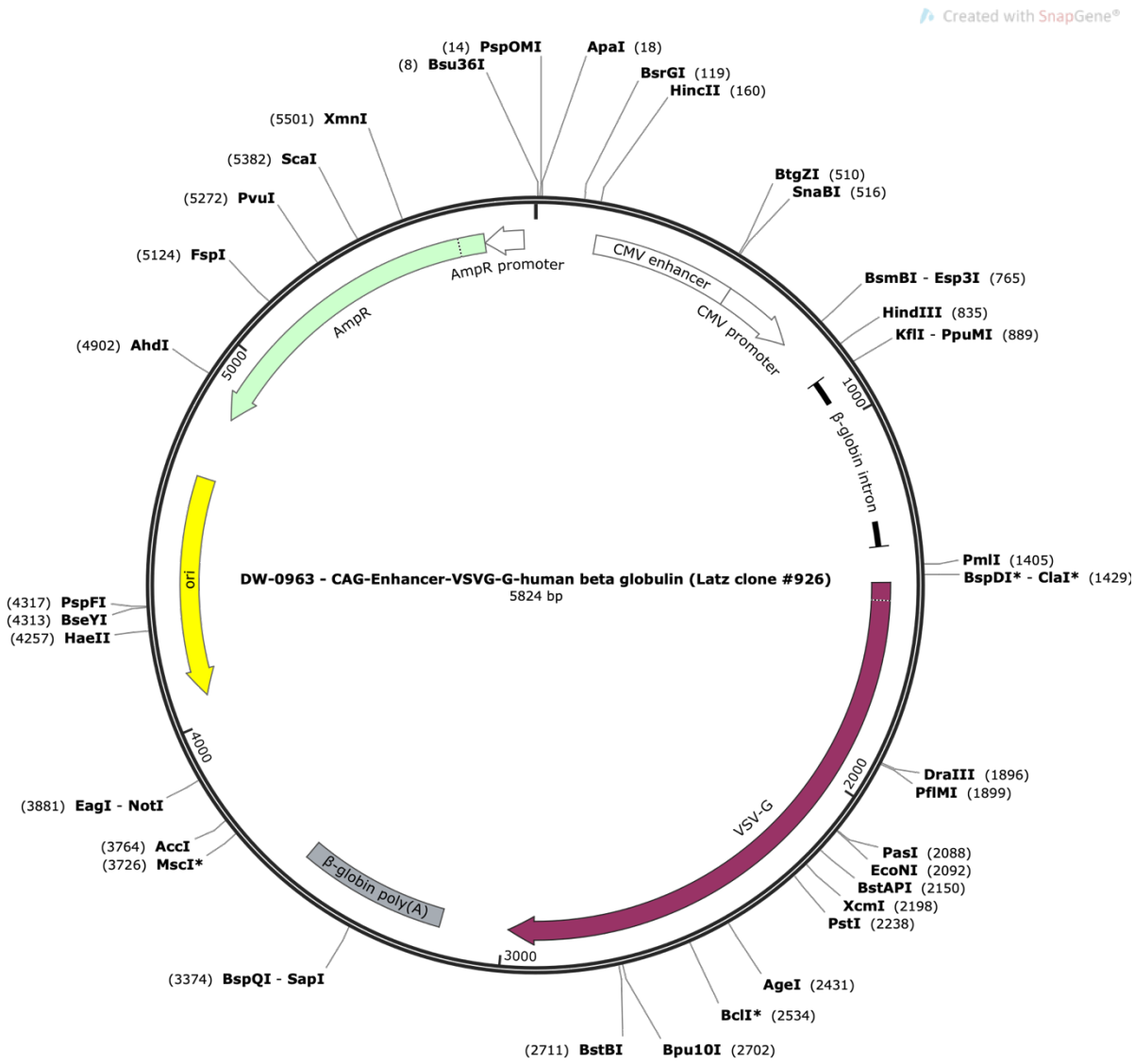

Figure 59: Plasmid map of CAG-Enhancer-VSVG-G-human beta globulin. The figure has been created with SnapGene Viewer.

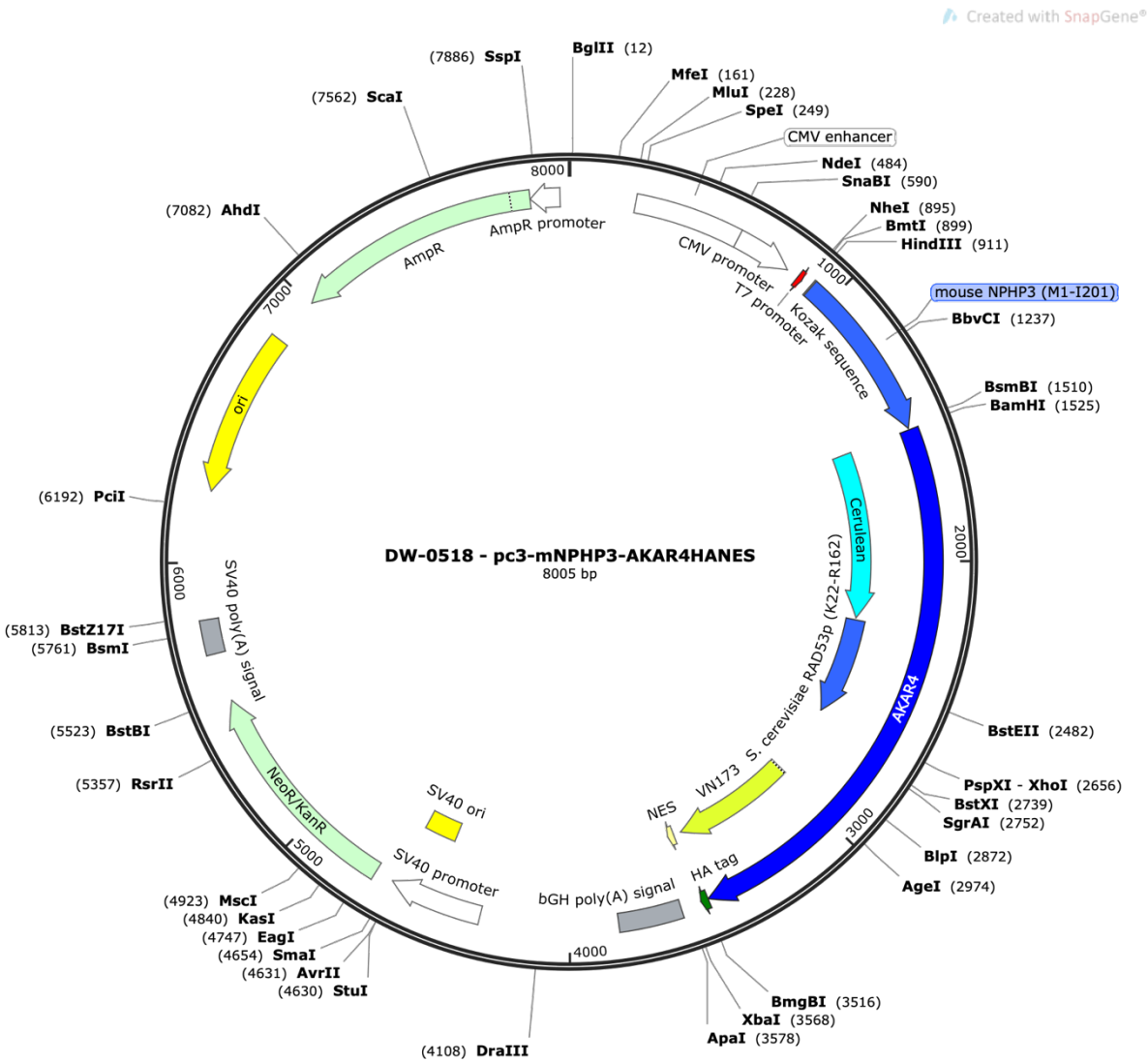

Figure 60: Plasmid map of pc3-mNPHP3-AKAR4HANES. The figure has been created with SnapGene Viewer.

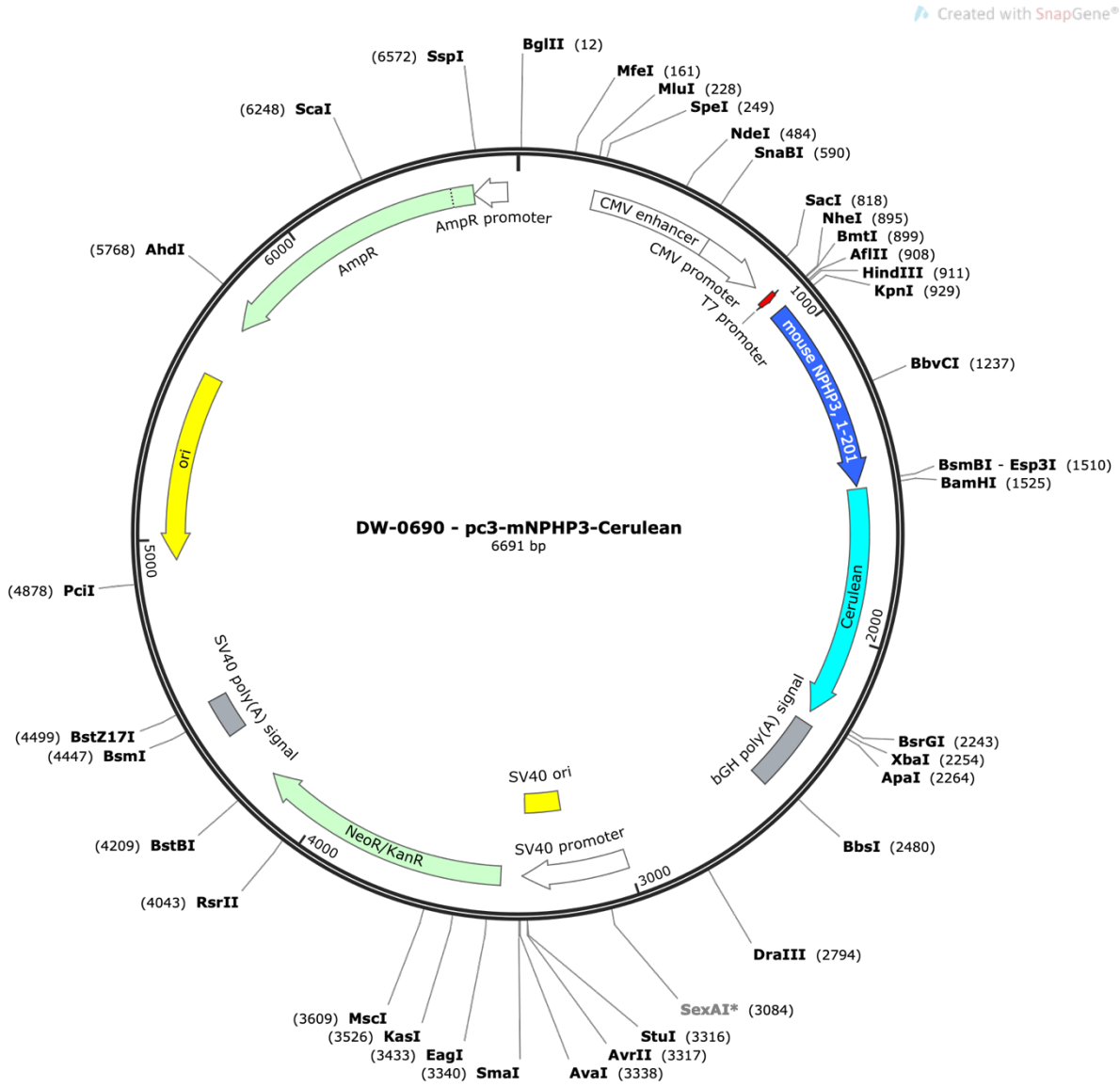

Figure 61: Plasmid map of pc3-mNPHP3-Cerulean-4. The figure has been created with SnapGene Viewer.

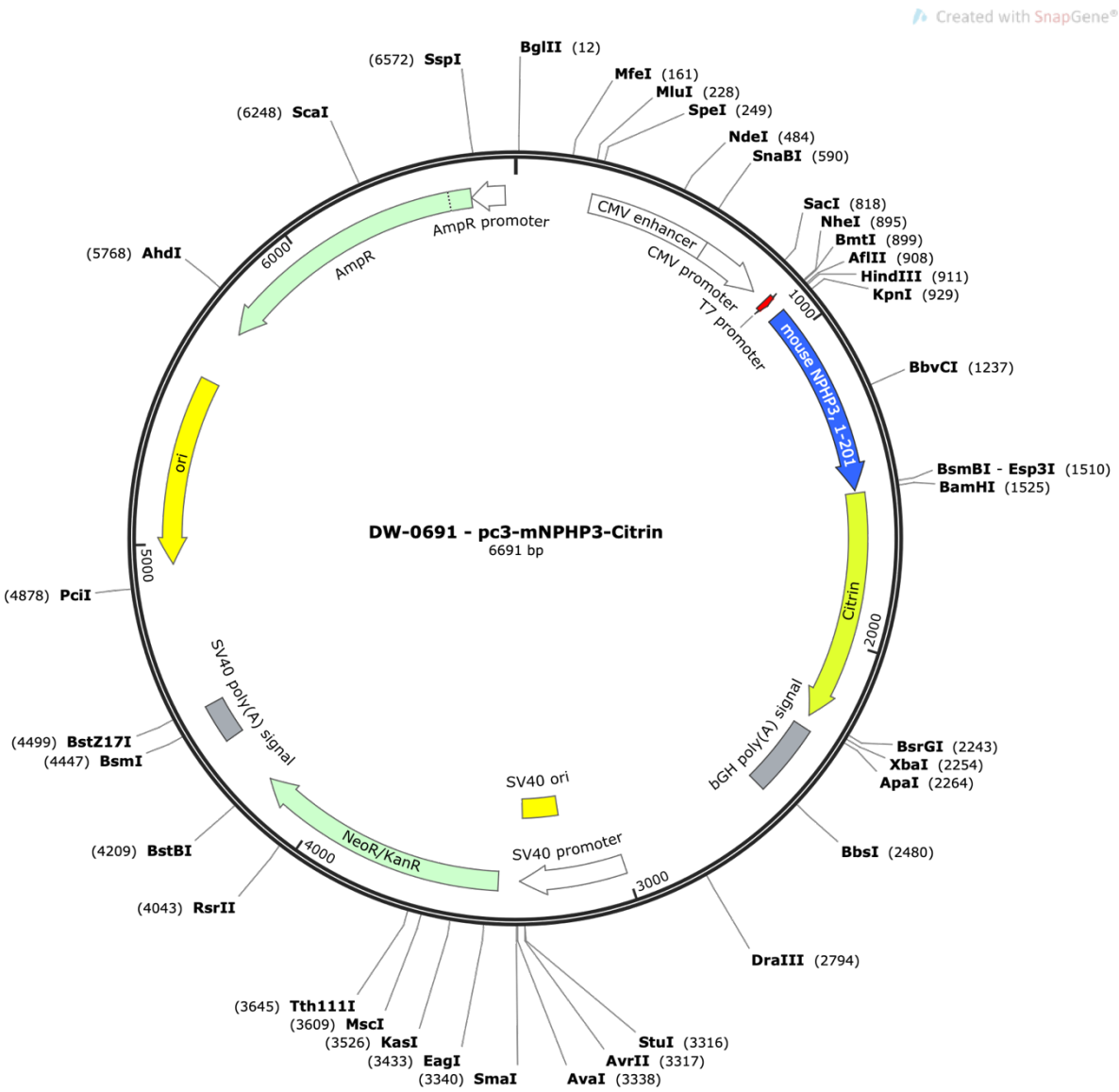

Figure 62: Plasmid map of pc3-mNPHP3-Citrin-3. The figure has been created with SnapGene Viewer.

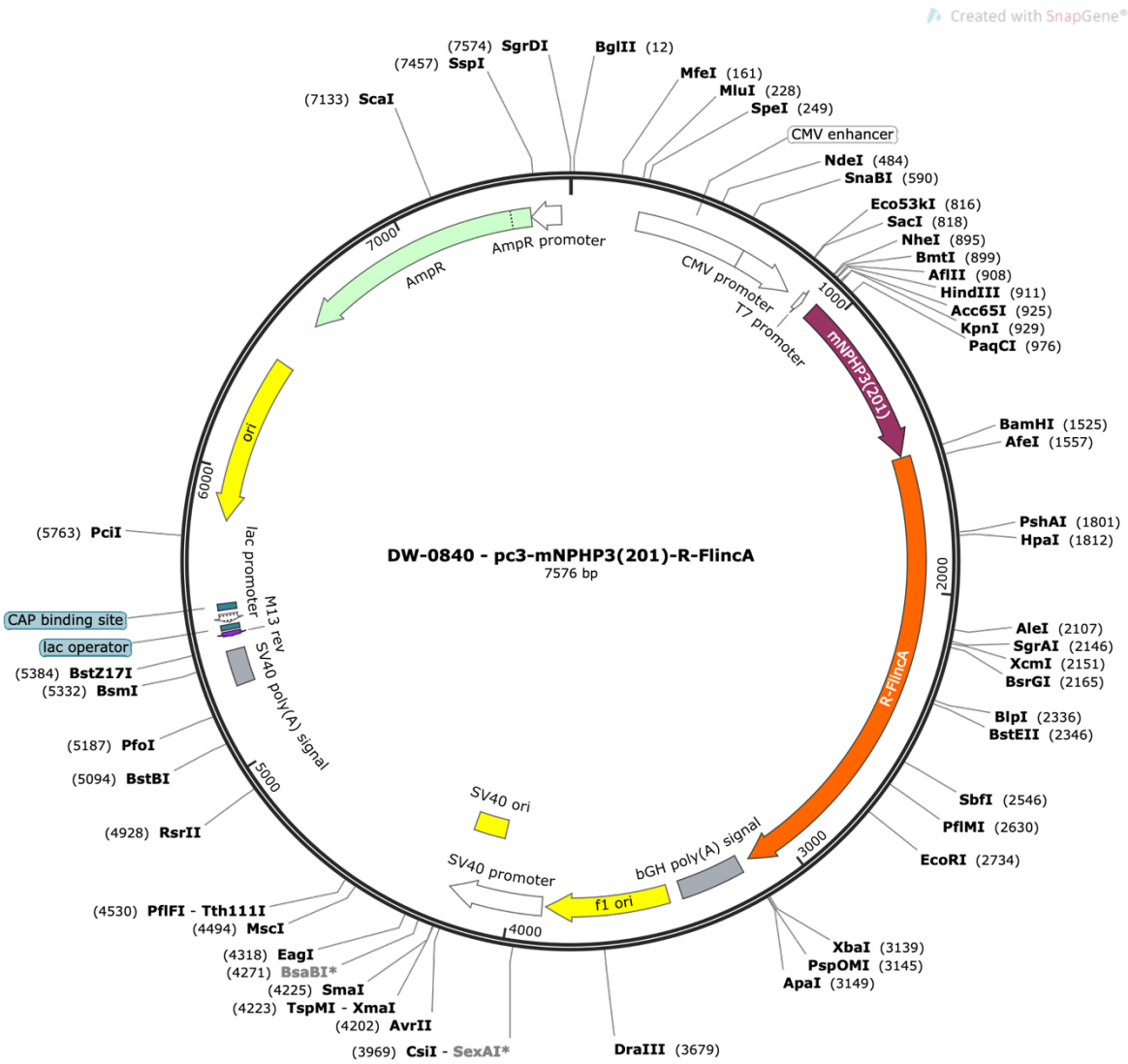

Figure 63: Plasmid map of pc3-mNPHP3-R-FlincA-12. The figure has been created with SnapGene Viewer.

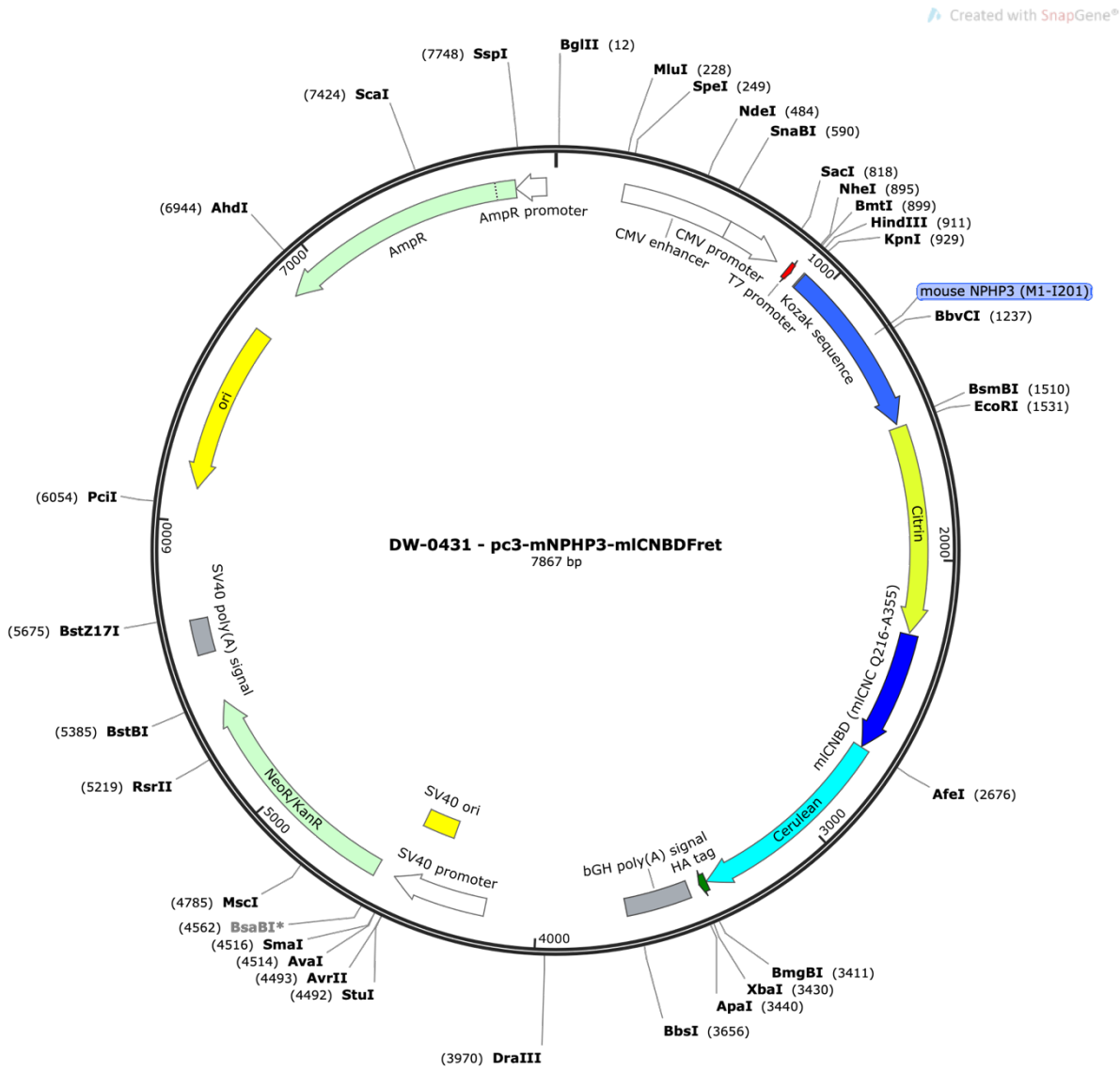

Figure 64: Plasmid map of pc3-mNPHP3(201)-mlCNBD-FRET-1. The figure has been created with SnapGene Viewer.

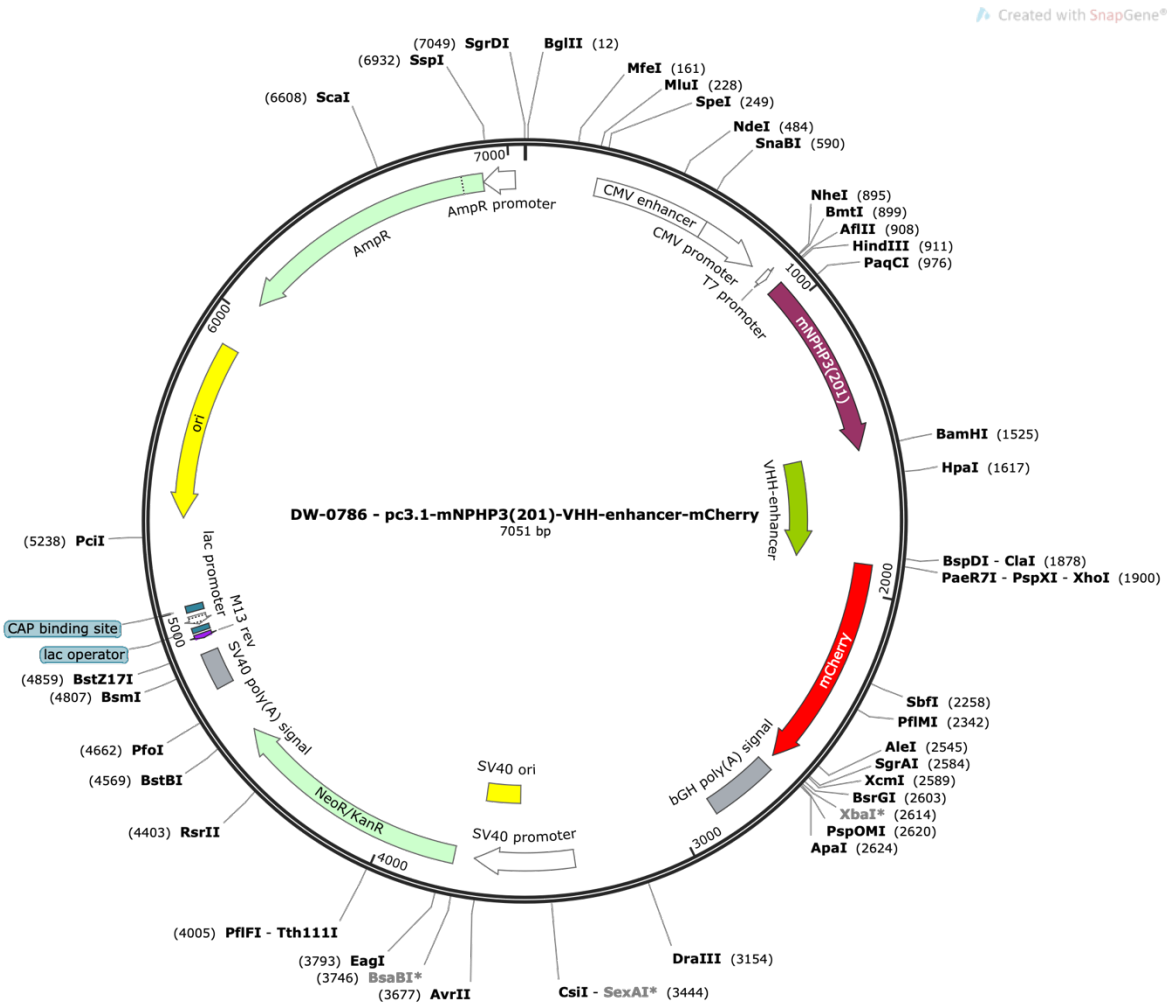

Figure 65: Plasmid map of pc3.1-mNPHP3(201)-VHH-enhancer-mCherry-7. The figure has been created with SnapGene Viewer.

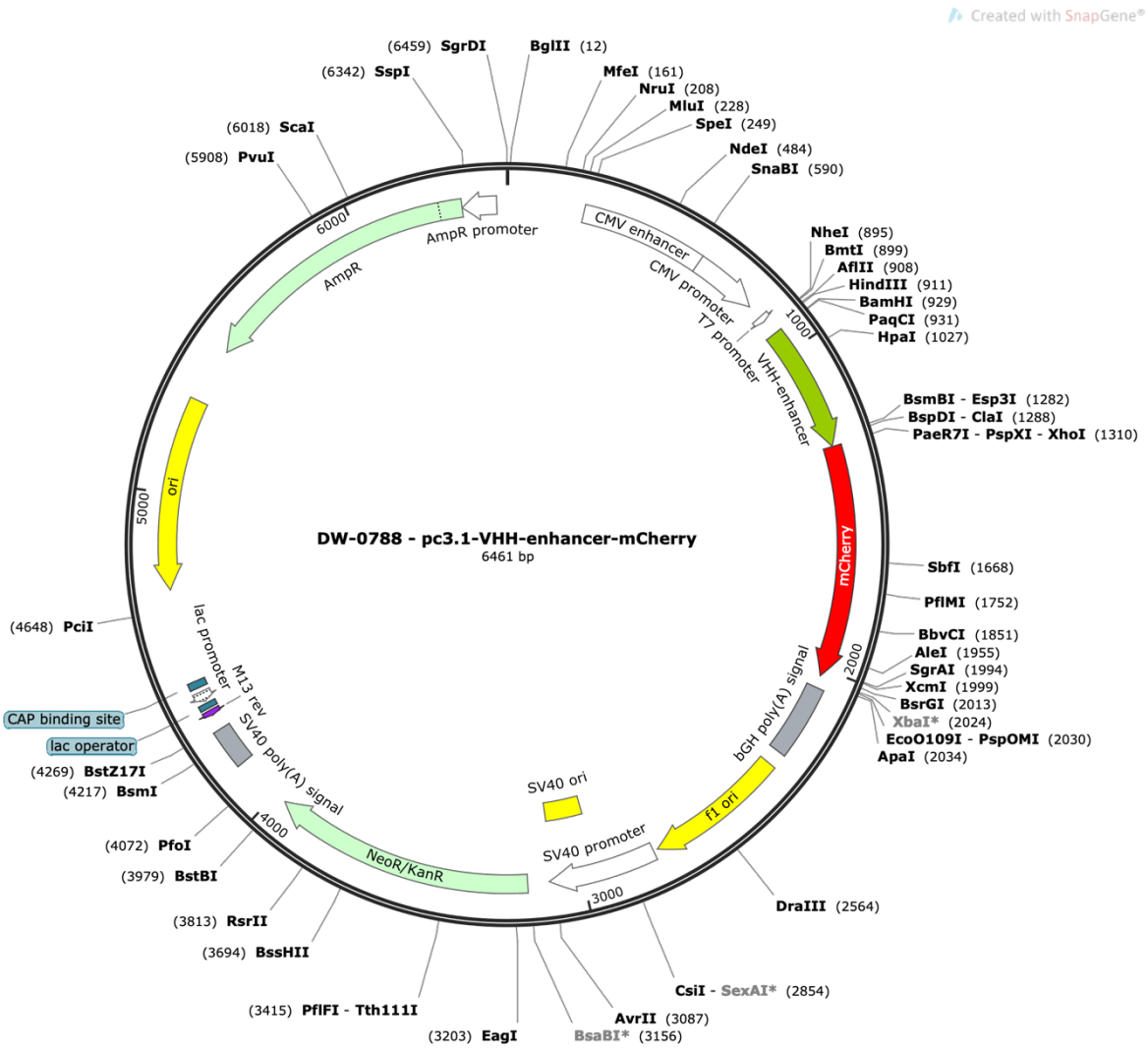

Figure 66: Plasmid map of pc3.1-VHH-enhancer-mCherry #4. The figure has been created with SnapGene Viewer.

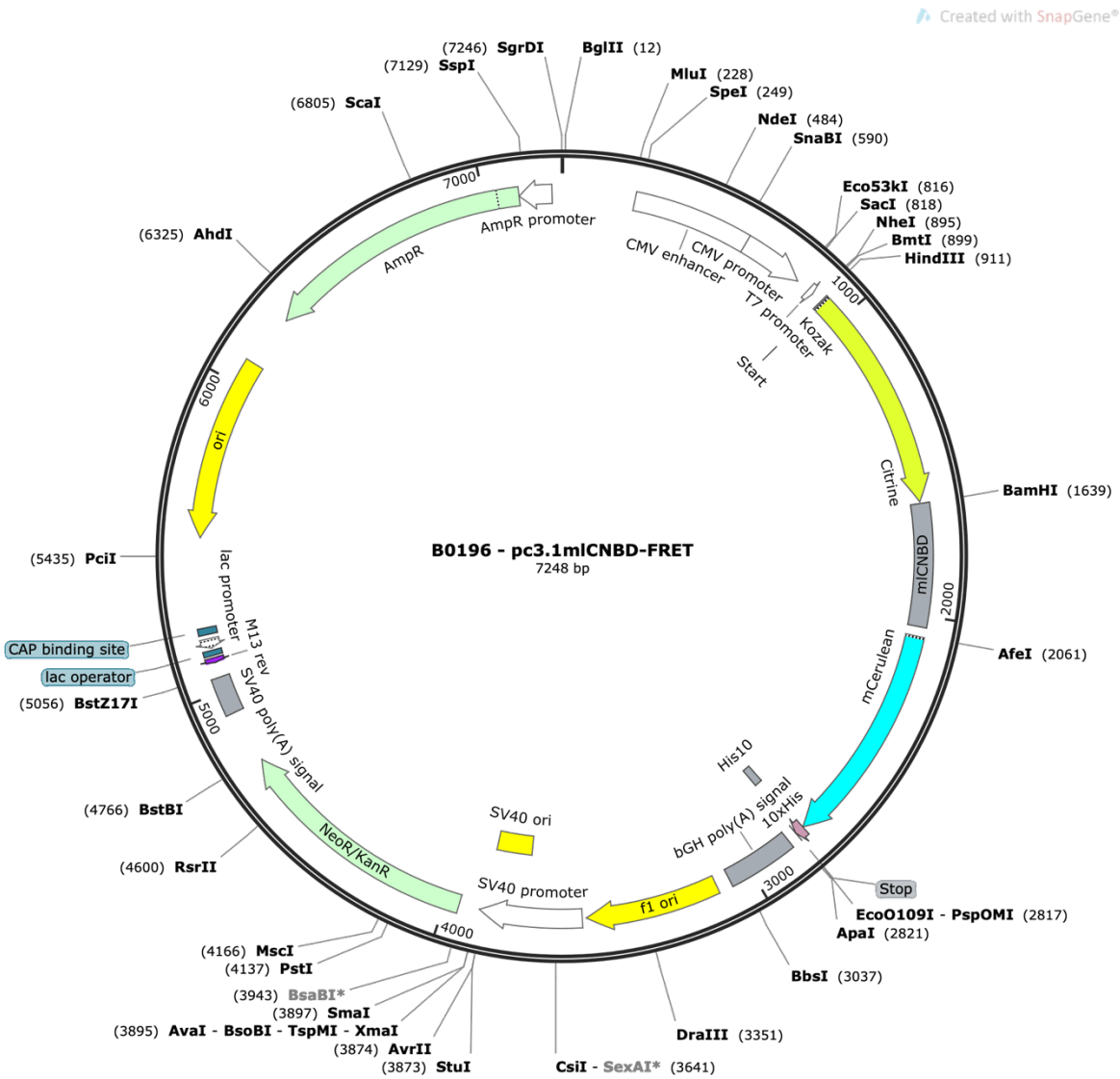

Figure 67: Plasmid map of pc3.1mlCNBD-FRET#9. The figure has been created with SnapGene Viewer.

Figure 68: Plasmid map of pcA-Cerulean. The figure has been created with SnapGene Viewer.

Figure 69: Plasmid map of pcA-Citrine. The figure has been created with SnapGene Viewer.

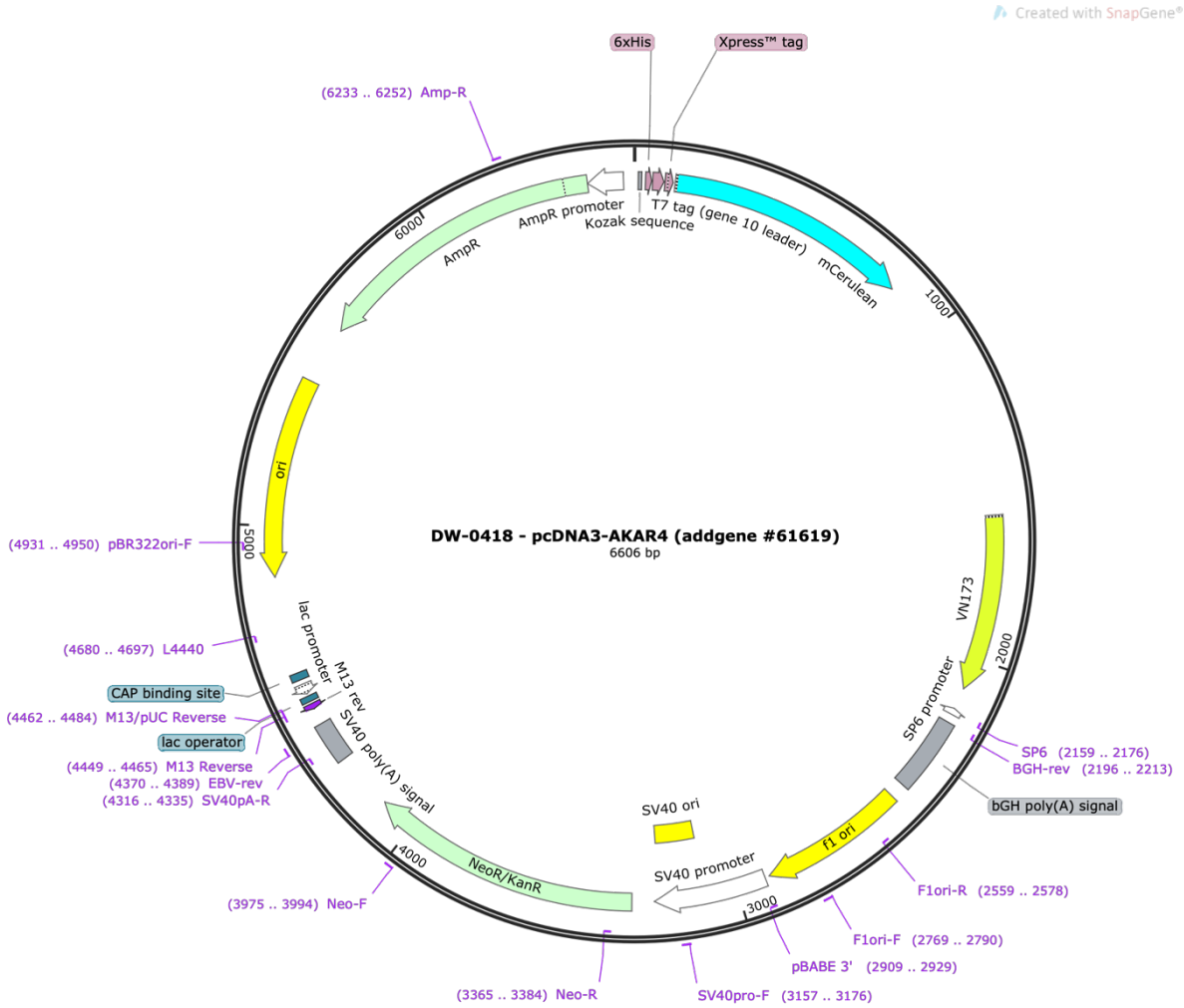

Figure 70: Plasmid map of pcDNA3-AKAR4. The figure has been created with SnapGene Viewer.

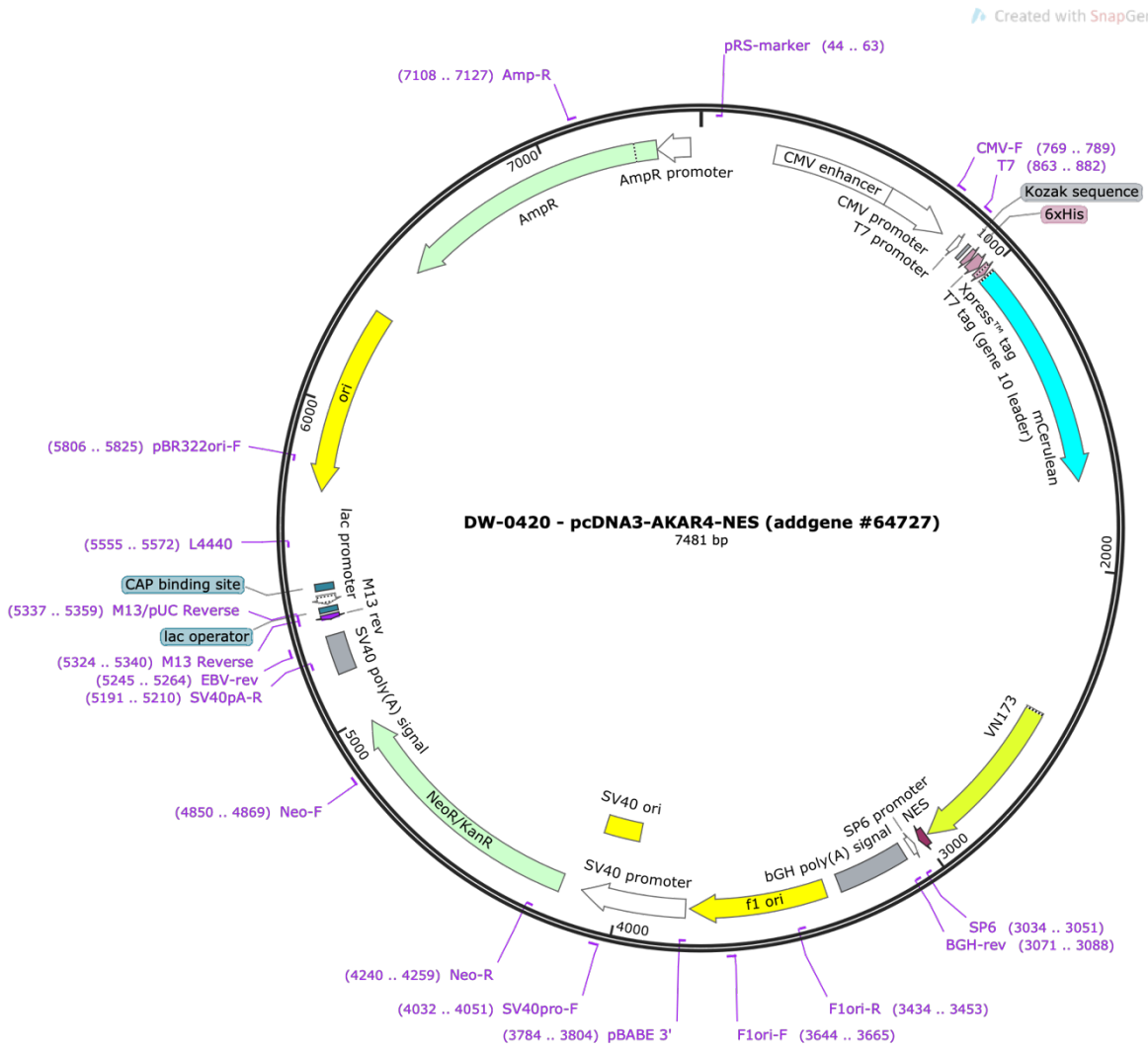

Figure 71: Plasmid map of pcDNA3-AKAR4-NES. The figure has been created with SnapGene Viewer.

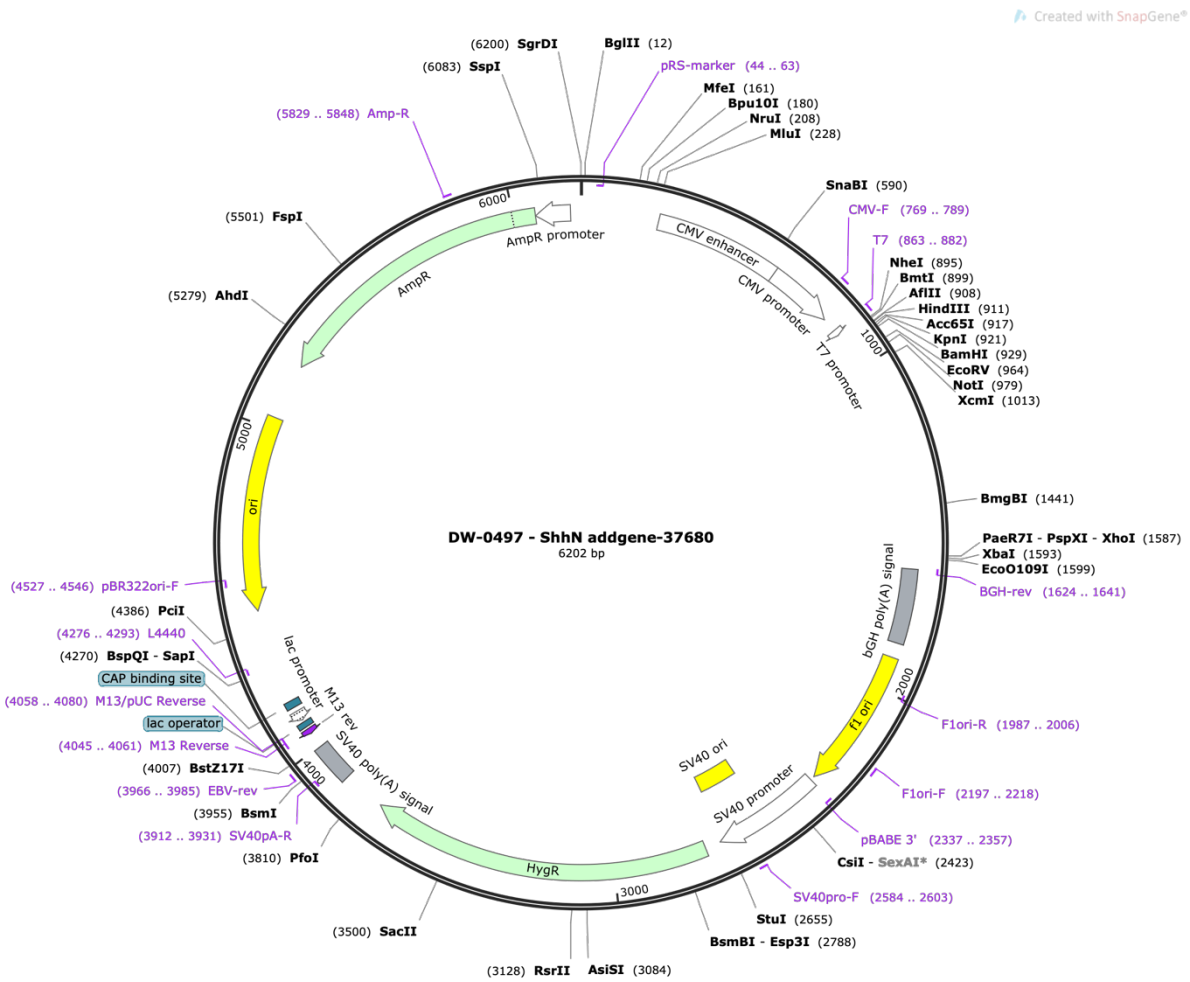

Figure 72: Plasmid map of pcDNA3.1-Shh-N. The figure has been created with SnapGene Viewer.

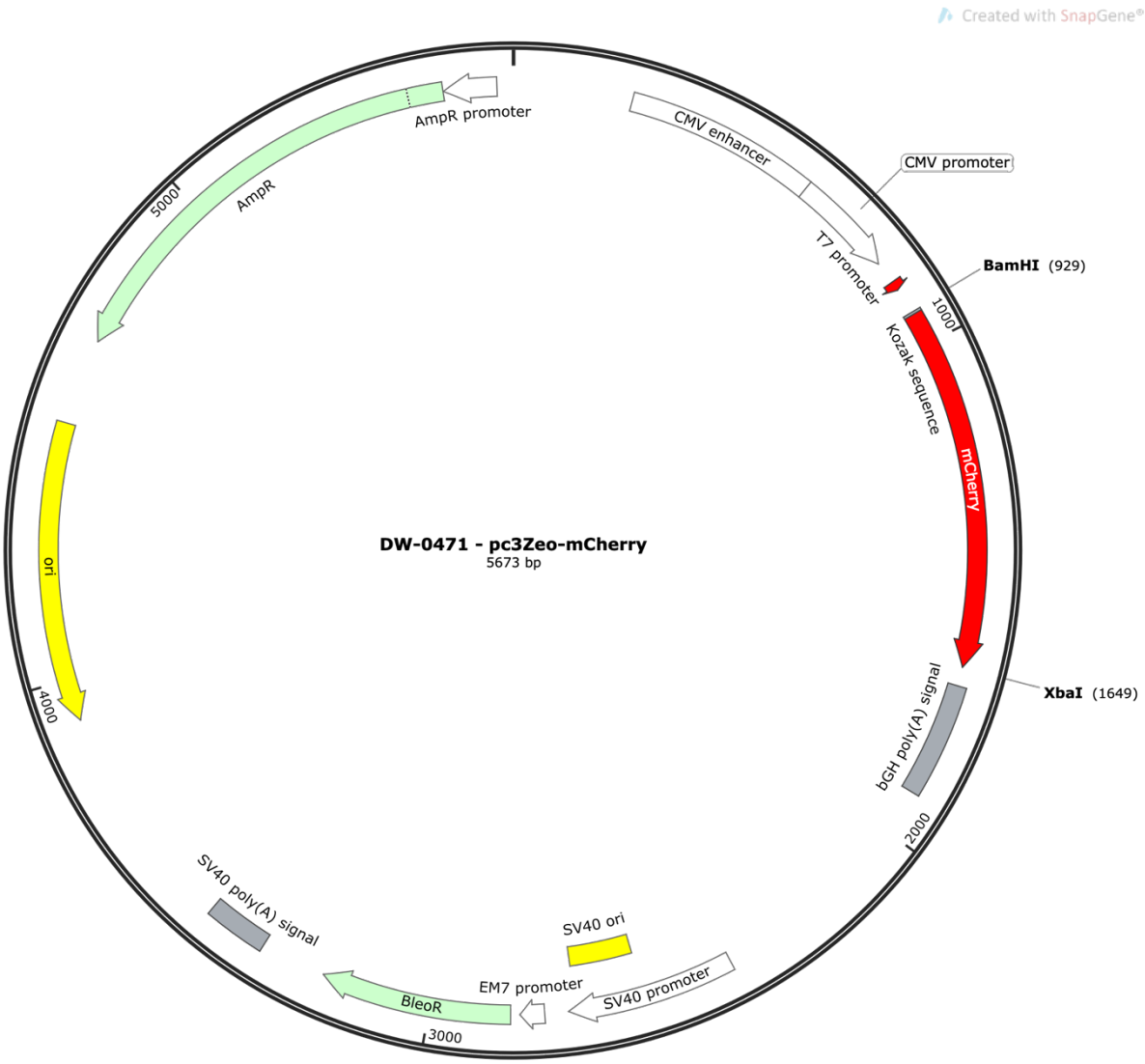

Figure 73: Plasmid map of pcDNA3.1zeo_mCherry. The figure has been created with SnapGene Viewer.

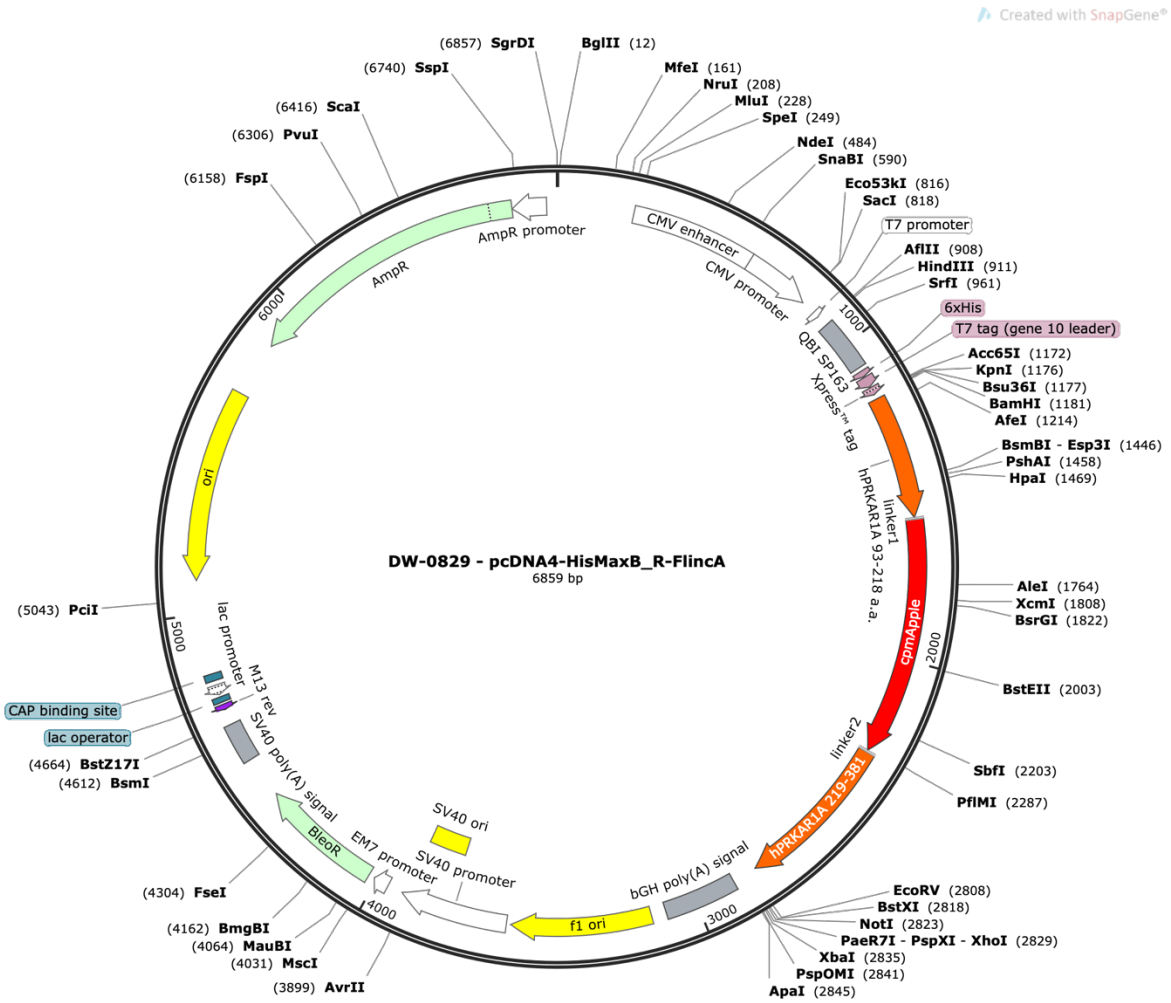

Figure 74: Plasmid map of pcDNA4-HisMaxB_R-FlincA. The figure has been created with SnapGene Viewer.

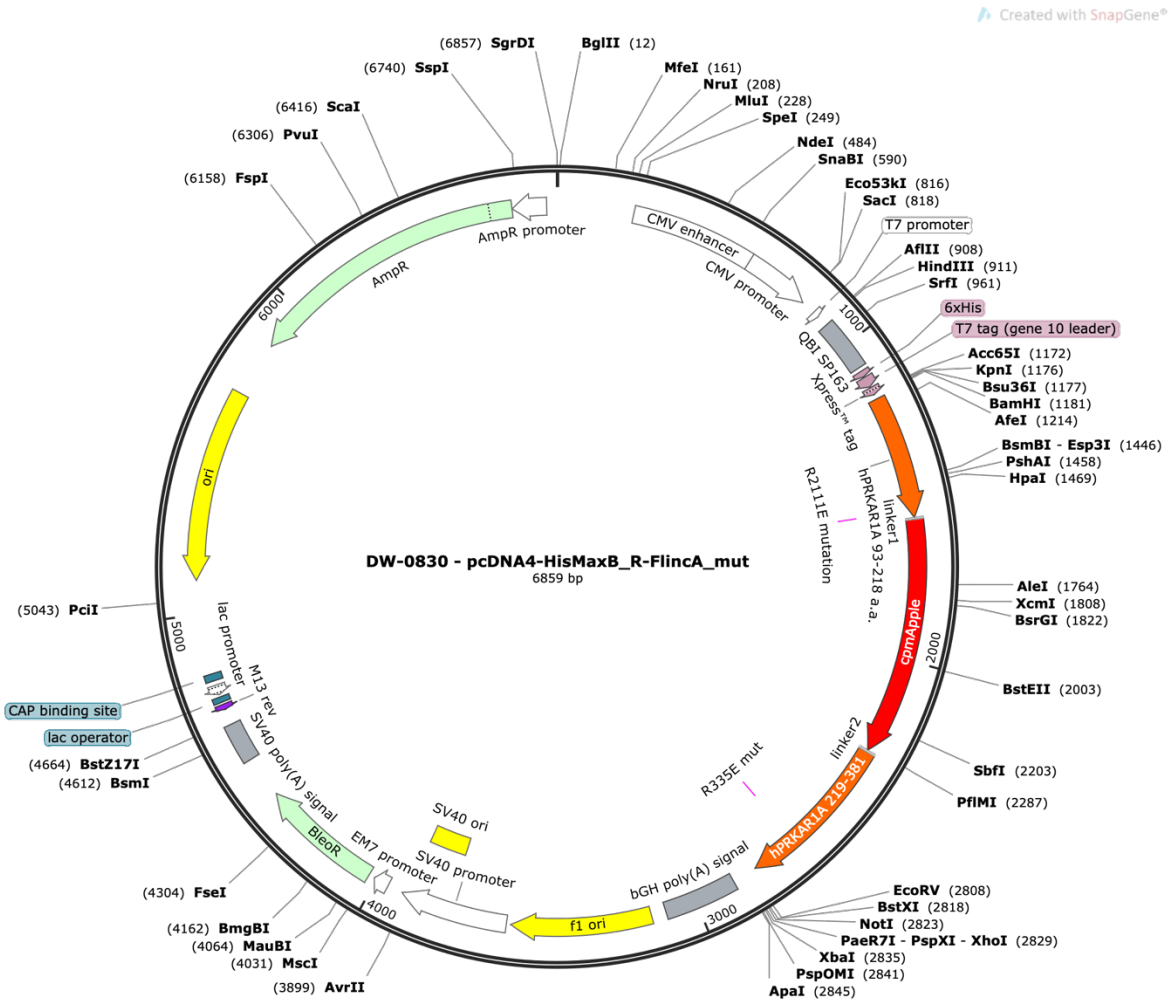

Figure 75: Plasmid map of pcDNA4-HisMaxB_R-FlincA-mut. The figure has been created with SnapGene Viewer.

Figure 76: Plasmid map of pEGFP-N1-bPAC #1. The figure has been created with SnapGene Viewer.

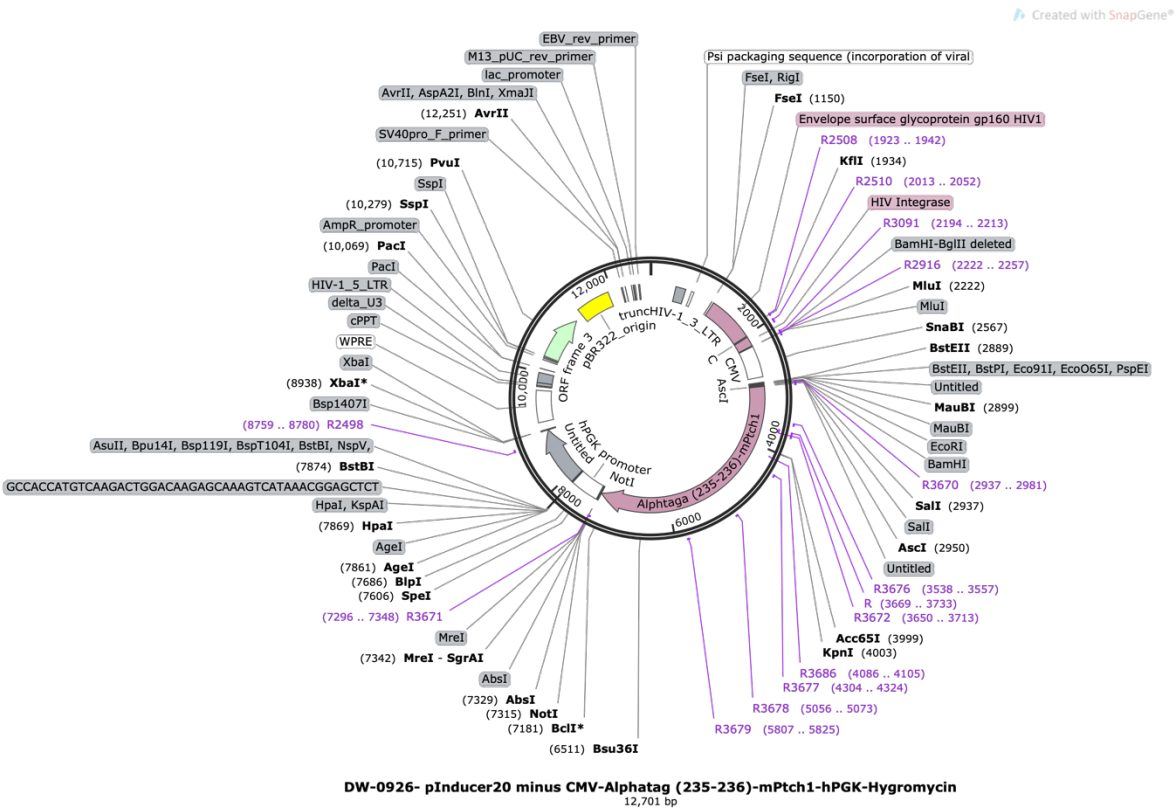

Figure 77: Plasmid map of pInducer20_minus_CMV_ALFAtag-(235-236)-mPtch1. The figure has been created with SnapGene Viewer.

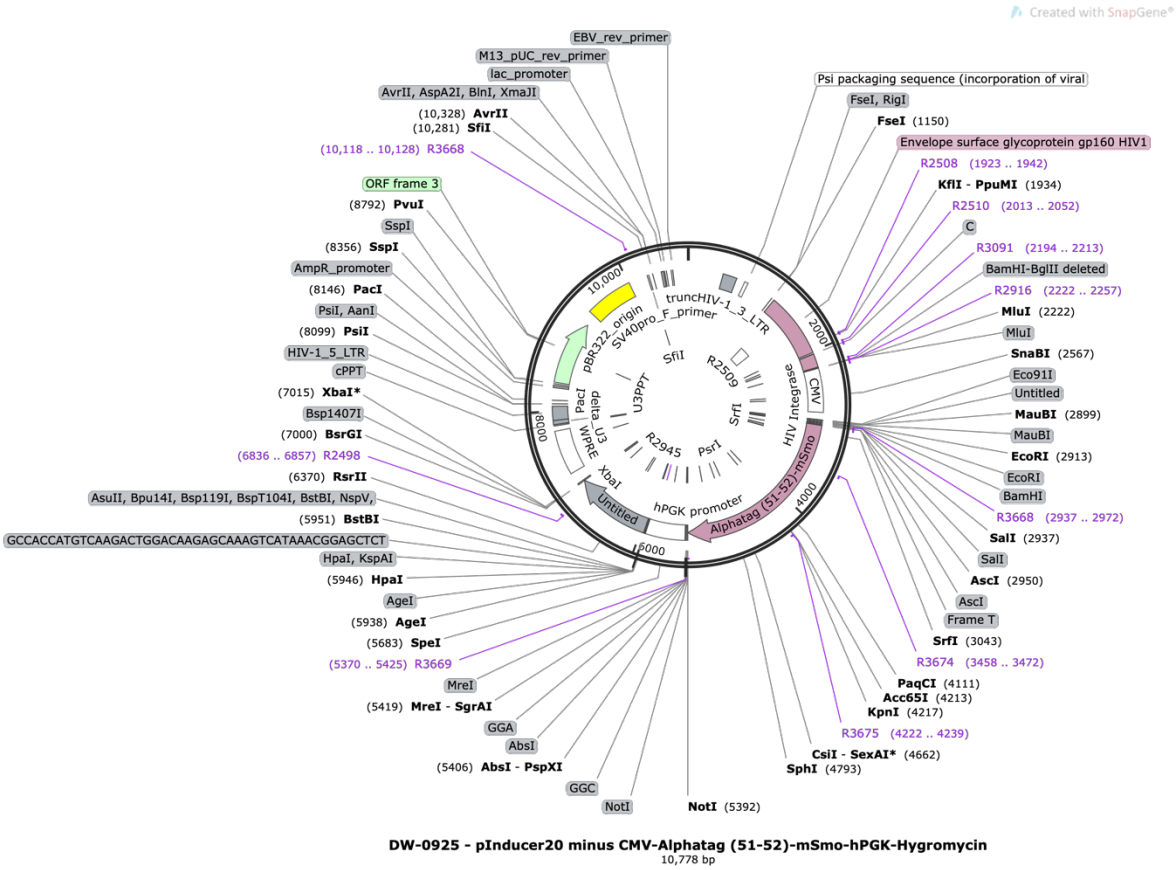

Figure 78: Plasmid map of pInducer20_minus_CMV_ALFAtag-(51-52)-mSmo. The figure has been created with SnapGene Viewer.

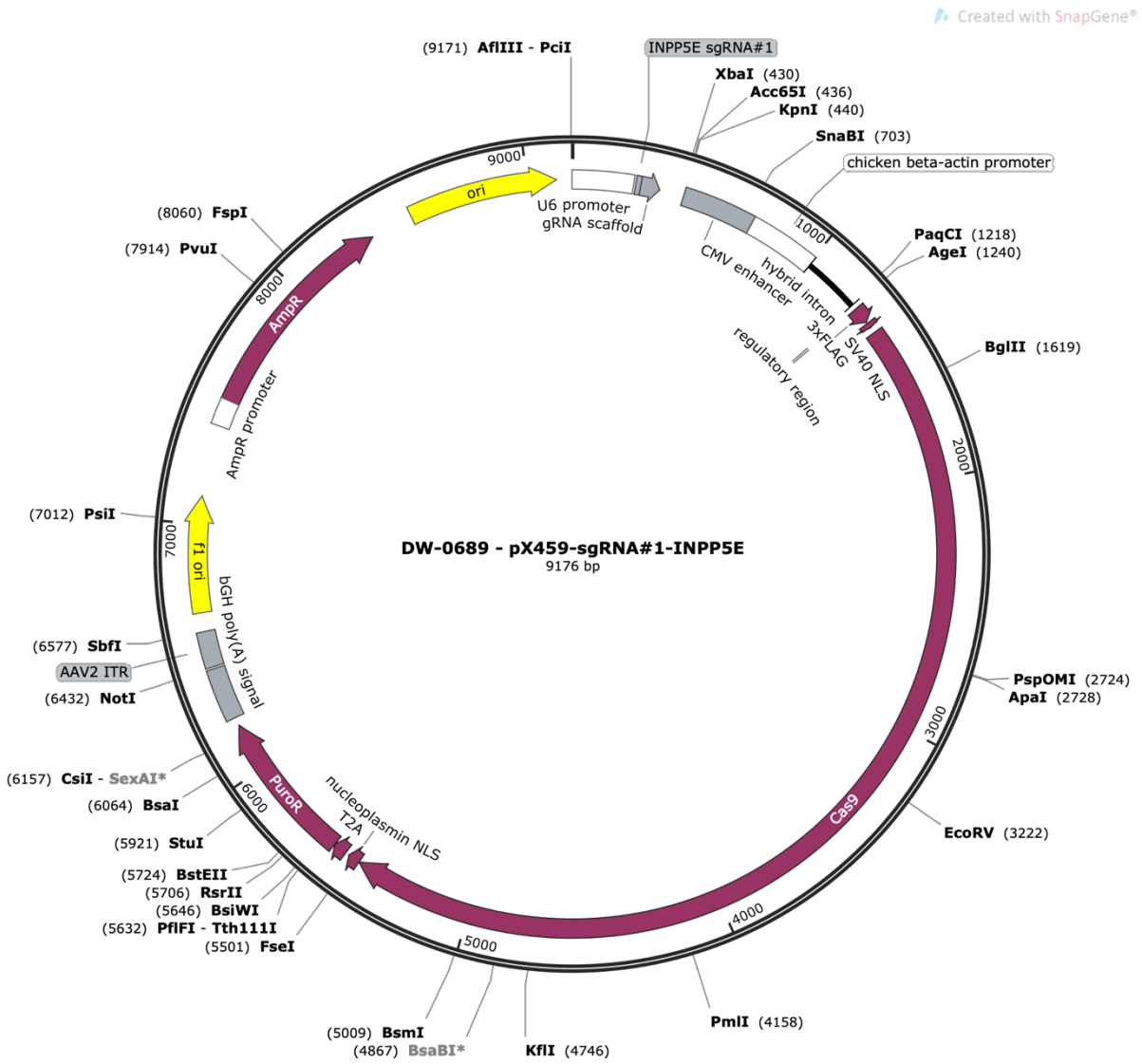

Figure 79: Plasmid map of pX459-sgRNA#1-INPP5E. The figure has been created with SnapGene Viewer.

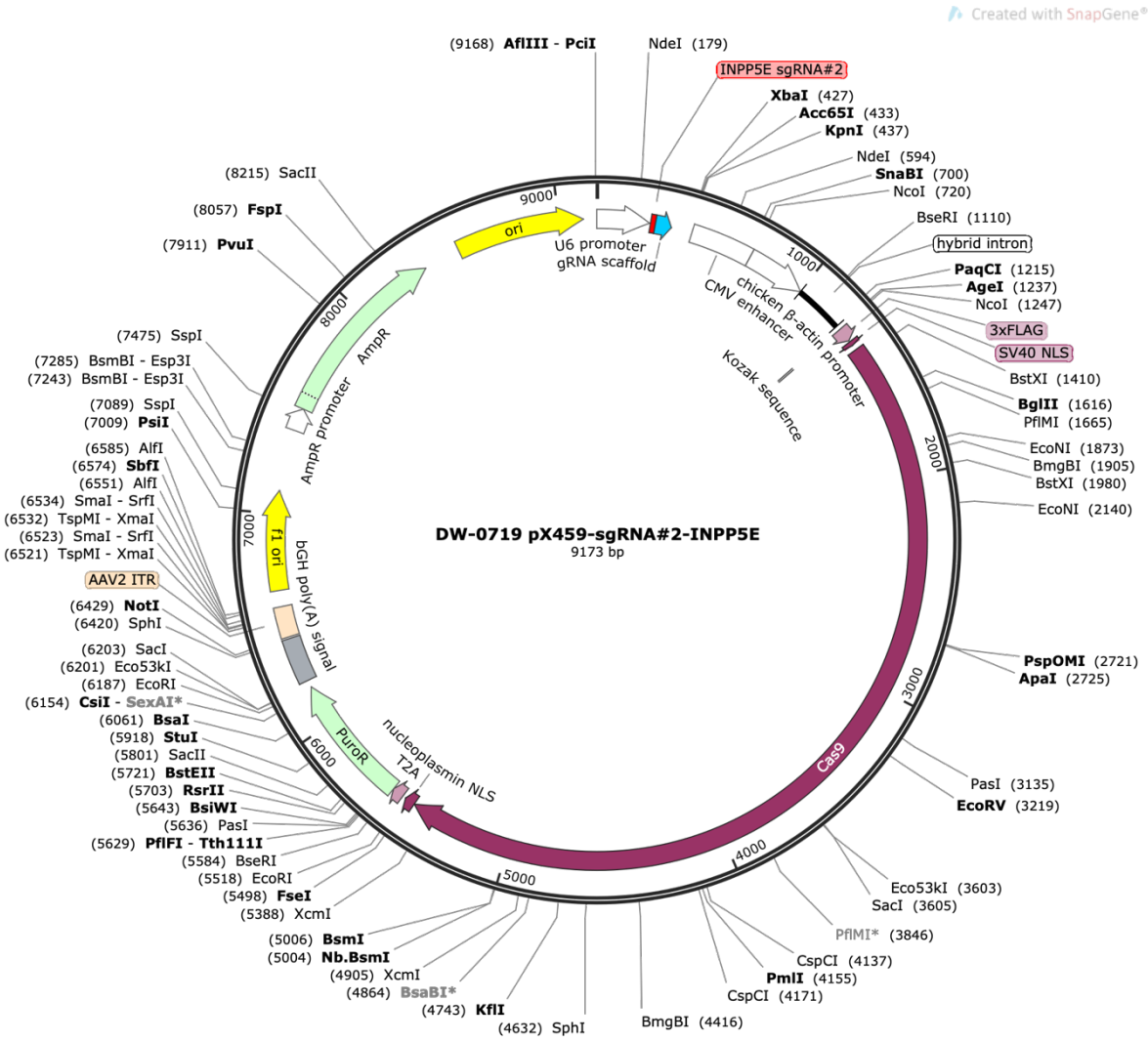

Figure 80: Plasmid map of pX459-sgRNA#2-INPP5E. The figure has been created with SnapGene Viewer.

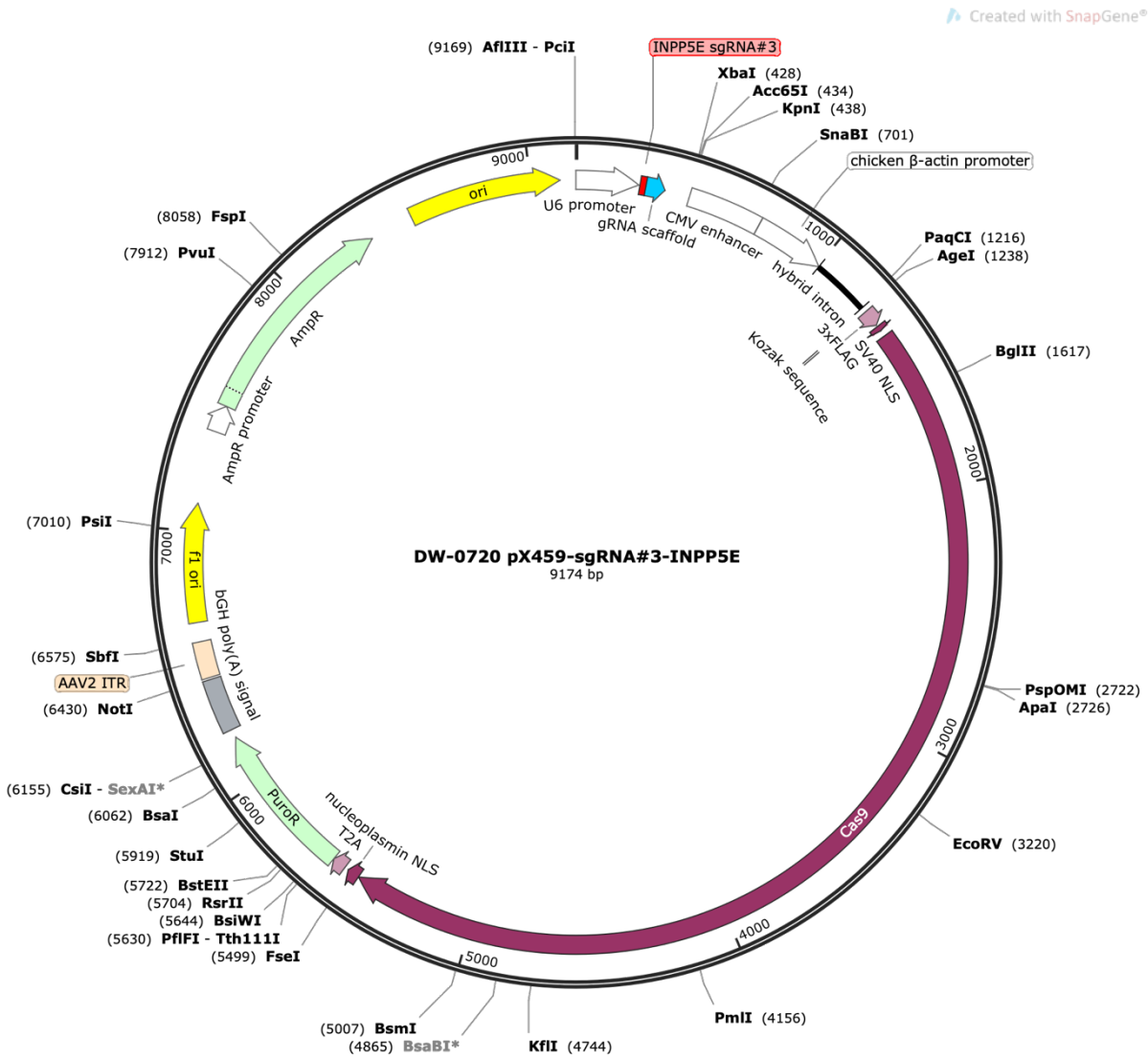

Figure 81: Plasmid map of pX459-sgRNA#3-INPP5E. The figure has been created with SnapGene Viewer.

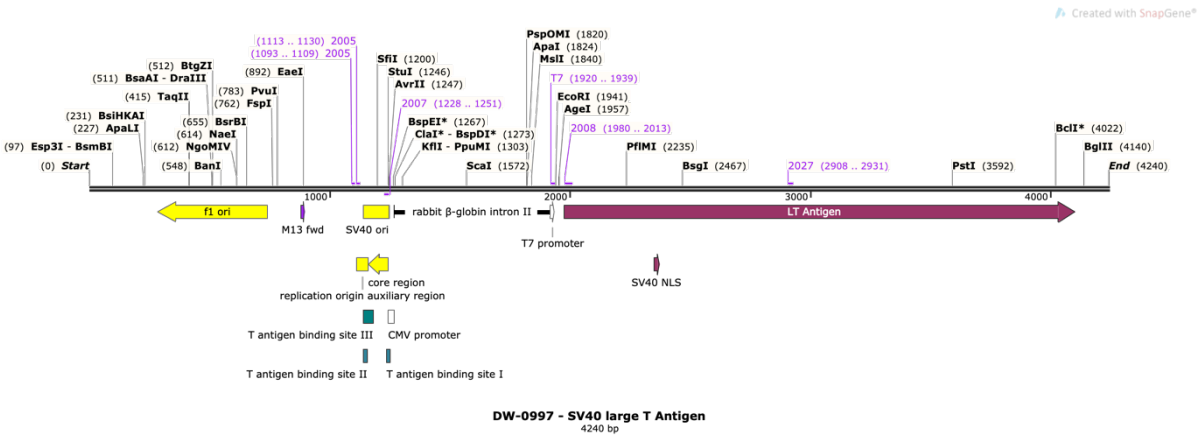

Figure 82: Plasmid map of SV-40 large T Antigen. The figure has been created with SnapGene Viewer.

Danksagung

Diese Arbeit wurde in der Forschungsgruppe von Prof. Dr. Dagmar Wachten am Max-Planck-Institut caesar in Bonn und am Institut für angeborene Immunität des Universitätsklinikums in Bonn angefertigt. Mein Dank gilt allen Mitarbeitern dieser Forschungsinstitute für die Unterstützung und Zusammenarbeit.

Insbesondere danke ich folgenden Personen:

- Prof. Dr. Dagmar Wachten für die Möglichkeit an diesem Projekt zu forschen, die vielen inspirierenden Gespräche und die tolle Unterstützung während dieser Zeit.
- Prof. Dr. Christoph Thiele für seine Unterstützung der Massenspektrometrie, deren Analyse, für seine Beiträge zu meiner Arbeit in meinem „Thesis committee“ und seine Beteiligung als Zweitgutachter in der Prüfungskommission.
- Prof. Dr. Florian I. Schmidt als Betreuer meines „Thesis committee“ und seiner hilfreichen Ratschläge.
- Prof. Dr. Stefanie Weidtkamp-Peters als Betreuerin meines „Thesis committee“ und ihrer hilfreichen Ratschläge.
- Prof. Dr. Michael J. Pankratz für seine Beteiligung als dritter, fachnaher Gutachter in der Prüfungskommission
- Prof. Dr. Ute Vothknecht für ihre Beteiligung als vierte, fachnahe Gutachterin in der Prüfungskommission.
- Nora Winnerling, Christina Klausen, Kim Dressler, Isabel Lux, Dana Herborn und Mona Völker für ihre Unterstützung der Tierstallangelegenheiten.
- Philipp Leyendecker für seine Unterstützung der Lipid-Extraktionen und Massenspektrometrie.
- Jan Niklas Hansen für seine Unterstützung der Bildauswertung mit seinen Fiji/ImageJ plugins.
- Jens-Henning Krause für seine Unterstützung im Labor.
- Dr. Mylene Hübecker für ihre Unterstützung bei lipid-basierten Fragen.
- Allen Mitgliedern der AG Wachten für eine angenehme Arbeitsatmosphäre und Unterstützung in jeder Hinsicht.

Bedanken möchte ich mich auch beim Bonner Forum Biomedizin für die zahlreichen Veranstaltungen und Seminare und meiner Familie für ihre Unterstützung.

Ein besonderer Dank gilt meiner Frau Caro; danke, dass du an meiner Seite bist und mich immer unterstützt!